Solving dynamical mean-field theory using matrix product states

Dissertation
der Fakultät für Physik
der Ludwig-Maximilians-Universität München

vorgelegt von

FABIAN ALEXANDER WOLF
aus Prien am Chiemsee

2015

Abstract

The present thesis advances and applies matrix product state (MPS) based algorithms to the solution of dynamical mean-field theory (DMFT) and its variants. This makes it possible to solve certain quantum many-body problems in and out of equilibrium, which were previously out of reach for any numerical treatment. In equilibrium, this concerns in particular the computation of the electronic — such as insulating, metallic, spin-freezed and many other — phases of highly complex realistic models for correlated materials. In non-equilibrium, this concerns in particular the understanding of the fundamental mechanisms of the relaxation behavior of quantum many-body systems on short and intermediate time scales.

The problem was first to determine a reliable and automatable method for computing Green's functions using MPS. Their computation relies on evaluating a sequence of many-body states, which is associated with an expansion of the Green's function in a family of orthogonal functions. We showed that one should choose plain waves (i.e. "perform time evolution") or, with reduced computational efficiency, Chebyshev polynomials for this. The most decisive question then was whether one evaluates the DMFT self-consistency equations on the (i) real- or on the (ii) imaginary-frequency axis. The fundamental difference stems from the fact that in case (i), the sequence of MPS becomes highly entangled, and computations therefore ultimately too costly, whereas in case (ii), no such entanglement growth occurs.

In case (i), we improved an algorithm based on the Chebyshev expansion of the single-particle spectral function. This allowed, for the first time, to provide a reliable DMFT solution beyond the single-site approximation for the single-band Hubbard by solving it in its two-site dynamical cluster approximation (DCA). In non-equilibrium, which necessarily involves a computation on the real axis, our implementation of DMFT could elucidate the fundamental mechanisms of the melting of Neel order in the Hubbard model. In case (ii), we used imaginary time evolution of matrix product states (itMPS) to compute the Green's function. This allowed, for the first time, to outperform all competing methods, such as continuous time quantum Monte Carlo or truncated configuration interaction impurity solvers, by solving a two-site DCA for a three-band model at zero temperature.

Aside from the results that regard DMFT directly, we obtained several related technical results. (a) We showed that, other than previously believed, entanglement of a quantum impurity problem is much lower in the "star" representation than in its "chain" representation. (b) We provided strong evidence that the Fourier expansion of a spectral function leads to less entanglement growth than the Chebyshev expansion, and is therefore computationally more favorable. We studied the convergence behavior of expansions of spectral functions in detail and found clear criteria for when such an expansion can be extrapolated using a technique called "linear prediction". (c) We suggested and implemented a new perturbation method that prevents the MPS optimization algorithm from getting stuck in local minima at low computational cost, which is particularly helpful for the complicated Hamiltonians associated with DMFT. (d) We showed that the problem of discretizing a continuous quantum bath on the real axis can only be optimally solved for quadratic Hamiltonians. For the latter, we showed that a strategy based on Gaussian quadrature reproduces the numerically exact time evolution of a continuous impurity model up to a non-zero time, for which we give a simple expression.

Kurzfassung

Diese Arbeit beschäftigt sich mit der Weiterentwicklung und Anwendung von Matrixprodukt-zustand (MPS) Algorithmen zur Lösung der Dynamischen Molekularfeld Theorie (DMFT). Die erzielten Fortschritte ermöglichen es Quantenvielteilchenprobleme, die zuvor für jede numerische Behandlung unzugänglich waren, zu lösen. Im Gleichgewicht betrifft dies insbesondere die Berechnung der elektronischen — wie isolierende, metallische, Spin-gefrorene und viele andere — Phasen von realistischen Modellen für korrelierte Materialien. Im Nicht-Gleichgewicht betrifft dies insbesondere das Verständnis der grundlegenden Mechanismen des Relaxationsverhaltens von Quantenvielteilchensystemen auf kurzen bis mittleren Zeitskalen.

Das Problem war zunächst, ein zuverlässiges und automatisierbares MPS-basiertes Verfahren zur Berechnung von Green Funktionen zu entwickeln. Diese stützt sich auf die Auswertung einer Folge von MPS, die aus der Entwicklung der Green Funktion in eine Familie von orthogonalen Funktionen hervorgeht. Nach dem wir gezeigt haben, dass dies am besten unter Verwendung von Tschebyscheff-Polynomen oder ebenen Wellen geschieht, war die entscheidende Frage, ob man die DMFT Selbstkonsistenz-Gleichungen auf der (i) reellen oder (ii) imaginären Frequenzachse löst. Der wesentliche Unterschied beruht auf der Tatsache, dass im Fall (i) die Folge der MPS stark verschränkt und Berechnungen damit letztlich zu teuer werden, während im Fall (ii) kein Verschränkungswachstum auftritt.

Im Fall (i) verbessern wir einen Algorithmus auf der Basis der Tschebyscheff-Entwicklung der Einteilchen-Spektralfunktion. Dies ermöglicht zum ersten Mal eine zuverlässige DMFT Lösung eines Modells mit einer höheren Komplexität als der des Ein-Band Hubbard-Modells: einer "two-site dynamical cluster approximation" (DCA) fuer ein Ein-Band Modell. Im Nicht-Gleichgewicht, was eine Berechnung auf der reellen Achse voraussetzt, konnte unsere Implementierung von DMFT die grundlegenden Mechanismen des Schmelzens der Neel Ordnung im Hubbard-Modell aufklären. Im Fall (ii) verwendeten wir die Fourierentwicklung der Matsubara Green Funktion, die mit Hilfe von MPS Zeitentwicklungs-Algorithmen berechnet werden kann. Dies erlaubt zum ersten Mal, alle konkurrierenden Verfahren — wie "continuous time quantum Monte Carlo" oder "truncated configuration interaction" Algorithmen — zu schlagen: durch die Lösung einer "two-site DCA" für ein Drei-Band Modell bei Temperatur Null.

Abgesehen von den genannten Ergebnissen, die die DMFT direkt betreffen, haben wir mehrere verwandte Ergebnisse erzielt. (a) Wir haben gezeigt, dass, anders als bisher angenommen, die Verschränkung eines Quantenstörstellenproblems in der "Stern"-Darstellung viel niedriger als in der "Ketten"-Darstellung ist. (b) Wir lieferten überzeugende Hinweise, dass die Fourier-Entwicklung der Spektralfunktion zu einer weniger stark verschränkten Folge von MPS Zuständen — und daher günstigeren Rechnung — als die Chebyshev Entwicklung führt. Wir untersuchten das Konvergenzverhalten von Reihenentwicklungen von Spektralfunktionen im Detail und fanden klare Kriterien für die Anwendung der sogenannten "linear prediction". (c) Wir haben eine neue "Störmethode" vorgeschlagen und implementiert. Diese verhindert bei niedrigen Rechenkosten, dass der MPS-Optimierungsalgorithmus in lokalen Minima stecken bleibt. Das ist besonders für die komplizierten Hamiltonianoperatoren, die in der DMFT auftreten, hilfreich. (d) Wir haben gezeigt, dass das Problem der Diskretisierung eines kontinuierlichen Quantenbads auf der reellen Achse nur optimal für quadratische Hamiltonians gelöst werden kann. Für letztere haben wir gezeigt, dass eine Strategie, die auf Gauß-Quadratur basiert, die numerisch exakte Zeitentwicklung eines kontinuierlichen Störstellenmodells bis zu einer endlichen Zeit liefert. Für letztere haben wir einen einfachen Ausdruck berechnen.

Publications

This dissertation is based on the following journal articles, listed in inverse chronological order.

▷ *Imaginary-time matrix product state impurity solver for dynamical mean-field theory*
  FA Wolf, A Go, IP McCulloch, AJ Millis, and U Schollwöck
  Sec. 3.2 / arXiv:1507.08650   Phys. Rev. X **5**, 041032 (2015)

▷ *How to discretize a quantum bath for real-time evolution*
  I de Vega, U Schollwöck, and **FA Wolf**
  Sec. 5.3 / arXiv:1507.07468   Phys. Rev. B **92**, 155126 (2015)

▷ *Non-thermal melting of Neel order in the Hubbard model*
  K Balzer, **FA Wolf**, IP McCulloch, P Werner, and M Eckstein
  Sec. 4.2 / arXiv:1504.02461   Phys. Rev. X **5**, 031039 (2015)

▷ *Strictly single-site DMRG algorithm with subspace expansion*
  C Hubig, IP McCulloch, U Schollwöck, and **FA Wolf**
  Sec. 5.2 / arXiv:1501.05504   Phys. Rev. B **91** 155115 (2015)

▷ *Spectral functions and time evolution from the Chebyshev recursion*
  FA Wolf, JA Justiniano, IP McCulloch, and U Schollwöck
  Sec. 5.1 / arXiv:1501.07216   Phys. Rev. B **91** 115144 (2015)

▷ *Solving nonequilibrium dynamical mean-field theory using matrix product states*
  FA Wolf, IP McCulloch, and U Schollwöck
  Sec. 4.1 / arXiv:1410.3342   Phys. Rev. B **90** 235131 (2014)

▷ *Chebyshev matrix product state impurity solver for dynamical mean-field theory*
  FA Wolf, IP McCulloch, O Parcollet, and U Schollwöck
  Sec. 3.1 / arXiv:1407.1622   Phys. Rev. B **90** 115124 (2014)

Acknowledgements

Contents

1. Introduction

Dynamical mean-field theory (DMFT) in its single-site (Metzner and Vollhardt, 1989; Georges and Kotliar, 1992; Georges *et al.*, 1996) and cluster (Maier *et al.*, 2005; Kotliar *et al.*, 2006) variants is among the most widely employed computational techniques for solving quantum many-body problems.[1] At the core of a numerical solution of DMFT is an algorithm for solving a quantum impurity problem,[2] a so-called *impurity solver*. The present thesis advances the mathematical and algorithmic foundations for using a combination of matrix product state (MPS) based algorithms as impurity solver. We will show that this allows to address fundamentally important classes of problems that have not yet been adequately treated. These problems originate in particular from the wish for a realistic description of *strongly correlated materials*:[3] while the technological revolution of the second half of the past century was initiated by the understanding of (uncorrelated) semi-conductors, a comparable understanding of strongly correlated materials could initiate a similar revolution. One route to such a revolution could be to directly exploit phenomena like high-temperature superconductivity.[4] Another route could be the general perspective of designing and tuning specific material properties to achieve desired functionalities.[5] In particular, one imagines materials that are tuned close to a phase transition and hence react on external stimuli extremely sensitively requiring, e.g., extremely little amounts of energy.

Why is there a need for developing new *impurity solvers*, given the rich variety of existing methods? To answer this question, let us discuss these methods in more detail. Continuous-time quantum Monte Carlo (CTQMC) (Rubtsov *et al.*, 2005; Werner *et al.*, 2006; Gull *et al.*, 2011a) is widely employed but its applications to situations involving low point symmetry, non-Hubbard interactions, multiple relevant orbitals, complex Hamiltonians[6] and to the general computation of real-time or real-frequency information is limited by the *sign (phase) problem*. Exact diagonalization (ED) (Caffarel and Krauth, 1994; Capone *et al.*, 2007; Liebsch and Ishida, 2012) makes no assumption on the interaction and does not have a sign problem. It is limited by the size of the Hilbert space that can be studied, meaning in practice that it is restricted to a small number of correlated sites to which only a small number of bath sites can be attached. Recently, improvements have been achieved by considering only restricted subspaces of the Hilbert space (Lu *et al.*, 2014; Zgid *et al.*, 2012; Lin and Demkov, 2013a,b), but the size of problem remains a significant limitation. The numerical renormalization group (NRG) (Bulla *et al.*, 2008) converges the DMFT loop on the real-frequency axis and very effectively obtains real-frequency information in the low-frequency limit. Current applications have been to relatively small problems[7] and it

---

[1] This is not only true for physics, but in recent years, DMFT found its way also into quantum chemistry (Zgid and Chan, 2010; Lin *et al.*, 2011).

[2] A quantum impurity problem is a quantum-field theory with $d = 0$ spatial dimension in contrast to typical lattice problems with $d = 2$ or $d = 3$ spatial dimensions. A wavefunction representation of a quantum impurity problem usually has $d = 1$ spatial dimension.

[3] Materials, in which the effective Coulomb interaction among particles is so strong that the assumption that particles can be regarded as independent ("uncorrelated") from each other is not valid.

[4] A recent review of computational studies on the foundations of high-temperature superconductivity has been authored by LeBlanc *et al.* (2015). Closer to technological applications are e.g. the studies of Graser *et al.* (2010); Wolf *et al.* (2012), who explain how supercurrent is affected by grain boundaries.

[5] There is a vast number of literature on this. Just a few examples were authored by Okamoto and Millis (2004); Millis and Schlom (2010); Mannhart and Schlom (2010); Assmann *et al.* (2013).

[6] As occur for synthetic gauge fields, which are an important emerging topic within the community, which becomes more and more interested in "topological matter", see e.g. Ketterle (2015) or Ozawa (2015).

[7] The most recent achievement is a solution of the single-site DMFT approximation to a three-band model by

remains to be seen how far the method can be extended.[8]

This thesis suggests to use MPS-based algorithms as *impurity solver*. The most prominent MPS algorithm is the *density matrix renormalization group* (DMRG) (White, 1992; Schollwöck, 2005, 2011). DMRG has been found to be extremely powerful for the calculation of ground states of one-dimensional quantum systems. Later it was successfully extended to the calculation of spectral functions which, in contrast to the numerical renormalization group (NRG), it obtains with equal resolution across the spectrum, see e.g. (Holzner *et al.*, 2011; Wolf *et al.*, 2015b). In pioneering work the method was applied as a DMFT impurity solver by García, Hallberg, and Rozenberg (2004) and Nishimoto, Gebhard, and Jeckelmann (2004) with important further work done by these and other authors (Karski *et al.*, 2005; Nishimoto *et al.*, 2006; García *et al.*, 2007; Karski *et al.*, 2008; Peters, 2011; Ganahl *et al.*, 2014b,a). However, the method has not been widely accepted, perhaps because high-quality data were presented only for the single-site approximation to the single-band Hubbard model.

Within this thesis, we develop the method further so that it was, for the first time, possible to use DMRG to reliably solve the single-band Hubbard model in the two-site DMFT approximation (Wolf *et al.*, 2014a). Also, insights into the entanglement of the impurity problem made it much more powerful (Wolf *et al.*, 2014b). Finally, a formulation of the method in imaginary-time allowed to again reduce computational costs tremendously, and by that allows to address problems that are beyond the possibilities of all other impurity solvers (Wolf *et al.*, 2015a). In view of these advances, DMRG now is a candidate for a highly flexible low-cost impurity solver.

Aside from these topics, which deal with the description of quantum many-body systems in thermal equilibrium, we applied DMRG in the non-equilibrium formulation of DMFT (Freericks *et al.*, 2006; Aoki *et al.*, 2014) in the Hamiltonian representation of (Eckstein, 2009; Gramsch *et al.*, 2013). We showed that our implementation of a DMRG solver is more powerful than ED impurity solvers (Wolf *et al.*, 2014b). As an application, we studied the fundamental problem of how Neel order in the Hubbard model melts (Balzer *et al.*, 2015).

Structure

The structure of the thesis is as follows. In Chapter 2, we introduce DMRG and DMFT in general. Chapters 3 and 4 present impurity solvers and applications in equilibrium and non-equilibrium, respectively. Chapter 5 presents several related technical results on computing spectral functions, stabilizing ground state optimization and discretizing a quantum bath. Chapter 6 concludes the thesis and gives an outlook.

Stadler *et al.* (2015)

[8]The field evolves rapidly, and we also mention other recent suggestions for impurity solvers (Li and Tong, 2015; Wang *et al.*, 2015; Arsenault *et al.*, 2015; Schüler *et al.*, 2015; Granath and Strand, 2012; Shinaoka *et al.*, 2014), and the computationally inexpensive density matrix embedding theory (DMET) (Knizia and Chan, 2012).

2. Methods

> *Many natural quantum lattice models have ground states that are little, in fact very little, entangled in a precise sense. This shows that "nature is lurking in some small corner of Hilbert space", one that can be essentially efficiently parametrized.*

Eisert (2013)

Introductory sections on matrix product states (Sec. 2.1) and quantum embedding techniques (Sec. 2.2.1 and Sec. 2.2.2) are followed by more technical sections devoted to the Baym-Kadanoff construction of dynamical mean-field theory (Sec. 2.2.3) and to the details of matrix product state algorithms (Sec. 2.3).

2.1. Introduction to matrix product states

This introduction to matrix product states (MPS),[1] the one-dimensional version of a *tensor network*, aims at generating an intuition for the method while neglecting any algorithmic details. In particular, this should allow readers to access the topic, who are not familiar with quantum many-body physics. We are rather inspired by the idea of applying MPS and tensor networks to classical systems.[2] But instead of what is found in the literature, here, the concept is explained using just the simplest example from statistical physics, the one-dimensional Ising model. In Sec. 2.1.2, we will then continue the discussion in the context of quantum many-body physics.

2.1.1. Statistical physics

To illustrate how useful the concept of MPS is, we solve the standard task of computing correlation functions for an interacting classical many-body system, for which the microscopic interactions are known in form of a Hamilton function $H(\boldsymbol{x})$ in its dependence on some degrees of freedom $\boldsymbol{x}$.

Ising model without interactions

Let us start with the example (i) of a non-interacting one-dimensional Ising model. This model is described by vector of random variables $\boldsymbol{X} \in \{-\frac{1}{2}, \frac{1}{2}\}^L$ with joint probability mass function

$$p(\boldsymbol{x}) = \tfrac{1}{Z} e^{-H(\boldsymbol{x})/T}, \quad H(\boldsymbol{x}) = \sum_{n=1}^{L} x_n \tag{2.1}$$

normalized with the partition function $Z = \sum_{\boldsymbol{x}} e^{-H(\boldsymbol{x})/T}$. The values x_n of the random variable X_n are interpreted as state or configuration of a "classical spin" as illustrated in Fig. 2.1. Let us define a tensor P of rank L with components

$$P_{\boldsymbol{x}} = P_{x_1,\ldots,x_L} := p(\boldsymbol{x}). \tag{2.2}$$

Evidently, P has 2^L components indexed with $\boldsymbol{x} \in \{(-\frac{1}{2}, -\frac{1}{2}, ..., -\frac{1}{2}), (-\frac{1}{2}, -\frac{1}{2}, ..., \frac{1}{2}), ...\}$. This number grows exponentially and for 100 classical spins, we already have $2^{100} \simeq 10^{30} \simeq 10^{15}$ TB.

---

[1] In the mathematical literature, these are known as tensor trains (TT).

[2] Examples for this are e.g. Murg *et al.* (2005), Temme and Verstraete (2010), Johnson *et al.* (2010), Evenbly and Vidal (2014) and Johnson *et al.* (2014).
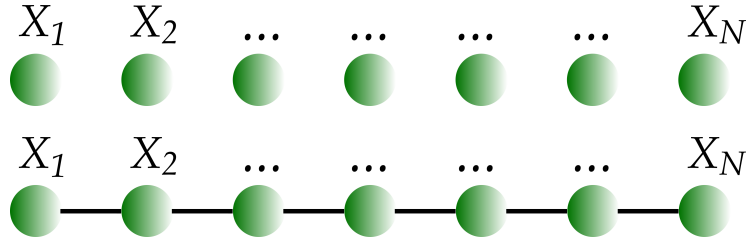
Fig. 2.1.: One-dimensional Ising model. Top: non-interacting (uncoupled) Ising model. Bottom: interacting (two-body coupled) Ising model.

Let us compute the correlations

$$\text{cov}(X_n, X_m) = \langle X_n X_m \rangle - \langle X_n \rangle \langle X_n \rangle, \tag{2.3}$$

which amounts to evaluating

$$\langle X_n X_m \rangle = \sum_{\boldsymbol{x}} x_n x_m P_{\boldsymbol{x}}. \tag{2.4}$$

Doing this naively requires 2^L operations, which is extremely inefficient. Doing it using Monte Carlo sampling, we have to sample in a space of 2^L configurations. This works fine, but we can do even better. The non-interacting degrees of freedom x_n mean independent random variables X_n, which implies full *separability* of the probability mass function

$$\begin{aligned} P_{\boldsymbol{x}} = P_{x_1, x_2, \dots, x_L} &= \tfrac{1}{Z} e^{-\sum_{n=1}^{L} x_n / T} \\ &= \tfrac{1}{Z} A_{x_1} A_{x_2} \dots A_{x_L}, \quad A_{x_n} = e^{-x_n/T}. \end{aligned} \tag{2.5}$$

It is important to realize that with this, we achieved a decomposition or factorization of the rank-L tensor P in L rank-1 tensors A. Using the factorized form of P, we only need $2L$ operations to evaluate (2.4)

$$\begin{aligned} \langle X_n X_m \rangle &= \frac{1}{Z} \Big(\sum_{x_n} x_n A_{x_n} \Big) \Big(\sum_{x_m} x_m A_{x_m} \Big) \prod_{k \neq n, m}^{L} \Big(\sum_{x_k} A_{x_k} \Big) \\ &= \langle X_n \rangle \langle X_m \rangle, \quad Z = \prod_{k=1}^{L} \Big(\sum_{x_k} A_{x_k} \Big), \end{aligned} \tag{2.6}$$

which evidently yields no correlations $\text{cov}\langle X_n X_m \rangle = 0$, as spins are independent from each other.

Ising model with two-body interactions

Let us now consider example (ii), the (interacting) one-dimensional Ising model

$$P_{\boldsymbol{x}} = \tfrac{1}{Z} e^{-H(\boldsymbol{x})/T}, \quad H(\boldsymbol{x}) = -\sum_{n=1}^{L-1} x_n x_{n+1}, \tag{2.7}$$

which is sketched in Fig. 2.1.[3]

---

[3]Within this figure, solid lines denote couplings. We will see that these couplings introduce *additional* summations. Therefore, this representation can be seen as a preliminary form of the standard diagrammatic representation of tensor networks introduced in Sec. 2.3.
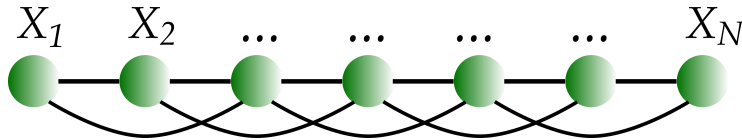
Fig. 2.2.: One dimensional Ising model with three-body interactions (couplings).

The quadratic exponent is simple to treat. It corresponds to a "discrete Gaussian" (continuous if one considers $x_n \in \mathbb{R}$) which leads to, using the vector notation, to a nearest-neighbor coupling matrix $\mathcal{H}$,

$$H(\boldsymbol{x}) = -\boldsymbol{x}^t \mathcal{H} \boldsymbol{x}, \quad \mathcal{H} = \frac{1}{2} \begin{pmatrix} 0 & 1 & 0 & \cdots \\ 1 & 0 & 1 & \ddots \\ 0 & 1 & 0 & \ddots \\ \vdots & \ddots & \ddots & \ddots \end{pmatrix} = T\mathrm{cov}(\boldsymbol{x}, \boldsymbol{y})^{-1} \tag{2.8}$$

The coupling matrix $\mathcal{H}$ of a Gaussian is just the inverse of the covariance matrix of a Gaussian: $\mathrm{cov}(\boldsymbol{x}, \boldsymbol{y})^{-1} = \frac{1}{T}\mathcal{H}^{-1}$. Correlations, i.e. the entries of the covariance matrix, are simply obtained by inverting the coupling matrix $\mathcal{H}$.

We can still solve the problem in a different way. Consider rewriting the rank-L tensor P

$$\begin{aligned} P_{x_1,\ldots,x_L} &= \frac{1}{Z} e^{x_1 x_2/T} e^{x_2 x_3/T} \cdots \\ &= \frac{1}{Z} A_{x_1,x_2} A_{x_2,x_3} \cdots, \qquad A_{x_n,x_{n+1}} = e^{x_n x_{n+1}/T}, \quad A \in \mathbb{R}^{2 \times 2}. \end{aligned} \tag{2.9}$$

This is not a factorization in vectors $A \in \mathbb{R}^2$, as in (2.9), but in matrices $A \in \mathbb{R}^{2 \times 2}$. We might refer to this factorization property of P as a weaker form of separability, and call the representation (2.9) *MPS format* of P. Using the matrix factorization (2.9), and interpreting summations over $\boldsymbol{x}$ as matrix products, one can compute the correlations in the system using $2^3 L$ operations (L matrix products)

$$Z = \sum_{\boldsymbol{x}} e^{x_1 x_2/T} e^{x_2 x_3/T} \cdots = \sum_{\boldsymbol{x}} A_{x_1,x_2} A_{x_2,x_3} \cdots = \sum_{y,z} (A^L)_{y,z},$$

$$\langle X_n X_m \rangle = \frac{1}{Z} \sum_{y,z} \left(\prod_{k=1}^{n-1} (A^{[k]}) M \prod_{k=n}^{m-1} (A^{[k]}) M \prod_{k=m}^{L-1} (A^{[k]}) \right)_{y,z}, \quad M = \begin{pmatrix} 1 & 0 \\ 0 & -1 \end{pmatrix}, \tag{2.10}$$

where M is a *measurement matrix*, which is known from the usual calculations with *transfer matrices* in statistical mechanics. Evidently, A is a transfer matrix.

Ising model with three-body interactions

Let us consider a third example (iii), an Ising model with three-body interactions

$$P_{\boldsymbol{x}} = \frac{1}{Z} e^{-H(\boldsymbol{x})/T}, \quad H(\boldsymbol{x}) = -\sum_{n=1}^{L-2} x_n x_{n+1} x_{n+2}. \tag{2.11}$$

For this, we can rewrite the the partition function using a factorization in L rank-3 tensors, but using *reshaping* indices, this can again be written as product of matrices, although with increased

dimensions

$$Z = \sum_{\boldsymbol{x}} \prod_{n=1}^{L-2} A_{x_n,x_{n+1},x_{n+2}}, \quad A_{x_n,x_{n+1},x_{n+2}} = e^{x_n x_{n+1} x_{n+2}/T}, \quad A \in \mathbb{R}^{2\times2\times2}$$

$$= \sum_{\boldsymbol{x}'} \prod_{n=1}^{L-2} B_{x'_n,x'_{n+1}} B^t_{x'_{n+1},x'_{n+2}}, \quad B_{x'_n,(x_{n+1},x_{n+2})} = A_{x'_n,x_{n+1},x_{n+2}}, \quad B \in \mathbb{R}^{2\times4}, \tag{2.12}$$

and we refer to this as MPS representation. Reshaping of indices means mapping a tuple of indices to a single index, as in the previous line. As this will appear very often also in Sec. 2.3, we note that we use the following convention

$$(x_1, x_2, x_3, ..., x_n) = x_1 \prod_{m=2}^{n} d_m + x_2 \prod_{m=3}^{n} d_m + \cdots + x_{n-1}d_n + x_n, \tag{2.13}$$

where each index $x_m \in \{0, 1, 2, \ldots, d_m\}$. If the index is associated with a physical discrete degree of freedom, as here, where it denotes a classical spin $x_n \in \{-\frac{1}{2}, \frac{1}{2}\}$, we understand an implicit (trivial) map to a set of the form $\{0, 1, 2, \ldots, d_m\}$, when considering x_n as an index: here $\{-\frac{1}{2}, \frac{1}{2}\} \mapsto \{0, 1\}$.

Summary

Let us summarize, what we have learned from the analysis of the three examples of the Ising model with different ranges of interaction.

- For a system with L discrete degrees of freedom x_n, rewrite the probability mass function $p(\boldsymbol{x})$ that occurs in the partition function

$$p : \{0, 1, ..., d\}^L \to [0, 1], \quad d, L \in \mathbb{N} \tag{2.14}$$

  as rank-L tensor

$$P_{\boldsymbol{x}} = P_{x_1,...,x_L} := p(\boldsymbol{x}), \tag{2.15}$$

  where the d^L components are *indexed and parametrized* by $\boldsymbol{x} \in \{0, 1, ..., d\}^L$.

- If $P_{\boldsymbol{x}} = p(\boldsymbol{x})$ does *not* couple *all* index components x_n among each other, there is a low rank MPS format or representation. This reduces computational cost in summations over $p(\boldsymbol{x})$ from *exponential* to *linear* in system size.

Obviously, this holds for any function $p(\boldsymbol{x})$, independent of whether it occurs in statistical physics or not.

2.1.2. Quantum mechanics

In the partition sums of the previous section, we considered sums over classical weights, such as

$$1 = \sum_{\boldsymbol{x}} p_{\boldsymbol{x}} = \sum_{\boldsymbol{x}} \langle \boldsymbol{x} | \hat{p} | \boldsymbol{x} \rangle. \tag{2.16}$$

where here, we defined a *diagonal* operator $\hat{p}$ via

$$\hat{p}|\boldsymbol{x}\rangle = p_{\boldsymbol{x}}|\boldsymbol{x}\rangle. \tag{2.17}$$

This is a somewhat exaggerated notation, as the operator does not change the state of the system $|\boldsymbol{x}\rangle$ (it is diagonal). The "operator" $\hat{p}$ is simply a *function* of the state[4] of the system. In classical mechanics, we exclusively deal with this kind of trivial operators and we never have to consider *superpositions* $\alpha|\boldsymbol{x}\rangle + \beta|\boldsymbol{y}\rangle$ of states. The fundamental object of computation therefore is a single state $\boldsymbol{x} \equiv |\boldsymbol{x}\rangle$ (for which the *bra-ket* notation is unnecessary).

In statistical physics, the MPS format helped us for the task of evaluating the sums over states that occur in partition functions and thermal expectation values. In quantum mechanics, sums over states already occur at zero temperature: *superpositions* of states $|\boldsymbol{x}\rangle$ are the fundamental objects of computation as quantum mechanics is a theory based on veritable (non-diagonal) operators.

Quantum many-body states

The fundamental object of computation, a general quantum many-body state, is

$$|\psi\rangle = \sum_{\boldsymbol{x}} c_{\boldsymbol{x}} |\boldsymbol{x}\rangle, \qquad (2.18)$$

where $|\boldsymbol{x}\rangle = |x_1\rangle \otimes |x_2\rangle \otimes \cdots \otimes |x_L\rangle = |x_1 x_2 \ldots x_L\rangle$ denotes a *canonical* many-body basis state, which is a tensor product of single-particle basis states $|x_l\rangle$ (Fock basis). For example

$$|\sigma_l\rangle \in \{|\uparrow_l\rangle, |\downarrow_l\rangle\}, \qquad (2.19)$$

if $|x_l\rangle = |\sigma_l\rangle$ describes a spin-$\frac{1}{2}$ degree of freedom. Many-body states "live in" a "many-body Hilbert space"

$$\mathcal{H} = \bigotimes_{i=1}^{L} \mathcal{H}_{\text{loc}}, \qquad (2.20)$$

where $\mathcal{H}_{\text{loc}}$ is the local Hilbert space (degrees of freedom associated with a "site"). The dimension of the many-body Hilbert space scales exponentially with the number of lattice sites

$$\dim H = d^L, \qquad d := \dim H_{\text{loc}}. \qquad (2.21)$$

This poses hard problems in any computation with a quantum many-body state. In particular, finding the ground state of a many-body Hamiltonian is exponentially hard. Can the MPS format help us with this standard problem in quantum mechanics?

In the previous section, we learned that the decisive question that determines the efficiency of the MPS format was the *degree* of coupling between indices of a high-dimensional tensor. Can we know anything about how the coefficient tensor $c_{\boldsymbol{x}}$ *couples* its components? Let us postpone this question for a moment, but instead simply compare different ways of making an ansatz to approximate (2.18).

Mean-field state

The simplest thing to do is the *mean-field* ansatz, which assumes (here, x_l is an index, not a power)

$$c_{\boldsymbol{x}} = c_{x_1,\ldots,x_L} \overset{!}{=} a^{x_1} a^{x_2} \ldots a^{x_L} = \prod_{l=1}^{L} a^{x_l}, \quad a^{x_l} \in \mathbb{C}. \qquad (2.22)$$

---

[4]A function of the degrees of freedom.
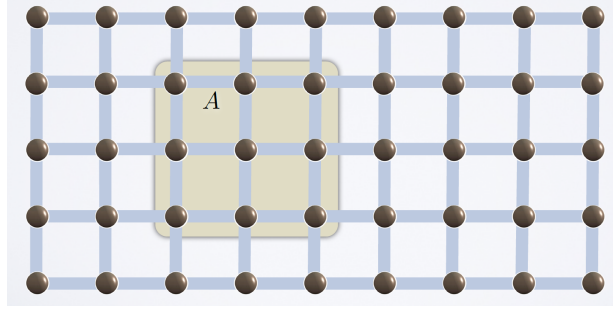
Fig. 2.3.: Lattice with a sublattice A. This figure is from Eisert (2013).

Within this ansatz, computations with the state can be done using $\sim L$ operations[5]

$$|\psi\rangle = \sum_{\boldsymbol{x}} c_{\boldsymbol{x}} |\boldsymbol{x}\rangle \stackrel{!}{=} |\psi_{\mathrm{MF}}\rangle = \sum_{\boldsymbol{x}} \prod_l a^{x_l} |\boldsymbol{x}\rangle = \prod_l^{\otimes} \left(\sum_{x_l} a^{x_l} |x_l\rangle \right). \tag{2.23}$$

How can we now come up with an approximation for the ground state of H using this ansatz? Let us simply use the *Ritz variational principle* and minimize the *Rayleigh quotient*

$$\partial_{a^{x_l}} \frac{\langle \psi | H | \psi \rangle}{\langle \psi | \psi \rangle} = 0. \tag{2.24}$$

Solution of this equation yields the parameters a^{x_l}. The approximation to the ground state that is obtained in this way is *good* if the true ground state is in the same *class* of states as the ansatz $|\psi_{\mathrm{MF}}\rangle$. But this for sure is in general not likely to be the case. Let us therefore generalize the *mean-field* ansatz to an ansatz in terms of an MPS.

Matrix product state

For this, relax the mean-field assumption of a factorization in rank-1 tensors (vectors) a^{x_l} as in (2.22) to a factorization in rank-3 tensors $M^{x_l}_{\nu_l, \nu_{i+1}}$ and two rank-2 tensors, $M^{x_1}_{\nu_1}$ and $M^{x_L}_{\nu_L}$. Fixing the physical index x_l, the rank-3 tensors become matrices and the rank-2 tensors become vectors so that

$$c_{\boldsymbol{x}} \stackrel{!}{=} \sum_{\{\nu_l\}} M^{x_1}_{\nu_1} M^{x_2}_{\nu_1, \nu_2} M^{x_3}_{\nu_2, \nu_3} \dots M^{x_L}_{\nu_L} = \prod_{l=1}^{L} M^{x_l}. \tag{2.25}$$

The matrix M^{x_l} has dimensions $m_{l-1} \times m_l$. Evidently, $m_0 = 1 = m_L$, in order for that the matrix product yields a scalar. A matrix product state can hence be defined by

$$|\psi_{\mathrm{MPS}}\rangle = \sum_{\boldsymbol{x}} \prod_l M^{x_l} |\boldsymbol{x}\rangle. \tag{2.26}$$

Evidently, an MPS can be manipulated with costs of Lm^3,[6] if the matrix dimensions are constant $m_l = m$. This is "cheap" if the bond dimension m is *not* exponentially large in the system size. Obviously, if we want $|\psi_{\mathrm{MPS}}\rangle$ to be an *exact* representation of $|\psi\rangle$, this is what happens. The number of parameters in the matrices then has to equal the number of parameters $c_{\boldsymbol{x}}$, which is exponentially large. Only then the equation system (2.25) is neither under- nor overdetermined

---

[5]The state is referred to as *mean-field* state, as it leads to factorizing expectation values, which corresponds to the typical *mean-field* decoupling assumption.

[6]The cost for L matrix products of matrices with dimension $m \times m$.
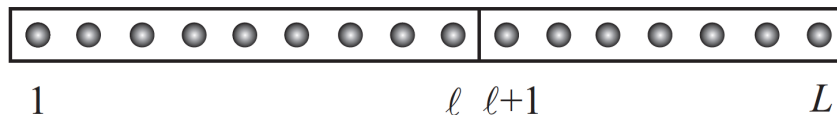
Fig. 2.4.: A one dimensional system with L lattice sites. The *bond* between sites l and $l+1$ is highlighted. This figure is from Schollwöck (2013).

and can be solved.[7] The question is therefore rather: Are MPS a useful approximation for a rather *small* maximal value of the bond dimension m? That is, are ground states in the same *class* as MPS so that $|\psi\rangle = \sum_{\boldsymbol{x}} c_{\boldsymbol{x}} |\boldsymbol{x}\rangle \simeq |\psi_{\mathrm{MPS}}\rangle$ is a good approximation for a *small* maximal m? Which is this class? Are the coefficients $c_{\boldsymbol{x}}$ in ground states in some sense *weakly* coupled?

Class of lowly entangled states

Many natural quantum lattice models have ground states that are little, in fact very little, entangled in a precise sense. This shows that "nature is lurking in some small corner of Hilbert space", one that can be essentially efficiently parametrized (Eisert, 2013). Postponing the mathematical definitions for a moment, this "small corner of the Hilbert space" refers to the class of *lowly entangled* states. To make this precise (Eisert *et al.*, 2010): the ground states of gapped ("non-critical") Hamiltonians with short-range interactions fulfill an *area law*: the entanglement of a sublattice A is proportional to the surface $|\partial A|$ of this sublattice, see Fig. 2.3. This is a highly unusual property of ground states. Almost all other states in the many-body Hilbert space come with an entanglement that scales with the volume $|A|$.

But how does the *class of lowly entangled states* have in common with the *class of MPS*? Using an example, we will see that they coincide. Or more precisely: MPS are an efficient parametrization of the class of lowly entangled states. Let us study the example of a one-dimensional system and roughly follow Schollwöck (2013) to show this in detail.

Schmidt decomposition and entanglement

A general many-body quantum state (2.18) for a one-dimensional system as skteched in Fig. 2.4 can be written as

$$|\psi\rangle = \sum_{\boldsymbol{x}_A} \sum_{\boldsymbol{x}_B} M_{\boldsymbol{x}_A, \boldsymbol{x}_B} |\boldsymbol{x}_A\rangle |\boldsymbol{x}_B\rangle \tag{2.27}$$

where $|\boldsymbol{x}_A\rangle$ and $|\boldsymbol{x}_B\rangle$ denote the canonical many-body basis states for sites $1, \ldots, l$ and $l+1, \ldots, L$, respectively, and the matrix M is obtained from the coefficient $c_{\boldsymbol{x}}$ by regrouping indices

$$M_{\boldsymbol{x}_A, \boldsymbol{x}_B} = c_{(x_1, \ldots, x_l), (x_{l+1}, \ldots, x_L)}. \tag{2.28}$$

In which case is $|\psi\rangle$ lowly entangled? To compute the entanglement, let us perform a singular value decomposition (SVD) for the matrix

$$M = USV^{\dagger}, \tag{2.29}$$

where

---

[7] Schollwöck (2011) shows an easy strategy for the solution of this highly non-linear system of equations. This shows that matrix dimensions in the center of the system take the value $m = d^{L/2}$ and decrease to the left and the right as $d^{L/2-1}, d^{L/2-2}, \ldots$.

- $U^\dagger U = I$ and $V^\dagger V = I$, i.e. U and V have columns of orthonormal vectors.

- S is diagonal.

Using the SVD for M represents $|\psi\rangle$ in the basis $|\nu_{A/B}\rangle$ that leads to a diagonal coupling matrix S with non-zero entries s_ν

$$|\psi\rangle = \sum_\nu s_\nu |\nu_A\rangle |\nu_B\rangle \tag{2.30}$$

where $|\nu_A\rangle = \sum_{\boldsymbol{x}_A} U_{\boldsymbol{x}_A \nu} |\boldsymbol{x}_A\rangle$ and $|\nu_B\rangle = \sum_{\boldsymbol{x}_B} V^*_{\nu \boldsymbol{x}_B} |\boldsymbol{x}_B\rangle$. The basis $|\nu_{A/B}\rangle$ inherits orthonormality $\langle \nu_{A/B}|\mu_{A/B}\rangle = \delta_{\nu,\mu}$ from the canonical basis $|\boldsymbol{x}_{A/B}\rangle$ by virtue of orthonormality of columns of U and of rows of $V^\dagger$. Eq. (2.30) is referred to as Schmidt decomposition of $|\psi\rangle$.

Using the Schmidt decomposition of $|\psi\rangle$, one readily obtains the reduced density operators as the trace over the sublattice B can be performed easily

$$\rho_A = \mathrm{tr}_B |\psi\rangle\langle\psi| = \sum_\nu s_\nu^2 |\nu\rangle\langle\nu|. \tag{2.31}$$

The entropy associated with the entanglement of A with B then is

$$S_{A|B} = -\mathrm{tr}\rho_A \ln\rho_A = \sum_\nu s_\nu^2 \ln s_\nu^2, \tag{2.32}$$

and referred to as *entanglement entropy*. We call the state $|\psi\rangle$ lowly entangled if the singular values s_ν decay rapidly to zero, such that the sums in the Schmidt decomposition (2.30) and in the entropy (2.32) can be truncated after a few terms without inducing a significant error. Then, the Schmidt decomposition becomes a very efficient representation of $|\psi\rangle$: instead of a summation over all canonical basis states as in the naive representation in terms of $|x_{A/B}\rangle$, only a summation over *a few* states $|\nu_{A/B}\rangle$ is needed.

Connection to MPS

Let us analyze partitioning an MPS at bond $(l, l+1)$ to generate subsystems A and B, just as we did for a general state $|\psi\rangle$ in (2.18)

$$\begin{aligned}
|\psi_{\mathrm{MPS}}\rangle &= \sum_{\boldsymbol{x}_A} \sum_{\boldsymbol{x}_B} \prod_{i=1}^{l} M^{x_i} \prod_{j=l+1}^{L} M^{x_j} \sum_{x_l} |\boldsymbol{x}_A\rangle |\boldsymbol{x}_B\rangle \\
&= \sum_\nu \sum_{\boldsymbol{x}_A} \underbrace{\left(\prod_{i=1}^{l} M^{x_i}\right)_\nu}_{U_{\boldsymbol{x}_A \nu}} |\boldsymbol{x}_A\rangle \sum_{\boldsymbol{x}_B} \underbrace{\left(\prod_{j=l+1}^{L} M^{x_j}\right)_\nu}_{V^*_{\nu \boldsymbol{x}_B}} |\boldsymbol{x}_B\rangle
\end{aligned} \tag{2.33}$$

Simply by making the summation of the matrix product between M^{x_l} and $M^{x_{l+1}}$ explicit, we learn that the structure of an MPS implies the representation of a state $|\psi\rangle$ in terms of its Schmidt decomposition, if the transformation matrices U and V defined in (2.33), have orthonormal

columns:

$$
\begin{aligned}
U^\dagger U &= \sum_{\boldsymbol{x}_A} \Big(\prod_{i=1}^{l} M^{x_i}\Big)_\mu^\dagger \Big(\prod_{i=1}^{l} M^{x_j}\Big)_\nu = \sum_{\boldsymbol{x}_A} \Big(\prod_{i=l}^{1} M^{x_i\dagger}\Big)_\mu \Big(\prod_{i=1}^{l} M^{x_j}\Big)_\nu \\
&= \sum_{\boldsymbol{x}_A} \Big(M^{x_l\dagger}\dots M^{x_1\dagger} M^{x_1}\dots M^{x_l}\Big)_{\mu\nu} \overset{!}{=} \delta_{\mu\nu} \\
V^\dagger V &= \sum_{\boldsymbol{x}_B} \Big(M^{x_{l+1}}\dots M^{x_L} M^{x_L\dagger}\dots M^{x_{l+1}\dagger}\Big)_{\mu\nu}^\dagger \overset{!}{=} \delta_{\mu\nu}
\end{aligned}
\tag{2.34}
$$

These constraints seem to be difficult to implement, as summations over a whole tuple of quantum numbers $\boldsymbol{x}_{A/B}$ are involved. But, we can immediately give a sufficient condition for this constraint: namely enforcing orthonormality (2.34) for each bond for the matrices on the left (for $i \le l$) and the matrices on the right (for $i \ge l+1$) in two different ways, respectively,

$$
\sum_{x_i} (A^{x_i\dagger} A^{x_i})_{\mu\nu} = \delta_{\mu\nu},
\tag{2.35a}
$$

$$
\sum_{x_i} (B^{x_i} B^{x_i\dagger})_{\mu\nu} = \delta_{\mu\nu}.
\tag{2.35b}
$$

As matrices with these properties are such an important concept, we called them *left-normalized* A_i^σ and *right-normalized* B_i^σ matrices, respectively, to distinguish them from matrices M_i^σ that fulfill no such constraint. Can any MPS be brought into this form? This can be easily checked, by performing operations on the MPS that leave it (i.e. the value of its coefficients $c_{\boldsymbol{x}}$) invariant. This again is the SVD, which we applied to the matrix $M_{(x_1,\dots,x_l),(x_{l+1},\dots,x_L)}$ in (2.28) before. Let us now apply it to the matrices M^{x_i} in (2.33) in the following way

$$
\sum_{\nu_1,\nu_2\dots,\nu_{L-1}} M^{x_1}_{1,\nu_1} M^{x_2}_{\nu_1,\nu_2}\dots M^{x_L}_{\nu_{L-1},1} = \sum_{\nu_1,\nu_2\dots,\nu_{L-1}} M_{(1,x_1),\nu_1} M^{x_2}_{\nu_1,\nu_2}\dots M^{x_L}_{\nu_{L-1},1}
\tag{2.36}
$$
$$
= \sum_{s_1,\nu_1,\nu_2\dots,\nu_{L-1}} U_{(x_1,1),s_1} S_{s_1,s_1}(V^\dagger)_{s_1,\nu_1} M^{x_2}_{\nu_1,\nu_2}\dots M^{x_L}_{\nu_{L-1},1} = \sum_{s_1,\nu_2\dots,\nu_{L-1}} A^{x_1}_{1,s_1} \widetilde{M}^{x_2}_{s_1,\nu_2}\dots M^{x_L}_{\nu_{L-1},1},
$$

where $A^{x_1}_{1,s_1} = U_{(x_1,1),s_1}$ and $\widetilde{M}^{x_2} = SV^\dagger M^{x_2}$. As U has orthonormal columns, one obtains a left-normalized A^{x_1}

$$
\sum_{x_1} (A^{x_1\dagger} A^{x_1})_{s_1,s_1'} = \sum_{x_1} (A^\dagger)^{x_1}_{s_1,1} A^{x_1}_{1,s_1'} = \sum_{x_1} (U^\dagger)_{s_1,(x_1,1)} U_{(x_1,1),s_1'} = \delta_{s_1,s_1'}.
\tag{2.37}
$$

Let us now perform the SVD for matrix $\widetilde{M}^{x_2}$, which occurs in the product with M^{x_3}

$$
\sum_{\nu_2} \widetilde{M}^{x_2}_{s_1,\nu_2} M^{x_3}_{\nu_2,\nu_3} = \sum_{\nu_2} \widetilde{M}_{(x_2,s_1),\nu_2} M^{x_3}_{\nu_2,\nu_3} = \sum_{s_2,\nu_2} U_{(x_2,s_1),s_2} S_{s_2,s_2}(V^\dagger)_{s_2,\nu_2} M^{x_3}_{\nu_2,\nu_3} = \sum_{s_2} A^{x_2}_{s_1,s_2} \widetilde{M}^{x_3}_{s_2,\nu_3}
$$

where $A^{x_2}_{s_1,s_2} = U_{(x_2,s_1),s_2}$ and $\widetilde{M}^{x_3} = SV^\dagger M^{x_3}$. Again

$$
\sum_{x_2} (A^{x_2\dagger} A^{x_2})_{s_2,s_2'} = \sum_{x_2,s_1} (A^\dagger)^{x_2}_{s_2,s_1} A^{x_2}_{s_1,s_2'} = \sum_{(x_2,s_1)} (U^\dagger)_{s_2,(x_2,s_1)} U_{(x_2,s_1),s_2'} = \delta_{s_2,s_2'}.
\tag{2.38}
$$

Obviously, this can be repeated until matrix l, and we obtain a sequence of A^{x_i} matrices. Let us then start a similar procedure starting from the right by performing an SVD for matrix $M^{x_L}_{\nu_L,1} = M_{\nu_L,(x_L,1)} = \sum_{s_L} U_{\nu_L,s_L} S_{s_L,s_L}(V^\dagger)_{s_L,(x_L,1)}$, and interpreting $B^{x_L}_{s_L,1} = (V^\dagger)_{s_L,(x_L,1)}$. Continuing this up to bond $M^{x_{l+1}}$ generates a sequence of B matrices. Finally, we end up with two matrices

$U_{\nu_l,s_l}S_{s_l,s_l}$ that remain between the sequence of A^{x_i} and the sequence of B^{x_i} matrices. Obviously, the matrix $\widetilde{A}^{x_l} = A^{x_l}U$ is still left-orthonormal,[8] and what remains is the following general form in which any MPS (and therefore any quantum many-body state $|\psi\rangle$ if choosing m high enough), can be brought

$$|\psi_{\mathrm{MPS}}\rangle = \sum_{\boldsymbol{x}_A} \sum_{\boldsymbol{x}_B} \prod_{i=1}^{l} A^{x_i} S \prod_{j=l+1}^{L} B^{x_j} \sum_{x_l} |\boldsymbol{x}_A\rangle |\boldsymbol{x}_B\rangle. \tag{2.39}$$

As the states at the left and the right as defined in (2.33) now fulfill the orthogonality property by virtue of (2.34), the state (2.39) is a Schmidt decomposition (2.30).

We conclude that the MPS format can easily be made equivalent to a Schmidt representation, which we have shown to have a low dimension if the state to represent is lowly entangled!

Density matrix renormalization group

DMRG, in the language of matrix product states,[9] then is simply the algorithm that solves the variational problem, as in the mean-field case (2.24)

$$\partial_{M^{x_l}_{\mu\nu}} \frac{\langle\psi|H|\psi\rangle}{\langle\psi|\psi\rangle} = 0. \tag{2.40}$$

We will show how to solve this in detail in Sec. 2.3.1, along with general technical details for MPS algorithms in Sec. 2.3.

Summary

To summarize this subsection on MPS in the context of quantum many-body states, let us note:

- The maximal matrix dimension m of an MPS directly translates into the number of allowed states in a Schmidt decomposition, and by that in the number of summands in the entanglement entropy (2.32).

- MPS can therefore serve as a valid (numerically exact) parametrization of lowly entangled quantum many-body states. The computational effort for manipulations of an MPS grows linearly with system size, whereas for a general quantum many-body state, it grows exponentially.

- Mean-field states with $m = 1$ are not entangled. On a computer, we can easily treat $m > 1000$, and by that carry out numerically exact computations for many quantum many-body systems.

2.1.3. Historical remarks

After the invention of DMRG by White (1992), it didn't take very long until its connection with MPS was realized (Fannes *et al.*, 1992; Östlund and Rommer, 1995; Rommer and Ostlund, 1997). Still, in numerical practice, the MPS formulation of DMRG only became widely spread in the 2000s. Area laws predict the smallest entanglement in one-dimensional gapped systems, where the surface of a partition of the system consists of a single bond (Hastings, 2007a,b; Schuch *et al.*, 2007; Amico *et al.*, 2008). DMRG revolutionized the description of one-dimensional quantum many-body systems.

---

[8] $\sum_{x_l}(\widetilde{A}^{x_l\dagger}\widetilde{A}^{x_l})_{s_l,s_l'} = \sum_{x_l}(U^\dagger A^{x_l\dagger}A^{x_l}U)_{s_l,s_l'} = (U^\dagger \sum_{x_l}(A^{x_l\dagger}A^{x_l})U)_{s_l,s_l'} = \delta_{s_l,s_l'}$

[9] The original formulation by White (1992) followed a different line of arguments.

2.2. Quantum embedding

Instead of delving into the technical details of MPS algorithms, let us now introduce a very different concept that allows to reduce the computational effort in the description of quantum lattice models tremendously, *quantum embedding* techniques. In particular, we will present the dynamical mean-field theory (DMFT)[10] and the density matrix embedding theory (DMET) (Knizia and Chan, 2012).

Consider again a sublattice as in Fig. 2.3. This time, we shall refer to this sublattice as *impurity cluster* or simply as *cluster*. Often it will consist in a single *impurity site*. The general intuitive idea of *quantum embedding* consists in approximating the coupling of the impurity cluster with the rest of the lattice by a coupling to an "artificial" environment, which we refer to as *bath*. This is only meaningful if the bath has a much simpler complexity than the original lattice environment, so that even though we cannot perform any computations for the full lattice problem, we can solve the effective *cluster-bath* problem.

Obviously, the task is to construct a *bath* that approximates the lattice environment in a meaningful way. The two most popular ideas for this construction consist in the the just mentioned DMFT and DMET. We will see that the fundamental difference is that DMET is a *static* theory, i.e., it does not account for the time evolution of the degrees of freedom in a many-body system, whereas DMFT is a *dynamic* theory.

To explain DMET and DMFT in more detail, let us consider a generic quantum many-body *lattice problem*, the Hubbard model on the two-dimensional square lattice

$$H_{\text{lat}} = -t \sum_{\langle ij \rangle \sigma} c_{i\sigma}^\dagger c_{j\sigma} + U \sum_i n_{i\uparrow} n_{i\downarrow} - \mu \sum_{i\sigma} n_{i\sigma}. \qquad (2.41)$$

Here, sums over lattice sites i, j run over an infinitely large square lattice, $\langle i, j \rangle$ denotes nearest neighbors, σ denotes a spin index, t and U denote hopping and interaction parameters, and $c_{i\sigma}^\dagger$ and $n_{i\sigma}$ denote the usual creation and occupation number operators.

2.2.1. Density matrix embedding theory

In brief: DMET constructs a *non-interacting* bath that is chosen such that the single-particle density matrix in the impurity-bath model equals the single-particle density matrix of an *approximate lattice model*

$$\langle c_i^\dagger c_j \rangle_{\text{imp-bath}} \overset{!}{=} \langle c_i^\dagger c_j \rangle_{\text{approx-lat}}. \qquad (2.42)$$

The approximate lattice model in DMET consists in the following quadratic Hamiltonian,

$$H_{\text{approx-lat}} = -t \sum_{\langle ij \rangle \sigma} c_{i\sigma}^\dagger c_{j\sigma} + u \sum_{i\sigma} n_{i\sigma}, \qquad (2.43)$$

which is characterized by an effective parameter u (which also includes the chemical potential term μ in (2.41)), whereas the hopping t has the same meaning as in (2.41).

The impurity-bath Hamiltonian, on the other hand, can be constructed by *embedding* an impurity cluster in this approximate lattice model. Consider the Schmidt decomposition (2.30) of the ground state $|E_0\rangle$ of the approximate lattice $|E_0\rangle = \sum_\nu s_\nu |d_\nu\rangle |b_\nu\rangle$, where $|d_\nu\rangle$ denotes the states of the impurity cluster, and $|b_\nu\rangle$ the states of the rest of the lattice. If the impurity cluster consists of a single impurity, the index ν runs over the dimension of a single site. Let us consider this case for the sake of simplicity. We can then identify the states $|d_\nu\rangle$ and $|b_\nu\rangle$ with states from the set

---

[10]Metzner and Vollhardt (1989); Georges and Kotliar (1992); Georges *et al.* (1996); Maier *et al.* (2005); Kotliar *et al.* (2006)

$\{|0\rangle, |\uparrow\rangle, |\downarrow\rangle, |\uparrow\downarrow\rangle\}$. We can associate operators $d_\sigma^\dagger$ and $b_\sigma^\dagger$ with these states, even though $|d_\nu\rangle$ and $|b_\nu\rangle$ denote *effective* single-particle states, which are *not* equivalent with the original degrees of freedom of the lattice. If we project the original Hamiltonian $H_\text{approx-lat}$ on the Schmidt basis, we therefore obtain

$$H'_\text{imp-bath} = \sum_{\nu\mu\nu'\mu'} |d_\nu b_\mu\rangle\langle d_\nu b_\mu|H_\text{approx-lat}|d_{\nu'} b_{\mu'}\rangle\langle d_{\nu'} b_{\mu'}|$$
$$= \sum_\sigma \langle \sigma 0|H_\text{approx-lat}|\sigma 0\rangle d_\sigma^\dagger d_\sigma + v\sum_\sigma d_\sigma^\dagger c_\sigma + \widetilde{u}\sum_\sigma c_\sigma^\dagger c_\sigma, \tag{2.44}$$

where $v = \langle \sigma 0|H_\text{approx-lat}|0\sigma\rangle$ and $\widetilde{u} = \langle 0\sigma|H_\text{approx-lat}|0\sigma\rangle$. The second line contains all matrix elements that are produced by a quadratic Hamiltonian. Obviously, $H'_\text{imp-bath}$ still is a quadratic Hamiltonian and we gain no insights in the physics of an interacting model by solving this projected Hamiltonian. Instead of using the term $\langle \sigma 0|H_\text{approx-lat}|\sigma 0\rangle d_\sigma^\dagger d_\sigma$ (a mean-field interaction), we therefore introduce the interaction of the original lattice problem (2.41) to define the following impurity-bath Hamiltonian

$$H_\text{imp-bath} = Un_{i\uparrow}n_{i\downarrow} + v\sum_\sigma (d_\sigma^\dagger c_\sigma + \text{h.c.}) + \widetilde{u}\sum_\sigma c_\sigma^\dagger c_\sigma. \tag{2.45}$$

Using an initial guess for v and $\widetilde{u}$, we can solve for the ground-state of $H_\text{imp-bath}$ and compute the single-particle density matrix $\langle c_i^\dagger c_j\rangle_\text{imp-bath}$. The single-particle density matrix of the quadratic lattice problem $\langle c_i^\dagger c_j\rangle_\text{approx-lat}$ can be obtained cheaply, and we can hence implement a minimization procedure that aims to fulfill (2.42) by searching for the parameter u in (2.43). Having found this parameter, we define a new impurity-bath Hamiltonian according to the previous description and iterate this procedure until convergence. That is, until the *self-consistency* condition (2.42) is fulfilled.

Evidently, DMET is exact in the atomic limit ($t = 0$), in the non-interacting limit ($U = 0$) and in the limit of infinite impurity cluster size. Furthermore, it is extremely cheap to compute and has e.g. been successfully applied to the long-standing problem of finding the phase diagram of the two-dimensional Hubbard model (Zheng and Chan, 2015). Still, one can come up with a more sophisticated theory, that is a bit less *ad hoc* in the sense that fulfills several consistency checks by construction. This is the dynamical mean-field theory.

2.2.2. Dynamical mean-field theory

In brief: DMFT and its extensions, the dynamical cluster approximation (DCA) and cellular DMFT, construct a non-interacting bath that is chosen such that the Green's function of an approximate lattice model is best reproduced

$$\langle c_K^\dagger \frac{1}{z - (H_\text{imp-bath} - E_0)} c_K\rangle_\text{imp-bath} \overset{!}{=} \langle c_K^\dagger \frac{1}{z - (H_\text{approx-lat} - E_0)} c_K\rangle_\text{approx-lat}, \tag{2.46}$$

or introducing the symbol G to denote Green's function,

$$G_K^\text{imp-bath}(z) \overset{!}{=} G_K^\text{approx-lat}(z). \tag{2.47}$$

Whereas the notation of (2.46), which we used to stress the analogy to (2.42), only took into account the *hole contribution* of a Green's function, here, Green's functions are defined as the usual superposition of hole and particle contributions (see Appendix A). In the preceding equations,

z is a frequency variable.[11] In contrast to DMET, this self-consistency condition incorporates *dynamic* information. The index K labels a set (patch) $\mathcal{P}_K$ of k-vectors in the Brillouin-zone, over which the Green's function of the original lattice problem is averaged in the sense

$$G_K^{\text{lat}}(z) = \frac{L_c}{L} \sum_{k \in \mathcal{P}_K} \frac{1}{G_{0k}^{\text{lat}}(z)^{-1} - \Sigma_k^{\text{lat}}(z)}, \qquad G_{0k}^{\text{lat}}(z) = (z - \epsilon_k + \mu)^{-1} \qquad (2.48)$$

where L is the number of k vectors in the Brillouin zone (number of lattice sites), L_c is the number of patches, $G_{0k}^{\text{lat}}(z)$ is the non-interacting Green's function of the lattice for momentum k, $\epsilon_k = -2t(\cos k_x + \cos k_y)$ is the single-particle dispersion of the lattice Hamiltonian (2.41), $\Sigma_k^{\text{lat}}(\omega)$ is the *exact* self-energy of the lattice problem, μ is the chemical potential. Of course, the exact self-energy $\Sigma_k^{\text{lat}}(z)$ of the lattice problem is unknown and we therefore cannot evaluate (2.48). To be able to do so, in DMFT, we make the approximation

$$\Sigma_k^{\text{lat}}(z) \simeq \Sigma_K(z) \text{ if } k \in \mathcal{P}_K, \qquad (2.49)$$

where $\Sigma_K(z)$ is an effective parameter of the theory.

Let us be concrete and give the equations for the single-site impurity cluster. Then, we only have a single index $K = 1$ (that we omit to specify in the following) and $\mathcal{P}_{K=1} \equiv \mathcal{BZ}$ is the whole Brillouin zone. The summation in (2.48) therefore produces the *local* Green's function $G_{ii}^{\text{lat}}(z)$,[12] where i denotes a lattice site as in (2.41). Suppressing this index the approximate lattice model can in analogy to (2.43) be expressed as

$$G^{\text{approx-lat}}(z) = \frac{1}{L} \sum_k \frac{1}{G_{0k}^{\text{lat}}(z)^{-1} - \Sigma(z)}. \qquad (2.50)$$

We now need to come up with an impurity-bath model that provides us with an estimation of the self-energy $\Sigma(z)$ by evaluating the many-body interaction term in (2.41) explicitly. This estimate for the self-energy is *local*, i.e. it has no dependence on momentum, and can therefore be associated with a zero-dimensional quantum field theory, or equivalently, with the single-impurity Anderson model (SIAM)

$$H^{\text{imp-bath}} = H_{\text{imp}} + H_{\text{coupl}} + H_{\text{bath}}, \qquad (2.51)$$

$$H_{\text{imp}} = U n_\uparrow n_\downarrow - \mu \sum_\sigma n_\sigma, \quad H_{\text{coupl}} = \sum_{k\sigma} (V_k d_\sigma^\dagger c_{k\sigma} + \text{h.c.}), \quad H_{\text{bath}} = \sum_{k\sigma} \epsilon_k c_{k\sigma}^\dagger c_{k\sigma},$$

where the index k is *not* a momentum quantum number, but simply an index that is *dense* on some interval on the real axis (it is a continuous index).[13]

---

[11] On the real axis, $z = \omega \pm i0$, the Green's function (retarded/advanced Green's function) is the Fourier transform of the real-time Green's function, and on the imaginary axis $z = i\omega_n$ (Matsubara Green's function), it is the Fourier transform of the imaginary-time Green's function. See Appendix A for more details.

[12] Simply by definition of the Fourier transform via integration over the Brillouin zone. Evidently, for the local contribution $i = j$, the exponential factor $e^{-i(\boldsymbol{r}_i - \boldsymbol{r}_j)k}$ reduces to 1.

[13] The sum $\sum_k$ has an infinite number of components and one could just as well (and often does) write it as an integral $\int d\epsilon$, that is $H_{\text{coupl}} = \sum_\sigma \int d\epsilon \, (\widetilde{V}_\epsilon d_\sigma^\dagger \widetilde{c}_{\epsilon\sigma} + \text{h.c.})$ and $H_{\text{bath}} = \sum_\sigma \int d\epsilon \, \epsilon \, \widetilde{c}_{\epsilon\sigma}^\dagger \widetilde{c}_{\epsilon\sigma}$. The creation and annihilation operator then depend on a veritable continuous index ϵ.

The Green's function for the impurity bath problem can readily be expressed as[14]

$$G^{\text{imp-bath}}(z) = \frac{1}{z + \mu - \Lambda(z) - \Sigma(z)}, \tag{2.55}$$

where we defined the *hybridization* function

$$\Lambda(z) = \sum_k \frac{|V_k|^2}{z - \epsilon_k}. \tag{2.56}$$

Equation (2.55) makes clear that the parameters V_k and ϵ_k of the impurity-bath model (2.51) can be characterized with a single function $\Lambda(z)$.

Now the question is to determine the function $\Lambda(z)$ so that the self-consistency condition (2.47) is fulfilled. This problem is, just as in DMET, solved by using a fixed point iteration, which is referred to as *DMFT loop*.

DMFT loop

With an initial guess for the self-energy $\Sigma(z)$ (usually one takes the non-interacting case $\Sigma(z) = 0$) iterate the following

$$G^{\text{approx-lat}}(z) = \frac{1}{L} \sum_k \frac{1}{z - \epsilon_k + \mu - \Sigma(z)}, \qquad \text{cf. (2.50)}$$

$$\frac{1}{G_0^{\text{imp-bath}}(z)} = \frac{1}{G^{\text{approx-lat}}(z)} + \Sigma(z), \qquad \text{self-consistency cf. (2.47)}$$

$$\Lambda(z) = \frac{1}{G_0^{\text{imp-bath}}(z)} - (z + \mu), \qquad \text{cf. (2.55)}$$

$$\Lambda(z) \overset{\text{approx}}{\mapsto} \Lambda^{\text{discr}}(z), \qquad \text{(only needed for certain impurity solvers)}$$

$$\Sigma(z) = \frac{1}{G^{\text{imp-bath}}(z)} - \frac{1}{G_0^{\text{imp-bath}}(z)}, \qquad \text{provided by an } \textit{impurity solver.} \tag{2.57}$$

As mentioned before, we can evaluate the DMFT loop either on the real-frequency $z = \omega + i0^+$, or on the imaginary frequency axis $z = i\omega_n$.[15] In the first case, the involved Green's functions are

---

[14] A brief derivation of the hybridization function works as follows (Hewson, 2003). The operator Green's function $\hat{G}(z)$ is the resolvent

$$(z - H)\hat{G}(z) = I. \tag{2.52}$$

Let us evaluate this for the Hamiltonian (2.51) in the *non-interacting* case $U = 0$ (single-particle case) by taking matrix elements with $\langle d | \ldots | d \rangle$ and $\langle k | \ldots | d \rangle$, where $|d\rangle = d^\dagger |\text{vac}\rangle$ and $|k\rangle = c_k^\dagger |\text{vac}\rangle$ (suppressing the spin index). Inserting the identity for the single-particle Hilbert space $I = |d\rangle\langle d| + \sum_k |k\rangle\langle k|$ one obtains

$$(z + \mu)G_{dd} - \sum_k V_k^* G_{kd} = 1, \tag{2.53a}$$

$$(z - \epsilon_k)G_{kd} - V_k G_{dd} = 0. \tag{2.53b}$$

Solving the second equation for G_{kd} and using this result in the first equation yields

$$G_{dd}(z) = \frac{1}{z + \mu - \Lambda(z)}, \tag{2.54}$$

where $\Lambda(z)$ is defined in (2.56). The hybridization function can also be derived by integrating over the quadratic bath terms in the action associated with H_{SIAM}.

[15] Most impurity solver are limited to either a computation on the real-frequency axis or the imaginary-frequency axis. ED is so strongly limited in the number of bath sites that a bath cannot be constructed in a meaningful
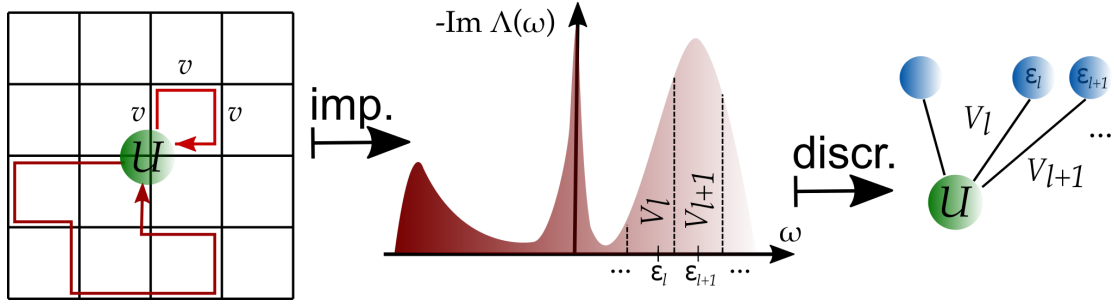
Fig. 2.5.: Illustration of the DMFT approximation. First, map the lattice model to a continuous impurity model characterized by the hybridization function $\Lambda(z)$ or its spectral density $\propto -\mathrm{Im}\Lambda(\omega + i0)$. Second, discretize the continuous impurity model to obtain a discrete Hamiltonian representation. The last step is discussed in detail in Sec. 5.3.

the retarded real-frequency Green's functions, in the second case, these are Matsubara Green's functions (see Appendix A for a reminder on the definitions).

All preceding equations were given in terms of continuous degrees of freedom: the continuous bath of the SIAM reflects that excitations into an infinite lattice environment can occur at arbitrary (infinitesimally spaced) energies. As DMRG, as well as ED and NRG, can only treat discrete Hamiltonian representations, we need to perform a *discretization step*, as indicated in (2.57). The whole technical idea of DMFT, including this discretization step, is sketched in Fig. 2.5.

The *discretization step* can be carried out either on the imaginary- or on the real-frequency axis. On the imaginary-frequency axis, the discretization step is the so-called *bath fitting* procedure of Caffarel and Krauth (1994). We explain this procedure in the proposal for an *imaginary-time impurity solver* in Sec. 3.2. On the real-frequency axis, there are several options. We summarize the *linear discretization strategy* in the proposal for a *real-frequency* impurity solver in in Sec. 3.1 and introduce a *cosine-spaced discretization* in Sec. 5.1. In Sec. 5.3, finally, we explain in detail all existing discretization strategies for the real-axis.

On the Bethe lattice

On the Bethe lattice, the DMFT loop (2.57) becomes even simpler. On any lattice, we can rewrite (2.50) in terms of the non-interacting density of states $A_0^{\mathrm{lat}}(\omega)$

$$G^{\mathrm{approx\text{-}lat}}(z) = \int d\epsilon \frac{A_0^{\mathrm{lat}}(\epsilon)}{z - \epsilon + \mu - \Sigma(z)}. \tag{2.58}$$

---

way on the real axis, where no notion of an optimal bath exists (de Vega *et al.*, 2015). In ED one therefore always converges the DMFT loop on the imaginary axis (Caffarel and Krauth, 1994; Liebsch and Ishida, 2012; Go and Millis, 2015). NRG, by contrast, is limited to the construction of a bath only on the real axis as it needs a logarithmic discretization, which obeys *energy scale separation* (Bulla *et al.*, 2008; de Vega *et al.*, 2015). QMC methods are considered powerful only on the imaginary axis. A long-standing problem for QMC on the imaginary-frequency axis is the ill-controlled analytic continuation to obtain real-frequency information. That this is ill-conditioned can either be seen by noting that Green's functions on the imaginary-axis are relatively uniform and smooth, or by realizing that solving

$$G^{\mathrm{mat}}(i\omega_n) = \int d\omega' \frac{A(\omega')}{i\omega_n - \omega'}, \quad A(\omega) = -\frac{1}{\pi} \mathrm{Im} G_{\mathrm{ret}}(\omega)$$

for $A(\omega)$ corresponds to inverting a "matrix" with extremely small eigenvalues, which is ill-controlled (the "matrix" $M^{-1}(\omega_n, \omega') = \frac{1}{i\omega_n - \omega'}$ has extremely large eigenvalues due to contributions where $i\omega_n \approx \omega'$; conversely, the "matrix" M has very small eigenvalues and can hardly be inverted). Only recently QMC methods have been advanced to provide information about longer times also on the real-frequency axis (Cohen *et al.*, 2014a,b; Gull *et al.*, 2011a,b), and might themselves be able to shed more light on the question of analytic continuation in the future (Dirks *et al.*, 2013).

Let us consider the function $R(z)$ that inverts $G(z) = \int d\epsilon \frac{A_0^{\text{lat}}(\epsilon)}{z-\epsilon}$ in the sense $R(G(z)) = z$, which allows to solve (2.58) for $\Sigma(z)$ directly

$$\Sigma(z) = z + \mu - R(G(z)). \tag{2.59}$$

Here we dropped the superscript $^{\text{approx-lat}}$ for clarity in notation. Inserting (2.59) in the second equation of (2.57) and using the result to evaluate the third equation of (2.57) yields

$$\Lambda(z) = \frac{1}{G(z)} - R(G(z)). \tag{2.60}$$

Using the self-consistency condition (2.47), we can immediately replace the approximate lattice Green's function $G(z) \equiv G^{\text{approx-lat}}(z)$ with the Green's function that we obtained in the previous DMFT iteration via an impurity model $G(z) = G^{\text{imp-bath}}(z)$.[16] The topology of the lattice is captured in the functional form of $R(G)$.

The function $R(z)$ can only rarely be obtained analytically as in the case of the Bethe lattice, where we have (Georges *et al.*, 1996, p. 117)

$$G_0^{\text{lat}}(z) = \frac{z - \sqrt{z^2 - 4t^2}}{2t^2}, \tag{2.61a}$$

$$A_0^{\text{lat}}(\omega) = \frac{\sqrt{\omega^2 - 4t^2}}{2\pi t}, \tag{2.61b}$$

$$R(G) = t^2 G + \frac{1}{G}. \tag{2.61c}$$

In this case, the hybridization function of the new impurity model can be directly obtained from the result of a impurity Green's function in the previous DMFT iteration

$$\Lambda(z) = t^2 G(z), \tag{2.62}$$

which is of course just a different way to state the self-consistency condition.

The DMFT loop (2.57) then reduces to

$$\begin{aligned}
\Lambda(z) &= t^2 G^{\text{approx-lat}}(z), \\
\Lambda(z) &\mapsto \Lambda^{\text{discr}}(z) && \text{(only needed for certain impurity solvers),} \\
G^{\text{approx-lat}}(z) &\stackrel{!}{=} G^{\text{imp-bath}}(z) && \text{provided by an } \textit{impurity solver.}
\end{aligned} \tag{2.63}$$

Summary

As DMET, DMFT is easily seen to be exact in the atomic ($t = 0$) and non-interacting ($U = 0$) limit, and in the limit of infinite impurity cluster size. In contrast to DMET, already the single-site DMFT provides the exact solution of a lattice model in the limit of infinite spatial dimensions or, equivalently, infinite lattice coordination number (Metzner and Vollhardt, 1989). In contrast to DMET, DMFT can be shown to be a *thermodynamically consistent* approximation to the lattice problem in the sense of a Baym-Kadanoff construction. Let us show this in the following.

2.2.3. Baym-Kadanoff construction of DMFT

We will here show that the definition of the approximate lattice problem in (2.49) is a *thermodynamically consistent* approximation of the original lattice problem (2.41) following Maier *et al.*

---

[16]In the first iteration, we would again simply start with the non-interacting Green's function.

(2005) and Kotliar *et al.* (2006). *Thermodynamically consistent* means that the theory fulfills all relevant conservation laws.

Consider the definition of the free energy F as the logarithm of the partition function for the action $S = \int dx\, \psi^\dagger(x)\partial_\tau\psi(x) + \int d\tau H$, which is associated with the Hamiltonian H in (2.41)

$$e^{F[J]} = \int \mathcal{D}[\psi^\dagger, \psi]e^{-S - \int dx dx' J(x,x')\hat{G}(x,x')}, \quad x = (\tau, r, \sigma), \quad \hat{G}(x,x') = \psi(x)^\dagger\psi(x'), \quad (2.64)$$

where the physical free energy is $F[J=0]$. Here, τ denotes imaginary time, r a position vector and σ a spin index. Equation (2.64) defines the generating functional for the Green's function[17]

$$G(x,x') = \langle \hat{G}(x,x') \rangle_S = \frac{\delta F}{\delta J(x,x')}\bigg|_{J=0}. \quad (2.65)$$

Interacting Green's function from non-interacting system

Let us split the action in the easily solvable non-interacting and the difficult interacting part, i.e.

$$S = S_0 + US_1. \quad (2.66)$$

We can expand the coupling according to

$$J = J_0 + UJ_1 + U^2 J_2 + \dots, \quad (2.67)$$

where we note that already the zeroth order contribution J_0 to J, allows to extract the *interacting* Green's function from F just as in (2.65)

$$G = \frac{\delta F}{\delta J_0}\bigg|_{J_0=0}. \quad (2.68)$$

In the non-interacting case $U = 0$, we can evaluate the integral (2.64) as it is Gaussian[18]

$$e^{F_0[J_0]} = \int D[\psi^\dagger, \psi]e^{-\int dx dx' \psi^\dagger(x)(\partial_\tau + H_0 + J_0)\psi(x')} = \det\left(-\partial_\tau + H_0 + J_0\right)$$

$$\Rightarrow F_0[J_0] = -\operatorname{tr}\ln(G_0^{-1} - J_0). \quad (2.69)$$

Evaluating (2.68) for F_0 yields

$$G_0 = \frac{\delta F_0}{\delta J_0} = (G_0^{-1} - J_0)^{-1}\big|_{J_0=0} = G_0, \quad (2.70)$$

as expected.

We can now ask: how do I have to modify the non-interacting system F_0 characterized by S_0 (or H_0) if I want to retain its simple Gaussian (non-interacting, single-particle) form, but still obtain the interacting Green's function? This is achieved by considering the hypothetical system

$$S' = S_0 + \operatorname{tr}J_0\hat{G}, \quad (2.71)$$

which adds to S_0 the quadratic term $\hat{G}(x,x') = \psi(x)^\dagger\psi(x')$ coupled with the function J_0. We just computed the partition function and free energy $F' = F_0$ for this system in (2.69). Demanding

---

[17] Instead of coupling the internal action S to the Green's function $\hat{G}$, we could just as well couple it to the density $\hat{\rho} = \psi(r,\sigma)^\dagger\psi(r,\sigma)$ and study its generating functional. The analogous discussion of this functional would lead us to the so-called *density functional theory*, the most popular approximate theory for quantum lattice models in material science.

[18] See e.g. Altland and Simons (2010) or the freely available lecture notes of Simons (2012).

that $\langle \hat{G}(x, x') \rangle_{S'}$ yields the interacting Green's function now gives a condition for the value of J_0 in (2.71)

$$G \overset{!}{=} \frac{\delta F'}{\delta J_0}\bigg|_{J_0=\Sigma} = \frac{\delta F_0}{\delta J_0}\bigg|_{J_0=\Sigma} = (G_0^{-1} - \Sigma)^{-1}. \tag{2.72}$$

The value $J_0 = \Sigma$ that has to be added to the *non-interacting* system in order to reproduce the *interacting* Green's function, coincides with the usual definition of the self energy Σ via the *Dyson equation*

$$\Sigma = G_0^{-1} - G^{-1}. \tag{2.73}$$

Almost all equations used in the previous derivations, e.g. (2.49) and (2.50), used the Dyson equation in order to be able to recycle all equations of the non-interacting problem, also in the interacting case. But let us move on to show how we can make use of this formalism to construct a thermodynamically consistent theory.

Baym-Kadanoff functional

Let us define the Legendre transform $\Omega[G]$ of $F[J]$, which we can identify, up to a prefactor $-k_bT$, with the grand potential $-k_bT\,\Omega[G]$[19]

$$\Omega[G] = F[J[G]] - \mathrm{tr}J[G]G, \tag{2.74}$$

where the trace denotes integration $\mathrm{tr}... = \int dx \int dx'...$. Let us separate the non-interacting contribution from the interacting contribution, by defining the *Baym-Kadanoff generating functional* $\Phi[G]$

$$\Omega[G] = \Omega_0[G] + \Phi[G]. \tag{2.75}$$

We can evaluate the non-interacting part $\Omega_0[G] = F_0[J_0[G]] - \mathrm{tr}J_0[G]G$,[20] using the result for F_0 in (2.69),

$$\Omega_0[G] = -\mathrm{tr}\ln(G_0^{-1} - J_0) - \mathrm{tr}J_0G \tag{2.76}$$

Baym and Kadanoff (1961) showed that stationarity of Ω guarantees thermodynamical consistence. Following Kotliar *et al.* (2006), we can view Ω as a functional in two variables[21] J_0 and G. Demanding stationarity of $\Omega[G, J_0]$ with respect to J_0 again reproduces the Dyson equation as in (2.72)

$$\frac{\delta\Omega[G, J_0]}{\delta J_0} = (G_0^{-1} - J_0)^{-1} - G = 0 \qquad \Rightarrow \qquad J_0 = G_0^{-1} - G^{-1} \tag{2.77}$$

which allows to identify the thermodynamically consistent value of J_0 with the self-energy Σ. Demanding stationarity of $\Omega[G, J_0]$ with respect to G leads to

$$\frac{\delta\Omega[G, J_0]}{\delta G} = -J_0 + \frac{\delta\Phi}{\delta G} \qquad \Rightarrow \qquad J_0 \equiv \Sigma = \frac{\delta\Phi}{\delta G}. \tag{2.78}$$

The Baym-Kadanoff generating functional $\Phi[G]$ is associated with all non-gaussian parts in the

---

[19]This is abuse of notation as the symbol Ω usually is reserved for the grand potential.

[20]Note that the dependence (2.68) allows to define already the zeroth order contribution $J_0[G]$ to $J[G]$ as a functional of the interacting Green's function G.

[21]Although previously, we eliminated the dependence on J_0 using the Legendre transform, we now regard it as a free parameter. It will become immediately clear that stationarity fixes it to its usual value.

integral (2.64). It can therefore be diagrammatically be expressed as the skeletal graph sum over all compact, distinct, closed, connected diagrams constructed from G. It is, of course, unkown and has in practice to be approximated.

Baym and Kadanoff (1961) now state that any theory that approximates Φ while still fulfilling (2.77) and (2.78) is thermodynamically consistent.

Approximating the Baym-Kadanoff functional

Let us restrict ourselves to theories that fulfill the Dyson equation. In this case, we can omit to specify J_0 as an argument as it is fixed by G through the Dyson equation. Aside from the argument G, let us introduce the interaction U as additional parameter of the grand potential. We will *not* demand stationarity with respect to U, but introduced it simply for technical reasons. Then (2.75) reads, using (2.76)

$$\Omega[G, U] = -\operatorname{tr}\ln G - \operatorname{tr}\Sigma G + \Phi[G, U]. \tag{2.79}$$

Considered as a function, U is no-longer meant to mean simply the scalar value of the interaction in (2.41), but also the *functional form* of the interaction, which is fully *local* in the Hubbard model (2.41). Fourier transforming the interaction part of (2.41) reveals the Laue function as the constraint for the vertices in a diagrammatic expansion around $U = 0$ in momentum space

$$\sum_r U e^{ir(k_1 + \cdots - k_1' - \cdots)} = L\, U \delta_{k_1 + \ldots, k_1' + \ldots}. \tag{2.80}$$

If the interaction took a different, non-local form and extended e.g. to nearest-neighbors or was slowly decaying with distance between particles, we would *not* obtain the Laue function as constraint on the interaction vertices.

In the DCA,[22] we approximate the exact functional $\Phi[G, U]$ with the functional $\Phi[\overline{G}[G], \overline{U}[G]]$, where $\overline{G}[G]$ and $\overline{U}[U]$ are defined as averages over the patches $\mathcal{P}_K$ of the Brillouin zone[23]

$$\overline{G}_K = \frac{L_c}{L} \sum_{k \in \mathcal{P}_K} G_k \tag{2.81a}$$

$$\overline{U}_K = \frac{L_c}{L} \sum_{k \in \mathcal{P}_K} U_k. \tag{2.81b}$$

Consequently, all diagrams collapse onto coarse-grained diagrams that fulfill a relaxed momentum conservation[24]

$$\sum_R U e^{iR(K_1 + \cdots - K_1' + \cdots)} = L_c U \delta_{K_1 + \ldots, K_1' + \ldots}. \tag{2.82}$$

But this is the only approximation made. It is very important to note that the approximation $\Phi[\overline{G}[G], \overline{U}[G]]$ retains the same *type* of diagrams as are present in $\Phi[G, U]$. In particular, no assumption about the *order* of diagrams is made, that is, diagrams are included to *all* orders.

---

[22] The following summary of parts of the review of Maier *et al.* (2005) is based on the presentation of Bilitewski (2013).

[23] The first of the following lines has already been defined in (2.48). There the notation using a bar to denote average was redundant. Here we use this additional notation as we consider G and $\overline{G}$ as matrices.

[24] It is important to note that the patches $\mathcal{P}_K$ need to have the same area. See e.g. the appendix of Ferrero *et al.* (2009) for a discussion on this.

Using $\frac{\delta \overline{G}_K}{\delta G_k} = \delta_{K,K'(k)}$ where

$$K'(k) = K \text{ for which } k \in \mathcal{P}_K \tag{2.83}$$

and demanding stationarity of the approximation of Ω

$$\Omega[\overline{G}, \overline{U}] = -k_b T \left(\Phi[\overline{G}, \overline{U}] - \text{tr}\ln\overline{G} - \text{tr}\Sigma\overline{G} \right). \tag{2.84}$$

that is generated by approximating $\Phi[G, U]$ with $\Phi[\overline{G}[G], \overline{U}[U]]$, one obtains

$$\frac{\delta\Omega[\overline{G}_K, \overline{U}_K]}{\delta G_k} = \Sigma_k - \frac{d\Phi[\overline{G}_K, \overline{U}_K]}{\delta G_k} = \Sigma_k - \Sigma_K = 0. \tag{2.85}$$

The DCA functional $\Phi[\overline{G}[G], \overline{U}[G]]$, whose coarse-grained diagrams can be generated by a general impurity-cluster model, therefore yields the approximation $\Sigma_k = \Sigma_K$ as was already heuristically argued in (2.49). Using this approximation in the Dyson equation, we obtain the approximate lattice Green's function

$$(G_k^{\text{approx-lat}})^{-1} = G_{0k}^{-1} - \Sigma_{K'(k)} \tag{2.86}$$

where $K'(k)$ was defined in (2.83). Using this approximation in the definition of (2.81a), one obtains

$$\overline{G}_K^{\text{approx-lat}} = \frac{L_c}{L} \sum_{k \in \mathcal{P}_K} (G_{0k}^{-1} - \Sigma_K)^{-1}. \tag{2.87}$$

Clearly, this is equivalent to what we studied previously in the single-site case, see (2.50), using a notation without bar $\overline{G}_K^{\text{approx-lat}} \equiv G_K^{\text{approx-lat}}$.

2.3. Matrix product state algorithms

Whereas Sec. 2.1 explained the motivation for the use of MPS in the description of quantum many-body systems, the present section will explain some of the algorithms used in the context of this thesis in more detail. In particular, we discuss the DMRG ground state optimization (Sec. 2.3.1) and the computation of Green's functions using the Lanczos algorithm (Sec. 2.3.2).

To this end, we also need to introduce matrix product operators (MPOs) in addition to the MPS introduced in Sec. 2.1. This is straight-forward by considering a single coefficient $\langle \boldsymbol{\sigma}|\psi\rangle$ of an MPS[25]

$$\langle \boldsymbol{\sigma}|\psi\rangle = A^{\sigma_1} A^{\sigma_2} \ldots A^{\sigma_{L-1}} A^{\sigma_L}, \tag{2.88}$$

which makes it plausible to write down coefficients for operators $\langle \boldsymbol{\sigma}|\hat{O}|\boldsymbol{\sigma}'\rangle$ as[26]

$$\langle \boldsymbol{\sigma}|\hat{O}|\boldsymbol{\sigma}'\rangle = W^{\sigma_1 \sigma_1'} W^{\sigma_2 \sigma_2'} \ldots W^{\sigma_{L-1} \sigma_{L-1}'} W^{\sigma_L \sigma_L'}, \tag{2.89}$$

where the $W^{\sigma\sigma'}$ are matrices just like the A^σ, with the only difference that they need both

---

[25] Here and in the following, we label general physical degrees of freedom with the common notation using the variable σ_l (and $\boldsymbol{\sigma}$ to denote the tuple $\boldsymbol{\sigma} = (\sigma_1, \ldots, \sigma_L)$), as in the example of the spin-$\frac{1}{2}$ degree of freedom (2.19). In Sec. 2.1, we used the notation x_l to denote physical degrees of freedom as in the case of classical systems, these were associated with random numbers X_l, for which no meaningful notation using σ_l can be established. As we aimed at highlighting parallels and differences of the classical and the quantum case, we wanted to keep the same notation for the two cases.

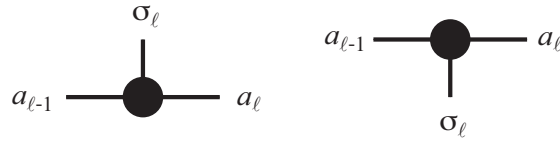[26] See e.g. Verstraete *et al.* (2004); McCulloch (2007).

Fig. 2.6.: Graphical representation of A-matrix: the left diagram represents $A_{a_{\ell-1},a_\ell}^{\sigma_\ell}$, the right diagram the *conjugate* $A_{a_{\ell-1},a_\ell}^{\sigma_\ell *}$. The solid circle represents the lattice sites, the vertical line the physical index, the horizontal lines the matrix (bond) indices. On the edge, the matrix A becomes a vector (as discussed before (2.26)) and the corresponding diagram then only has a single left (or right) horizontal line. This figure is from Schollwöck (2011).
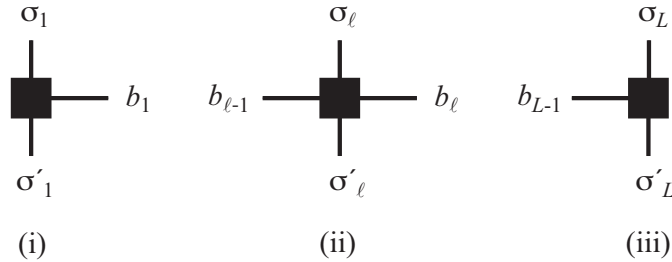

$$\text{(i)} \qquad\qquad \text{(ii)} \qquad\qquad \text{(iii)}$$

Fig. 2.7.: Elements of a matrix product operator: (i) a corner matrix operator $W_{1,b_1}^{\sigma_1\sigma_1'}$ at the left end of the chain, (ii) a bulk matrix operator $W_{b_{\ell-1},b_\ell}^{\sigma_\ell\sigma_\ell'}$, and (iii) a corner operator $W_{b_{L-1},1}^{\sigma_L\sigma_L'}$ at the right end: the physical indices points up and down, the matrix indices are represented by horizontal lines. This figure is Schollwöck (2011).

outgoing and ingoing physical states:

$$\hat{O} = \sum_{\boldsymbol{\sigma},\boldsymbol{\sigma}'} W^{\sigma_1\sigma_1'} W^{\sigma_2\sigma_2'} \ldots W^{\sigma_{L-1}\sigma_{L-1}'} W^{\sigma_L\sigma_L'} |\boldsymbol{\sigma}\rangle\langle\boldsymbol{\sigma}'|. \tag{2.90}$$

Let us also introduce the typical diagrammatic language for tensor networks, which will be of help. We depict the A matrices in an MPS as in Fig. 2.6 and the W matrices of an MPO as in Fig. 2.7.

2.3.1. DMRG or variational MPS

Let us give the details for the fundamental ground state optimization algorithm. For this, we follow Sec. 6.3 of Schollwöck (2011) quite closely.

Just as for the mean-field state (2.24), in order to find the optimal approximation to the ground state within a class of MPS with fixed bond dimension, we have to find the MPS $|\psi\rangle$ that minimizes

$$E = \frac{\langle\psi|H|\psi\rangle}{\langle\psi|\psi\rangle}, \tag{2.91}$$

i.e. we extremize, using the Lagrangian multiplier λ,

$$\langle\psi|H|\psi\rangle - \lambda\langle\psi|\psi\rangle. \tag{2.92}$$

After optimization, $|\psi\rangle$ will be an approximation to the ground state and λ and approximation to the ground state energy. The MPS network that represents Eq. (2.92) is shown in Fig. 2.8.

As the matrix elements $M_{\nu\nu'}^\sigma$ in $|\psi\rangle$ appear in the form of products, this is a highly non-linear optimization problem. But it can be decomposed in *local* linear optimizations: while keeping
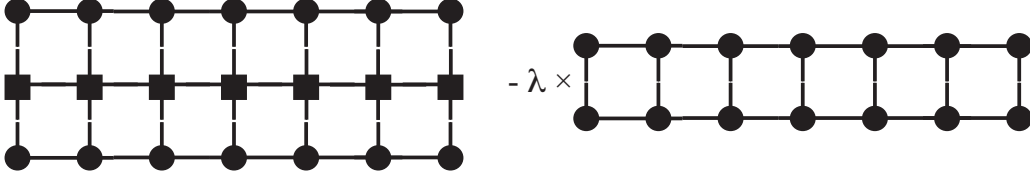
Fig. 2.8.: Network to be contracted to obtain the functional to be extremized to find the ground state and its energy. The left-hand side represents the term $\langle\psi|H|\psi\rangle$, the right-hand side the squared norm $\langle\psi|\psi\rangle$. This figure is from Schollwöck (2011).

the matrices on all sites but one (ℓ) constant, consider only the matrix entries $M^{\sigma_\ell}_{\nu_{\ell-1}\nu_\ell}$ on site ℓ as variables. Then the variables appear in Eq. (2.92) only in quadratic form, for which the determination of the extremum is a benign linear algebra problem. This will lower the energy, and one finds a variationally better state. It is the *locally* optimal state that depends on the values of all the fixed the other matrices. It only is the *globally* optimal state, if all other matrices have already reached the global maximum. Now one continues to vary the matrix elements on another site for finding a state again lower in energy, moving through all sites multiple times, until the energy does not improve anymore.

Let us first consider the calculation of the overlap, while keeping the chosen M^{σ_ℓ} explicit. We find

$$\langle\psi|\psi\rangle = \sum_{\sigma_\ell}\sum_{\nu_{\ell-1}\nu_\ell}\sum_{\nu'_{\ell-1}\nu'_\ell} \Psi^A_{\nu_{\ell-1},\nu'_{\ell-1}} M^{\sigma_\ell *}_{\nu_{\ell-1},\nu_\ell} M^{\sigma_\ell}_{\nu'_{\ell-1},\nu'_\ell} \Psi^B_{\nu_\ell,\nu'_\ell}, \tag{2.93}$$

where

$$\Psi^A_{\nu_{\ell-1},\nu'_{\ell-1}} = \sum_{\sigma_1,\dots,\sigma_{\ell-1}} (M^{\sigma_{\ell-1}\dagger}\dots M^{\sigma_1\dagger} M^{\sigma_1}\dots M^{\sigma_{\ell-1}})_{\nu_{\ell-1},\nu'_{\ell-1}} \tag{2.94a}$$

$$\Psi^B_{\nu_\ell,\nu'_\ell} = \sum_{\sigma_{\ell+1},\dots,\sigma_L} (M^{\sigma_{\ell+1}}\dots M^{\sigma_L} M^{\sigma_L\dagger}\dots M^{\sigma_{\ell+1}\dagger})_{\nu'_\ell,\nu_\ell}. \tag{2.94b}$$

In the case where sites 1 through $\ell-1$ are *left-normalized* (2.35a) and sites $\ell+1$ through L *right-normalized* (2.35b), we have

$$\Psi^A_{\nu_{\ell-1},\nu'_{\ell-1}} = \delta_{\nu_{\ell-1},\nu'_{\ell-1}} \qquad \Psi^B_{\nu_\ell\nu'_\ell} = \delta_{\nu_\ell\nu'_\ell}. \tag{2.95}$$

Let us now consider $\langle\psi|H|\psi\rangle$ to

$$\langle\psi|H|\psi\rangle = \sum_{\sigma_\ell,\sigma'_\ell}\sum_{\nu'_{\ell-1}\nu'_\ell}\sum_{\nu_{\ell-1}\nu_\ell}\sum_{b_{\ell-1},b_\ell} L^{\nu_{\ell-1},\nu'_{\ell-1}}_{b_{\ell-1}} W^{\sigma_\ell,\sigma'_\ell}_{b_{\ell-1},b_\ell} R^{\nu_\ell,\nu'_\ell}_{b_\ell} M^{\sigma_\ell *}_{\nu_{\ell-1},\nu_\ell} M^{\sigma'_\ell}_{\nu'_{\ell-1},\nu'_\ell} \tag{2.96}$$

where L and R contain the contracted left and right parts of the graphical network:

$$L^{\nu_{\ell-1},\nu'_{\ell-1}}_{b_{\ell-1}} = \sum_{\{\nu_i,b_i,\nu'_i;i<\ell-1\}} \left(\sum_{\sigma_1\sigma'_1} A^{\sigma_1 *}_{1,\nu_1} W^{\sigma_1,\sigma'_1}_{1,b_1} A^{\sigma'_1}_{1,\nu'_1}\right) \dots \left(\sum_{\sigma_{\ell-1}\sigma'_{\ell-1}} A^{\sigma_{\ell-1} *}_{\nu_{\ell-2},\nu_{\ell-1}} W^{\sigma_{\ell-1},\sigma'_{\ell-1}}_{b_{\ell-2},b_{\ell-1}} A^{\sigma'_{\ell-1}}_{\nu'_{\ell-2},\nu'_{\ell-1}}\right)$$

$$R^{\nu_\ell,\nu'_\ell}_{b_\ell} = \sum_{\{\nu_i,b_i,\nu'_i;i>\ell\}} \left(\sum_{\sigma_{\ell+1}\sigma'_{\ell+1}} B^{\sigma_{\ell+1} *}_{\nu_\ell,\nu_{\ell+1}} W^{\sigma_{\ell+1},\sigma'_{\ell+1}}_{b_\ell,b_{\ell+1}} B^{\sigma'_{\ell+1}}_{\nu'_\ell,\nu'_{\ell+1}}\right) \dots \left(\sum_{\sigma_L\sigma'_L} B^{\sigma_L *}_{\nu_{L-1},1} W^{\sigma_L,\sigma'_L}_{b_{L-1},1} B^{\sigma'_L}_{\nu'_{L-1},1}\right)$$
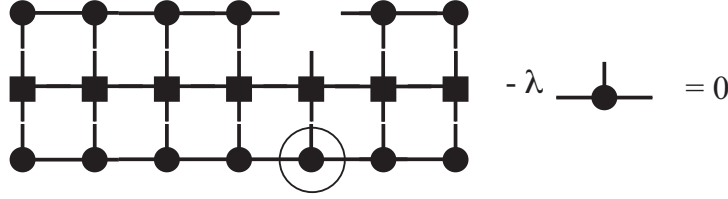
Fig. 2.9.: Standard eigenvalue problem for the optimization of $M^{\sigma_\ell}_{\nu_{\ell-1},\nu_\ell}$. The unknown matrix is circled on the left network. This figure is from Schollwöck (2011).

Taking the derivative of Eq. (2.92) with respect to $M^{\sigma_\ell*}_{\nu_{\ell-1},\nu_\ell}$, this yields

$$\sum_{\sigma'_\ell} \sum_{\nu'_{\ell-1}\nu'_\ell} \sum_{b_{\ell-1},b_\ell} L^{\nu_{\ell-1},\nu'_{\ell-1}}_{b_{\ell-1}} W^{\sigma_\ell,\sigma'_\ell}_{b_{\ell-1},b_\ell} R^{\nu_\ell,\nu'_\ell}_{b_\ell} M^{\sigma'_\ell}_{\nu'_{\ell-1},\nu'_\ell} - \lambda \sum_{\nu'_{\ell-1}\nu'_\ell} \Psi^A_{\nu_{\ell-1},\nu'_{\ell-1}} \Psi^B_{\nu_\ell \nu'_\ell} M^{\sigma_\ell}_{\nu'_{\ell-1},\nu'_\ell} = 0. \quad (2.97)$$

This is a simple eigenvalue equation, which becomes clear if we interpret the summations over all indices as the summation over the combined single index of *effective* operators that contain just the same data

$$H_{(\sigma_\ell \nu_{\ell-1}\nu_\ell),(\sigma'_\ell \nu'_{\ell-1}\nu'_\ell)} = \sum_{b_{\ell-1},b_\ell} L^{\nu_{\ell-1},\nu'_{\ell-1}}_{b_{\ell-1}} W^{\sigma_\ell,\sigma'_\ell}_{b_{\ell-1},b_\ell} R^{\nu_\ell,\nu'_\ell}_{b_\ell} \quad (2.98\text{a})$$

$$N_{(\sigma_\ell \nu_{\ell-1}\nu_\ell),(\sigma'_\ell \nu'_{\ell-1}\nu'_\ell)} = \Psi^A_{\nu_{\ell-1},\nu'_{\ell-1}} \Psi^B_{\nu_\ell,\nu'_\ell} \delta_{\sigma_\ell,\sigma'_\ell} \quad (2.98\text{b})$$

$$v_{(\sigma_\ell \nu_{\ell-1}\nu_\ell)} = M^{\sigma_\ell}_{\nu_{\ell-1},\nu_\ell} \quad (2.98\text{c})$$

Using the fact that Ψ^A and Ψ^B are identities if one uses a normalized MPS, and therefore $N = I$ is just an identity (the sums on the left-hand side of (2.97) collapse), one arrives at a simple *eigenvalue problem* of matrix dimension $(dm^2 \times dm^2)$,

$$Hv - \lambda v = 0, \quad (2.99)$$

represented in Fig. 2.9. Solving for the lowest eigenvalue λ_0 gives us a $v^0_{\sigma_\ell \nu_{\ell-1}\nu_\ell}$, which is reshaped back to $M^{\sigma_\ell}_{\nu_{\ell-1}\nu_\ell}$, λ_0 being the current ground state energy estimate. Once the solution is obtained, left-normalize M^{σ_ℓ} into A^{σ_ℓ} by SVD (or QR) to maintain the desired normalization structure. The remaining matrices of the SVD are multiplied to the $M^{\sigma_{\ell+1}}$ to the right, which will be the starting guess for the eigensolver for the next site. Build iteratively the L expression by adding one more site. Once the solution is obtained, right-normalize M^{σ_ℓ} into B^{σ_ℓ} by SVD (or QR) to maintain the desired normalization structure. The remaining matrices of the SVD are multiplied to the $M^{\sigma_{\ell-1}}$ to the left, which will be the starting guess for the eigensolver for the next site. Build iteratively the R expression by adding one more site. Move on by one site, $\ell \to \ell - 1$, and repeat.

Evaluating the variance tells one whether one reached an eigens state

$$\langle\psi|H^2|\psi\rangle - (\langle\psi|H|\psi\rangle)^2. \quad (2.100)$$

In this iterative process, the energy can only go down, as we continuously improve by varying the parameters. Two problems occur: starting from a random state, the guesses for the M^{σ_ℓ} in the iterative eigensolvers will be very bad in the initial sweeps, leading to large iteration numbers and bad performance. Moreover, we cannot guarantee that the global minimum is actually reached by this procedure instead of being stuck in a non-global minimum. We will show in Sec. 5.2 in detail how this can be circumvented.

2.3.2. Spectral functions using adapted Lanczos algorithm

How can we obtain Green's and spectral functions within the MPS framework? This thesis started with analyzing the suggestion of Dargel *et al.* (2012) for this, who introduced an MPS-adapted version of the original Lanczos algorithm (Lanczos, 1950).[27] We already mention here that the study presented in the following concludes that other algorithmic approaches for computing Green's functions are more attractive. Still this study has conceptional value and shows where the weakness of the approach of Dargel *et al.* (2012) lies.

Let us note here that other strategies for obtaining Green's functions are based on expanding the spectral function in plain waves or the Chebyshev polynomials. This amounts to performing time evolution (White and Feiguin, 2004; Daley *et al.*, 2004) with a subsequent Fourier transform (White and Feiguin, 2004; White and Affleck, 2008), or using the Chebyshev recursion (Holzner *et al.*, 2011). We explain both techniques in the course of the thesis: in Sec. 3.1 and Sec. 5.1, we treat the "Chebyshev approach" in detail, and in Sec. 3.2 and Sec. 4.1, the "time evolution approach".

To conclude these preliminary remarks, let us also note that another much used approach for the computation of Green's functions is *correction vector* DMRG (Kühner and White, 1999; Jeckelmann, 2002). Holzner *et al.* (2011) though showed that the "Chebyshev approach" is much more efficient. We then provided strong evidence that the "time evolution method" is again superior to the "Chebyshev approach" (Wolf *et al.*, 2015b). Within this thesis, we refrained from studying correction vector DMRG.

Lanczos algorithm

The Lanczos algorithm constructs an orthogonal basis $\{|f_0\rangle, |f_1\rangle, |f_2\rangle, \dots\}$ of the Hilbert space, by orthogonalizing the *Krylov basis* $\{|f_0\rangle, H|f_0\rangle, H^2|f_0\rangle, \dots\}$ for some *initial* vector $|f_0\rangle$. This can be done iteratively, by orthogonalizing $|f_k\rangle$ with respect to all $|f_{k'}\rangle$ with $k' < k$. Due to hermiticity of H this reduces to orthogonalization with respect to only *two* previous vectors, therefore (Arbenz, 2012, Ch. 9)

$$
\begin{aligned}
\alpha_k &= \langle f_k|H|f_k\rangle, \\
|r\rangle &= H|f_k\rangle - \alpha_k|f_k\rangle - \beta_{k-1}|f_{k-1}\rangle, \\
\beta_k &= |\langle r|r\rangle|^{\frac{1}{2}}, \quad \beta_{-1} = 0, \\
|f_{k+1}\rangle &= \frac{1}{\beta_k}|r\rangle, \quad k = 0, 1, \dots, n-1.
\end{aligned}
\tag{2.101}
$$

The Green's function associated with a single-particle excitation $|f_0\rangle = d^\dagger|E_0\rangle$ of the ground-state $|E_0\rangle$ with energy E_0 (and $d^\dagger$ creates a particle) reads (Appendix A)

$$
G(z) = \langle f_0|\frac{1}{z - (H - E_0)}|f_0\rangle = \sum_k \frac{|w_k|^2}{z - (E_k - E_0)}, \quad w_k = \langle f_0|E_k\rangle
\tag{2.102}
$$

where $|E_k\rangle$ denote the *exact* eigen states of H. This can not be computed in the general case.

One can use the Lanczos algorithm to approximate the Green's function (Gagliano and Balseiro, 1987). Instead of evaluating (2.102) using the exact eigen states $|E_k\rangle$ and energies E_k, one simply uses the eigen states $|E_k^{(n)}\rangle$ and $E_k^{(n)}$ of the truncated Krylov representation $M^{(n)}$ (an $n \times n$

---

[27]In the *classic* (non-MPS) formulation of DMRG, Hallberg (1995) had also already used Lanczos to compute Green's functions.

matrix) of H

$$M_{kl}^{(n)} := \langle f_k|H|f_l\rangle, \qquad k,l = 0,1,\ldots,n-1, \quad M \in \mathbb{C}^{n\times n},$$
$$D^{(n)} := U^{(n)\dagger}M^{(n)}U^{(n)}, \ D_{kl}^{(n)} = E_k^{(n)}\delta_{k,l}, \ U_{kl}^{(n)} = \langle f_l|E_k^{(n)}\rangle, \quad D \in \mathbb{R}^{n\times n}. \qquad (2.103)$$

This approximates the weights in (2.102) as[28]

$$w_k^{(n)} = \langle f_0|E_k^{(n)}\rangle = U_{0k}^{(n)}. \qquad (2.105)$$

Now note that instead of using the definition (2.103), we will use the following definition of the matrix $M^{(n)}$ in practice

$$M_{k,k}^{(n)} := \alpha_k, \quad k = 0,1,\ldots,n-1,$$
$$M_{k,k+1}^{(n)} := \beta_k = M_{k+1,k}^{(n)*} \quad k = 0,1,\ldots,n-2.$$

In exact arithmetics, this simply corresponds to an evaluation of the previous definition $M_{kl}^{(n)} = \langle f_k|H|f_l\rangle$ as the Lanczos basis $\{|f_k\rangle\}$ is orthogonal. In double precision arithmetics, when the Lanczos basis can become non-orthogonal, the definition of a tridiagonal $M^{(n)}$ via α_k and β_k might not coincide with the matrix $(\langle f_k|H|f_l\rangle)_{l,k=0}^{n-1}$. But the full computation of the latter matrix is not practicable and highly costly: it would destroy the whole elegance of Lanczos, which consists in the computational simplicity of involving just the computation of two inner products in (2.101).

Let us define the residual of the approximation of $E_k^{(n)}$ to an exact eigen value as the square root of the variance

$$\mathrm{res}_k^{(n)} = \sqrt{\langle E_k^{(n)}|(H - E_k^{(n)})^2|E_k^{(n)}\rangle} = \sqrt{\langle E_k^{(n)}|H^2|E_k^{(n)}\rangle - (E_k^{(n)})^2}. \qquad (2.106)$$

Evaluating this expression involves in principle evaluating $\langle f_k|H^2|f_l\rangle$, which can be very costly. To avoid this, let us use the following formula (Arbenz, 2012, p. 161)

$$\mathrm{res}_k^{(n)} = \big||H|E_k^{(n)}\rangle - E_k^{(n)}|E_k^{(n)}\rangle\big|| = \beta_n|U_{nk}^{(n)}| \qquad (2.107)$$

where the norm $||.||$ is defined via (2.106), the matrix $U^{(n)}$ is the matrix of eigen vectors of $M^{(n)}$ as defined in (2.103) and $\beta_n > 0$ has been defined in (2.101). The residual rigorously bounds the distance of $E_k^{(n)}$ to a true eigenvalue E of H

$$|E - E_k^{(n)}| \leq \mathrm{res}_k^{(n)}. \qquad (2.108)$$

The formula (2.107) is of great advantage in practical computations.

---

[28] Equivalently to using the approximations $E_k^{(n)}$ and $w_k^{(n)}$ to evaluate (2.102) in order to generate an approximation of the Green's function, one can evaluate the continued fraction representation of the Green's functions directly using the Lanczos parameters

$$G(z) = \cfrac{\langle f_0|f_0\rangle}{z - \alpha_0 - \cfrac{\beta_0^2}{z - \alpha_1 - \cfrac{\cdots}{z - \alpha_{n-1} - \frac{\beta_{n-1}^2}{z - \alpha_n}}}}. \qquad (2.104)$$

Reorthogonalization by Dargel *et al.* (2012)

The Lanczos algorithm is numerically unstable as it involves frequent subtractions. If using MPS, truncation errors severely enhance this instability and the Lanczos basis becomes highly *non-orthogonal*. To avoid this, there are many approaches in the literature that reorthogonalize the Lanczos basis while computing it (Arbenz, 2012), using subtractions of many more than just the two previous Lanczos vectors in (2.101). Such a treatment is dangerous when using MPS: the additional subtractions increase entanglement in the state and make computations much more costly. Dargel *et al.* (2012) therefore devises an *a posterior* reorthogonalization as follows.

Disposing of the presumably non-orthogonal basis of *all* vectors $|f_n\rangle$, which are computed using (2.101), one can obviously perform an *a posterior* reorthogonalization via $|\psi_n\rangle = |f_n\rangle - \sum_{i=0}^{n-1} \langle f_i|f_n\rangle|f_i\rangle$,[29] which defines orthogonal vectors $|\psi_n\rangle$ that we can use to construct a different representation for H

$$\langle \psi_n|H|\psi_m\rangle = \sum_{i=0}^{n}\sum_{j=0}^{m} S_{in}^* S_{jm}\langle f_i|H|f_j\rangle, \tag{2.109}$$

where here the basis transform was written in terms of a matrix S defined via $|\psi_n\rangle = \sum_{i=0}^{n} S_{in}|f_i\rangle$. One can now study the properties of the eigen states and eigen values of the representation (2.109), and see if they lead to a better approximation of the Green's function. We will do so in the following.

Numerical checks

We checked our implementation of Lanczos and of the *posterior* reorthogonalization method by Dargel *et al.* (2012) for the example of non-interacting spinless fermions, comparing eigen values and spectral weights with the exact solution. The Hamiltonian, as well as exact eigen energies and spectral weights are given by

$$H = -\sum_{i=0}^{L-1}(c_i^\dagger c_{i+1} + \text{h.c.}), \quad E_k = -2\cos k, \quad |w_k|^2 = \frac{2}{L+1}\sin^2(k) \tag{2.110}$$

and $k = \kappa\frac{\pi}{L+1}$, $\kappa \in \{1, \ldots, L\}$.

Using the ordinary Lanczos algorithm (2.101), we compute spectrum and weights. Results for this without posterior reorthogonalization are shown in Fig. 2.10 in the two upper rows of panels. We perform a calculation without truncating the MPS representations[30] of the Lanczos vectors and show the result in the upper panels of Fig. 2.10. The algorithm produces the exact eigen energies and weights at high accuracy after 40 iterations and 3 min of computation time.

Truncating to a maximal matrix dimension of $m_L = 16$ in each Lanczos step, results for which are shown in the center panels of Fig. 2.10, decreases orthogonality of Lanczos vectors tremendously. After 40 iterations, $|\langle f_0|f_{40}\rangle| \simeq 0.02$, and after 80 iterations, $|\langle f_0|f_{80}\rangle| \simeq 0.2$. Nevertheless, the approximation of the lower parts of the spectrum stays fairly stable with reasonable errors. Only for high numbers of iterations, the upper part of the spectrum is lost (the approximate tridiagonal representation of $M^{(n)}$ no longer captures this information). But this does not imply that the errors in the lower part of the spectrum increase. The calculation takes 0.6 min.

Using the posterior reorthogonalization necessitates to measure $\langle f_k|H|f_l\rangle$ for all $k, l < n$.[31] These additional measurements are computationally *extremely* costly and the calculation shown

---

[29]Posterior means that the states $|\psi_n\rangle$ are *not* used within the Lanczos algorithm (2.101).

[30]using extremely high bond dimensions that lead to a numerically exact representation

[31]To compute the error, we additionally have to measure $\langle f_k|H^2|f_l\rangle$ as the neat formula (2.107) does not hold true any more.
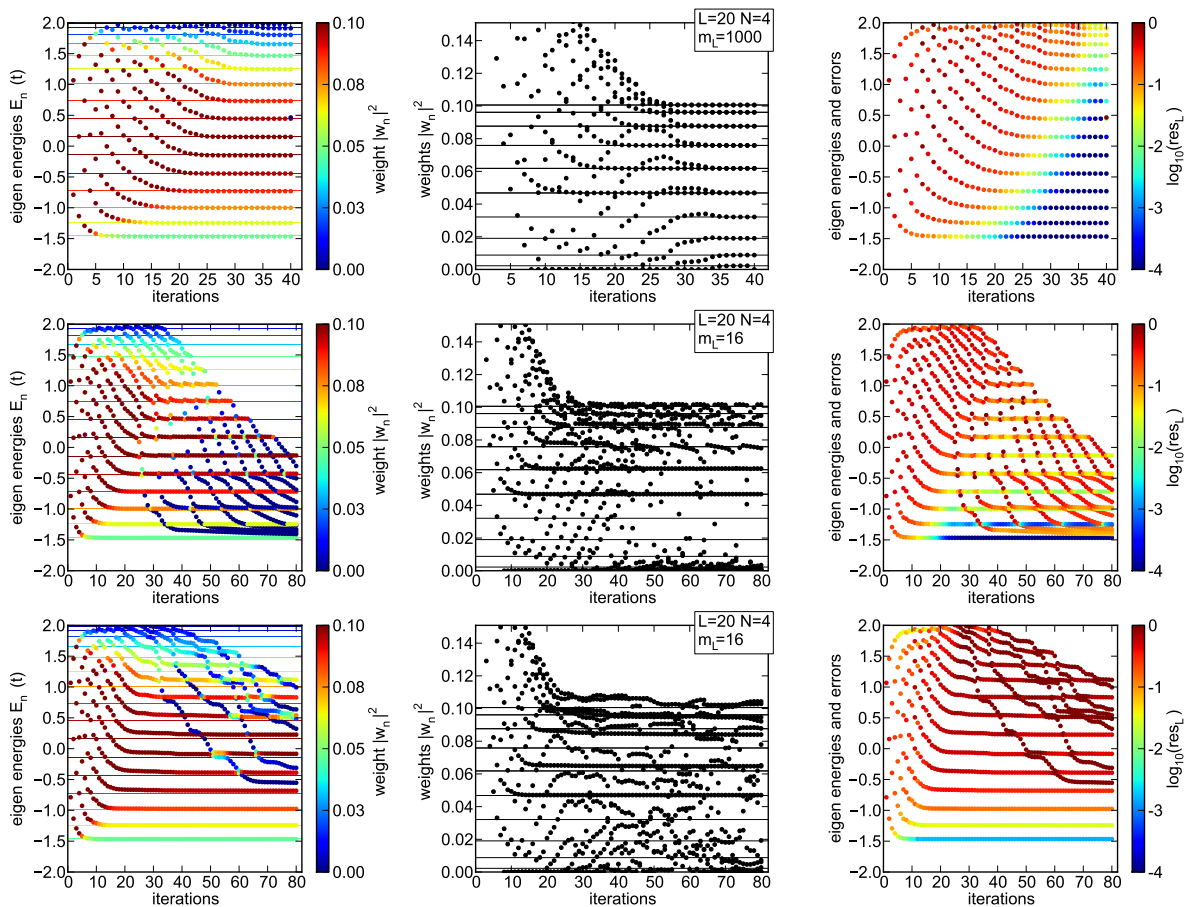
Fig. 2.10.: Approximation to eigen energies, weights and residuals for non-interacting spinless fermions ($L = 20$ lattice sites, $N = 4$ particles) obtained using the Lanczos algorithm (2.101) with MPS. Solid lines depict exact solutions. Upper panels: without truncation and without reorthogonolization (bond dimension is $m_L = 1000$). Center panels: with truncation and without reorthogonalization ($m_L = 16$). Lower panels: with truncation and with reorthogonalization ($m_L = 16$).

in Fig. 2.10 took 101 min (40 iterations took 2.7 min). In the lower left panel, the behavior of convergence of the eigen energies now seems much more stable than in the center left panel (without reorthogonalization). Looking at the detailed errors of the eigen values in the lower right panel, though, one realizes that the calculation converges only very slowly. In particular, the lowest eigen value has a higher error than without reorthogonalization. The quality of the approximation of many weights is not satisfactory, either.

In conclusion, one has to doubt that investing so much more computation time while still not being able to reproduce a numerically exact result, is worth the effort. In the rest of this thesis, we therefore use the Chebyshev expansion, which we explain in detail in Sec. 3.1 and Sec. 5.1, and time evolution algorithms, which we explain in Sec. 3.2 and Sec. 4.1.

3. Impurity solvers in equilibrium

3.1. Chebyshev matrix product state impurity solver for dynamical mean-field theory

Using the Chebyshev expansion of the spectral function of a quantum many-body system to construct an algorithm has been known as *kernel polynomial method* for quite some time (Weiße *et al.*, 2006). The implementation of Holzner *et al.* (2011) using matrix product states was a promising candidate to construct a powerful solver for dynamical mean-field theory. The main advantage of this technique is, that the algorithm involves only the representation of the Hamilton operator H, for which an MPO representation is readily available, and not of a function of the Hamilton operator, for which deriving MPO expressions usually is very difficult. The following article (Wolf *et al.*, 2014a) advances the technique in particular by realizing that bond dimensions have to to be adaptively chosen, and that convergence of the series expansion depends crucially on the free parameters of a rescaling procedure necessary for the expansion. These advancements then allowed to solve a two-site DCA for the single band Hubbard model.

▷ *Chebyshev matrix product state impurity solver for dynamical mean-field theory*
   FA Wolf, IP McCulloch, O Parcollet and U Schollwöck
   Phys. Rev. B **90** 115124 (2014)

Chebyshev matrix product state impurity solver for dynamical mean-field theory

F. Alexander Wolf,[1] Ian P. McCulloch,[2] Olivier Parcollet,[3] and Ulrich Schollwöck[1]

[1]*Theoretical Nanophysics, Arnold Sommerfeld Center for Theoretical Physics, LMU München, Theresienstrasse 37,
D-80333 München, Germany*
[2]*Centre for Engineered Quantum Systems, School of Physical Sciences, The University of Queensland, Brisbane, Queensland 4072, Australia*
[3]*Institut de Physique Théorique, CEA, IPhT, CNRS, URA 2306, F-91191 Gif-sur-Yvette, France*

We compute the spectral functions for the two-site dynamical cluster theory and for the two-orbital dynamical mean-field theory in the density-matrix renormalization group (DMRG) framework using Chebyshev expansions represented with matrix product states (MPS). We obtain quantitatively precise results at modest computational effort through technical improvements regarding the truncation scheme and the Chebyshev rescaling procedure. We furthermore establish the relation of the Chebyshev iteration to real-time evolution and discuss technical aspects as computation time and implementation in detail.

PACS number(s): 71.27.+a

I. INTRODUCTION

The dynamical mean-field theory (DMFT) [1–4] and its cluster extensions [5] are among the most successful methods to study strongly correlated electron systems in dimensions higher than one. The impurity problem within DMFT is usually solved with continuous-time quantum Monte Carlo (CTQMC) algorithms [6–9], the numerical renormalization group (NRG) [10] or exact diagonalization (ED) [11–13]. While CTQMC is computationally feasible even for problems with many bands or a high number of cluster sites, it provides numerically exact results only on the imaginary frequency axis. Many experimentally relevant frequency-dependent quantities like, e.g., the conductivity therefore can only be obtained via the numerically ill-conditioned analytical continuation. NRG, by contrast, solves the problem on the real frequency axis. However, it badly resolves spectral functions at high energies and cannot treat DMFT calculations with more than, e.g., two bands. The limiting factor for this is the exponential growth of the *local* Hilbert space with the number of bands. Only recently, a reformulation of the mapping problem could avoid this exponential growth [14], but it is still unclear whether this can be efficiently exploited in the context of DMFT. ED faces the problem of a limited spectral resolution due to the limited number of bath sites it can treat, although recent publications could substantially improve that [12,13].

As the impurity problem of DMFT is one-dimensional, there has been a long-time interest to solve it using density matrix renormalization group (DMRG) [15–17], which operates on the class of matrix product states (MPS). DMRG features an unbiased energy resolution and shows no exponential growth of the local Hilbert space with respect to the number of baths. It also works directly on the real-frequency axis, avoiding analytic continuation. The earliest DMRG approach to spectral functions, the Lanczos algorithm approach [18], is computationally cheap, but does not yield high-quality DMFT results due to its intrinsic numerical instability [19]. Recent improvements using a fully MPS-based representation of this algorithm [20] are not sufficient to resolve this issue [21]. The dynamical DMRG (DDMRG) approach [22,23] yields very precise results for single-site DMFT on the real frequency axis [24–26], but is computationally extremely costly and therefore not competitive with other impurity solvers for DMFT.

Recently, a new approach to spectral functions based on expansions in Chebyshev polynomials [27] represented with matrix product states (CheMPS) [28–31] was introduced by two of us in Ref. [28], which gave essentially the same accuracy as the DDMRG approach at a fraction of the computational cost. At the same time, the availability of real-time evolution [32–34] within time-dependent DMRG (tDMRG) and closely related methods generally also permits access to spectral functions by a Fourier transformation [34]. Both Chebyshev expansions (CheMPS) [31] and tDMRG [35] were recently seen to be applicable to the solution of the DMFT. Both approaches are computationally cheaper than DDMRG and numerically stable. For the single-impurity single-band case, results on the real-frequency axis are excellent, but for more typical present-day DMFT setups involving clusters or multiple bands, results are not available in the case of Chebyshev expansions or do so far not reach the quality of the competing QMC and NRG methods in the case of real-time evolution.

In this paper, we push the application of CheMPS to DMFT further. (i) We solve the dynamical cluster approximation (DCA) [5] for a two-site cluster and the DMFT for a two-band Hubbard model. The accuracy of the results for the latter case is better than those shown in Ref. [35], where the problem has been solved using tDMRG (ii). We consider the experimentally relevant case of finite doping, which is significantly more complicated than the half-filled cases treated so far. (iii) We suggest a new truncation scheme for CheMPS, which allows to maintain the same error level at strongly reduced computational cost. (iv) We establish that the Chebyshev recurrence iteration can be interpreted as a discrete real-time evolution. (v) By comparing different methods to set up CheMPS, we obtain another substantial increase in computation speed. (vi) We discuss limitations of post-processing methods, which have been crucial to the success of DMRG as an DMFT impurity solver.

With these improvements, CheMPS immediately provides an efficient, precise and controlled way to solve DMFT problems with two baths (two-site clusters) on the real-frequency axis with feasible extensions to problems with more bands. The presentation proceeds as follows. After a general introduction to Chebyshev expansions of spectral functions

in Sec. II, we move on to discuss its implementation in the approximate framework of MPS: in Sec. III, we present a new truncation scheme, and in Sec. IV, we discuss the mapping of the Hamiltonian to the $[-1, +1]$ convergence interval of Chebyshev polynomials, because this interacts nontrivially with efficient MPS calculations. Section V treats the post-processing of Chebyshev moments obtained in the expansion. These improvements are then applied to various DMFT problems. As the case of the single-impurity single-band DMFT has been treated extensively in the literature and just serves as an initial benchmark, we move those results to the Appendixes. In the main text, we give examples for the relevance of our improvements to CheMPS by solving a two-site DCA in Sec. VI A and a single-site two-orbital DMFT in Sec. VI B. Technical details of these calculations are again found in Appendix. Section VII concludes the paper.

II. CHEBYSHEV EXPANSION OF SPECTRAL FUNCTIONS

In this section, we establish notation and explain the general ideas behind Chebyshev expansions of spectral functions. The zero-temperature single-particle Green's function associated with a many-body Hamiltonian H is

$$G(\omega) = \langle E_0 | c \frac{1}{\omega + i0^+ - (H - E_0)} c^\dagger | E_0 \rangle, \quad (1)$$

where $c^\dagger$ creates a particle in a particular quantum state and $|E_0\rangle$ is the ground state with energy E_0. The spectral function $A(\omega) = -\frac{1}{\pi} \text{Im} \, G(\omega)$ reads

$$A(\omega) = \langle E_0 | c \, \delta(\omega - (H - E_0)) c^\dagger | E_0 \rangle$$
$$= \sum_n W_n \delta(\omega - (E_n - E_0)), \quad (2)$$

with weights $W_n = |\langle E_n | c^\dagger | E_0 \rangle|^2$. If evaluated exactly in a finite system, $A(\omega)$ is a comb of delta peaks, which only in the thermodynamic limit becomes a smooth function $A_{\lim}(\omega)$. If evaluated in an approximate way that averages over the finite-size structure of $A(\omega)$, it is possible to extract $A_{\lim}(\omega)$ also from a sufficiently big finite-size system. Among various techniques that provide such an approximation [36], the most popular one is the definition of a *broadened* representation of $A(\omega)$,

$$A_\eta(\omega) = \sum_n W_n h_\eta(\omega - E_n), \quad (3)$$

where the broadening function $h_\eta(\omega - E_n)$ is given by the Gaussian kernel

$$h_\eta(x) = \frac{1}{\sqrt{2\pi} \eta} e^{-\frac{x^2}{2\eta^2}}. \quad (4)$$

Besides the Gaussian kernel, a Lorentzian kernel

$$h_\eta(x) = \frac{\eta}{\pi} \frac{1}{x^2 + \eta^2} \quad (5)$$

is often implicitly used as it emerges automatically when computing the spectral function $A_\eta = -\frac{1}{\pi} \text{Im} \, G(\omega + i\eta)$ from the shifted Green's function $G(\omega + i\eta)$. In general, $A_\eta(\omega)$ is indistinguishable from $A_{\lim}(\omega)$ if the latter has no structure on a scale smaller than η.

An efficient way to generate the broadened version $A_\eta(\omega)$ of $A(\omega)$ is via iterative expansions in orthogonal polynomials. Historically, most frequently used in this context is the Lanczos algorithm, which is intrinsically numerically unstable, though. By contrast, expansions in Chebyshev polynomials can be generated in a numerically stable way. As they have not been used much in either the DMRG or DMFT community so far, we briefly introduce them based on Ref. [27].

A. General implementation

The Chebyshev polynomials of the first kind $T_n(x)$ can be represented explicitly by

$$T_n(x) = \cos(n \arccos(x)) \quad (6)$$

or generated with the recursion

$$T_n(x) = 2x T_{n-1}(x) - T_{n-2}(x), \quad T_0 = 1, \quad T_1 = x, \quad (7)$$

which is numerically stable if $|x| \leqslant 1$. Chebyshev polynomials are orthonormal with respect to the weighted scalar product

$$\int_{-1}^{1} dx \, w_n(x) T_m(x) T_n(x) = \delta_{nm}, \quad (8a)$$

$$w_n(x) = \frac{2 - \delta_{n0}}{\pi \sqrt{1 - x^2}}. \quad (8b)$$

Any sufficiently well-behaved function $f(x)|_{x \in [-1,1]}$ can be expanded in Chebyshev polynomials

$$f(x) = \sum_{n=0}^{\infty} w_n(x) \mu_n T_n(x), \quad (9a)$$

$$\mu_n = \int_{-1}^{1} dx f(x) T_n(x), \quad (9b)$$

where the definition of the so-called *Chebyshev moments* μ_n via the *nonweighted* scalar product follows when applying $\int_{-1}^{1} dx \, T_m(x) \dots$ to both sides of (9a).

If $f(n)$ is smooth, the envelope of μ_n decreases at least exponentially to zero with respect to n; if $f(n)$ is the step function, the envelope decreases algebraically; and if $f(n)$ is the delta function, the envelope remains constant [37]. For a smooth function, the truncated expansion $f_N(x) = \sum_{n=0}^{N} w_n(x) \mu_n T_n(x)$ therefore approximates $f(x)$ very well if N is chosen high enough. However, for the delta function, any truncated expansion yields an approximation with spurious (Gibbs) oscillations. A controlled damping scheme for the oscillations, the so-called *kernel polynomial approximation* (KPM), can be obtained with a simple modification of the Chebyshev expansion,

$$f_N^{\text{kernel}}(x) = \sum_{n=0}^{N} w_n(x) g_n \mu_n T_n(x), \quad (10a)$$

$$g_n = \frac{(N - n + 1) \cos \frac{\pi n}{N+1} + \sin \frac{\pi n}{N+1} \cot \frac{\pi}{N+1}}{N + 1}, \quad (10b)$$

where g_n is the so-called Jackson kernel that leads to a very good Gaussian approximation $h_{\eta(x)}(x)$ with x-dependent width $\eta(x) = \sqrt{1 - x^2} \, \pi / N$ of the delta function, and hence directly leads to (4).

In the case of the spectral function (2), one aims at an expansion of a superposition of delta functions. This can in practice often be done without damping: when expanding (2) in Chebyshev polynomials, the integration in (9b) averages over the delta peak as well as over the finite-size peak structure of $A(\omega)$. If the weights W_n vary slowly on the scale of the spacing of finite-size peaks, the sequence μ_n approaches zero as soon as the characteristic form of this slow variation is resolved. The value of n at which this pseudoconvergence occurs is the one that resolves the spectral function in the thermodynamic limit $A_{\lim}(\omega)$, provided that $A_{\lim}(\omega)$ has no structure on a smaller scale than the spacing of finite-size peaks. Only for much higher values of n, the Chebyshev moments start deviating from zero again to then oscillate forever, resolving first the finite-size structure of $A(\omega)$ and finally the delta-peak structure. Therefore, if one can generate the sequence up to pseudoconvergence, then there is no need for Jackson damping.

B. Operator valued Chebyshev expansion

In order to expand the spectral function (2), one usually introduces a rescaled and shifted version of H to map its spectrum into the interval $[-1, 1]$, where Chebyshev polynomials are bounded and have a stable recursion relationship,

$$H' = \frac{H - E_0 + b}{a}, \quad \omega' = \frac{\omega + b}{a}. \quad (11)$$

Obviously, there is a lot of leeway in the choice of a and b, which will be found to have large implications for CheMPS (Sec. IV). Generally,

$$A(\omega) = \frac{1}{a} A' \left(\frac{\omega + b}{a} \right),$$

where $\quad A'(\omega') = \langle t_0 | \delta(\omega' - H') | t_0 \rangle, \quad |t_0\rangle = c^\dagger |E_0\rangle. \quad (12)$

Expanding $A'(\omega')$ in Chebyshev polynomials yields the moments

$$\mu_n = \int_{-1}^{1} d\omega' \langle t_0 | \delta(\omega' - H') | t_0 \rangle T_n(\omega')$$

$$= \sum_i \int_{-1}^{1} d\omega' \langle t_0 | \delta(\omega' - E_i') T_n(\omega') | E_i \rangle \langle E_i | t_0 \rangle$$

$$= \langle t_0 | t_n \rangle, \quad |t_n\rangle = T_n(H') | t_0 \rangle. \quad (13)$$

Inserting the recursive definition (7) of $T_n(H')$ in the definition of $|t_n\rangle$ one obtains a practical calculation scheme for the power series expansion of $T_n(H')$:

$$|t_n\rangle = 2H' |t_{n-1}\rangle - |t_{n-2}\rangle, \quad (14a)$$

$$|t_0\rangle = c^\dagger |E_0\rangle, \quad |t_1\rangle = H' |t_0\rangle. \quad (14b)$$

One can double the expansion order with the following relation [27]:

$$\bar{\mu}_{2n-1} = 2 \langle t_n | t_{n-1} \rangle - \mu_1, \quad (15a)$$

$$\bar{\mu}_{2n} = 2 \langle t_n | t_n \rangle - \mu_0, \quad (15b)$$

but has to be aware of the fact that moments computed this way are more prone to numerical errors [28].

C. Retarded fermionic Green's function

In the case of fermionic problems, as encountered in DMFT, an additional technical complication comes up. The spectral representation of the fermionic retarded Green's function is the sum of its particle and hole parts:

$$A(\omega) = A^>(\omega) + A^<(-\omega),$$

$$A^>(\omega) = \langle E_0 | c_0 \, \delta(\omega - (H - E_0)) c_0^\dagger | E_0 \rangle, \quad (16)$$

$$A^<(\omega) = \langle E_0 | c_0^\dagger \, \delta(\omega - (H - E_0)) c_0 | E_0 \rangle.$$

As $A^{\lessgtr}(\omega)$ have steps at $\omega = 0$, their representation in terms of smooth polynomials is notoriously ill-conditioned. One should therefore try to represent the smooth function $A(\omega)$ by a single Chebyshev expansion; allowing for two different rescaling prescriptions, one has

$$A^>(\omega) = \frac{1}{a_1} \sum_n w_n(\omega_1'(\omega)) \mu_n^> T_n(\omega_1'(\omega)), \quad (17a)$$

$$A^<(-\omega) = \frac{1}{a_2} \sum_n w_n(\omega_2'(-\omega)) \mu_n^< T_n(\omega_2'(-\omega)). \quad (17b)$$

In order to write $A(\omega)$ in terms of a single Chebyshev expansion, one can use the symmetries $T_n(x) = (-1)^n T_n(-x)$ and $w_n(x) = w_n(-x)$. These restrict the rescaling parameters via $\omega_1'(\omega) = -\omega_2'(-\omega)$ to $a_1 = a_2 = a$ and $b_1 = -b_2$. Making the particular choice $b_1 = b_2 = b = 0$ hence defines a common expansion via [31]

$$A(\omega) = \frac{1}{a} \sum_n w_n \left(\frac{\omega}{a} \right) (\mu_n^> + (-1)^n \mu_n^<) T_n \left(\frac{\omega}{a} \right). \quad (18)$$

Although $b = 0$ provides one with a controlled treatment of the step function, it comes at the price of a loss in computational speed. We will compare advantages and disadvantages of two practical shifting possibilities ($b = 0$ and $b = -a$) in detail in Sec. IV.

III. MATRIX PRODUCT IMPLEMENTATION

So far, everything has been general, or it was somehow assumed that all calculations can be carried out exactly, which meets severe limitations in computational practice. Representing Chebyshev states $|t_n\rangle$ with matrix product states (MPS) [28] enables more efficient computations than in an exact representation, as the size of the effective Hilbert space can be tremendously reduced. As an MPS is usually only an approximate representation of a strongly correlated quantum state, the issue of optimal compression, i.e., the representation of a quantum state as an MPS using finite-dimensional matrices with a minimal loss of accuracy (information), is crucial. Here, we argue in the following that instead of controlling the maximal matrix dimension [28,30,31], one should rather control the cumulated truncated weight (a proxy measure of the loss of accuracy), allowing for more efficient and more controlled calculations of Chebyshev moments.

A. Adaptive matrix dimension

If one follows through the recursive scheme for Chebyshev vectors, one starts out from a ground state, which we may

assume has been obtained by a standard DMRG (MPS) calculation to extremely high precision, this means that an optimally compressed starting MPS is available where matrices have some computationally feasible dimension at very small loss of accuracy compared to the exact starting state. This, in turn, yields an extremely precise starting Chebyshev state $|t_0\rangle$. Now, in each step of the recursion (14a), one applies H' and subtracts a preceding Chebyshev state. As is well-known for MPS, the application of H' (and to a lesser extent the subtraction) lead to a drastic increase in matrix dimension, which necessitates a state compression (Sec. 4.5 of Ref. [17]) of the new Chebyshev state $|\widetilde{t_n}\rangle$ to a computationally manageable state $|t_n\rangle$ with smaller matrix dimension m, which generates the error δ:

$$\mu_n = \langle t_0|\widetilde{t_n}\rangle = \langle t_0|t_n\rangle \pm \delta,$$

$$|\widetilde{t_n}\rangle = 2H'|t_{n-1}\rangle - |t_{n-2}\rangle,$$

$$\delta^2 = |\langle t_0|(|\widetilde{t_n}\rangle - |t_n\rangle)|^2$$

$$< ||t_0\rangle|^2 ||\widetilde{t_n}\rangle - |t_n\rangle|^2 < ||t_0\rangle|^2 \varepsilon_{\mathrm{compr}}(m). \quad (19)$$

Here, we used the upper error bound [38] provided by the cumulated truncated weight $\varepsilon_{\mathrm{compr}}(m)$,

$$||\widetilde{t_n}\rangle - |t_n\rangle|^2 \leqslant \varepsilon_{\mathrm{compr}}(m) = \sum_{i=1}^{L-1} \epsilon_i(m), \quad (20)$$

where $\epsilon_i(m)$ is the sum over the discarded reduced density-matrix eigenvalues per bond and the sum over i is over all bonds. This error bound for a single step of the recursion unfortunately does *not* provide a statement about the total error that accumulates over all compression steps in preceding Chebyshev recursion steps. Still, we experienced that the numerical stability of the Chebyshev recursion rather leads to a helpful compensation of errors of single recursion steps. Figure 1 shows that the *total* error stays at the order of the error of a *single* step $||t_0\rangle|^2 \varepsilon(m)$ also for high iteration numbers n. In the case in which one fixes the matrix dimension m, Fig. 1 shows a steady, uncontrolled increase of the total error. This is particularly undesirable in view of the desired post-processing of Chebyshev moments (Sec. V).

Another possibility would be to fix the local discarded weight $\epsilon_i(m)$ as defined in (20). However, this does in general *not* lead to a viable computation scheme for impurity models; in the simplest and most-employed chain representation of impurity models, the impurity site is located at an edge of the chain. Fixing the same value for $\epsilon_i(m)$ for all bonds then leads to extremely high matrix dimensions in the center of the chain, i.e., in the center of the bath, where entanglement for systems with open boundary conditions is maximal. The relevant entanglement, by contrast, is the one between the impurity site and the bath. This becomes clear when noticing that upon projecting the Chebyshev state $|t_n\rangle$ on $|t_0\rangle$ to compute μ_n, only correlations with respect to the *local* excitation $c^\dagger|E_0\rangle$ are measured. The high computational effort of high matrix dimensions that follows when faithfully representing entanglement *within* the bath, is therefore in vain. For geometries with the impurity at the center, like the two-chain geometry used for the two-bath problems in this paper, the preceding argument is not valid. An inhomogeneous
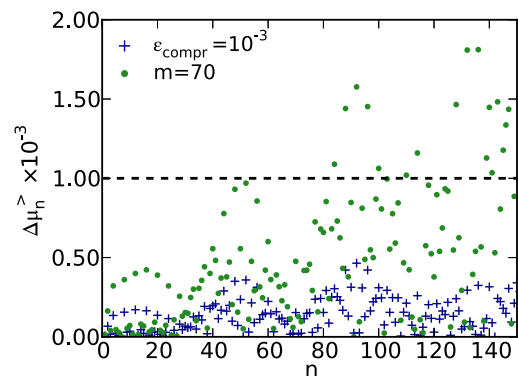

FIG. 1. (Color online) Error of Chebyshev moments $\mu_n^>$ [as they appear in (17a)], computed as $\Delta\mu_n^> = |\mu_n^> - \tilde{\mu}_n^>|$, where $\tilde{\mu}_n^>$ is obtained with a quasiexact calculation with high matrix dimension $m = 200$. If one fixes the matrix dimension m, the error steadily increases. If, instead, one fixes the cumulated truncated weight $\varepsilon_{\mathrm{compr}}$, the error remains approximately constant and does not accumulate. This is the procedure followed in this paper. As here, $||t_0\rangle|^2 = 1$, $\varepsilon_{\mathrm{compr}}$ equals the upper error bound of a single compression step. Results shown are for the spectral function of the half-filled single-impurity Anderson model (SIAM) (Appendix C1) with semielliptic density of states of half-bandwidth D, interaction $U = 2D$, represented on a chain with $L = 40$ lattice sites. This is equivalent to considering the local density of states at the first site of a fermionic chain with constant hopping $t = D/2$ and an interaction of $U = 4t$ that acts solely at the first site.

distribution of matrix dimensions with high values at the center and low values at the boundaries is *a priori* consistent with open boundary conditions. This distribution can therefore be achieved by fixing a constant value for $\epsilon_i(m)$ for each bond. Another possible truncation scheme could be obtained by using an estimator for the correlations of the impurity with the bath, which then fixes the matrix dimensions as a function of bonds $m(i)$ (distance to the impurity). Both approaches constitute possible future refinements. For simplicity, in this paper, we consider the truncation scheme that fixes a constant value of m based on the cumulative truncated weight.

B. State compression

During the repeated solution of (14a) we monitor the truncated weight $\varepsilon_{\mathrm{compr}}$. If $\varepsilon_{\mathrm{compr}}$ exceeds a certain threshold of the order of 10^{-4} to 10^{-3}, we slightly increase the matrix dimension m, and repeat the compression. For the first compression step, we take as an initial guess the previous Chebyshev state $|t_{n-1}\rangle$. For repeated compression steps, we take as an initial guess the state of the previous compression step. It turns out that, in practice, one almost never faces repeated compressions, which gains one approximately a factor 2 in computation speed compared to the error monitoring of Ref. [28]; in Ref. [28], the authors keep the matrix dimension fixed and variationally [17] compress an exact representation of the right hand side of (14a) for fixed m by repeated iterations ("sweeps") until the error

$$\left| 1 - \frac{\langle t_n'|t_n\rangle}{||\,|t_n'\rangle\,||\,||\,|t_n\rangle\,||} \right| \quad (21)$$

drops below a certain threshold. Here, $|t_n'\rangle$ denotes the state before a sweep, and $|t_n\rangle$ the state after a sweep. This error measure is not related to the factual error of Chebyshev moments, for any but the first sweep. Its monitoring is costly to compute and leads to at least two compression sweeps.

IV. OPTIMAL CHEBYSHEV SETUP

One can generally state that the effectiveness of the MPS evaluation of the Chebyshev recursion (14a) for a certain system is unknown *a priori* but must be experienced by observing how strong entanglement in the Chebyshev vectors, and therefore matrix dimension m needed for a faithful representation grows as compared to the speed of convergence of μ_n. For very high iteration numbers, one will always reach a regime in which matrix dimensions have grown so much that further calculations become too expensive computationally. This is known from tDMRG as *hitting an exponential wall* and defines an *accessible time scale*, or in our case, an accessible expansion order. In the case of the computation of Chebyshev moments, the accessible time scale strongly depends on the choice of the shifting parameter b, which leads us to consider the two cases $b = 0$ and $b = -a$.

Comparing these cases, one finds a much slower speed of convergence of the Chebyshev moments in the case $b = 0$ than in the case $b = -a$. Putting that differently: per fixed amount of entanglement growth [application of H in one step of (14a)], much less information about the spectral function is extracted in case $b = 0$ than in case $b = -a$. Independent of that, one finds that the advantage of the choice $b = 0$ to provide one with an analytic expression for $A(\omega)$ in terms of a single Chebyshev expansion (Sec. II C) can be detrimental. We therefore need to study both cases in more detail.

A. No shift: $b = 0$

If choosing $b = 0$, one can derive a scaling property of Chebyshev moments that simplifies extracting the thermodynamic limit as well as the examination of computational performance. The spectral function of a one-particle operator $A(\omega)$ is nonzero only in the vicinity of the ground-state energy $\omega = 0$, up to a distance of the order of the single-particle bandwidth W_{single}. The rescaled spectral function $A'(\omega')$ is nonzero up to a distance of W_{single}/a from $\omega' = 0$. For all rescaling parameters a that have been proposed up to now [27,28,31], one has $W_{single}/a < \frac{1}{2}$. Usually W_{single}/a is much smaller than the upper bound $\frac{1}{2}$. As $\arccos(x) = \pi/2 - x - x^3/6 + \dots$ is well approximated by its linear term already for $|x| < 0.5$, Chebyshev polynomials (6) behave like a shifted cosine function in the region where $A'(\omega')$ is nonzero. The expansion of $A'(\omega')$ in Chebyshev polynomials is therefore essentially equivalent to a Fourier expansion. This means that the iteration number n of the Chebyshev expansion has the same meaning as a discrete propagation time, the evolution of which is mediated by simple applications of H instead of the ordinary continuous time propagation e^{-iHt}. To answer the question of whether an ordinary time evolution [35] is more effective in generating information about the spectral function, one has to study the entanglement entropy production

of repeated applications of H compared to the one of e^{-iHt}. The following results are the first steps in this direction.

In discrete time evolution, the rescaling of the frequency directly translates to an inverse scaling of time. Considering two calculations of Chebyshev moments, one for $\mu_n^{(1)}$ performed with H' and another for $\mu_n^{(a)}$ performed with H'/a, one therefore has the simple approximate relation

$$\mu_n^{(1)} \sim \langle t_0| \cos(nH')|t_0\rangle$$
$$= \langle t_0| \cos(anH'/a)|t_0\rangle \sim \mu_{na}^{(a)}. \qquad (22)$$

This means that if rescaling with a, one has to compute a times more Chebyshev moments than in the case without rescaling. An exact version of statement (22) is given in (A2) in Appendix A. Figure 2(a) illustrates the scaling property (22) for a system of fixed size.
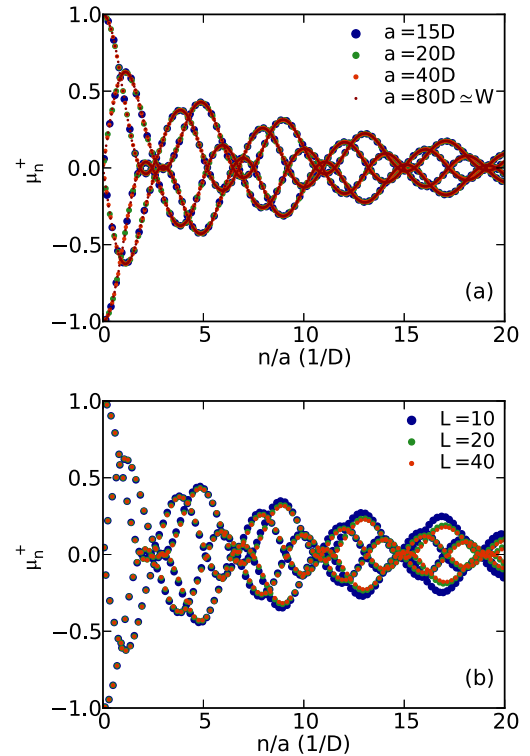
FIG. 2. (Color online) (a) Chebyshev moments $\mu_n^>$ vs n/a for fixed system size and different values of a and $b = 0$. Except for a different total number of points, the rescaled moments all lie on the line obtained when $a \to \infty$ and n/a becomes continuous. Here, we study the half-filled SIAM (Appendix C1) with semielliptic density of states of half-bandwidth D and $U = 2D$, represented on a chain with length $L = 80$. The full many-body bandwidth is $W \simeq 80D$. (b) Chebyshev moments for different system sizes L. Except for the system size and the scaling parameter, parameters are the same as in (a). Here, all calculations were done with a rescaling constant of $a = 20D$. For low values of n, the results for different system sizes are virtually indistinguishable. For higher values of n, moments start to disagree as finite-size features start to be resolved. The $L = 80$ and the $L = 40$ results would be indistinguishable in this plot.

1. Extracting the thermodynamic limit

One direct application of the scaling property (22), lies in the study of the thermodynamic limit by comparing systems of increasing size L. For low values of n, even small systems have the same Chebyshev moments as in the thermodynamic limit. Finite-size features are averaged out in the integral (9b) as long as $T_n(x)$ oscillates slowly enough. $T_n(x)$ oscillates n times on $[-1,1]$. An Nth order Chebyshev expansion therefore resolves features on the scale $2/N$, which on the original energy scale is $2a/N$. Finite-size oscillations appear at a spacing of W_{single}/L, where W_{single} is the single-particle bandwidth. Equating resolution with the spacing of finite-size oscillations,

$$2a/N_{\text{finsize}} = W_{\text{single}}/L, \tag{23}$$

gives the expansion order N_{finsize} at which finite-size features are first resolved. Figure 2(b) illustrates these statements by comparing Chebyshev moments computed for different system sizes.

2. Optimizing computation time

Figure 3 shows how computation time depends on the rescaling constant a for the example of the moments shown in Fig. 2(a). As already qualitatively stated previously [28,31], one observes that upon using a lower value of a computation time is reduced. In all cases, computation time diverges exponentially [Fig. 2(b)]. Note that rescaling with a higher value of a allows to compute at smaller matrix dimensions. Note further that if choosing a too small, numerical errors can render the recursion (14a) unstable. In contrast to common belief, it is possible to use much smaller values of a than the full many-body bandwidth. Achieving even smaller values of a can be done with the so-called *energy truncation* [28], but after several tests, we did not find this to lead to an effective speed-up of calculations. We therefore discard it in our calculations as a source of additional tuning parameters. We have also tested the idea of Ganahl *et al.* [31] to map the spectrum of H into $[-1,1]$ via $1 - \exp(\beta H)$. The idea might be worth to study in more detail, but again, we could not gain any performance improvement over a simple rescaling procedure.

B. Shifting by $b = -a$

The choice $b = -a$ in (11) makes an analytic expression of the complete spectral function $A(\omega) = A^+(\omega) + A^-(-\omega)$ in terms of a single Chebyshev expansion impossible, but has beneficial effects on the computation time. This is to be understood in the following sense: Due to the increased oscillation frequency of $T_n(x)$ close to the interval boundaries of $[-1,1]$, the integral (9a) extracts much more information about the spectral function in the vicinity of these boundaries. This is reflected, e.g., in the fact that the width of the Gaussian obtained by the kernel polynomial expansion approaches zero close the interval boundaries of $[-1,1]$ [see the discussion below (10b)]. It is therefore desirable to shift the relevant part of the spectral function, the part slightly above the Fermi edge, to match the left boundary -1. This is achieved by the choice $b = -a$. In practice, one adds a small correction $a\epsilon$, $\epsilon \sim 10^{-3}$, to avoid problems with the diverging weight function $w_n(x)$ in (8b).
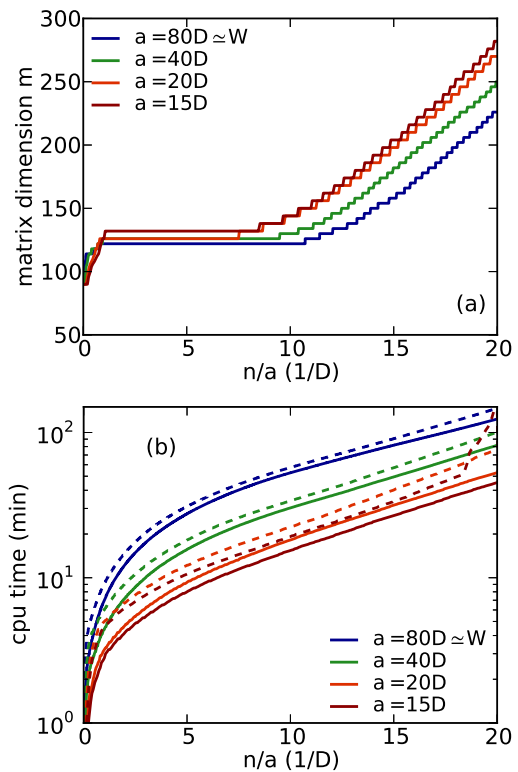

FIG. 3. (Color online) Performance of the adaptive matrix dimension algorithm (Sec. III A) for the example described in the caption of Fig. 2. (a) Adaption of matrix dimensions for different rescaling factors, fixing a truncation error of $\varepsilon_{\text{compr}} = 10^{-3}$. (b) Computer time needed to generate the same amount of information for different scalings running on a single-core 2.0-GHz workstation. Solid lines: fixing a truncation error of $\varepsilon_{\text{compr}} = 10^{-3}$. Dashed lines: $\varepsilon_{\text{compr}} = 5 \times 10^{-4}$. The iteration number where the irregular behavior of the dashed line for $a = 15D$ starts corresponds to the point where numerical errors render the Chebyshev recursion unstable. Note that while small a leads to the largest matrix sizes, which is costly in MPS, the overall cost of CPU time nevertheless is lowest, as a smaller expansion order is needed.

Another advantage of the $b = -a$ setup is that one can use a smaller scaling constant a than in the $b = 0$ setup. The Chebyshev iteration becomes unstable when the iteration number n becomes so high that $|t_n\rangle$ has accumulated erroneous contributions from eigen states with eigen energies $E'_n = (E_n - E_0 + b)/a > 1$. For fixed a, the additional subtraction in the $b = -a$ setup ensures that the instability appears for a higher iteration number than in the $b = 0$ setup. Therefore the $b = -a$ setup allows smaller values of a. We finally note that the choice $b = -a$ is equivalent to the choice suggested by Weiße *et al.* [27], if one rescales with the full many-body bandwidth $a = W$. In this case, the computation can be carried out to arbitrarily high order and will never become unstable. In the $b = 0$ setup, one would have to choose $a = 2W$ to reach arbitrarily high expansion orders.

In Fig. 4(a), we plot Chebyshev moments for both types of shifts $b = 0$ and $b = -a$. The moments obtained for $b = 0$ show a slow structureless oscillation whereas the moments obtained for $b = -a$ show a much faster oscillation.
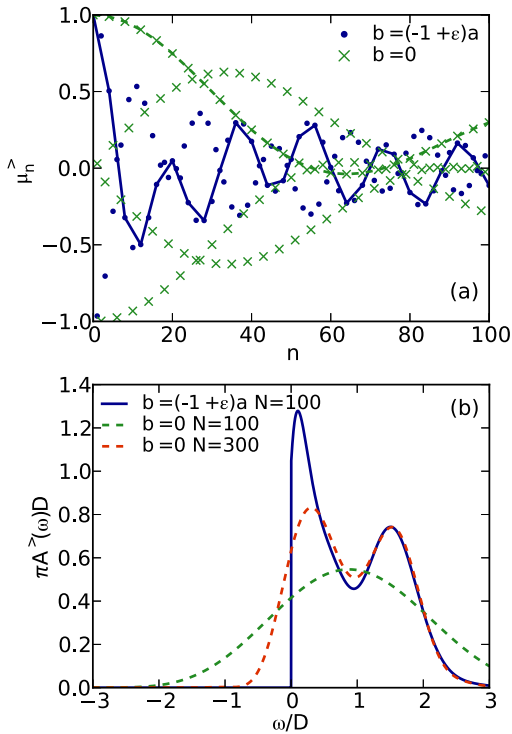
FIG. 4. (Color online) Local particle density of states of the half-filled SIAM (Appendix C1) with semielliptic density of states of half-bandwidth D. $L = 40$, $U = 2D$, and $a = 30D$ in all cases. (a) Chebyshev moments. Lines connect every fourth moment and by that reveal the relevant slow oscillation. They are a guide to the eye. (b) Corresponding spectral functions evaluated using Jackson damping (10b). The $b = 0$ calculation requires three times more iterations than the $b = -a$ calculation to resolve the right Hubbard peak with the same resolution. In this case, the central peak is still much better resolved for $b = -a$.

Figure 4(b) shows that upon using the same rescaling constant a and the same expansion order $N = 100$, which leads to very similar entanglement growth, both shift types differ strongly in the achieved resolution. To resolve at least the right Hubbard peak with a $b = 0$ calculation at the resolution of $b = -a$ calculation, one needs $N = 300$ moments. As computation time increases exponentially [Fig. 3(b)] with respect to expansion order N in both cases, this difference is highly relevant.

We apply both setups, $b = 0$ and $b = -a$, to the benchmark test of the DCA in Sec. VI A, and find a significant speed-up for $b = -a$ at a small loss in accuracy. Previously [31], only $b = 0$ has been considered for the solution of the DMFT.

V. POST-PROCESSING MOMENTS

Whereas Jackson damping (10b) can be seen as one possibility to post-process Chebyshev moments in order to achieve uniform convergence even for the truncated Chebyshev expansion of a delta function, there is another, fundamentally different approach. The computation of the Chebyshev moments becomes very costly for high iteration numbers. In the case in which Chebyshev moments start to follow a regular pattern when n exceeds a certain threshold,

it is possible to continue this pattern to infinity, and one can avoid the costly computation of moments. Consider a typical example in which the spectral function is a superposition of Lorentzians (quasiparticle peaks) and of a slowly varying background density. As for low values of n, $T_n(x)$ extracts information via (9b) only about the slowly varying background density, while for high values of n, $T_n(x)$ extracts information only about the sharp and regular Lorentzian structures, μ_n starts to follow a regular pattern for high numbers of n. For a sum of Lorentzians, with weights α_i, widths η_i, and positions ω_i, this pattern can be obtained analytically:

$$A_{\mathrm{Lor}}(\omega) = \sum_i \alpha_i \frac{\eta_i}{\pi} \frac{1}{(\omega - \omega_i)^2 + \eta_i^2},$$

$$\Rightarrow \quad \mu_n \simeq \sum_i \alpha_i \cos\left[n\left(\omega_i - \frac{\pi}{2}\right)\right] e^{-n\eta_i}, \quad (24)$$

as shown in Appendix B. If one recalls (Sec. IV) that the Chebyshev recursion corresponds to a discrete time evolution if choosing $b = 0$, the result of (24) could have been anticipated.

Figure 5(a) shows the spectral density for a SIAM together with a fitted superposition of three Lorentzians. Their difference corresponds to a background density that is composed of either slowly varying features or features with negligible weight. Figure 5(b) shows the corresponding Chebyshev moments. The slowly varying background density only contributes for the first 200 moments. After that, the Chebyshev moments for the superposition of Lorentzians starts
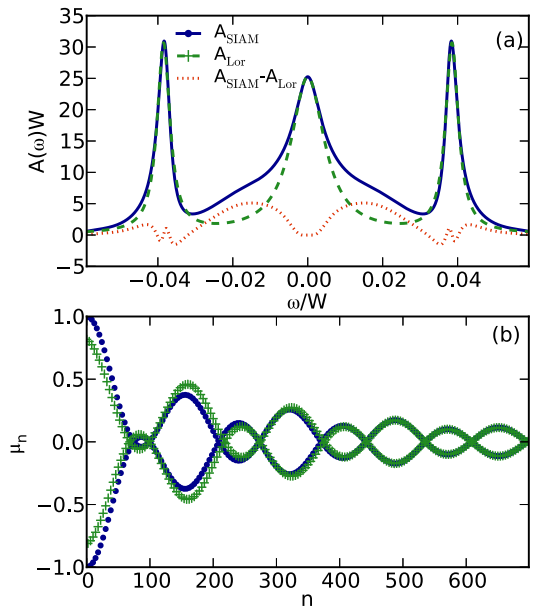
FIG. 5. (Color online) (a) $A_{\mathrm{SIAM}}(\omega)$ for a semielliptic density of states, half-filling and $U = 2D$ (Appendix C1). Quantities are shown in units of the full many-body bandwidth W. The superposition of three Lorentz peaks $A_{\mathrm{Lor}}(\omega)$ has been fitted to $A_{\mathrm{SIAM}}(\omega)$. (b) Corresponding Chebyshev moments. The result presented here was obtained with a $L = 40$ fermionic chain and CheMPS. It agrees with the result of Raas et al. [39], see Appendix C1. The legend in (a) is valid also for (b).

to be a very good approximation to the original moments, and it seems unnecessary to compute more than about 400 moments. For $200 < n < 400$, one can simply fit the analytical expression (24) to the original data. Using the analytical expression with the fitted parameters, one can then continue the Chebyshev moments to infinity.

Fitting (24) to the data between iterations 200 and 400 is a nonlinear optimization problem, which can easily be solved numerically. Still, there exists a linear reformulation of this optimization problem, coined under the name *linear prediction* [40]. The linear problem can be analytically reformulated as a matrix inversion problem. Its solution is faster and more stable than that of the original nonlinear problem. This allows in principle to optimize a superposition of many more Lorentzians than in the nonlinear case.

A. Linear prediction

In the context of time evolution *linear prediction* has been long established in the DMRG community [41,42], but it has only recently been applied to the computation of Chebyshev moments [31]. The optimization problem for the sequence μ_n becomes linear, if the sequence can be defined *recursively*:

$$\tilde{\mu}_n = -\sum_{i=1}^{p} a_i \mu_{n-i}, \qquad (25)$$

which is easily found to be equivalent to (24) [42]. The strategy is then as follows. Compute $n = N_c$ Chebyshev moments, and predict moments for higher values of n using (25). The coefficients a_i are optimized by minimizing the least-square error $\sum_{n \in \mathcal{N}_{\text{fit}}} |\tilde{\mu}_n - \mu_n|^2$ for a subset $\mathcal{N}_{\text{fit}} = \{N_c - n_{\text{fit}}, \ldots, N_c - 1, N_c\}$ of the computed data. We confirmed $n_{\text{fit}} = N_c/2$ to be a robust choice [31,42], small enough to go beyond spurious short-time behavior and large enough to have a good statistics for the fit. Minimization yields

$$R\boldsymbol{a} = -\boldsymbol{r}, \quad \boldsymbol{a} = -R^{-1}\boldsymbol{r},$$

$$R_{ji} = \sum_{n \in \mathcal{N}_{\text{fit}}} \mu_{n-j}^* \mu_{n-i}, \quad r_j = \sum_{n \in \mathcal{N}_{\text{fit}}} \mu_{n-j}^* \mu_n. \qquad (26)$$

We found that linear prediction loses its favorable filter properties if choosing p to be very high. Therefore one should restrict the number of Lorentzians to $p = \min(n_{\text{fit}}/2, 100)$. Furthermore, one adds a small constant $\delta = 10^{-6}$ to the diagonal of R in order to enable the inversion of the singular matrix R. Defining [42]

$$M = \begin{pmatrix} -a_1 & -a_2 & -a_3 & \ldots & -a_p \\ 1 & 0 & 0 & \ldots & 0 \\ 0 & 1 & 0 & \ldots & 0 \\ \vdots & \ddots & \ddots & \ddots & \vdots \\ 0 & 0 & \ldots & 1 & 0 \end{pmatrix},$$

one obtains the predicted moments $\tilde{\mu}_{N_c+n} = (M^n \boldsymbol{\mu}_{N_c})$, where $\boldsymbol{\mu}_{N_c} = (\mu_{N_c-1}\ \mu_{N_c-2}\ \ldots\ \mu_{N_c-p})^T$. The matrix M usually has eigenvalues with absolute value larger than 1, either due to numerical inaccuracies or due to the fact that linear prediction cannot be applied as μ_n rather increases than decreases on the training subset $\mathcal{N}_{\text{fit}}$. In order to obtain a convergent prediction,

we set the weights that correspond to these eigenvalues to zero measuring the ratio of the associated discarded weight compared to the total weight. If this ratio is higher than a few percent, we conclude that linear prediction cannot yet be applied and restart the Chebyshev calculation to increase the number of computed moments N_c.

B. Failure of linear prediction

It is not *a priori* clear that the spectral function can be well approximated by a superposition of Lorentzians, although this is true for the SIAM as shown in Fig. 5. Other types of smooth functions lead to a different functional dependence of the moments on n than the exponentially damped behavior. Close to phase transitions, e.g., one might find an algebraic decay in the time evolution, corresponding to an algebraic decay in the Chebyshev moments. If the spectral function has rather Gaussian shaped peaks, the decrease of Chebyshev moments is $\propto e^{-(\sigma n)^2}$ (Appendix B). For both scenarios, linear prediction is a noncontrolled extrapolation scheme. It still extracts oscillation frequencies (peak positions) with high reliability, but predicts a wrong decrease of the envelope, which often leads to an overestimation of peak weights.

In practice, it turns out that a combination of *damping* with a Jackson kernel (kKernel polynomial method) and *linear prediction* is a powerful way to get controlled estimates for the spectral function. While damping always underestimates peak heights, linear prediction typically overestimates peak heights. Both methods trivially converge to the exact result, when $N_c \to \infty$. One therefore obtains upper and lower bounds for the spectral function. This is particularly valuable in the DMFT as overestimated (diverging) peak heights can spoil convergence of the DMFT loop.

A historically much used alternative to linear prediction, suitable for arbitrary forms of the spectral function, is an extrapolation of Chebyshev moments using maximum entropy methods [43]. These suffer from severe numerical instabilities, though. Of course, one might also think of fitting another ansatz than the one of the exponential decrease. As it is *a priori* not clear which ansatz should be better, it is meaningful to stick to the easily implemented linear prediction that is moreover known to be applicable for the description of quasiparticle features.

VI. RESULTS FOR DMFT CALCULATIONS WITH TWO BATHS

A. Results for two-site DCA (VBDMFT)

In order to benchmark the Chebyshev technique for a two-bath situation, which goes beyond previous work [31] (see Appendix C), we study the Hubbard model on the two-dimensional square lattice,

$$H_{\text{Hub}} = \sum_{\boldsymbol{k}\sigma} \varepsilon_{\boldsymbol{k}} c_{\boldsymbol{k},\sigma}^\dagger c_{\boldsymbol{k},\sigma} + U \sum_i n_{i\uparrow} n_{i\downarrow},$$

$$\varepsilon_{\boldsymbol{k}} = -2t[\cos(\boldsymbol{k}_x) + \cos(\boldsymbol{k}_y)] - 4t' \cos(\boldsymbol{k}_x)\cos(\boldsymbol{k}_y), \quad (27)$$

in a two-site dynamical cluster approximation [5] (DCA) developed by Ferrero *et al.* [44]. This so-called *valence bond* DMFT (VBDMFT) is a minimal description of the

normal phase of the high-temperature superconductors, using a minimal two patches DCA cluster. It leads to a simple physical picture of the pseudogap phase in terms of a selective Mott transition in the momentum space. We choose this model here as a benchmark since its solution contains low energy features in the spectral functions (pseudogap), which have required high-precision QMC computations followed by a careful Padé analytic continuation. Moreover, real-frequency computations are very important for the comparison with experiments that measure, e.g., the optical conductivity along c axis [45]. It is therefore a nontrivial case where DMRG impurity solvers would bring significant improvements over the QMC in practice.

To set up the VBDMFT, one splits the Brioullin zone into a *central* patch $P_+ = \{\mathbf{k} | |k_x| < k_0 \wedge |k_y| < k_0\}$, where $k_0 = \pi(1 - 1/\sqrt{2})$, and a *border* patch $P_- = \{\mathbf{k} | \mathbf{k} \notin P_+\}$. In the DCA, the $\mathbf{k}$ dependence of the self-energy $\Sigma_\kappa(\omega)$ within each patch is neglected and one computes a Green's function for a patch by averaging over all $\mathbf{k}$ vectors in the patch

$$G_\kappa(\omega) = \frac{1}{|P_\kappa|} \sum_{\mathbf{k} \in P_\kappa} \frac{1}{\omega + \mu - \varepsilon_{\mathbf{k}} - \Sigma_\kappa(\omega)}, \quad (28a)$$

$$\Sigma_\kappa(\omega) = G_{0\kappa}(\omega)^{-1} - G_\kappa(\omega)^{-1}. \quad (28b)$$

Representing the noninteracting baths in a chain-geometry, and taking the two impurities to be the first of two chains $c_{\kappa\sigma} \equiv c_{0\kappa\sigma}$, the model Hamiltonian that needs to be solved is

$$H = H_d + H_{b,+} + H_{b,-},$$

$$H_d = \sum_{\substack{\kappa = \pm \\ \sigma = \uparrow, \downarrow}} (\bar{t}_\kappa + \varepsilon_0) n_{\kappa\sigma} + \frac{U}{2} \sum_{\substack{\kappa = \pm \\ \bar{\kappa} = -\kappa}} (n_{\kappa\uparrow} n_{\kappa\downarrow} + n_{\kappa\uparrow} n_{\bar{\kappa}\downarrow})$$

$$+ c_{\kappa\uparrow}^\dagger c_{\kappa\downarrow}^\dagger c_{\bar{\kappa}\downarrow} c_{\bar{\kappa}\uparrow} + c_{\kappa\uparrow}^\dagger c_{\bar{\kappa}\downarrow}^\dagger c_{\kappa\downarrow} c_{\bar{\kappa}\uparrow}),$$

$$H_{b,\kappa} = \sum_{i=0,\sigma}^{L_\kappa - 2} t_{i\kappa} (c_{i\kappa\sigma}^\dagger c_{i+1,\kappa\sigma} + \text{H.c.}) + \sum_{i=1,\sigma}^{L_\kappa - 1} \varepsilon_{i\kappa} n_{i\kappa\sigma}, \quad (29)$$

where $\varepsilon_0 = -\mu$ and the term $\bar{t}_\kappa = \frac{1}{|P_\kappa|} \sum_{\mathbf{k} \in P_\kappa} \varepsilon_k$ accounts for high-frequency contributions of the hybridization function (see Appendix D4).

The κ-space interaction term in (29) arises when diagonalizing the hybridization function of a real-space two-site cluster $c_{\pm\sigma} = \frac{1}{\sqrt{2}}(c_{1\sigma} \pm c_{2\sigma})$, where $c_{1\sigma}, c_{2\sigma}$ are annihilation operators for the cluster sites in real space, and $c_{\pm\sigma}$ for the cluster sites in κ space. In real space, the interaction is a simple Hubbard expression, but then the hybridization function is nondiagonal. A diagonal hybridization function, which leads to two uncoupled baths for the patches and by that allows a simple chain geometry for the whole system, is therefore only possible in κ space. The more complex form of the interaction in κ space does not affect the efficiency of DMRG.

We iteratively solve the self-consistency equation obtained by inserting the self-energy estimates of the impurity model (29) into the lattice Green functions (28a). We do that on the real-energy axis with an unbiased energy resolution. The details of this calculation are described in Appendix D.

In Figs. 6(a) and 6(b), we compare our CheMPS results for the spectral densities of the two momentum patches with those of Ferrero *et al.* [44] obtained using CTQMC and
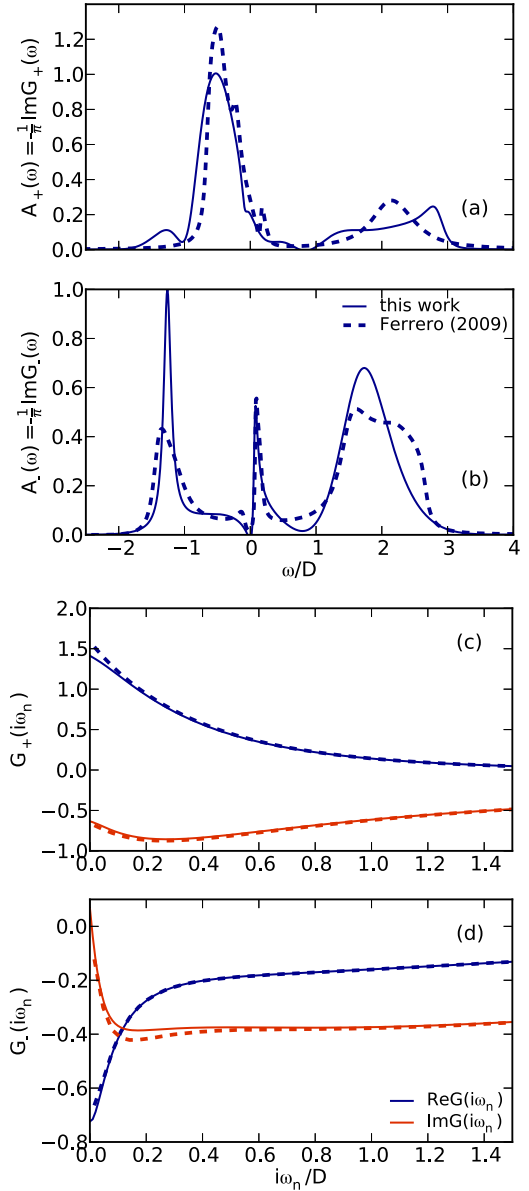
FIG. 6. (Color online) Spectral functions [(a) and (b)] and Green's functions on the imaginary axis [(c) and (d)] within VBDMFT [44] for $U = 2.5D$ and $n = 0.96$. We compare our zero-temperature CheMPS results (solid lines) with CTQMC data for $T = 1/200$ (dashed lines) from Ferrero *et al.* [44]. For this computation, we used the $b = 0$ setup, a chain length of $L = 30$ per patch, a truncation error of $\varepsilon_{\text{compr}} = 10^{-3}$, $N/a = 60/D$, and $a = 40D$.

analytical continuation. We observe a good overall agreement between the two methods, in particular at low frequencies. Low-energy features (pseudogap), in particular in $A_-(\omega)$, are well reproduced by both methods. At high energy (Hubbard bands), however, there are some differences between QMC and CheMPS (and also between the two variants of CheMPS). This is to be expected since the Padé analytic continuation technique used on the QMC data in Ref. [44] is not a precision method at high energy.

In Figs. 6(c) and 6(d), we do the analogous comparison on the imaginary axis, and find much better agreement.

On the imaginary axis, the QMC results can be considered numerically exact. The very low temperature ($\beta D = 200$) used for QMC should yield results that are indistinguishable from a zero-temperature calculation. The slight disagreement of our data and the QMC data on the Matsubara axis could probably be removed if we were able to reach higher expansion orders. One DMFT iteration for the presented $b = 0$ calculation took around 5 h running on four cores with 2.5 GHz. Convergence is achieved after ten iterations starting from the noninteracting solution. Convergence is defined via the maximal distance of the spectral densities obtained in two subsequent iterations i and $i + 1$: $\max_{\omega \in \mathbb{R}} |\rho_{i+1}(\omega) - \rho_i(\omega)| < 5 \times 10^{-3} D$. The calcula-

tion has been carried out with two attached chains of $L = 30$ lattice sites each. We did not observe changes for higher chain lengths up to $L = 40$, but could not reach high enough expansion orders for chains longer than $L = 40$. We computed $N = 2500$ moments using a scaling constant $a = 40D$, which corresponds to the full bandwidth.

The calculation can be accelerated significantly by using the $b = -a$ setup of Sec. IV B and avoiding *linear prediction*. This leads to the same quality of agreement with QMC on the Matsubara axis, but on the real axis, peaks are a bit less pronounced while the pseudogap is still well resolved (Fig. 7). While the study of systems with higher bath sizes increases the computational cost tremendously in the $b = 0$ setup, we could easily go to $L = 50$ within the $b = -a$ setup. This did not change the results. Computation times varied from 1.2 h per iteration for $L = 30$, over 3 h for $L = 40$ to around 10 h for the $L = 50$ calculation. We computed $N = 450$ moments using a scaling of $a = 15D$ in all cases.
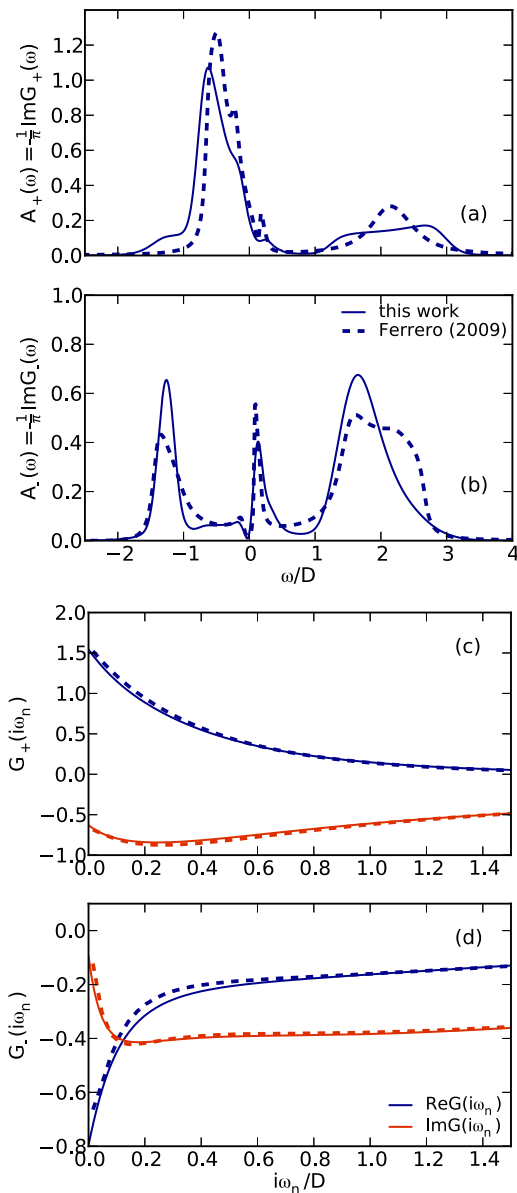

FIG. 7. (Color online) The same comparison as in Fig. 6. For this computation, we used the $b = -a$ setup, a chain length of $L = 40$ per patch, a truncation error of $\varepsilon_{\mathrm{compr}} = 10^{-3}$, $N = 450$, and $a = 15D$. For the $b = -a$ setup, one can use a smaller value of a as in the $b = 0$ setup, as discussed in Sec. IV.
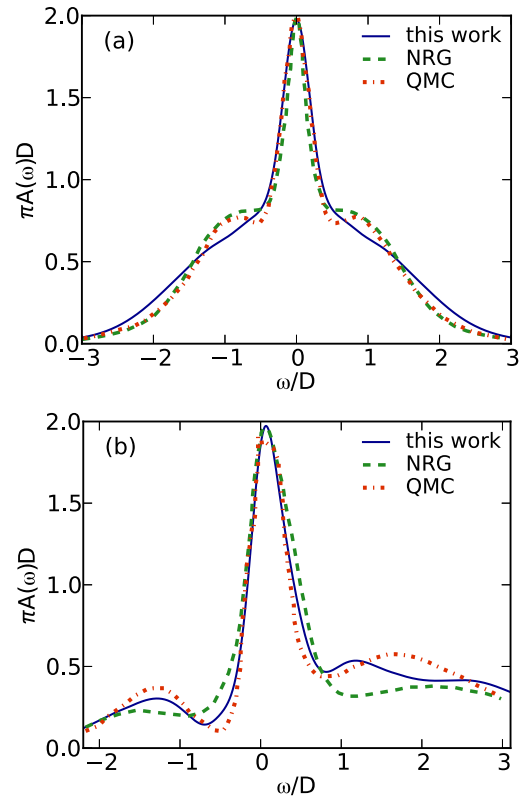
FIG. 8. (Color online) Spectral function for the two-band Hubbard model. (a) $U/D = 1.6$, $n = 2$ (half-filling). Panel (b) $U/D = 3.8$, $n = 1$ (quarter filling). In both cases, $J = \frac{1}{6}U$ and $U' = U - 2J$. We fixed a truncation error $\varepsilon_{\mathrm{compr}} = 10^{-3}$, used a scaling $a = 25D$, computed $N_c = 150$ moments and used linear prediction. To represent the two baths, we used two chains of length $L = 20$ each, obtained with a logarithmic discretization parameter of $\Lambda = 2$, leading to grid energies Λ^{-n} (see, e.g., Ref. [10]). The NRG calculation was done for temperature $T/D = 0.0025$, the QMC calculation for $T/D = 0.01$. Both should be almost indistinguishable from a $T = 0$ calculation. NRG data from K. Stadler [47] computed with a code of A. Weichselbaum [48], QMC data from M. Ferrero [49].

B. Single-site two-orbital DMFT

In the following, we apply CheMPS to the DMFT treatment of the two-orbital Hubbard model:

$$H = \sum_{\boldsymbol{k}v\sigma} \varepsilon_{\boldsymbol{k}v} n_{\boldsymbol{k}v\sigma} + U \sum_{iv} n_{iv\uparrow} n_{iv\downarrow} + \sum_{i\sigma\sigma'} (U_1 - \delta_{\sigma\sigma'} J) n_{i1\sigma} n_{i2\sigma'}$$

$$+ \frac{J}{2} \sum_{iv\sigma} c_{iv\sigma}^{\dagger} (c_{i\overline{v}\overline{\sigma}}^{\dagger} c_{iv\overline{\sigma}} + c_{iv\overline{\sigma}}^{\dagger} c_{i\overline{v}\overline{\sigma}}) c_{i\overline{v}\sigma}^{\dagger} \qquad (30)$$

on the Bethe lattice. We study a parameter regime close to the metal-insulator phase transition. This regime is computationally particularly expensive and we had to use a logarithmic discretization to reach Chebyshev expansion orders at which spectral functions are completely converged with respect to expansion order and system size. The linear discretization was feasible in the case of the VBDMFT studied in the previous section, as there, we faced a smaller entanglement entropy production during Chebyshev iterations.

Using a logarithmic discretization is not necessary for CheMPS. However, as it leads to exponentially decaying hopping constants, it gives rise to three advantages: (i) One can use smaller scaling constants a as the many-body bandwidth is considerably reduced due to the exponentially small value of most hopping constants in the system. (ii) One faces a smaller entanglement entropy production: at the edges of the bath chains (far away from the impurity), hopping constants are exponentially small, and application of H therefore creates much less entanglement than in the case in which a linear discretization is used. In (14a), the action of H' on $|t_{n-1}\rangle$ is then only a small perturbation for most parts of the system, and the recursion is therefore dominated by the second term $|t_{n-2}\rangle$. Entanglement therefore builds up only in the region where it is relevant, that is, in the vicinity of the impurity. Hence, matrix

dimensions grow considerably more slowly when using a logarithmic discretization as compared to a linear discretization. (iii) One faces a faster speed of convergence of the Chebyshev moments as in the linear case: The complexity of the spectral function is considerably reduced when averaging over possible peaks in the high-energy structure of the spectral function, as is done when using a logarithmic grid. The associated Chebyshev expansion therefore converges more quickly than in the case of a linear grid.

When using a logarithmic discretization, one has to convolute the resulting spectral function with a Gaussian [46] to average over the finite-size features that originate from the coarse log resolution at high energies. In Fig. 8, we compare exemplary calculations for the two-band Hubbard model with NRG and analytically continued QMC data. We find good agreement in the regions around the Fermi energy, where the pinning criterion is respected to high accuracy without being enforced. We explain the observed disagreement far away from the Fermi energy with a different specific implementation of the broadening convolution. One DMFT iteration for our calculations took around 20 min running on two 2.5 GHz cores.

In Fig. 9, we study the case of Ref. [35], which is very similar to the one studied in Fig. 8(a). Our results suggest that the data shown in Ref. [35] is not fully converged with respect to computed time in tDMRG, as it does not fulfill the pinning criterion. We face a similar problem when using a linear discretization: for the reachable Chebyshev expansion orders, we do not observe convergence of the central peak height for increasing expansion orders. All peaks, side peaks as well as central peak, increase for increasing expansion order and the pinning criterion is not fulfilled. The additional structure in the Hubbard band, which is not visible in the calculation with the logarithmic discretization, is seen to be similar to the one observed in Ref. [35]. One DMFT iteration for the

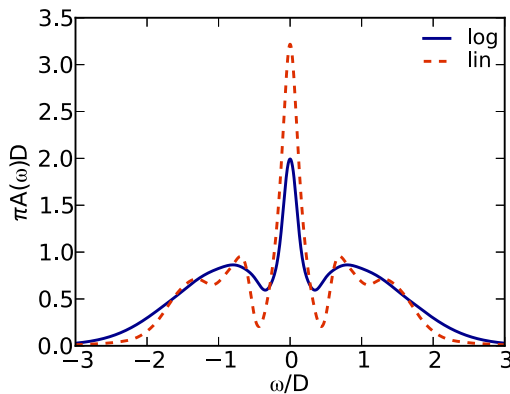

FIG. 9. (Color online) Spectral function for the two-band Hubbard model. The system parameters $U/D = 1.6$, $J/U = \frac{1}{4}$, $U' = U - 2J$, and $n = 2$ are very similar to the one in Fig. 8(a). We performed a calculation with linear ("lin", $L = 40$ per bath) and one with logarithmic discretization ("log", $L = 20$ per bath). We fixed a truncation error $\varepsilon_{\text{compr}} = 10^{-3}$. For the calculation with logarithmic discretization, we used a scaling $a = 25D$ and computed $N_c = 300$ moments. For the calculation with linear discretization, we used a scaling of $a = 125D$ and computed $N_c = 1250$ moments. We used linear prediction in all cases. The logarithmic discretization used a discretization parameter $\Lambda = 2$, leading to grid energies Λ^{-n} (see, e.g., Ref. [10]).

FIG. 10. (Color online) Results for the spectral densities in the two orbitals for $J = 0$. Our results are for $U = 2.6D$, $U' = 1.3D$, and $n = 2$ (half-filling) and depicted by the solid lines. The reference NRG results [50] are for $U = 2.8D$, $U' = 1.4D$ and depicted by the dashed lines. We had to choose a slightly smaller interaction for a meaningful comparison, as for the parameters of Greger *et al.* [50], we converged, though very slowly, into an insulating solution without central peak. The noninteracting single-particle half-bandwidth of the first band is D, and the one of the second band is $1.4D$. We used two chains of length $L = 20$ each, and a logarithmic discretization parameter of $\Lambda = 2$, leading to grid energies Λ^{-n} (see, e.g., Ref. [10]).

computation that uses a logarithmic grid took 20 minutes running on two 2.5 GHz cores. For the linear grid, this time was 10 h per DMFT iteration.

Finally, we study parameters that lead to a system close to the metal-insulator phase transition. Figure 10 shows that we obtain satisfactory agreement with NRG data, given the fact that we had to reduce the interaction slightly in order to stay in the metallic phase. This slight quantitative mismatch can possibly again be explained with a differing broadening convolutions in the two calculations. One DMFT iteration took 2 h for the calculation of Fig. 10, when fixing a truncated weight of $\varepsilon_{\text{compr}} = 2 \times 10^{-3}$.

VII. CONCLUSIONS

We solved several DMFT problems with two baths on the real frequency axis with unbiased energy-resolution based on an DMRG impurity solver using Chebyshev polynomials for the representation of spectral functions at moderate numerical effort. DMRG is thereby seen to be a viable alternative for DMFT impurity solvers also beyond the well-understood single-impurity single-band case.

Technically, it was crucial to apply the adaptive truncation scheme of Sec. III to maintain a modest numerical effort: in all cases, the new scheme gave much better results than the previously employed scheme based on fixed matrix dimensions. Another important way of tuning the calculation is provided by the mapping of the spectrum to the convergence interval of Chebyshev polynomials: The different options to set up a CheMPS calculation can be summarized to yield two alternatives. (i) One uses the $b = 0$ setup and post-processes moments with linear prediction. (ii) One uses the $b = -a$ setup and avoids linear prediction, using simple Jackson damping. Depending on the problem, the first or the second method can be more efficient. The second alternative is computationally much more efficient for cases in which linear prediction is a noncontrolled extrapolation scheme, but has problems to resolve sharp peaks at the Fermi edge.

The method presented in this paper can in principle be extended to the case of more than two baths without major changes to the DMFT-DMRG interface and the Chebyshev-based impurity solver as such. However, while two baths can still be modeled by a single chain with the impurity at the center (instead of at the end, as in single-band DMFT), this is no longer possible for three and more baths. This will necessitate a new setup of the DMRG calculation replacing the chainlike by a starlike geometry with the impurity at the center of the star, hence a generalization from a matrix-based to a tensor-based representation at the location of the impurity. It remains to be seen at which numerical cost reliable results on the real frequency axis will be obtainable.

APPENDIX A: SCALING OF CHEBYSHEV MOMENTS WITH RESPECT TO ENERGY SCALING

The Chebyshev moments obtained by using two different scalings $H_1' = H/a_1$ and $H_2' = H/a_2$ are from (13) $\mu_n^{a_1} = \sum_i W_i T_n((E_i - E_0)/a_1)$ and $\mu_n^{a_2} = \sum_i W_i T_n((E_i - E_0)/a_2)$. As we consider one-particle operators $c^\dagger$ the weights $W_i = |\langle E_i | c^\dagger | E_0 \rangle|^2$ fulfill

$$W_i = 0 \quad \text{for} \quad E_i \quad \text{with} \quad |E_i - E_0| \gtrsim W_{\text{single}}, \quad \text{(A1)}$$

where W_{single} is the single-particle bandwidth. If the scalings $a = \min(a_1, a_2)$ are chosen large enough, $W_{\text{single}}/a \ll 1$, then

$$\mu_{a_1 n}^1 = \mu_{a_2 n}^2 \quad \text{if} \quad \frac{a_1 n}{4} \in \mathbb{N} \quad \text{and} \quad \frac{a_2 n}{4} \in \mathbb{N}. \quad \text{(A2)}$$

Proof. If these requirements are met, the eigenvalues E_i with $W_i \neq 0$ are close to the ground-state energy: $x = (E_i - E_0)/a \ll 1$. The Taylor expansion $\arccos(x) = \pi/2 - x - x^3/6 + \dots$ becomes reliable already when $x \lesssim \frac{1}{2}$, which is fulfilled if a is at least twice the single-particle bandwidth as in all hitherto known applications [27,28,31].

Consider a particular energy $E = E_i - E_0$ for which $W_i > 0$. It holds

$$T_{a_1 n}(E/a_1) = T_{a_2 n}(E/a_2),$$

$$\cos(a_1 n \arccos(E/a_1)) = \cos(a_2 n \arccos(E/a_2)),$$

$$\cos(a_1 n(\pi/2 - E/a_1)) \simeq \cos(a_2 n(\pi/2 - E/a_2)),$$

$$a_1 n(\pi/2 - E/a_1) \bmod 2\pi \simeq a_2 n(\pi/2 - E/a_2) \bmod 2\pi,$$

$$a_1 n\pi/2 \bmod 2\pi \simeq a_2 n\pi/2 \bmod 2\pi,$$

$$a_1 n/2 \bmod 2 \simeq a_2 n/2 \bmod 2.$$

A sufficient condition for the last line to hold is that both $a_1 n/2$ and $a_2 n/2$ are multiples of 2, i.e., the statement of (A2). ∎

APPENDIX B: CHEBYSHEV MOMENTS OF LORENTZIAN AND GAUSSIAN

If we fix the shift to be $b = 0$, Eq. (24) is obtained as follows. As $\mu_n = \sum_i \alpha_i \mu_n^{li}$, we only have to compute the moments for a single Lorentzian, which allows to drop the index i:

$$\mu_n^l = \frac{\eta}{\pi} \int_{-1}^1 d\omega \frac{\cos(n \arccos(\omega))}{(\omega - \omega_0)^2 + \eta^2}$$

$$\simeq \frac{\eta}{\pi} \int_{-1}^1 d\omega \frac{\cos\left(n\left(\frac{\pi}{2} - \omega\right)\right)}{(\omega - \omega_0)^2 + \eta^2}$$

$$= \frac{\eta}{\pi} \int_{-1}^1 d\omega \frac{\cos(n(\omega + \omega_0'))}{\omega^2 + \eta^2}, \quad \omega_0' = \omega_0 - \frac{\pi}{2};$$

$$= \frac{\eta}{\pi} \text{Re} \int_{-1}^1 d\omega \frac{\exp(in(\omega + \omega_0'))}{\omega^2 + \eta^2}$$

$$= \frac{\eta}{\pi} 2\pi i \, \text{Res} \left[\frac{\cos(in(\omega + \omega_0'))}{\omega^2 + \eta^2} \right]\Big|_{\omega = i\eta}$$

$$= \cos\left[n\left(\omega_0 - \frac{\pi}{2}\right) \right] e^{-n\eta}.$$

When closing the integral in the complex plane, we assumed that the Lorentzian concentrates almost all of its weight within $[-1,1]$, which is a meaningful assumption, as we are calculating with the rescaled frequencies.

For the Gaussian, one has

$$A_{\text{Gauss}}(\omega) = \sum_i \alpha_i \frac{1}{\sqrt{2\pi}\sigma_i} e^{-\frac{(\omega-\omega_i)^2}{2\sigma_i^2}},$$
$$\Rightarrow \quad \mu_n^g \simeq \sum_i \alpha_i \cos\left[n\left(\omega_i - \frac{\pi}{2}\right)\right] e^{-(\sigma_i n)^2/2}, \quad \text{(B1)}$$

as shown by a similar calculation:

$$\mu_n^g = \frac{1}{\sqrt{2\pi}\sigma} \int_{-1}^1 d\omega\, e^{-\frac{(\omega-\omega_0)^2}{2\sigma^2}} \cos(n \arccos(\omega))$$
$$= \frac{1}{\sqrt{2\pi}\sigma} \int_{-1}^1 d\omega\, e^{-\frac{\omega^2}{2\sigma^2}} \cos(n(\omega + \omega_0')), \quad \omega_0' = \omega_0 - \frac{\pi}{2}$$
$$= \frac{1}{\sqrt{2\pi}\sigma} \text{Re} \int_{-1}^1 d\omega\, e^{-\frac{\omega^2}{2\sigma^2} + in\omega + in\omega_0'}$$
$$= \text{Re}\, e^{-\frac{\sigma^2 n^2}{2} + in\omega_0'} = \cos\left[n\left(\omega_0 - \frac{\pi}{2}\right)\right] e^{-\frac{\sigma^2 n^2}{2}}.$$

From the third to the fourth line, the extension of the integral limits to $\pm\infty$ in order to apply the Gaussian integral formula is well justified, as the Gaussian concentrates all its weight within $[-1,1]$.

APPENDIX C: SINGLE-BATH IMPURITY CALCULATIONS

1. Single-impurity Anderson model

The single impurity Anderson model (SIAM) in its truncated chain representation is

$$H = \sum_{n=0,\sigma}^{L-2} t_n(c_{n\sigma}^\dagger c_{n+1\sigma} + \text{H.c.}) + \sum_{n=0,\sigma}^{L-1} \varepsilon_i n_{0\sigma} + U n_{0\downarrow} n_{0\uparrow}, \quad \text{(C1)}$$

with hybridization function [51]

$$\Delta(z) = \cfrac{t_0^2}{z - \varepsilon_1 - \cfrac{t_1^2}{z - \varepsilon_2 - \cfrac{\cdots}{z - \varepsilon_{L-1} - \cfrac{t_{L-1}}{z - \varepsilon_L}}}}. \quad \text{(C2)}$$

For an infinitely long chain, the continuous version of the SIAM is recovered. The bath density of states is $\Gamma(\omega) = -\frac{1}{\pi}\text{Im}\,\Delta(\omega + i0^+)$. For an infinite homogeneous system with $t_i = t = D/2$, $\varepsilon_i = 0$, $\Gamma(\omega)$ is the semielliptic density of states at half-bandwidth D [51]:

$$\Gamma(\omega) = \frac{2}{\pi D}\sqrt{1 - (\omega/D)^2}. \quad \text{(C3)}$$

In the noninteracting case, also the spectral function $A(\omega)$ is semielliptic.

The computation of the spectral function $A(\omega)$ for the SIAM is much less demanding than for most DMFT applications: $A(\omega)$ has only few sharp features, which in addition are well approximated by Lorentzians (Sec. V 1). Hence linear prediction can be applied and we observe very good agreement
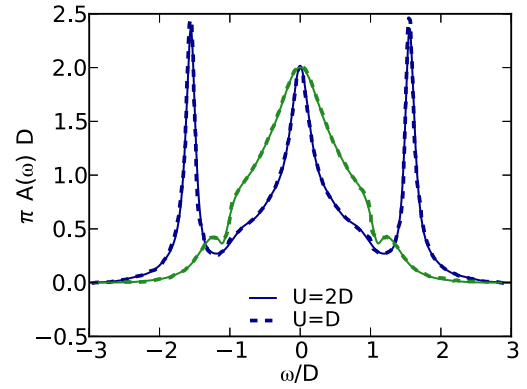

FIG. 11. (Color online) Single impurity Anderson model with semielliptic density of states of half-bandwidth D. We compute the spectral function with CheMPS allowing a cumulative truncated weight of $\varepsilon_{\text{compr}} = 7 \times 10^{-4}$ and post-process moments with linear prediction (solid lines). These results are compared to data obtained with dynamic DMRG (dashed lines) by Raas et al. [39]. We used a fermionic representation of the SIAM on a chain with length $L = 80$.

with DDMRG data of Raas et al. [39] in Fig. 11, confirming results of Ref. [31]. For the case $U = D$, we observe a slight disagreement in the region of the shoulders, where the linear prediction predicts two small peaks, whereas DDMRG shows a perfectly flat shoulder. This might point out a failure of linear prediction for the description of this feature. Although this should be of minor importance here, it could matter in other cases.

2. Single-site single-orbital DMFT

The single-site DMFT of the one-orbital Hubbard model

$$H = \sum_{k\sigma} \varepsilon_k n_{k\sigma} + U \sum_{i\nu} n_{i\uparrow} n_{i\downarrow} \quad \text{(C4)}$$

is well established [3] and amounts to the determination of the self-consistent parameters $\{t_i, \varepsilon_i\}$ of a SIAM (C1). We give a derivation of the DMFT equations only for the more complicated case of the cluster DMFT (Sec. D), which can easily be reduced to the single site case.

Figure 12 shows our results for which we fixed a maximum cumulative truncated weight of $\varepsilon_{\text{compr}} = 5 \times 10^{-4}$. For the quite featureless spectral function of Fig. 12(a) ($U = D$), the thermodynamic limit is already obtained for $L = 40$ and one DMFT iteration took 0.3 h. For Fig. 12(b) ($U = 2D$), we needed $L = 80$ and one DMFT iteration took around 3h. For Fig. 12(b) ($U = 2.4D$), we obtained converged DMFT loops, which violate the pinning criterion $A(0) = 2\pi/D$, though. When employing large bath sizes of $L = 100$ and more, we could not reach sufficiently high numbers of Chebyshev moments within reasonable computation times of up to 12 h per DMFT iteration; the linear prediction then overestimates the height of the central peak.

APPENDIX D: TECHNICAL DETAILS OF VBDMFT

In this appendix, we provide the technical details for the VBDMFT calculation.
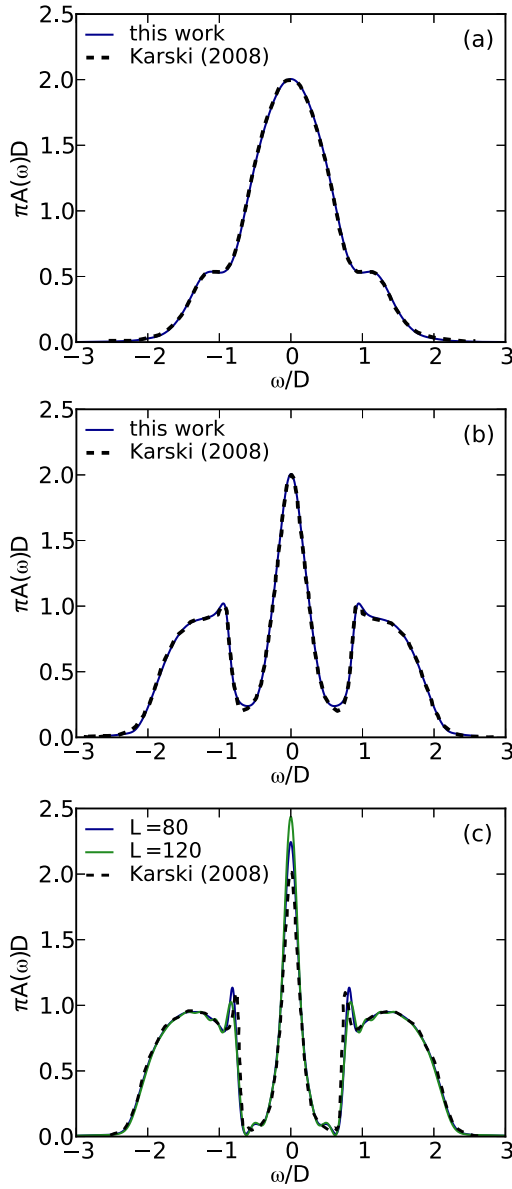
FIG. 12. (Color online) Local density of states within DMFT for the single-band Hubbard model on the Bethe lattice. Computed using CheMPS with an allowed cumulative truncated weight of $\varepsilon_{\text{compr}} = 5 \times 10^{-4}$. (a) $U = D$, (b) $2D$, and (c) $2.4D$. We compare our results with data from Karski *et al.* [24].

1. Self-consistency loop

The Green's function for a patch κ has been introduced in Sec. VI A and reads

$$G_\kappa(z) = \frac{1}{|P_\kappa|} \sum_{\boldsymbol{k} \in P_\kappa} \frac{1}{z + \mu - \varepsilon_{\boldsymbol{k}} - \Sigma_\kappa(z)}. \quad \text{(D1)}$$

Within the DCA, one obtains an estimate for $\Sigma_\kappa(z)$ by solving an auxiliary impurity-bath system, the Green's function of which is

$$G_\kappa^{\text{imp}}(z)^{-1} = z + \mu - \Delta_\kappa(z) - \Sigma_\kappa(z), \quad \text{(D2)}$$

where the bath is completely characterized by the hybridization function $\Delta_\kappa(z)$.

The problem is then to determine $\Delta_\kappa(z)$ such that the impurity-bath system best approximates the actual lattice environment, which amounts to the *self-consistency* condition

$$G_\kappa(z) = G_\kappa^{\text{imp}}(z). \quad \text{(D3)}$$

This equation constitutes a fixed-point problem for the hybridization function $\Delta(z)$ and can hence be solved iteratively, starting with some initial guess, e.g., the noninteracting solution.

Solving the impurity problem for the initial guess of $\Delta(z)$, one obtains $G_\kappa^{\text{imp}}(z)$. From that one obtains the estimate for the self-energy as $\Sigma_\kappa(z) = G_{0\kappa}^{\text{imp}}(z)^{-1} - G_\kappa^{\text{imp}}(z)^{-1}$, or by the method of Bulla *et al.* [52] (we found the latter not to yield advantages for the CheMPS setup). The self-energy is then inserted into (D1) to obtain a new value for $G_\kappa(z)$. Using self-consistency, this defines a new hybridization function by inserting (D3) in (D2):

$$\Delta_\kappa(z) = -G_\kappa(z)^{-1} + z + \mu - \varepsilon_0 - \Sigma_\kappa(z). \quad \text{(D4)}$$

In QMC calculations, one defines all quantities on the imaginary axis. In this work as in NRG calculations, we define all quantities on the real axis: the spectral density of the bath is

$$\Gamma(\omega) = -\frac{1}{\pi} \text{Im} \Delta(\omega + i0^+), \quad \text{(D5)}$$

which leads to a slightly modified version of (D4):

$$\Gamma_\kappa(\omega) = \frac{1}{\pi} \text{Im}(G_\kappa(\omega)^{-1} + \Sigma_\kappa(\omega)). \quad \text{(D6)}$$

If one considers ordinary single-site DMFT, all equations remain the same and the momentum patch index κ can be dropped. In a multiband calculation, the index κ plays the role of the band index. For DMFT carried out for the Bethe lattice, self-consistency can be written as $\Gamma(\omega) = \frac{D^2}{4} A^{\text{imp}}(\omega)$ [3], where $A^{\text{imp}}(\omega) = -\frac{1}{\pi} \text{Im} \, G^{\text{imp}}(\omega + i0^+)$. An iterative solution is particularly simple in this case, as only the spectral function has to be computed and summations over $\boldsymbol{k}$ space are not necessary. In the general case, also the real part of the Green's function is needed. This can either be accessed from the spectral function by the Kramers-Kronig relation or directly from the Chebyshev moments through [27]

$$G^{\text{imp}}(\omega) = -\frac{i}{a} \sum_n w_n(\omega') \mu_n \exp\left(-in \arccos(\omega')\right), \quad \text{(D7)}$$

where $\omega' \equiv \omega'(\omega)$ is the rescaled frequency defined in (11). The preceding equation should be evaluated slightly away from the real axis $\omega' \to \omega' + i0^+$. In our computations, we parallelized the independent computations for the particle and the hole part of the Green's (spectral) function, as well as those for different impurity sites.

2. Bath discretization

In order to represent the continuous hybridization function $\Delta(z)$ using a discrete chain, we use the general procedure of

Bulla *et al.* [10] (in the notation of Ref. [47]) adding details for the special case of the linear discretization. If we know the hybridization function $\Gamma(\omega)$ (D5) on the real axis, the bath and coupling Hamiltonian can be written as

$$H_b = \int_{-1}^{1} d\varepsilon \, \varepsilon a_\varepsilon^\dagger a_\varepsilon + \int_{-1}^{1} d\varepsilon \, \sqrt{\Gamma(\varepsilon)} (d^\dagger a_\varepsilon + \text{H.c.}). \quad \text{(D8)}$$

We discretize the Hamiltonian using a linear discretization of the bath energies

$$I_n = [\epsilon_n, \epsilon_{n+1}],$$
$$\epsilon_n = n\Delta\epsilon + \epsilon_0 \quad \text{for} \quad n \in \{1, 2, \ldots, L_b\}. \quad \text{(D9)}$$

For a given bath size L_b, we fix the free parameters ϵ_0 and $\Delta\epsilon$ by requiring $\int_{\epsilon_0}^{\epsilon_{L_b}} d\omega \Gamma(\omega) = 0.97 \int_{-\infty}^{\infty} d\omega \Gamma(\omega)$. This leads to outer interval borders ϵ_0 and ϵ_{L_b} that are close enough to minimize finite-size effects, and far enough apart from each other, to contain almost the complete support of $\Gamma(\omega)$. Starting with an interval $[\epsilon_0^{\text{init}}, \epsilon_{L_b}^{\text{init}}]$ that contains the full integrated weight of $\Gamma(\omega)$, we repeatedly shift the boundaries by a fixed small number to shrink it down to the required size. In a single step, we choose the boundary, that can be shifted with a smaller reduction of the total integral weight. The boundary that leads to a higher reduction is left unchanged in this step. When using a logarithmic discretization, we defined the discretization intervals via energies $\epsilon_m \propto \pm\Lambda^{-m}$, where $m \in [1, \ldots, L_b/2]$ [10]. The specific choice of boundaries of the support is not of much importance in this case.

The discretized SIAM then couples to L_b bath states created by $a_n^\dagger$ each of which corresponds to a bath energy interval I_n. One approximates the continuous H_b by the discrete version

$$H_b \simeq \sum_{n=1}^{L_b} \xi_n a_n^\dagger a_n + \sum_{n=1}^{L_b} \gamma_n (d^\dagger a_n + \text{H.c.}),$$
$$\gamma_n^2 = \int_{I_n} d\varepsilon \, \Gamma(\varepsilon), \quad \xi_n = \frac{1}{\gamma_n^2} \int_{I_n} d\varepsilon \, \varepsilon \Gamma(\varepsilon).$$

In order to use an MPS representation, one has to map the preceding Hamiltonian on a chain Hamiltonian. This is done using the Lanczos algorithm with high-precision arithmetics for the diagonal quadratic matrix $(\xi_n \delta_{nm})_{n,m=1}^{L_b}$ applied to the initial vector $(\gamma_n)_{n=1}^{L_b}$. After L_b Lanczos iterations one obtains the site potentials ε_i as the diagonal of the tridiagonal Lanczos matrix, and the hopping terms as the side-diagonal entries t_i. The hopping term from the impurity site to the first bath chain site is the square root of the total hybridization magnitude $t_0^2 = \sum_n \gamma_n^2 = \int d\varepsilon \Gamma(\varepsilon)$. With these definitions, the final chain Hamiltonian reads

$$H_b \simeq \sum_{i=0}^{L_b-1} t_i (c_{i+1}^\dagger c_i + \text{H.c.}) + \sum_{i=1}^{L_b} \varepsilon_i c_i^\dagger c_i, \quad \text{(D10)}$$

where the impurity site is the first site of the chain $c_0^\dagger \equiv d^\dagger$.

An alternative method to directly obtain the bath parameters by truncating the continued fraction expansion of the hybridization function as put forward by Karski *et al.* [24], did not show any advantages but led to equivalent results. As the method of Karski *et al.* [24] leads to hopping energies that

converge to a constant far away from the impurity, while the linear discretization scheme leads to polynomially decreasing hopping energies, the linear discretization method leads to a smaller many-body bandwidth. This allows to use smaller rescaling values in CheMPS.

3. Finding the ground state

The first problem to solve is finding the ground state of the model Hamiltonian.

a. Initializing the wave function

For the two-chain layout (29) of the model, the following problem arises: the chemical potential of both chains can be strongly different, in which case the particle numbers on the left $N_{\kappa=+}$ and the right $N_{\kappa=-}$ chain may be strongly different. Note that the Hamiltonian of (29) commutes with $N_{\kappa=+}$ and $N_{\kappa=-}$, as the chains are merely coupled by an interaction, not a hopping term. If starting a DMRG ground-state search with a global random state for such a system, convergence can be expected to be very slow, as the local optimization does not pick up the global potential variation. Even worse, the absence of an hopping term between the two chains prevents that during minimization the particle numbers in the left $N_{\kappa=+}$ and the right $N_{\kappa=-}$ chain change. This can in principle be compensated by choosing the White's *mixing factor* [53] to be large when starting to sweep, reducing it when being close to convergence. However, still we found it impossible to implement a reliable automatized ground-state search under these circumstances.

The problem can be solved by using a $U = 0$ solution as an initial guess for the ground-state search. One should realize that the partition between N_- and $N_+ = N - N_-$ (where N is the total particle number) only weakly depends on the interaction U; the total potential and hopping energies scale with the bath length, whereas the interaction energy is a single-site quantity. Given the system parameters $\{\varepsilon_{\kappa i}\}$ and $\{t_{\kappa i}\}$ for each chain κ, we diagonalize the $L = L_b + 1$ dimensional tridiagonal single-particle representation of a single chain with its associated impurity site. This gives us the particle sectors $N_\pm$ of the ground state of each subsystem. The $U = 0$ estimate for the total particle number sector is $N = N_+ + N_-$, as in this case both subsystems are uncoupled. Given an initial guess for the chemical potential μ, one should initialize a wave function that fulfills the $U = 0$ estimates for N and N_+/N_-.

b. Finding the correct symmetry sector

As the DMFT is grand canonical, one still needs to solve the problem of finding the correct particle number sector for the DMRG calculation. This can be greatly accelerated using the $U = 0$ estimate for N, which constitutes a *rigorous* upper bound for the particle number in the interacting system. For a given μ, one can therefore use a bisection search, starting with N, $N - \Delta N$ and $N - 2\Delta N$. In case $N - 2\Delta N$ yields the lowest energy estimate, one has to extend the search regime to lower values of N. If N or $N - \Delta N$ yield the lowest energy, one can continue the ordinary bisection search. For typical interaction values, $\Delta N/N = 0.05$ is a meaningful choice. If

searching for the maximum energy state, which is necessary if one wants to determine the full many-body bandwidth $W = E_{\max} - E_0$, one searches for the ground state of $-H$. In this case, the interaction between electrons becomes attractive, and the $U = 0$ solution for the particle number sector of $|E_{\max}\rangle$ becomes a rigorous lower bound for the interacting system.

Having found the correct symmetry sector together with its ground state for a given value of μ, one has to check whether the requirements for the local impurity densities are fulfilled,

$$n - \sum_\kappa \langle c_\kappa^\dagger c_\kappa \rangle \overset{?}{=} 0. \qquad (D11)$$

To find the correct value of the chemical potential, a simple update of the chemical potential μ with the residuum of (D11) is usually not sufficient to achieve convergence. Instead, we use this method until we found a lower and upper bound for μ and then use a bisection again.

In some cases, the algorithm has to break its search before reaching the required tolerance. This is when the desired chemical potential lies directly on the boundary which separates two different particle number sectors. If this is the case, due to the discrete nature of our model, no solution can be found. Such a case is typically detected by observing oscillations in the residuum of (D11).

When setting up the ground-state search naively, it can easily take most of the computation time of the calculation. Using the procedures just described, it usually takes only a negligible few percent of the total computation time.

4. Definition of the model Hamiltonian

In the following, we outline the standard procedure that eliminates the high-energy contributions in the hybridization function. We want to represent the noninteracting patch

Green's function

$$G_{0\kappa}(z) = \frac{1}{|P_\kappa|} \sum_{\kappa \in P_\kappa} \frac{1}{z + \mu - \varepsilon_{\boldsymbol{k}}}, \qquad (D12)$$

by an impurity model with Green's function $G_{0\kappa}^{\text{imp}}(z) = \frac{1}{z + \mu - \Delta(z)}$, such that

$$G_{0\kappa}(z) = G_{0\kappa}^{\text{imp}}(z). \qquad (D13)$$

When defining the bath hybridization function naively via

$$\Delta_\kappa(z) = z + \mu - G_{0\kappa}^{-1}(z), \qquad (D14)$$

one observes that $\Delta_\kappa(z) \to \bar{t}_\kappa$ for $|z| \to \infty$, when expanding for high values of $|z|$, as

$$G_{0\kappa}(z) = \frac{1}{z + \mu} \left(1 + \frac{\bar{t}_\kappa}{z + \mu} + \mathcal{O}(z^{-1}) \right), \qquad (D15a)$$

$$G_{0\kappa}^{-1}(z) = z + \mu - \bar{t}_\kappa + \mathcal{O}(z^{-1}), \qquad (D15b)$$

where $\bar{t}_\kappa = \frac{1}{|P_\kappa|} \sum_{k \in P_\kappa} \varepsilon_k$.

This means that the corresponding spectral density of the bath $\Gamma(\omega) = -\frac{1}{\pi} \text{Im} \, \Delta(\omega + i0^+)$ has contributions at arbitrarily high energies and the discretization procedure that maps $\Gamma(\omega)$ onto the discrete bath Hamiltonian H_b must fail. This problem is solved by defining an impurity model at a shifted chemical potential $\mu \to \mu - \bar{t}_\kappa$. In the hybridization function of this shifted impurity model

$$\Delta_\kappa(z) = z + \mu - \bar{t}_\kappa - G_{0\kappa}^{-1}(z), \qquad (D16)$$

the constant $\bar{t}_\kappa$ in the high-energy expansion of $G_{0\kappa}^{-1}(z)$ (D15b) cancels out. It therefore approaches zero for $|z| \to \infty$ while still fulfilling (D13) for $G_{0\kappa}^{\text{imp}}(z) = \frac{1}{z + \mu - \bar{t}_\kappa - \Delta(z)}$. As $\bar{t}_\kappa$ is a simple constant shift of the chemical potential, one can as well incorporate it into the Hamiltonian description of the impurity model, as done in (29).

[1] W. Metzner and D. Vollhardt, Phys. Rev. Lett. **62**, 324 (1989).

[2] A. Georges and G. Kotliar, Phys. Rev. B **45**, 6479 (1992).

[3] A. Georges, G. Kotliar, W. Krauth, and M. J. Rozenberg, Rev. Mod. Phys. **68**, 13 (1996).

[4] G. Kotliar, S. Savrasov, K. Haule, V. Oudovenko, O. Parcollet, and C. Marianetti, Rev. Mod. Phys. **78**, 865 (2006).

[5] T. Maier, M. Jarrell, T. Pruschke, and M. Hettler, Rev. Mod. Phys. **77**, 1027 (2005).

[6] E. Gull, A. J. Millis, A. I. Lichtenstein, A. N. Rubtsov, M. Troyer, and P. Werner, Rev. Mod. Phys. **83**, 349 (2011).

[7] A. N. Rubtsov, V. V. Savkin, and A. I. Lichtenstein, Phys. Rev. B **72**, 035122 (2005).

[8] E. Gull, P. Werner, O. Parcollet, and M. Troyer, Europhys. Lett. **82**, 57003 (2008).

[9] P. Werner, A. Comanac, L. de' Medici, M. Troyer, and A. J. Millis, Phys. Rev. Lett. **97**, 076405 (2006).

[10] R. Bulla, T. Costi, and T. Pruschke, Rev. Mod. Phys. **80**, 395 (2008).

[11] M. Caffarel and W. Krauth, Phys. Rev. Lett. **72**, 1545 (1994).

[12] M. Granath and H. U. R. Strand, Phys. Rev. B **86**, 115111 (2012).

[13] Y. Lu, M. Höppner, O. Gunnarsson, and M. W. Haverkort, Phys. Rev. B **90**, 085102 (2014).

[14] A. K. Mitchell, M. R. Galpin, S. Wilson-Fletcher, D. E. Logan, and R. Bulla, Phys. Rev. B **89**, 121105 (2014).

[15] S. R. White, Phys. Rev. Lett. **69**, 2863 (1992).

[16] U. Schollwöck, Rev. Mod. Phys. **77**, 259 (2005).

[17] U. Schollwöck, Ann. Phys. **326**, 96 (2011).

[18] K. A. Hallberg, Phys. Rev. B **52**, R9827 (1995).

[19] D. J. García, K. Hallberg, and M. J. Rozenberg, Phys. Rev. Lett. **93**, 246403 (2004).

[20] P. E. Dargel, A. Wöllert, A. Honecker, I. P. McCulloch, U. Schollwöck, and T. Pruschke, Phys. Rev. B **85**, 205119 (2012).

[21] F. A. Wolf (unpublished).

[22] T. D. Kühner and S. R. White, Phys. Rev. B **60**, 335 (1999).

[23] E. Jeckelmann, Phys. Rev. B **66**, 045114 (2002).

[24] M. Karski, C. Raas, and G. S. Uhrig, Phys. Rev. B **77**, 075116 (2008).

[25] M. Karski, C. Raas, and G. S. Uhrig, Phys. Rev. B **72**, 113110 (2005).

[26] S. Nishimoto and E. Jeckelmann, J. Phys.: Condens. Matter **16**, 613 (2004).

[27] A. Weiße, G. Wellein, A. Alvermann, and H. Fehske, Rev. Mod. Phys. **78**, 275 (2006).

[28] A. Holzner, A. Weichselbaum, I. P. McCulloch, U. Schollwöck, and J. von Delft, Phys. Rev. B **83**, 195115 (2011).

[29] A. Braun and P. Schmitteckert, arXiv:1310.2724.

[30] A. C. Tiegel, S. R. Manmana, T. Pruschke, and A. Honecker, Phys. Rev. B **90**, 060406(R) (2014).

[31] M. Ganahl, P. Thunström, F. Verstraete, K. Held, and H. G. Evertz, Phys. Rev. B **90**, 045144 (2014).

[32] A. J. Daley, C. Kollath, U. Schollwöck, and G. Vidal, J. Stat. Mech.: Theor. Exp. (2004) P04005.

[33] G. Vidal, Phys. Rev. Lett. **93**, 040502 (2004).

[34] S. R. White and A. E. Feiguin, Phys. Rev. Lett. **93**, 076401 (2004).

[35] M. Ganahl, M. Aichhorn, P. Thunström, K. Held, H. G. Evertz, and F. Verstraete, arXiv:1405.6728.

[36] L. Lin, Y. Saad, and C. Yang, arXiv:1308.5467.

[37] J. B. Boyd, *Chebyshev and Fourier Spectral Methods* (Dover, Mineola, New York, 2001).

[38] F. Verstraete and J. I. Cirac, Phys. Rev. B **73**, 094423 (2006).

[39] C. Raas, G. S. Uhrig, and F. B. Anders, Phys. Rev. B **69**, 041102 (2004).

[40] W. H. Press, S. A. Teukolsky, W. T. Vetterling, and B. P. Flannery, *Numerical Recipes: The Art of Scientific Computing*, 3rd ed. (Cambridge University Press, New York, NY, USA, 2007).

[41] S. R. White and I. Affleck, Phys. Rev. B **77**, 134437 (2008).

[42] T. Barthel, U. Schollwöck, and S. R. White, Phys. Rev. B **79**, 245101 (2009).

[43] R. N. Silver and H. Röder, Phys. Rev. E **56**, 4822 (1997).

[44] M. Ferrero, P. S. Cornaglia, L. De Leo, O. Parcollet, G. Kotliar, and A. Georges, Phys. Rev. B **80**, 064501 (2009).

[45] M. Ferrero, O. Parcollet, A. Georges, G. Kotliar, and D. N. Basov, Phys. Rev. B **82**, 054502 (2010).

[46] A. Weichselbaum and J. von Delft, Phys. Rev. Lett. **99**, 076402 (2007).

[47] K. Stadler, Master's thesis, LMU Munich, 2013.

[48] A. Weichselbaum, Ann. Phys. **327**, 2972 (2012).

[49] M. Ferrero (private communication).

[50] M. Greger, M. Kollar, and D. Vollhardt, Phys. Rev. Lett. **110**, 046403 (2013).

[51] C. Raas, Ph.D. thesis, University of Cologne, 2005.

[52] R. Bulla, A. C. Hewson, and T. Pruschke, J. Phys.: Condens. Matter **10**, 8365 (1998).

[53] S. R. White, Phys. Rev. B **72**, 180403 (2005).

3.2. Imaginary-time matrix product state impurity solver for dynamical mean-field theory

Realizing that imaginary time-evolution does not create entanglement, and would therefore allow to treat much more complex models as compared to real-time evolution or the Chebyshev recursion, was the main idea for the investigation documented in the following article (Wolf *et al.*, 2015a).

▷ *Imaginary-time matrix product state impurity solver for dynamical mean-field theory*
FA Wolf, A Go, IP McCulloch, AJ Millis and U Schollwöck
Phys. Rev. X **5**, 041032 (2015)

Imaginary-Time Matrix Product State Impurity Solver for Dynamical Mean-Field Theory

F. Alexander Wolf,[1] Ara Go,[2] Ian P. McCulloch,[3] Andrew J. Millis,[2] and Ulrich Schollwöck[1,4]

[1]*Department of Physics, Arnold Sommerfeld Center for Theoretical Physics,*
LMU Munich, 80333 München, Germany
[2]*Department of Physics, Columbia University in the City of New York, New York, New York 10027, USA*
[3]*Centre for Engineered Quantum Systems, School of Physical Sciences,*
The University of Queensland, Brisbane, Queensland 4072, Australia
[4]*Center for NanoScience, LMU Munich, 80799 München, Germany*

We present a new impurity solver for dynamical mean-field theory based on imaginary-time evolution of matrix product states. This converges the self-consistency loop on the imaginary-frequency axis and obtains real-frequency information in a final real-time evolution. Relative to computations on the real-frequency axis, required bath sizes are much smaller and no entanglement is generated, so much larger systems can be studied. The power of the method is demonstrated by solutions of a three-band model in the single- and two-site dynamical mean-field approximation. Technical issues are discussed, including details of the method, efficiency as compared to other matrix-product-state-based impurity solvers, bath construction and its relation to real-frequency computations and the analytic continuation problem of quantum Monte Carlo methods, the choice of basis in dynamical cluster approximation, and perspectives for off-diagonal hybridization functions.

Subject Areas: Computational Physics,
Condensed Matter Physics,
Materials Science

I. INTRODUCTION

Dynamical mean-field theory (DMFT) in its single-site [1–3] and cluster [4,5] variants is among the most widely employed computational techniques for solving quantum many-body problems. Fundamentally, DMFT in its simplest version becomes exact in the limit of high coordination numbers and was originally applied to simple model Hamiltonians. At least over the past decade, DMFT has been applied increasingly to more realistic models of materials, also of low dimensionality. To this purpose, the initial setup of a single impurity site coupled to a single band has been replaced by impurities consisting of multiple sites and multiple local orbitals. The degree of realism of DMFT is mainly determined by progress made in the size of these generalized impurities.

At the core of a numerical solution of DMFT is an impurity solver: an algorithm for solving a quantum impurity problem. The size of the impurity problem that can be treated is essentially limited by progress in the power of the impurity solver, which emerges as the key limitation of DMFT. The purpose of this paper is to present a new impurity solver and its power to address problems hitherto inaccessible to DMFT. The most prominent

examples of impurity solvers are the continuous-time quantum Monte Carlo (CTQMC) methods [6–8], exact diagonalization (ED) [9–11], the numerical renormalization group (NRG) [12], and the density matrix renormalization group (DMRG) [13]. Other recent suggestions for impurity solvers [14–19], including, in particular, the computationally inexpensive density matrix embedding theory [20], are promising but have not been tested in detail.

While all methods have their strengths, key limitations mean that fundamentally important classes of problems have not yet been adequately addressed. Many of the approaches have been developed in the context of the single-band Hubbard model (one spin-degenerate orbital per site and a correspondingly simple structure for the electron-electron interaction), but in many correlated electron materials of current interest (for example, metallic Fe or Co, or the heavy fermion compounds and the iron arsenide family of high transition temperature superconductors), the physics involves electrons in partly filled d or f shells where multiplet effects associated with orbital degeneracy and its partial lifting by ligand fields and interactions play a crucial role. Our current ability to treat these effects is limited to the single-site approximation and to situations in which the correlated orbitals have a large point group symmetry. Further, intersite correlations beyond the scope of the single-site approximation are believed to play a crucial role in materials with strong electronic anisotropy ("low-dimensional systems," such as the high-T_c cuprates, iron arsenide materials, or the

dicalcogenides). This has been explicitly demonstrated in cluster dynamical mean-field solutions of the two-dimensional single-orbital Hubbard model, but the techniques used in this case rely on simplifications associated with the interaction structure of the single-orbital Hubbard model, and no efficient generalization to the multiorbital situation is known. Intersite correlations are believed to be of somewhat less importance for three-dimensional materials, but the question of their importance simply cannot be addressed with current techniques. Thus, in summary, new methods are needed to go beyond (or at least validate) the single-site dynamical mean-field approximation and lift the restriction to the single-orbital or high point symmetry situations.

CTQMC is widely employed, but its application to situations involving low point symmetry, non-Hubbard interactions, or multiple relevant orbitals is limited by the fermionic sign problem. Reaching low temperatures becomes highly computationally expensive while calculating real-frequency information requires analytical continuation, a numerically ill-posed procedure fraught with practical difficulties.

ED makes no assumption on the interaction and does not have a sign problem. It is limited by the size of the Hilbert space that can be studied, meaning in practice that it is restricted to a small number of correlated sites to which only a small number of bath sites can be attached. Recently, improvements have been achieved by considering only restricted subspaces of the Hilbert space [21–24], but the size of the problem remains a significant limitation.

NRG converges the DMFT loop on the real-frequency axis and very effectively obtains real-frequency information in the low-frequency limit. Current applications have been to relatively small problems (the most recent achievement is a solution of the single-site DMFT approximation to a three-band model [25]) and it remains to be seen how far the method can be extended.

DMRG [26] is a set of algorithms operating on the space of matrix product states (MPS) [27]. It has been found to be extremely powerful for the calculation of ground states of one-dimensional quantum systems [27,28]; it was very successfully extended to the calculation of spectral functions which, in contrast to NRG, it obtains with equal resolution across the spectrum (see, e.g., Refs. [29,30]). In pioneering work the method was applied as a DMFT solver by García *et al.* [13] and Nishimoto *et al.* [31] with important further work done by these and other authors [32–38]. However, the method has not been widely accepted, perhaps because high-quality data were presented only for the single-site approximation to the single-band Hubbard model. Recently, the method was shown to provide a reliable and highly efficient solver for the two-site dynamical cluster approximation (DCA) approximation to the single-band Hubbard model [39], and insights into the entanglement of the impurity problem make it even

more powerful [40]. In view of these advances, DMRG now is a promising candidate for a highly flexible low-cost impurity solver, which can, in addition, be efficiently employed in the nonequilibrium formulation of DMFT [40–42]. However, the key issue of the ability to treat a multiorbital, multisite, low symmetry situation has not yet been demonstrated.

This paper takes a further step forward in the development of DMRG as a tool to study systems with multiple relevant orbitals and important intersite correlations. The important technical advance is a reformulation of the method on the imaginary-time axis. As we show, this strongly reduces entanglement and requires smaller bath sizes, enabling treatment of a large class of problems, including some that are unreachable by other methods, due, e.g., to the sign problem, the size of the correlated cluster, or the number of bands. The price to be paid is a reduced resolution on the real-frequency axis (not needed for converging the DMFT equations or obtaining thermodynamic quantities and phase boundaries), which we study in detail by comparing with calculations that converge the DMFT loop on the real-frequency axis.

The paper is organized as follows. Section II presents the basics of the method. Section III compares the new imaginary-axis formulation with existing real-axis formulations and documents the reduction in bath sizes and the implications for real-axis spectra. We illustrate the method with calculations for three-band models in the single-site and two-site DMFT approximation in Sec. IV and summarize our work in Sec. V. We append discussions of the optimization of typical DMFT Hamiltonians (Appendix A), the entanglement in different representations of the DCA, including a discussion of off-diagonal hybridization functions (Appendix B), and general aspects regarding the computation of Green's functions using MPS (Appendix C).

II. METHOD

A. Overview: Green's functions in DMRG

The computational key challenge in DMFT is the computation of the full frequency dependence of the Green function of a quantum impurity model involving an essentially arbitrary bath. The "size" (number of correlated sites L_c) of the impurity model should be as large as possible and the kinds of interaction that can be treated should be as general as possible. The Green function is used in a self-consistency loop, which may require many iterations for convergence. The solution should be as inexpensive as feasible, and must run automatically, without need for manual optimization of parameters or procedures. In this section, we present a qualitative discussion of the issues involved in computing the Green function using DMRG methods, to motivate the work described in detail below.

Within DMRG one computes Green's functions by first representing the system ground state $|E_0\rangle$ as a MPS. One then generates a one-electron (one-hole) excitation $|\psi_0^>\rangle = d^\dagger|E_0\rangle$ $(|\psi_0^<\rangle = d|E_0\rangle)$ by applying a creation (annihilation) operator $d^\dagger$ (d) to $|E_0\rangle$. While the state $|\psi_0^{\gtrless}\rangle$ is at most as entangled as the ground state $|E_0\rangle$ [30], in order to compute a Green function one has to perform further operations on $|\psi_0^{\gtrless}\rangle$. These operations typically increase entanglement and by that the bond dimension of a MPS, which ultimately limits all computations.

Let us be more concrete and consider a general MPS of bond dimension m for a system with L sites and open boundary conditions. Defining A^{σ_i}, $B^{\sigma_i} \in \mathbb{C}^{m\times m}$ for $i \neq 1$, L and $A^{\sigma_1} \in \mathbb{C}^{1\times m}$, $B^{\sigma_L} \in \mathbb{C}^{m\times 1}$, where $\sigma_i \in \{0, \uparrow, \downarrow, \uparrow\downarrow\}$ labels a local basis state of the Hilbert space, any MPS can be represented as [27]

$$|\psi_{\text{MPS}}\rangle = \sum_{\sigma_1,...,\sigma_L} A^{\sigma_1}... A^{\sigma_l} S B^{\sigma_{l+1}}... B^{\sigma_L}|\sigma_1, ..., \sigma_L\rangle, \quad (1)$$

where $S = \text{diag}(s_1, ..., s_m)$ is a diagonal matrix and A^{σ_i} are left normalized and B^{σ_i} are right normalized, respectively:

$$\sum_{\sigma_i} A^{\sigma_i\dagger}A^{\sigma_i} = I, \qquad \sum_{\sigma_i} B^{\sigma_i}B^{\sigma_i\dagger} = I. \quad (2)$$

Here, I are identity matrices. Left and right normalization make Eq. (1) the Schmidt decomposition of $|\psi_{\text{MPS}}\rangle$ that is associated with partitioning the system at bond $(i, i+1)$. The bond entanglement entropy for the associated reduced density matrix can therefore simply be read off from Eq. (1) [27]:

$$S_{(i,i+1)}^{\text{ent}} = \sum_{\nu=1}^{m} s_\nu^2 \ln s_\nu^2. \quad (3)$$

When subsequently we refer to an entanglement growth associated with repeated operations on $|\psi_{\text{MPS}}\rangle$, this implies the need to adjust the bond dimension m such that $|\psi_{\text{MPS}}\rangle$ still faithfully represents a physical state. If entanglement in the physical state becomes too large, we have to choose m so large that computations with MPS become impractical.

Since the first suggestion for computing spectral functions within DMRG [43], the field has evolved by the important development of the correction vector method [44,45]. The subsequent understanding of the connection between DMRG and MPS [27] opened the door to many further approaches to computing spectral and Green's functions, in particular, time evolution and subsequent Fourier transform [46,47], an improved Lanczos algorithm [48], and the Chebyshev recursion [29,30,49]. All of these are formulated for the calculation of spectral functions at $T = 0$, as considered in the present paper, and came at much cheaper computational cost than the correction vector method [29,30]. We note that for $T > 0$, there are

perspectives for even more powerful algorithms: it was recently demonstrated that the numerically exact spectral function of a molecule consisting of several hundreds of interacting spins could be computed [50].

These developments (see Appendix C for more details) make MPS-based solvers an attractive possibility for dynamical mean-field theory. However, the growth of entanglement arising in all calculations of the Green function has limited the system sizes that have been addressed to date. Also, in MPS computations manual adjustments, for example, choosing optimal broadening [29] or combining results of different systems sizes [48], are still common practice. In the rest of this section, we show that these problems can, to a large degree, be circumvented by computing Matsubara Green's functions using imaginary-time evolution. The imaginary-time framework naturally extends existing techniques based on real-time evolution [38,40], which have been shown to provide the currently most efficient algorithmic approach to compute real-frequency spectral functions [30].

B. Imaginary-time computation

The central objects of technical interest in this paper are the greater and the lesser correlation functions $\tilde{G}^{\gtrless}$, which we define for imaginary time τ:

$$\tilde{G}^{\gtrless}(\tau) = \langle\psi_0^{\gtrless}|e^{\mp(H-E_0)\tau}|\psi_0^{\gtrless}\rangle, \quad (4a)$$

$$\tilde{G}^{\gtrless}(it) = \langle\psi_0^{\gtrless}|e^{\mp i(H-E_0)t}|\psi_0^{\gtrless}\rangle. \quad (4b)$$

In the second line, we evaluate $\tilde{G}^{\gtrless}(\tau)|_{\tau=it}$ and by that obtain a correlation function for real time t, which will be useful later on. The functions $\tilde{G}^{\gtrless}$ carry spin and orbital indices associated with the spin and orbital indices of the single-particle (hole) excitation $|\psi_0^{\gtrless}\rangle$, but these indices are not explicitly written here. We discuss the relationship of $\tilde{G}^{\gtrless}$ to the physical Green's functions (which we denote by G) below.

While it is not essential in principle, we evaluate Eq. (4) using a Krylov algorithm [51], which represents the time-evolution operator in a local Krylov space and is able to treat Hamiltonians with long-ranged interactions. Before performing a time-evolution computation, one has to compute the initial state $|\psi_0^{\gtrless}\rangle$ using a MPS optimization of the ground state. As impurity models come with open boundary conditions, this is well suited for DMRG. We discuss this optimization for typical DMFT Hamiltonians in Appendix A 1.

Figure 1 presents representative results based on parameters obtained from a two-site DMFT solution of the Hubbard model. Figure 1(a) shows the time evolution of $\tilde{G}^{\gtrless}(\tau)$ out to times as long as 350 times the basic time scale (inverse half-bandwidth D) of the model, which suffices to
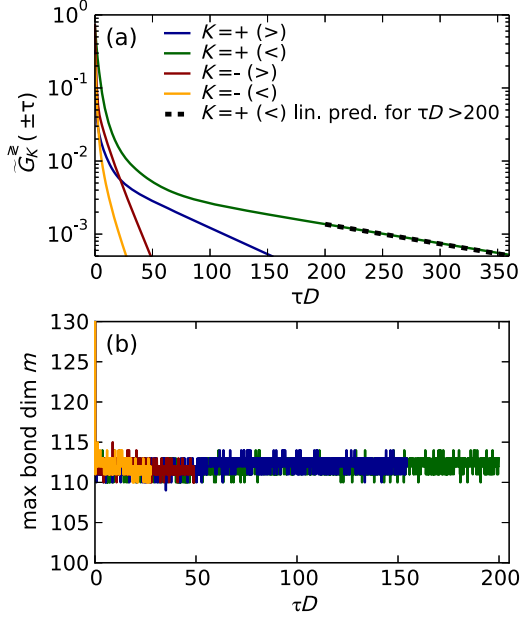
FIG. 1. (a) Imaginary-time correlation functions $\tilde{G}^{\gtrless}(\tau)$ defined in Eq. (4a) for an impurity model arising in the context of the two-site dynamical cluster approximation to the single-band Hubbard model on the square lattice with next-nearest neighbor hopping $t'/t = 0.3$, half-bandwidth $D = 4t$, interaction $U = 2.5D$, and band filling $n = 0.96$ in the paramagnetic phase. See Ref. [52] for definition of the model and the meaning of the orbital (patch) quantum number $K = \pm$. The dashed line is obtained using linear prediction for times $\tau D \geq 200$. (b) Maximal bond dimension m of time-evolved states. The MPS computation uses a Hamiltonian representation of the discrete (approximate) impurity model with $L_c = 2$ correlated sites and $L_b = 14$ bath sites. The hybridization function of the impurity model Λ^{discr} is fitted using Eq. (13) for $\beta_{\text{eff}} = 315/D$ and $\alpha = 0$. For the ground state optimization, we enforce a maximal bond dimension of $m = 300$. The Krylov time evolution uses a time step of $\Delta t = 0.1/D$ and allows for a maximal global truncation error of 10^{-4} at each time step, adjusting bond dimensions automatically. This leads to an immediate decay of m at $\tau \simeq 0$ from $m = 300$ down to $m \simeq 110$, as seen in (b). We use the global SU(2) symmetry of the Hamiltonian to reach these low values of the bond dimension.

converge $\tilde{G}^{\gtrless}(\tau)$ to a precision of 5×10^{-4}. Figure 1(b) demonstrates the key advantage that makes this computation possible: the lack of growth of maximal bond dimensions m with time of the associated imaginary-time evolved states $|\psi^{\gtrless}(\tau)\rangle = e^{-(H-E_0)\tau}|\psi_0^{\gtrless}\rangle$. The imaginary-time evolution operator does not create entanglement as it projects on the lowly entangled ground state.

Figure 1(a) reveals additional information about the nature and rate of convergence of $\tilde{G}^{\gtrless}(\tau)$. In the insulating phase, H has a gap and $\tilde{G}^{\gtrless}(\tau)$ decays exponentially irrespective of whether one considers a finite system or the thermodynamic limit. In the metallic phase, $\tilde{G}^{\gtrless}(\tau)$ decays algebraically in the thermodynamic limit. For a

finite system though, there always remains a small gap, and even though the decay resembles an algebraic decay for short times, it always becomes exponential at long times. The exponential decay can be exploited to speed up computations considerably by a simple technique known as linear prediction [30,47,53,54]. This technique is an efficient formulation of the fitting problem for the ansatz function $f(\tau) = \sum_n \alpha_n e^{\beta_n \tau}$, $\alpha_n, \beta_n \in \mathbb{C}$, $\tau \in \mathbb{R}$, which can then be used to reliably extrapolate functions with an exponentially decaying envelope. This is illustrated by the dashed black line in Fig. 1(a), which is fitted to match $\tilde{G}^{\gtrless}(\tau)$ for $\tau D \in [150, 200]$ and is then extrapolated for higher times. The solid green line, by contrast, is the result of the MPS computation. Agreement can be seen to be perfect.

C. Physical Green's functions

Of particular interest in the rest of this paper are the imaginary-time Green functions $G^{\text{mat}}(\tau)$ defined via

$$G^{\text{mat}}(\tau) = -\theta(\tau)\tilde{G}^{>}(\tau) + \theta(-\tau)\tilde{G}^{<}(\tau), \qquad (5)$$

whose Fourier transform gives the Matsubara Green function [we distinguish the Fourier transform $G^{\text{mat}}(i\omega_n)$ of $G^{\text{mat}}(\tau)$ only by its argument to keep the notation simple]

$$G^{\text{mat}}(i\omega_n) = \int_{-\infty}^{\infty} d\tau e^{i\omega_n \tau} G^{\text{mat}}(\tau), \qquad (6)$$

at zero temperature, where $\omega_n = (2n+1)\pi/\beta$ and $\beta \to \infty$. We are also interested in the retarded real-time Green function,

$$G^{\text{ret}}(t) = -i\theta(t)[\tilde{G}^{>}(it) + \tilde{G}^{<}(it)], \qquad (7)$$

from which the retarded frequency-dependent Green function is obtained as [again, we distinguish the Fourier transform $G^{\text{ret}}(\omega)$ of $G^{\text{ret}}(t)$ only by its argument]

$$G^{\text{ret}}(\omega) = \int_{-\infty}^{\infty} dt e^{i(\omega+i0^+)t} G^{\text{ret}}(t). \qquad (8)$$

This allows one to obtain the spectral function as $A(\omega) = -(1/\pi)\text{Im} G^{\text{ret}}(\omega)$.

In numerical practice, we evaluate the Fourier transforms leading to Eqs. (6) and (8) approximately as

$$G^{\text{mat}}(i\omega_n) = -\int_0^{\tau_{\max}} d\tau \tilde{G}^{>}(\tau)e^{i\omega_n t} + \int_{-\tau_{\max}}^0 d\tau \tilde{G}^{<}(\tau)e^{i\omega_n t},$$

$$G^{\text{ret}}(\omega) = -i\int_0^{t_{\max}} dt[\tilde{G}^{>}(it) + \tilde{G}^{<}(it)]e^{i\omega t}, \qquad (9)$$

with cutoff times $\tau_{\max}$ and $t_{\max}$. This approximation is controlled only if we are able to reach long enough times

$\tau_{\max}$ and $t_{\max}$, such that $\tilde{G}^{\gtrless}(\tau)$ and $\tilde{G}^{\gtrless}(it)$ have converged to zero to any desired accuracy.

In contrast to a computation on the imaginary axis, reaching arbitrarily long times $t_{\max}$ on the real axis is prohibited by a logarithmic growth of entanglement, which comes with a power-law growth of bond dimensions. In addition, finite-size effects are a severe source of errors because the long-time behavior is determined by the bath size. For a numerically exact computation, one has to choose the system large enough to observe exponential "pseudoconvergence" of $\tilde{G}^{\gtrless}(it)$ to zero [30]. This means that—after an initial regime—the envelope of $\tilde{G}^{\gtrless}(it)$ decays exponentially up to the time at which finite-size effects begin to be resolved. In the context of the present paper, we deal with small system sizes and will never observe pseudoconvergence. In particular, there is no exponential pseudoconvergence, so that linear prediction cannot be employed [30]. Therefore, when computing the real-frequency spectral function after converging the DMFT loop, one has to use the further approximation of *damping* the finite-size effects that emerge at long times by computing, instead of $G^{\mathrm{ret}}(\omega)$ in Eq. (9),

$$G_\eta^{\mathrm{ret}}(\omega) = -i \int_0^\infty dt [\tilde{G}^>(it) + \tilde{G}^<(it)] e^{i\omega t} e^{-\eta^2 t^2/2}, \quad (10)$$

which yields the *broadened* spectral function $A_\eta(\omega) = -(1/\pi)\mathrm{Im}G_\eta^{\mathrm{ret}}(\omega) = (1/\sqrt{2\pi}\eta) \int d\omega' A(\omega') e^{-(\omega-\omega')^2/2\eta^2}$. Instead of a Gaussian damping and broadening, one could also use an exponential damping leading to Lorentzian broadening, which damps out the original time-evolution information more strongly, though.

Before presenting detailed benchmark results for the solution of DMFT using imaginary-time evolution of MPS, let us clarify the price we have to pay for profiting from the great advantage of not facing entanglement growth. We do this by comparing the imaginary-time approach (ITMPS) to approaches that solve the DMFT loop on the real axis.

III. COMPARISON OF IMAGINARY-AXIS WITH REAL-AXIS COMPUTATIONS

The *self-consistency* equation in DMFT relates an impurity model specified by a hybridization function and a self-energy to a lattice model specified by a lattice Hamiltonian and the same self-energy. We discuss the issues using the example of the dynamical cluster approximation to the single-band Hubbard model:

$$G_K^{\mathrm{latt}}(z) = \frac{N_c}{N} \sum_{k \in \mathcal{P}_K} \frac{1}{z + \mu - \varepsilon_k - \Sigma_K(z)},$$

$$\overset{!}{=} [z + \mu - \varepsilon_K - \Sigma_K(z) - \Lambda_K(z)]^{-1}$$

$$= G_K^{\mathrm{imp}}(z). \quad (11)$$

Here, ε_k denotes the single-particle dispersion of the lattice and μ is the chemical potential. In the dynamical cluster approximation, the Brillouin zone, consisting in N momentum vectors k, is covered by N_c (for single band $L_c = N_c$) equal-area tiles (patches), labeled here by P_K and the self-energy $\Sigma_K(\omega)$ is taken to be piecewise constant, with $\Sigma_K(\omega)$ being a potentially different function of frequency in each tile. The impurity model is specified by the on-site energy ε_K and the hybridization function $\Lambda_K(z)$, which is to be determined using a fixed point iteration referred to as the DMFT loop. This works as follows. Make an initial guess for $\Lambda_K(z)$, then compute $\Sigma_K(z)$ using a MPS calculation of $G_K^{\mathrm{imp}}(z)$ via

$$\Sigma_K(z) = z + \mu - \varepsilon_K - \Lambda_K(z) - [G_K^{\mathrm{imp}}(z)]^{-1}, \quad (12a)$$

then update Λ_K using the first line of Eq. (11) via

$$\Lambda_K(z) = z + \mu - \varepsilon_K - \Sigma_K(z) - [G_K^{\mathrm{latt}}(z)]^{-1}, \quad (12b)$$

and repeat this procedure until convergence.

We discuss two aspects of the comparison of real- and imaginary-frequency solutions of the DMFT self-consistency equation (11). The first has to do with the number of bath sites needed to obtain a solution of the self-consistency equation. The second is the accuracy to which the spectral functions of physical interest can be reproduced.

The DMFT self-consistency equation (11) defines the hybridization function Λ_K as a continuous function in terms of the difference between the computed self-energy and the inverse of the lattice Green function. In DMRG-type methods, the hybridization function Λ_K is approximated as the hybridization function $\Lambda_K^{\mathrm{discr}}$ (a sum of poles) of a discrete impurity model with a finite number L_b of bath sites. If the number L_b of bath sites is too small, one cannot construct a meaningful approximation on the real axis [55] and a DMFT loop cannot be converged. For this reason, DMRG-based solutions of DMFT up to now [13,31–40], all of which were real axis computations, have been performed using numbers of bath sites of at least $L_b/L_c \gtrsim 30$, and in the case of the single-band Hubbard model, even much more, $L_b/L_c \gtrsim 120$. Use of such a large number of bath sites means that with modest broadening the hybridization function can be reasonably approximated as a continuum, enabling a stable solution of Eq. (11).

By contrast, formulating the problem on the imaginary axis (as is typically done in standard ED solvers where the number of bath sites is strictly limited) automatically smoothens the hybridization function $\Lambda_K^{\mathrm{discr}}$ and permits a stable solution. From the imaginary-axis solution, one must then determine the discrete set of bath parameters to represent $\Lambda_K^{\mathrm{discr}}$. This is typically done [9,11,56] by numerical minimization of a cost function defined as

$$\chi^2 = \frac{1}{N_{\text{fit}}} \sum_{n=1}^{N_{\text{fit}}} \omega_n^{-\alpha} |\Lambda_K(i\omega_n) - \Lambda_K^{\text{discr}}(i\omega_n)|^2. \quad (13)$$

Here, α defines a weighting function $\omega_n^{-\alpha}$. Choosing $\alpha > 0$, e.g., $\alpha = 1$, attributes more weight to smaller frequencies [11,56,57], which we find helpful when using small bath sizes $L_b/L_c < 5$. To define the frequency grid for the fit $\omega_n = (2n+1)\pi/\beta_{\text{eff}}$, one defines a fictitious inverse temperature β_{eff}, which has no physical significance. We further employ a cutoff frequency ω_c, which implies a finite number N_{fit} of fitted Matsubara frequencies.

If one tries to define an analogous cost function for the real axis, the result is useless as then $\Lambda_K^{\text{discr}}(\omega + i0^+)$ is a sum of poles, whereas the hybridization function $\Lambda_K(\omega + i0^+)$, as encountered in Eq. (11), is continuous [55]. One can overcome this problem only when using a Lindbladt formalism [58], which increases the complexity of the problem substantially.

The minimization of Eq. (13) is done using standard numerical optimization. The optimization in the initial DMFT iteration should be done using a global optimization scheme [59], and in subsequent iterations using a local optimization scheme (e.g., conjugate gradient), which takes as an initial guess for the new bath parameters the values of the previous iteration. Figure 2 shows the convergence of the fit of the hybridization function with the number of bath sites L_b/L_c. For $L_b/L_c = 7$, one already obtains errors as little as $\simeq 10^{-3}$, and for values $L_b/L_c \gtrsim 9$, the quality of the fit already stops improving. It is at this point, where we (and all ED-like techniques) face the problem of "analytic continuation" encountered in imaginary-time CTQMC methods, namely, that Green's functions on the imaginary axis encode information in a much less usable form than on the real axis.

Consider again the example of the two-site DCA for the single-band Hubbard model on the square lattice. In Ref. [39], this problem has been solved entirely on the

real axis using $L_b/L_c = 39$ bath orbitals. Here, we converge the DMFT loop on the imaginary axis and compute the spectral function in a final real-time evolution using $L_b/L_c = 3, 5, 7$ bath orbitals. We compare both solutions
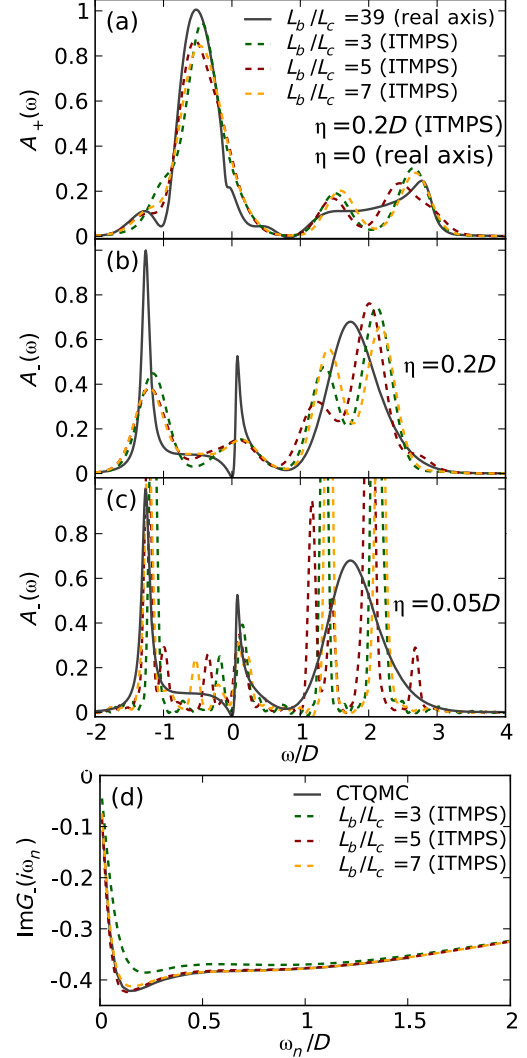
FIG. 3. Real- and imaginary-frequency Green's functions computed by converging the DMFT self-consistency equation [Eq. (11)] for the two-site dynamical cluster approximation to the single-band Hubbard model on the square lattice with next-nearest neighbor hopping $t'/t = 0.3$, half-bandwidth $D = 4t$, interaction $U = 2.5D$, and band filling $n = 0.96$ in the paramagnetic phase (as in Fig. 1). See Ref. [52] for definition of the model and the meaning of the orbital (patch) quantum number $K = \pm$. (a)–(c) Electron spectral function $A_+(\omega)$ (a) and $A_-(\omega)$ (b) obtained by converging on imaginary-frequency axis (ITMPS) using number of bath sites and different broadenings as specified in the figure, and compared to unbroadened ($\eta = 0$) real-frequency axis computation using $L_b/L_c = 39$ bath sites per correlated site of Ref. [39]. (d) Converged Matsubara Green's function for number of bath sites shown, compared to numerically exact quantum Monte Carlo result of Ref. [52], computed at $\beta = 200/D$.
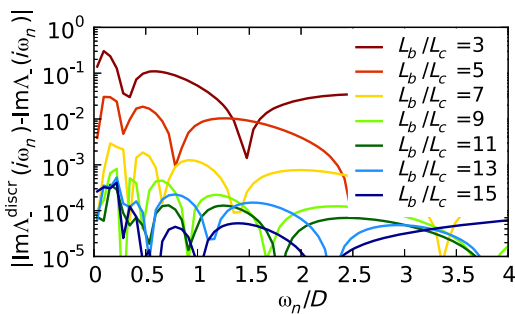

FIG. 2. Fit of the hybridization function in the two-site DCA problem studied in Figs. 1 and 3, but here for the case $U = 0$. The minimization [Eq. (13)] is done using $\alpha = 0$ and a frequency grid defined by $\beta_{\text{eff}} = 100/D$ and a cutoff frequency of $\omega_c = 6D$. Evidently, the quality of the fit does not improve any more for $L_b/L_c \gtrsim 9$.

in Fig. 3(a). Whereas for the (central) momentum patch "+" shown in Fig. 3(a), we find satisfactory agreement of the imaginary-axis with the real-axis calculation, this is not the case for the (outer) momentum patch "−" shown in Fig. 3(b), even though the corresponding imaginary-axis Green function is well reproduced; see Fig. 3(d). Evidently, in Fig. 3(b), the central peak and the pseudogap at the Fermi edge are smeared out by a broadening $\eta = 0.2D$ that hides finite-size effects to a large degree. Reducing the broadening to $\eta = 0.05D$, as shown in Fig. 3(c), again reveals the pseudogap and the central peak, but together with unphysical finite-size effects. We observe that the nature of these finite-size effects is qualitatively comparable when using different numbers of bath sites, $L_b/L_c = 3, 5, 7$. On the imaginary axis, by contrast, $L_b/L_c = 5, 7$ still improve over $L_b/L_c = 3$ and almost agree with the numerically exact QMC data for $\beta = 200/D$ of Ref. [52]; see Fig. 3(d). However, we emphasize that even with the modest number of bath sites used here, the basic features of the spectral function are reproduced (for example, the areas in given frequency ranges).

IV. THREE-BAND CALCULATIONS

A. Three-band model in single-site DMFT

We now demonstrate the power of the method by applying it to three-band problems in the single-site approximation (where comparison to existing calculations can be made) and the two-site approximation. Both have hitherto not been accessible to DMFT + DMRG computations.

We study the three-band Hubbard-Kanamori model with Hamiltonian (omitting the site index i in the following definition of $H_{\text{loc},i}$)

$$
H = \sum_{k,a,b,\sigma} \varepsilon_k^{ab} d_{k,a,\sigma}^\dagger d_{k,b,\sigma} + \sum_i H_{\text{loc},i},
$$
$$
H_{\text{loc}} = -\sum_{a,\sigma}(\mu - \Delta_a)n_{a,\sigma} + \sum_a U n_{a,\uparrow} n_{a,\downarrow}
$$
$$
+ \sum_{a>b,\sigma}[U' n_{a,\sigma} n_{b,-\sigma} + (U'-J)n_{a,\sigma} n_{b,\sigma}]
$$
$$
- \sum_{a \neq b} J(d_{a,\downarrow}^\dagger d_{b,\uparrow}^\dagger d_{b,\downarrow} d_{a,\uparrow} + d_{b,\uparrow}^\dagger d_{b,\downarrow}^\dagger d_{a,\uparrow} d_{a,\downarrow} + \text{H.c.}),
$$
$$
(14)
$$

where i labels sites in a lattice and k labels wave vectors in the first Brillouin zone, $n_{i,a,\sigma} = d_{i,a,\sigma}^\dagger d_{i,a,\sigma}$ is the density of electrons of spin σ in orbital a on site i, μ is the chemical potential, Δ_a is a level shift for orbital a, ε_k^{ab} is the band dispersion, U is the intraorbital and U' the interorbital Coulomb interaction, and J is the coefficient of the Hund coupling and pair-hopping terms. We adopt the conventional choice of parameters, $U' = U - 2J$, which follows from symmetry considerations for d orbitals in free

space and holds (at least for reasonably symmetric situations) for the t_{2g} manifold in solids [60].

We study the orbital-diagonal and orbital-degenerate case ($\Delta_a = 0$) on the Bethe lattice, i.e., the noninteracting density of states is semielliptic,

$$
A_{a,0}(\omega) = \frac{1}{\pi t}\sqrt{1 - \left(\frac{\omega}{2t}\right)^2}.
$$
$$
(15)
$$

In the single-site approximation, the impurity Hamiltonian used within DMFT is given by

$$
H = H_{\text{loc}} + H_{\text{coupl}} + H_{\text{bath}},
$$
$$
H_{\text{coupl}} = \sum_{l,a,\sigma} V_{l,a,\sigma} d_{a,\sigma}^\dagger c_{l,a,\sigma} + \text{H.c.},
$$
$$
H_{\text{bath}} = \sum_{l,a,\sigma} \varepsilon_{l,a,\sigma} c_{l,a,\sigma}^\dagger c_{l,a,\sigma},
$$
$$
(16)
$$

where $c_{l,a,\sigma}^\dagger$ creates a fermion in the bath orbital l, $V_{l,a,\sigma}$ describes the coupling of the impurity to the orbital l, and $\varepsilon_{l,a,\sigma}$ denotes the potential energy of orbital l. The hybridization function is then given by

$$
\Lambda_{a,\sigma}^{\text{discr}}(z) = \sum_{l=1}^{L_b/L_c} \frac{|V_{l,a,\sigma}|^2}{z - \varepsilon_{l,a,\sigma}}.
$$
$$
(17)
$$

Figure 4 compares the dependence of the particle density n on the chemical potential μ obtained by the MPS methods used here to those obtained by numerically exact CTQMC methods [61]. The plateaus in $n(\mu)$ are the Mott insulating regimes of the phase diagram. The agreement is very good in general, confirming the reliability of our new procedure even with only three bath sites per correlated site. This leads to an extremely cheap computation, for which a single iteration of the DMFT loop takes about 30 min on two 2.8-GHz cores (see Appendix A 2 for more details).

In Fig. 5(a), we show a more stringent test, namely, the dependence of the self-energy on Matsubara frequency, in a parameter regime where the self-energy was previously found [62] to exhibit an anomalous $\omega^{1/2}$ frequency dependence and (in some regimes) a nonzero intercept as $\omega \to 0$. These phenomena are associated with a spin-freezing transition [61,62].

Figure 5(a) shows that the low-frequency $\omega \lesssim t$ self-energy obtained using CTQMC is already accurately reproduced even for the computationally inexpensive choice of $L_b/L_c = 3$, although one observes deviations for the high-frequency behavior. The deviations at high frequency decrease as the number of bath sites is increased, although full convergence at all frequencies has not been demonstrated. Figure 5(b) shows that the deviations are linked to the impossibility of fitting the hybridization function equally well for all frequencies using only a small
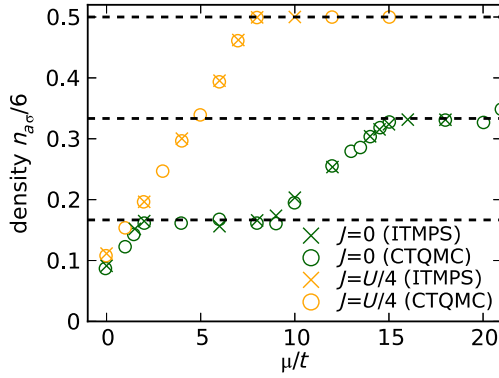
FIG. 4.   Density per orbital as function of chemical potential for three-band Hubbard-Kanamori model Eq. (14) using the semi-elliptic density of states Eq. (15) and $U = 12t$, obtained from single-site DMFT approximation evaluated using imaginary-time MPS (crosses) and CTQMC data (circles, Fig. 1 of Ref. [61], inverse temperature $\beta = 50/t$). In the DMRG computations the bath fitting is performed using $\beta_{\text{eff}} = 100/t$, $\omega_c = 6t$, and $\alpha = 1$, with three bath sites per correlated site ($L_b/L_c = 3$). The maximal matrix dimensions is $m = 300$ for the ground state calculation, exploiting the SU(2) symmetry, which leads to the high precision $\langle (H - E)^2 \rangle \simeq 10^{-14}$. For the time evolution, we compute $\tilde{G}_a^{\gtrless}(\tau)$ in Eq. (4a) in steps of $\Delta\tau = 0.1/t$ allowing for a global truncation error of 5×10^{-4} per step, up to imaginary time $\tau_{\text{max}} = 100/t$, and use linear prediction for higher times.

number of bath sites. The large deviations at high frequencies are due to the choice $\alpha = 1$ in Eq. (13), which enforces good agreement for low frequencies and allows us to successfully reproduce the metal-insulator transition (MIT) in Fig. 4. Increasing the number of bath sites to $L_b/L_c = 5$ leads to a much better approximation of the hybridization function also for high frequencies, with concomitant improvement in the self-energy [Fig. 5(a)].

B. Three-band model in two-site DCA

We now present results obtained using a two-site DCA approximation to the three-band model of the previous section. For this problem there are no low-temperature results available in the literature. The size of the problem is beyond the scope of standard ED. The truncated configuration interaction (CI) impurity solver [20] allows one to access a relatively high number of bath sites but is limited in the number of correlated sites: for example, in Ref. [24], a problem with $L_c = 3$ and $L_b = 30$ was computed, and in Ref. [56], one with $L_c = 4$ and $L_b = 20$. The three-band two-site DCA though has $L_c = 6$ correlated sites and it remains to be seen whether this is in reach for the CI solver. The problem is also challenging for standard CTQMC. Recent technical improvements on mitigating the sign problem [63] enabled Ref. [64] to treat this model at the temperature of $T = 0.025D$, with D the half-bandwidth, although large computational resources were required. As the authors noted, this temperature is high relative to the
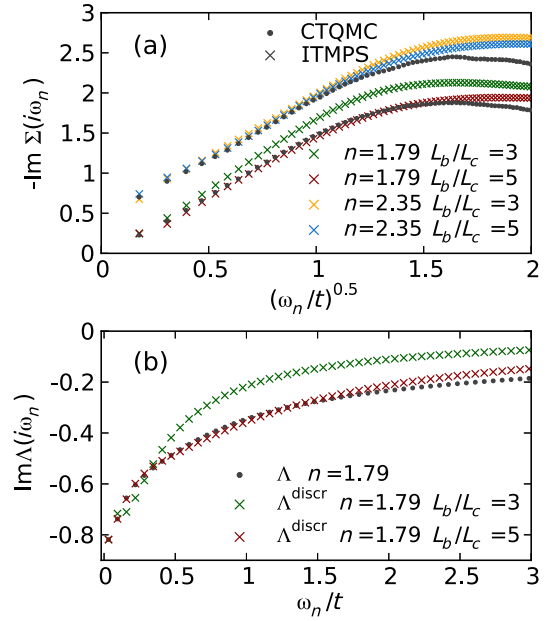

FIG. 5.   (a) Imaginary part of Matsubara axis self-energy Σ and (b) imaginary part of hybridization function Λ for densities shown obtained from converged ITMPS solution of single-site DMFT for three-band Hubbard-Kanamori model [Eq. (16)] for $U = 8t$ and $J = U/6$. Crosses represent ITMPS data and black circles depict CTQMC data from Fig. 3 of Ref. [62], computed at inverse temperature $\beta = 100/t$. We choose all parameters as described in the caption of Fig. 4; in particular, for the bath fitting [Eq. (13)], we use $\beta_{\text{eff}} = 100/t$, $\omega_c = 6t$, and $\alpha = 1$. Choosing $\alpha = 1$ enforces agreement for low frequencies at the price of disagreement at high frequencies, which is observed in both (a) and (b). In (b), Λ denotes the hybridization function that is fitted with the hybridization function Λ^{discr} of the discrete impurity model.

effective Fermi energy. In a study of a simpler two-band two-site model the authors reached $T = 0.0125D$, but this is not yet low enough to resolve a Fermi liquid phase (if one exists for these parameters) [63].

We study the model on the two-dimensional square lattice, i.e., using $\varepsilon_k^{ab} = -2t(\cos k_x + \cos k_y)\delta^{ab}$. We use the momentum patching of Ref. [52]; this definition is also used in the single-band computations of Figs. 1 and 3. We note that this model is not directly relevant to layered materials where the t_{2g} orbitals are relevant, because in the physical situation the two dimensionality will break the threefold orbital degeneracy. However the system is well defined as a theoretical model and is useful to demonstrate the power of our methods.

As is the case for the CI method, the DMRG method we use here is easily able to treat a large number of bath sites if the number of correlated sites is small: for $L_c = 1$, DMRG has already often be proven to treat $L_b > 120$ bath sites, and for $L_c = 2$, $L_b > 80$ is easily accessible [39,40]. However, for more correlated sites, the number of bath

sites that can be added at given computational cost decreases. For $L_c = 6$, we use $L_b = 18$, i.e., $L_b/L_c = 3$, which we showed to be sufficient to produce reliable results (previous sections). The solution does not require overly large computation resources (computation time of several hours per DMFT iteration on two cores).

We test the two-site calculation by converging the DMFT loop for the three-band Hubbard model Eq. (16) with U' and $J = 0$ and comparing the results with a corresponding two-site single-band DCA. Perfect agreement is obtained (not shown). Nonzero values of U' and J create additional entanglement and make computations more costly. It is then a decisive question whether a real-space or a momentum-space representation of the impurity cluster is less entangled. We discuss this in Appendix B, finding that for the single-band Hubbard interaction both representations yield similar entanglement, whereas for the Hubbard-Kanamori interaction, the real-space representation is much less entangled. Computational cost is therefore tremendously reduced by using the real-space representation, which comes with an off-diagonal hybridization function. This is the opposite behavior as observed for the QMC method, where the off-diagonal hybridization function creates a severe sign problem. We further note that in the real-space representation, strong interactions yield a less and less entangled impurity problem, as electrons become more and more localized.

We now present results for the more physically relevant case, $U' = U - 2J$ with $J = U/4$. For these parameters, at half filling the critical interaction for the MIT in the single-site DMFT approximation is $U_c \simeq 1.3D$ [65]. Figure 6(a) shows that our results are consistent with this estimate: the dashed lines depict the single-site (1s) results, showing a metallic solution (spectral function nonzero at $\omega = 0$) for $U = D$, and an insulating solution (spectral function zero at $\omega = 0$) for $U = 2D$. In the two-site (2s) DCA (solid lines), by contrast, the critical value U_c for the MIT is lowered. Even at $U = D$, the $\omega = 0$ spectral function is zero [the small nonzero value in Fig. 6(a) is an effect of broadening, as seen in Fig. 6(b)]. The different nature of the metallic and insulating solutions is also visible on the imaginary axis in the different nature of the decay of the imaginary-time Green function. This is plotted in Fig. 6(c) for $U = D$; clearly, a power-law decay is observed for the metallic solution obtained in the single-site DMFT, whereas an exponential decay is obtained for the insulating solution obtained within the two-site DCA.

The much higher value of the critical interaction strength in the single-site approximation is due to the complete neglect of intersite correlations (here, mainly antiferromagnetic). These are known to have a crucial effect on the critical interaction strength, and the two-site approximation accounts for this. Furthermore, for example, Ref. [66] shows that the critical interaction strength of the two-site approximation is much closer to those of the
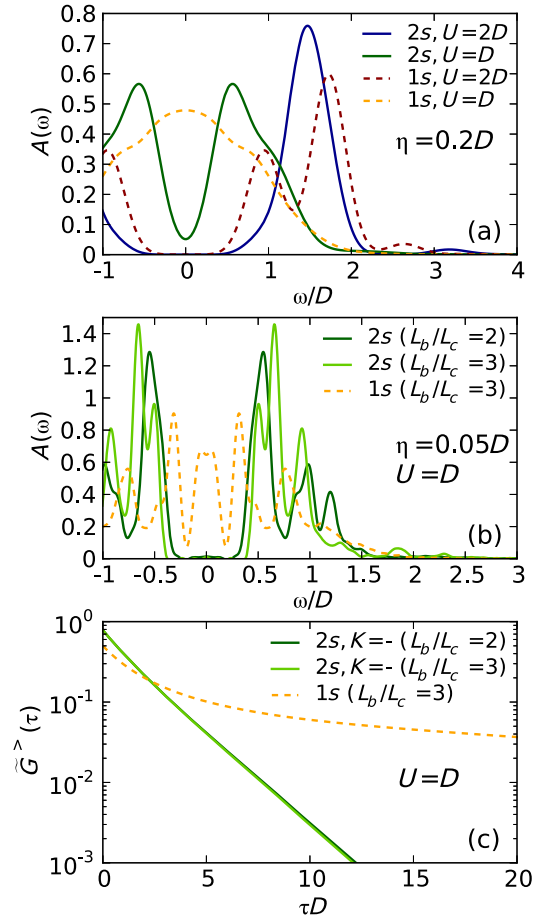
FIG. 6. Comparison of results obtained using imaginary-time MPS with $L_b/L_c = 3$ for single-site (1s) and two-site (2s) DMFT approximations to the Hubbard-Kanamori model [Eq. (14)] on the two-dimensional square lattice with half-bandwidth $D = 4t$, $\varepsilon_k^{ab} = -2t(\cos k_x + \cos k_y)\delta^{ab}$, $U' = U - 2J$, $J = U/4$, and $n = 3$ ($\mu = 5U/2 - 5J$), that is, in the particle-hole symmetric case. (a) Spectral functions for broadening $\eta = 0.2D$; (b) broadening $\eta = 0.05D$. In (c), we show the imaginary-time evolution of $\tilde{G}^>(\tau)$ as defined in Eq. (4a), confirming by comparison to a calculation for a smaller bath $L_b/L_c = 2$ that this quantity has been converged with respect to the bath size. The maximal bond dimension for the ground state search is $m = 1000$.

four- and eight-site approximations than to the single-site approximation.

V. CONCLUSION

This paper introduces an imaginary-time MPS (ITMPS) solver for DMFT and shows that it can treat complex models, not easily accessible with other methods, at modest computational cost. This development establishes DMRG as a flexible low-cost impurity solver for realistic problems, such as those encountered in the study of strongly correlated materials. The crucial advance stems from the fact that imaginary-time evolution does not create entanglement, and

hence allows one to compute Green's functions numerically exactly, provided a ground state calculation is feasible. We note that this reduces the computational cost to the same level as necessary for the density matrix embedding theory [20], although the latter requires a smaller bath due to a different self-consistency condition.

The method can be improved in many ways. In particular, different representations of the impurity problem exhibit different degrees of entanglement, so optimizing the representation of the impurity problem is a promising route. Ideas from ED approaches for constructing relevant subspaces [21–24] of the Hilbert space may lead to further improvements. Such techniques have been successfully combined with MPS [67]. Another route to reduce computational effort and by that reach even more complex models could consist in performing computations for the reduced dynamics of the impurity [68]. Extending the method towards nonzero temperature requires the calculation of Green's functions at nonzero temperature, for which numerous MPS-based techniques have already been developed. At very low temperatures one could combine a strategy based on Lanczos algorithms [10] with its MPS implementation [43,48] or use minimally entangled typical thermal states [69]. The most frequently used method is purification [70,71], whose usefulness for the calculation of spectral functions, combined with linear prediction, has been amply demonstrated [54,72–74]. At very high temperatures, an extremely cheap algorithm for computing Green's functions has been presented in Ref. [50]. Finally, we note that using MPS as an impurity solver makes using entanglement as a quantity for understanding the properties of the embedded impurity cluster very easily accessible. Proposals in this direction have been made for cellular DMFT [75] and for impurity models generally [76].

APPENDIX A: FURTHER TECHNICAL DETAILS

1. Ground state optimization

The main challenge in solving the ground state problem of a typical cluster-bath Hamiltonian as encountered in DMFT stems from the fact that DMRG is a variational procedure that is initialized with a random state, which is

then optimized locally. A local optimization procedure is slow when optimizing a global energy landscape. In addition, the local optimization is prone to getting stuck in local minima, if no "perturbation steps that mix symmetry sectors" are applied. The standard perturbation techniques for single-site DMRG [77–79] rely on "perturbation terms" that are produced by contracting the Hamiltonian with the MPS. If the Hamiltonian itself does not contain terms that mix the symmetry sector, these methods do not work.

A typical cluster-bath Hamiltonian has both features, a global variation of the potential energy and parts that are not connected with symmetry-mixing terms, such as in the three-band Hubbard-Kanamori model at $J = 0$. This situation is sketched in Fig. 7.

In Ref. [39], the models under study allowed one to solve this problem using the noninteracting solution. For the general models studied in the present paper, an unbiased numerical technique has to be employed. What we do in practice is to first find the ground state of a system with additional symmetry-mixing couplings (denoted as red solid lines in Fig. 7) that are then adiabatically switched off. In practice, we sweep 5–10 times with additional hoppings of 10% magnitude of the physical hoppings, and another 5–10 times with additional hoppings of 1% magnitude. After these preliminary sweeps, the quantum number (e.g., particle number) distribution has globally converged, and we can continue with converging the ground state of the exact Hamiltonian.

2. Convergence of DMFT iteration

The calculations for the three-band single-site DMFT in Sec. IV A are only trivially parallelized using one core to compute the imaginary time evolution of each the particle ($>$) and the hole ($<$) Green functions $\tilde{G}^{\gtrless}(\tau)$.

In Fig. 8, we show the converged DMFT loop for the single-site DMFT for the three-band Hubbard-Kanamori model as studied in Fig. 5. Figure 8(a) shows the convergence of the Matsubara Green function down to a precision of 10^{-3}. Figures 8(b) and 8(c) show the convergence of the density and of the ground state energy per particle, respectively. Figure 8(d) shows the
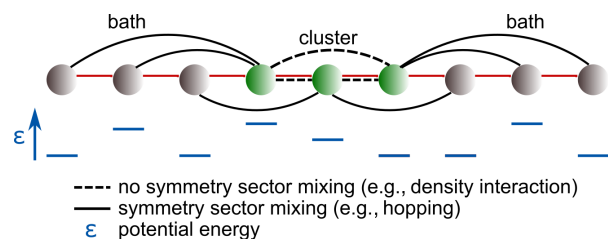

FIG. 7. Sketch of a typical cluster-bath Hamiltonian ($L_c = 3$, $L_b = 6$) when it is mapped to a one-dimensional chain. Dashed lines depict couplings that do not mix symmetry sectors, and solid lines depict couplings that mix symmetry sectors.
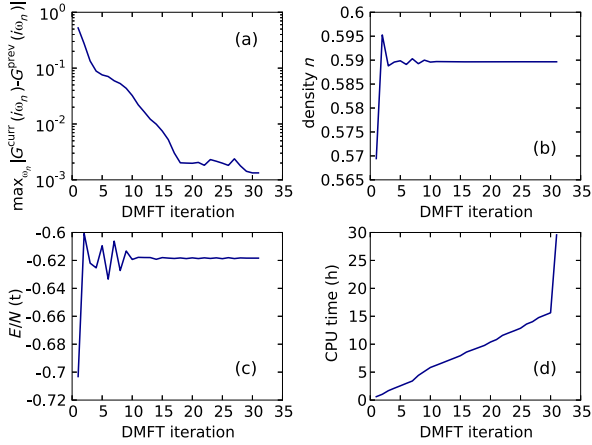
FIG. 8. Single-site DMFT for three-band Hubbard-Kanamori model as studied in Fig. 5. Here for the case $n = 1.77$ ($\mu = 5.0$) and $L_b/L_c = 3$. To obtain the solution for $n = 1.79$ as shown in Fig. 5, we choose $\mu = 5.1$ and start from the $n = 1.77$ solution. (a) Convergence of Matsubara Green's function in the DMFT loop, starting from the noninteracting solution. (b) Convergence of the density in the DMFT loop. (c) Convergence of the ground state energy per particle in the DMFT loop. (d) Computation time. An iteration on the Matsubara axis takes about 30 min. The final real-axis computation (iteration 31) is considerably more expensive, but can still be optimized.

computation time. An iteration on the Matsubara axis takes about 30 min. The final real-axis computation (iteration 31) is considerably more expensive, but can still be optimized.

APPENDIX B: LEAST-ENTANGLED REPRESENTATION AND OFF-DIAGONAL HYBRIDIZATION FUNCTIONS

1. Geometry and general considerations

In Ref. [40], some of us showed that the star geometry of the impurity problem can have substantially lower entanglement than its chain geometry. In the star geometry, DMRG profits from the small entanglement of the almost occupied states with low potential energy with the almost unoccupied states with high potential energy. A high weight for the superposition of a low- with a high-energy state is physically irrelevant. In the star geometry, DMRG is able to eliminate these superpositions as potential energy is separated locally, i.e., in the same basis in which DMRG optimizes the reduced density matrix in order to discard irrelevant contributions. In principle, as mentioned in Appendix C, ideas from basis-selective approaches in exact diagonalization are a different method to account for the fact that many states in the Hilbert space have a negligible weight for the computation of the Green function and only few physically relevant states occupy a small fraction of the Hilbert space. Among these are the truncated configuration interaction [20,23,24,56], the basis-selective ED [21], or

the coupled cluster methods in quantum chemistry. As these methods can be combined with DMRG [67], they might be a further route to construct efficient representations of the impurity-cluster problem.

In the present paper, the question of the least entangled representation of the impurity problem is restricted to the question of which basis to choose in a DCA calculation. This is of high relevance also in another context: In the real-space representation, the hybridization function becomes off-diagonal. For the CTQMC method, this generates a sign problem. In our approach, this does not affect computational cost much in the single-band Hubbard model. It even leads to a tremendous reduction of computational cost for the three-band Hubbard-Kanamori interaction.

2. DCA in momentum or real space

The complexity of the interaction determines whether the real- or the momentum-space representation of the cluster-bath Hamiltonian is less entangled. In real space, the interaction has a simple form, but the hybridization function has off-diagonal contributions, which result in additional couplings of cluster and bath sites. In momentum space, the hybridization function is diagonal but the interaction becomes off diagonal. The additional couplings induced by that depend on the complexity of the interaction.

Let us be more concrete. For the two-site case, the discrete Fourier transform yields the even and odd superposition of the real-space cluster.

$$\tilde{d}_1^\dagger = \frac{1}{\sqrt{2}}(d_1^\dagger + d_2^\dagger), \tag{B1}$$

$$\tilde{d}_2^\dagger = \frac{1}{\sqrt{2}}(d_1^\dagger - d_2^\dagger), \tag{B2}$$

where the index of $\tilde{d}_K^\dagger$ labels momentum patches K and the index of $d_i^\dagger$ labels real-space cluster sites i. There might be further indices labeling spin or orbital.

In real space, the hybridization function has the form

$$\Lambda_{ij}(z) = \sum_{l=1}^{L_b} \frac{V_{il}^* V_{jl}}{z - \varepsilon_l}, \tag{B3}$$

where the symmetry of the real-space cluster imposes $\Lambda_{ij}(z) = \Lambda_{ji}(z)$. In momentum space, the hybridization function is diagonal,

$$\tilde{\Lambda}_K(z) = \sum_{l=l_K=1}^{L_b'} \frac{\tilde{V}_{Kl}^* \tilde{V}_{Kl}}{z - \tilde{\varepsilon}_{Kl}}, \tag{B4}$$

and symmetry is reflected in the reduced number of bath sites per patch, $L_b' = L_b/L_c$, where $L_c = 2$ is the number of momentum patches.

We choose to use the momentum representation for the bath discretization, as was done for the real axis in Ref. [39]. While on the real-frequency axis this is the only viable option, the bath fitting on the imaginary-frequency axis via Eq. (13) is possible also for the off-diagonal real-space case. In real space, e.g., particle-hole symmetry can be easily imposed in the fitting procedure, while this is not possible in momentum space.

Given the parameters of the momentum-space representation obtained by performing a bath fit via Eq. (13), we define the parameters of the equivalent real-space representation as follows: In momentum space, bath parameters are indexed by $l_K = 1, \ldots, L_b'$, $L_b' = L_b/L_c$, and in real space, bath parameters are indexed by $l = 1, \ldots, L_b$, then

$$\varepsilon_l = \tilde{\varepsilon}_{1,l_1=l}, \quad \text{for } l = 1, \ldots, L_b',$$
$$\varepsilon_l = \tilde{\varepsilon}_{2,l_2=l-L_b'}, \quad \text{for } l = L_b'+1, \ldots, L_b,$$
$$V_{1l} = V_{2l} = \frac{1}{\sqrt{2}} \tilde{V}_{1,l_1=l}, \quad \text{for } l = 1, \ldots, L_b',$$
$$V_{1l} = -V_{2l} = \frac{1}{\sqrt{2}} \tilde{V}_{2,l_2=l-L_b'} \quad \text{for } l = L_b'+1, \ldots, L_b. \quad \text{(B5)}$$

Whereas the momentum-space Hamiltonian has L_b nonzero couplings V_{Kl_K}, the real-space Hamiltonian has $L_c \times L_b$ couplings V_{il}. On the other hand, the interaction part generates $L_c \times (L_c - 1)$ additional nonlocal couplings in the momentum-space representation as compared to the real-space Hamiltonian.

From this one could naively expect that the real-space representation is less entangled if $L_c \times (L_c - 1) > L_c \times L_b$. Numerical experiments show that the real-space representation is much more favorable than this estimate. For a single-band Hubbard model, we find about the same entanglement in the real-space and the momentum-space representation, with slight advantages for momentum space. In the three-band Hubbard-Kanamori model, the real-space representation is considerably less entangled and leads to a tremendous reduction of computational cost. In particular, we are not able to obtain the results of Fig. 6 in the momentum-space representation when using $L_b/L_c = 3$, only for $L_b/L_c = 2$ but then at much higher computational cost.

APPENDIX C: GREEN'S FUNCTIONS FROM MATRIX PRODUCT STATES

Even though the following discussion is not *needed* to set up the imaginary-time MPS impurity solver, it describes the context of the method.

A computation of $A(\omega) = \langle \psi_0 | \delta(\omega - (H - E_0)) | \psi_0 \rangle$ via a computation of all eigenstates of H is extremely redundant as only a tiny neighborhood $\mathcal{N} = \{|\psi\rangle | \langle \psi | H | \psi_0 \rangle \neq 0\}$ of a the single-particle excitation $|\psi_0\rangle$ contributes in the sum (inserting identities $\sum_n |E_n\rangle \langle E_n|$) in $A(\omega)$. In ED, this

is exploited by systematically constructing the subspace $\mathcal{N}$ by spanning it using particle-hole excitations [20,21], which might also be a viable route for further developments within DMRG [67]. In DMRG, one needs to make a statement about the entanglement of the states in the subspace $\mathcal{N}$: one might note that these are, in general, more strongly entangled than the single-particle excitation $|\psi_0\rangle$, but should still be much less entangled than the rest of the Hilbert space. This is illustrated in Fig. 9.

In Ref. [30], some of us argued that expanding the spectral function in a family of orthogonal functions is a natural way to construct a basis for $\mathcal{N}$, starting from the lowly entangled $|\psi_0\rangle$ and successively increasing entanglement of states and thereby computational complexity in a sequence of basis states $|\psi_n\rangle$. Reference [30] discussed the expansion of $A(\omega)$ in Chebyshev polynomials $T_n(\omega/a) = \arccos[n \cos(\omega/a)]$, which are orthogonal with respect to an inner product weighted by $w(x) = \sqrt{1 - x^2}$ [80], and in the plane waves $\exp[i\omega(n/a)]$ [orthogonal with weight function $w(x) = 1$], where the energy a is chosen larger than the support of $A(\omega)$. The associated generated sequences of basis states are then

$$|\psi_n^{\text{Che}}\rangle = 2\left(\frac{H - E_0}{a} + b\right)|\psi_{n-1}^{\text{Che}}\rangle - |\psi_{n-2}^{\text{Che}}\rangle, \quad b \in [-1, 1],$$
$$|\psi_n^{\text{time}}\rangle = \exp\left[-i(H - E_0)\frac{n}{a}\right]|\psi_0\rangle, \quad \text{(C1)}$$

and have different entanglement properties. The states $|\psi_n^{\text{time}}\rangle$ associated with time evolution are in general less entangled than the states $|\psi_n^{\text{Che}}\rangle$ associated with the Chebyshev recursion [30]. This is due to the observation that error accumulation in the Chebyshev recursion is worse conditioned than in time propagation [30], which necessitates keeping the error in a single step of the Chebyshev recursion much smaller than in the equivalent
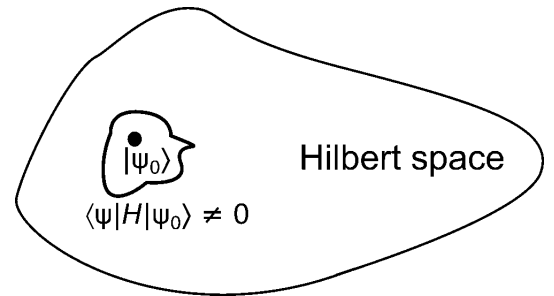
FIG. 9. Single-particle excitation $|\psi_0\rangle$ of the ground state $|E_0\rangle$ and the subspace $\mathcal{N} = \{|\psi\rangle | \langle \psi | H | \psi_0 \rangle \neq 0\}$ of the Hilbert space that is relevant for the computation of a single-particle spectral function of the form $\langle \psi_0 | \delta(\omega - H) | \psi_0 \rangle$. The single-particle excitation is very lowly entangled, the subspace is more strongly entangled, but still in general more lowly entangled than the rest of the Hilbert space.

time-evolution step, which in turn requires the use of higher bond dimensions in the Chebyshev recursion making it less efficient. In addition to the statements of Ref. [30], we note here that the sequence produced by the Lanczos algorithm,

$$|\psi_n^{\text{Lan}}\rangle = H - \alpha_n|\psi_{n-1}^{\text{Lan}}\rangle - |\psi_{n-2}^{\text{Lan}}\rangle, \qquad \alpha_n, \qquad \beta_n \in \mathbb{R}, \quad (\text{C2})$$

can be associated with an expansion of the spectral function in polynomials that are orthogonal with respect to an inner product weighted by $w(x) = A(x)$ [81]. This is very efficient but numerically unstable.

In contrast to the previous methods, which generate an increasingly complex basis when determining the spectral function to a higher and higher precision, correction-vector DMRG aims to optimize a state in frequency space, which *a priori* contains contributions that have undergone an infinitely long time evolution. As time evolution creates entanglement, these states are much too strongly entangled for an efficient treatment. They are "far away" from the controlled, lowly entangled single-particle excitation $|\psi_0\rangle$. In order to still perform a meaningful computation in frequency space, one introduces a so-called (Lorentzian) broadening parameter η that damps out contributions from an infinite time evolution. One then does not obtain the exact spectral function but a broadened version as in Eq. (10). The broadening parameter has to be guessed *a priori*: If it is chosen too small, high entanglement prevents convergence of the calculation. If it is chosen too large, one will be far from the exact version of the spectral function. In the expansion methods discussed above, by contrast, one can stop the computation simply when it becomes too costly. If one has not recovered the exact $A(\omega)$ at this point, a broadened version can be systematically constructed with an *a posteriori* determined η as in Eq. (10).

[1] W. Metzner and D. Vollhardt, *Correlated Lattice Fermions in $d = \infty$ Dimensions*, Phys. Rev. Lett. **62,** 324 (1989).

[2] A. Georges and G. Kotliar, *Hubbard Model in Infinite Dimensions*, Phys. Rev. B **45,** 6479 (1992).

[3] A. Georges, G. Kotliar, W. Krauth, and M. J. Rozenberg, *Dynamical Mean-Field Theory of Strongly Correlated Fermion Systems and the Limit of Infinite Dimensions*, Rev. Mod. Phys. **68,** 13 (1996).

[4] T. Maier, M. Jarrell, T. Pruschke, and M. Hettler, *Quantum Cluster Theories*, Rev. Mod. Phys. **77,** 1027 (2005).

[5] G. Kotliar, S. Savrasov, K. Haule, V. Oudovenko, O. Parcollet, and C. Marianetti, *Electronic Structure Calculations with Dynamical Mean-Field Theory*, Rev. Mod. Phys. **78,** 865 (2006).

[6] A. N. Rubtsov, V. V. Savkin, and A. I. Lichtenstein, *Continuous-Time Quantum Monte Carlo Method for Fermions*, Phys. Rev. B **72,** 035122 (2005).

[7] P. Werner, A. Comanac, L. de Medici, M. Troyer, and A. J. Millis, *A Continuous-Time Solver for Quantum Impurity Models*, Phys. Rev. Lett. **97,** 076405 (2006).

[8] E. Gull, A. J. Millis, A. I. Lichtenstein, A. N. Rubtsov, M. Troyer, and P. Werner, *Continuous-Time Monte Carlo Methods for Quantum Impurity Models*, Rev. Mod. Phys. **83,** 349 (2011).

[9] M. Caffarel and W. Krauth, *Exact Diagonalization Approach to Correlated Fermions in Infinite Dimensions: Mott Transition and Superconductivity*, Phys. Rev. Lett. **72,** 1545 (1994).

[10] M. Capone, L. de Medici, and A. Georges, *Solving the Dynamical Mean-Field Theory at Very Low Temperatures Using the Lanczos Exact Diagonalization*, Phys. Rev. B **76,** 245116 (2007).

[11] A. Liebsch and H. Ishida, *Temperature and Bath Size in Exact Diagonalization Dynamical Mean Field Theory*, J. Phys. Condens. Matter **24,** 053201 (2012).

[12] R. Bulla, T. Costi, and T. Pruschke, *Numerical Renormalization Group Method for Quantum Impurity Systems*, Rev. Mod. Phys. **80,** 395 (2008).

[13] D. J. García, K. Hallberg, and M. J. Rozenberg, *Dynamical Mean Field Theory with the Density Matrix Renormalization Group*, Phys. Rev. Lett. **93,** 246403 (2004).

[14] H. Li and N.-H. Tong, *A Standard Basis Operator Equation of Motion Impurity Solver for Dynamical Mean Field Theory*, arXiv:1501.07689.

[15] P. Wang, G. Cohen, and S. Xu, *Numerical Operator Method for the Real-Time Dynamics of Strongly Correlated Quantum Impurity Systems Far from Equilibrium*, Phys. Rev. B **91,** 155148 (2015).

[16] L.-F. Arsenault, O. A. von Lilienfeld, and A. J. Millis, *Machine Learning for Many-Body Physics: Efficient Solution of Dynamical Mean-Field Theory*, arXiv:1506.08858.

[17] M. Schüler, C. Renk, and T. O. Wehling, *Variational Exact Diagonalization Method for Anderson Impurity Models*, Phys. Rev. B **91,** 235142 (2015).

[18] M. Granath and H. U. R. Strand, *Distributional Exact Diagonalization Formalism for Quantum Impurity Models*, Phys. Rev. B **86,** 115111 (2012).

[19] H. Shinaoka, M. Dolfi, M. Troyer, and P. Werner, *Hybridization Expansion Monte Carlo Simulation of Multi-Orbital Quantum Impurity Problems: Matrix Product Formalism and Improved Monte Carlo Sampling*, J. Stat. Mech. (2014) P06012.

[20] G. Knizia and G. K.-L. Chan, *Density Matrix Embedding: A Simple Alternative to Dynamical Mean-Field Theory*, Phys. Rev. Lett. **109,** 186404 (2012).

[21] Y. Lu, M. Höppner, O. Gunnarsson, and M. W. Haverkort, *Efficient Real-Frequency Solver for Dynamical Mean-Field Theory*, Phys. Rev. B **90,** 085102 (2014).

[22] D. Zgid, E. Gull, and G. Chan, *Truncated Configuration Interaction Expansions as Solvers for Correlated Quantum Impurity Models and Dynamical Mean Field Theory*, Phys. Rev. B **86,** 165128 (2012).

[23] C. Lin and A. A. Demkov, *Efficient Variational Approach to the Impurity Problem and Its Application to the Dynamical Mean-Field Theory*, Phys. Rev. B **88,** 035123 (2013).

[24] C. Lin and A. A. Demkov, *Electron Correlation in Oxygen Vacancy in* $SrTiO_3$, Phys. Rev. Lett. **111,** 217601 (2013).

[25] K. M. Stadler, A. Weichselbaum, Z. P. Yin, J. von Delft, and G. Kotliar, *DMFT + NRG Study of Spin-Orbital Separation in a Three-Band Hund's Metal*, Phys. Rev. Lett. **115**, 136401 (2015).

[26] S. R. White, *Density Matrix Formulation for Quantum Renormalization Groups*, Phys. Rev. Lett. **69**, 2863 (1992).

[27] U. Schollwöck, *The Density-Matrix Renormalization Group in the Age of Matrix Product States*, Ann. Phys. (Amsterdam) **326**, 96 (2011).

[28] U. Schollwöck, *The Density-Matrix Renormalization Group*, Rev. Mod. Phys. **77**, 259 (2005).

[29] A. Holzner, A. Weichselbaum, I. P. McCulloch, U. Schollwöck, and J. von Delft, *Chebyshev Matrix Product State Approach for Spectral Functions*, Phys. Rev. B **83**, 195115 (2011).

[30] F. A. Wolf, J. A. Justiniano, I. P. McCulloch, and U. Schollwöck, *Spectral Functions and Time Evolution from the Chebyshev Recursion*, Phys. Rev. B **91**, 115144 (2015).

[31] S. Nishimoto, F. Gebhard, and E. Jeckelmann, *Dynamical Density-Matrix Renormalization Group for the Mott-Hubbard Insulator in High Dimensions*, J. Phys. Condens. Matter **16**, 7063 (2004).

[32] M. Karski, C. Raas, and G. S. Uhrig, *Electron Spectra Close to a Metal-to-Insulator Transition*, Phys. Rev. B **72**, 113110 (2005).

[33] S. Nishimoto, F. Gebhard, and E. Jeckelmann, *Dynamical Mean-Field Theory Calculation with the Dynamical Density-Matrix Renormalization Group*, Physica (Amsterdam) **378–380B**, 283 (2006).

[34] D. J. García, E. Miranda, K. Hallberg, and M. J. Rozenberg, *Mott Transition in the Hubbard Model Away from Particle-Hole Symmetry*, Phys. Rev. B **75**, 121102 (2007).

[35] M. Karski, C. Raas, and G. S. Uhrig, *Single-Particle Dynamics in the Vicinity of the Mott-Hubbard Metal-to-Insulator Transition*, Phys. Rev. B **77**, 075116 (2008).

[36] R. Peters, *Spectral Functions for Single- and Multi-impurity Models Using Density Matrix Renormalization Group*, Phys. Rev. B **84**, 075139 (2011).

[37] M. Ganahl, P. Thunström, F. Verstraete, K. Held, and H. G. Evertz, *Chebyshev Expansion for Impurity Models Using Matrix Product States*, Phys. Rev. B **90**, 045144 (2014).

[38] M. Ganahl, M. Aichhorn, P. Thunström, K. Held, H. G. Evertz, and F. Verstraete, *Efficient DMFT Impurity Solver Using Real-Time Dynamics with Matrix Product States*, Phys. Rev. B **92**, 155132 (2015).

[39] F. A. Wolf, I. P. McCulloch, O. Parcollet, and U. Schollwöck, *Chebyshev Matrix Product State Impurity Solver for Dynamical Mean-Field Theory*, Phys. Rev. B **90**, 115124 (2014).

[40] F. A. Wolf, I. P. McCulloch, and U. Schollwöck, *Solving Nonequilibrium Dynamical Mean-Field Theory Using Matrix Product States*, Phys. Rev. B **90**, 235131 (2014).

[41] C. Gramsch, K. Balzer, M. Eckstein, and M. Kollar, *Hamiltonian-Based Impurity Solver for Nonequilibrium Dynamical Mean-Field Theory*, Phys. Rev. B **88**, 235106 (2013).

[42] K. Balzer, F. A. Wolf, I. P. McCulloch, P. Werner, and M. Eckstein, *Nonthermal Melting of Néel Order in the Hubbard Model*, Phys. Rev. X **5**, 031039 (2015).

[43] K. A. Hallberg, *Density-Matrix Algorithm for the Calculation of Dynamical Properties of Low-Dimensional Systems*, Phys. Rev. B **52**, R9827 (1995).

[44] T. D. Kühner and S. R. White, *Dynamical Correlation Functions Using the Density Matrix Renormalization Group*, Phys. Rev. B **60**, 335 (1999).

[45] E. Jeckelmann, *Dynamical Density-Matrix Renormalization-Group Method*, Phys. Rev. B **66**, 045114 (2002).

[46] S. R. White and A. E. Feiguin, *Real-Time Evolution Using the Density Matrix Renormalization Group*, Phys. Rev. Lett. **93**, 076401 (2004).

[47] S. R. White and I. Affleck, *Spectral Function for the $S = 1$ Heisenberg Antiferromagetic Chain*, Phys. Rev. B **77**, 134437 (2008).

[48] P. E. Dargel, A. Wöllert, A. Honecker, I. P. McCulloch, U. Schollwöck, and T. Pruschke, *Lanczos Algorithm with Matrix Product States for Dynamical Correlation Functions*, Phys. Rev. B **85**, 205119 (2012).

[49] A. Braun and P. Schmitteckert, *Numerical Evaluation of Green's Functions Based on the Chebyshev Expansion*, Phys. Rev. B **90**, 165112 (2014).

[50] D. V. Savostyanov, S. V. Dolgov, J. M. Werner, and I. Kuprov, *Exact NMR Simulation of Protein-Size Spin Systems Using Tensor Train Formalism*, Phys. Rev. B **90**, 085139 (2014).

[51] M. Hochbruck and C. Lubich, *On Krylov Subspace Approximations to the Matrix Exponential Operator*, SIAM J. Numer. Anal. **34**, 1911 (1997).

[52] M. Ferrero, P. S. Cornaglia, L. De Leo, O. Parcollet, G. Kotliar, and A. Georges, *Pseudogap Opening and Formation of Fermi Arcs as an Orbital-Selective Mott Transition in Momentum Space*, Phys. Rev. B **80**, 064501 (2009).

[53] W. H. Press, S. A. Teukolsky, W. T. Vetterling, and B. P. Flannery, *Numerical Recipes: The Art of Scientific Computing*, 3rd ed. (Cambridge University Press, New York, 2007).

[54] T. Barthel, U. Schollwöck, and S. R. White, *Spectral Functions in One-Dimensional Quantum Systems at Finite Temperature Using the Density Matrix Renormalization Group*, Phys. Rev. B **79**, 245101 (2009).

[55] I. de Vega, U. Schollwöck, and F. A. Wolf, *How to Discretize a Quantum Bath for Real-Time Evolution*, Phys. Rev. B **92**, 155126 (2015).

[56] A. Go and A. J. Millis, *Spatial Correlations and the Insulating Phase of the High-T_c Cuprates: Insights from a Configuration-Interaction-Based Solver for Dynamical Mean Field Theory*, Phys. Rev. Lett. **114**, 016402 (2015).

[57] D. Senechal, *Bath Optimization in the Cellular Dynamical Mean-Field Theory*, Phys. Rev. B **81**, 235125 (2010).

[58] A. Dorda, M. Nuss, W. von der Linden, and E. Arrigoni, *Auxiliary Master Equation Approach to Nonequilibrium Correlated Impurities*, Phys. Rev. B **89**, 165105 (2014).

[59] D. J. Wales and J. P. K. Doye, *Global Optimization by Basin-Hopping and the Lowest Energy Structures of Lennard-Jones Clusters Containing Up to 110 Atoms*, J. Phys. Chem. A **101**, 5111 (1997).

[60] A. Georges, L. de' Medici, and J. Mravlje, *Strong Electronic Correlations from Hund's Coupling*, Annu. Rev. Condens. Matter Phys. **4**, 137 (2013).

[61] P. Werner, E. Gull, and A. J. Millis, *Metal-Insulator Phase Diagram and Orbital Selectivity in Three-Orbital Models with Rotationally Invariant Hund Coupling*, Phys. Rev. B **79**, 115119 (2009).

[62] P. Werner, E. Gull, M. Troyer, and A. J. Millis, *Spin Freezing Transition and Non-Fermi-Liquid Self-Energy in a Three-Orbital Model*, Phys. Rev. Lett. **101**, 166405 (2008).

[63] Y. Nomura, S. Sakai, and R. Arita, *Multiorbital Cluster Dynamical Mean-Field Theory with an Improved Continuous-Time Quantum Monte Carlo Algorithm*, Phys. Rev. B **89**, 195146 (2014).

[64] Y. Nomura, S. Sakai, and R. Arita, *Nonlocal Correlations Induced by Hund's Coupling: A Cluster DMFT Study*, Phys. Rev. B **91**, 235107 (2015).

[65] L. de' Medici, J. Mravlje, and A. Georges, *Janus-Faced Influence of the Hund's Rule Coupling in Strongly Correlated Materials*, Phys. Rev. Lett. **107**, 256401 (2011).

[66] E. Gull, M. Ferrero, O. Parcollet, A. Georges, and A. J. Millis, *Momentum-Space Anisotropy and Pseudogaps: A Comparative Cluster Dynamical Mean-Field Analysis of the Doping-Driven Metal-Insulator Transition in the Two-Dimensional Hubbard Model*, Phys. Rev. B **82**, 155101 (2010).

[67] Y. Ma and H. Ma, *Assessment of Various Natural Orbitals as the Basis of Large Active Space Density Matrix Renormalization Group Calculations*, J. Chem. Phys. **138**, 224105 (2013).

[68] G. Cohen, E. Y. Wilner, and E. Rabani, *Generalized Projected Dynamics for Non-System Observables of Non-Equilibrium Quantum Impurity Models*, New J. Phys. **15**, 073018 (2013).

[69] S. R. White, *Minimally Entangled Typical Quantum States at Finite Temperature*, Phys. Rev. Lett. **102**, 190601 (2009).

[70] F. Verstraete, J. J. Garcia-Ripoll, and J. I. Cirac, *Matrix Product Density Operators: Simulation of Finite-Temperature and Dissipative Systems*, Phys. Rev. Lett. **93**, 207204 (2004).

[71] M. Zwolak and G. Vidal, *Mixed-State Dynamics in One-Dimensional Quantum Lattice Systems: A Time-Dependent Superoperator Renormalization Algorithm*, Phys. Rev. Lett. **93**, 207205 (2004).

[72] C. Karrasch, J. H. Bardarson, and J. E. Moore, *Finite Temperature Dynamical Density Matrix Renormalization Group and the Drude Weight of Spin-1/2 Chains*, Phys. Rev. Lett. **108**, 227206 (2012).

[73] T. Barthel, *Precise Evaluation of Thermal Response Functions by Optimized Density Matrix Renormalization Group Schemes*, New J. Phys. **15**, 073010 (2013).

[74] B. Lake, D. A. Tennant, J. S. Caux, T. Barthel, U. Schollwöck, S. E. Nagler, and C. D. Frost, *Multispinon Continua at Zero and Finite Temperature in a Near-Ideal Heisenberg Chain*, Phys. Rev. Lett. **111**, 137205 (2013).

[75] M. Udagawa and Y. Motome, *Entanglement Spectrum in Cluster Dynamical Mean-Field Theory*, J. Stat. Mech. (2015) P01016.

[76] S. S. B. Lee, J. Park, and H. S. Sim, *Macroscopic Quantum Entanglement of a Kondo Cloud at Finite Temperature*, Phys. Rev. Lett. **114**, 057203 (2015).

[77] S. R. White, *Density Matrix Renormalization Group Algorithms with a Single Center Site*, Phys. Rev. B **72**, 180403 (2005).

[78] S. V. Dolgov and D. V. Savostyanov, *Alternating Minimal Energy Methods for Linear Systems in Higher Dimensions*, SIAM J. Sci. Comput. **36**, A2248 (2014).

[79] C. Hubig, I. P. McCulloch, U. Schollwöck, and F. A. Wolf, *Strictly Single-Site DMRG Algorithm with Subspace Expansion*, Phys. Rev. B **91**, 155115 (2015).

[80] A. Weiße, G. Wellein, A. Alvermann, and H. Fehske, *The Kernel Polynomial Method*, Rev. Mod. Phys. **78**, 275 (2006).

[81] W. Gautschi, *Orthogonal Polynomials (in Matlab)*, J. Comput. Appl. Math. **178**, 215 (2005).

4. Impurity solvers out of equilibrium

4.1. Entanglement of impurity models and solution of non-equilibrium DMFT

Aside from questions in equilibrium, one is also interested in the behavior of quantum many-body systems in out of equilibrium (in non-equilibrium). This being the motivation for the following article (Wolf *et al.*, 2014b), we found additionally that the "star" representation of an impurity model showed a much more favorable entanglement than its typical "chain" representation.

▷   *Solving non-equilibirium dynamical mean-field theory using matrix product states*
    FA Wolf, IP McCulloch, and U Schollwöck
    Phys. Rev. B **90** 235131 (2014)

Solving nonequilibrium dynamical mean-field theory using matrix product states

F. Alexander Wolf,[1] Ian P. McCulloch,[2] and Ulrich Schollwöck[1]

[1]*Theoretical Nanophysics, Arnold Sommerfeld Center for Theoretical Physics, LMU Munich, Theresienstrasse 37, 80333 München, Germany*
[2]*Centre for Engineered Quantum Systems, School of Physical Sciences, The University of Queensland, Brisbane, Queensland 4072, Australia*

We solve nonequilibrium dynamical mean-field theory (DMFT) using matrix product states (MPS). This allows us to treat much larger bath sizes and by that reach substantially longer times (factor ~ 2–3) than with exact diagonalization. We show that the star geometry of the underlying impurity problem can have substantially better entanglement properties than the previously favored chain geometry. This has immense consequences for the efficiency of an MPS-based description of general impurity problems: in the case of equilibrium DMFT, it leads to an orders-of-magnitude speedup. We introduce an approximation for the two-time hybridization function that uses time-translational invariance, which can be observed after a certain relaxation time after a quench to a time-independent Hamiltonian.

I. INTRODUCTION

The dynamical mean-field theory (DMFT) [1–4] is among the most successful methods to study strongly correlated electron systems in higher dimensions. DMFT maps a lattice model such as the Hubbard model onto an effective impurity model, which can be solved at considerably lower numerical cost. The resulting approximation becomes exact in the limit of infinite dimensions [1], and is usually good for three-dimensional systems. In the past years, the nonequilbrium formulation of DMFT (NEQDMFT) [5–7], which generalizes DMFT to the Keldysh formalism, has become widely employed.

To advance DMFT in the nonequilibrium regime, one still needs efficient methods to solve the real-time dynamics of the effective underlying impurity model far from equilibrium. Impurity solvers that have been used so far include real-time continuous-time quantum Monte Carlo [8], which is numerically exact, but restricted to short times due to the *phase* problem. Furthermore, there are strong- [9] and weak-coupling expansions [10–12], which are restricted to certain parameter regimes, and a formulation of NEQDMFT, that is able treat the steady-state case efficiently [13]. Recently, a Hamiltonian-based impurity solver scheme has been developed, which maps the DMFT impurity model onto a single-impurity Anderson model (SIAM) with a finite number of bath orbitals [14]. This could be solved with exact diagonalization in all parameter regimes. While the representation of the DMFT bath with a SIAM can be made exact for small times, it requires an increasing number of bath orbitals to reach longer times [14,15]. The exponential scaling of the Hilbert space dimension as a function of the number of bath orbitals therefore prohibits to acquire the dynamics at long time scales.

Various approaches exist to overcome this limitation in the representation of the wave function. These notably include (time-dependent) DMRG [16,17], which is based on a matrix product state (MPS) representation, and tensor-network representations of many-fermion states [18,19]. Recently, the so-called multiconfiguration time-dependent Hartree method [20] was applied to solve the Hamiltonian representation of DMFT. In this paper, we study the application of MPS-based methods to it.

The paper is organized as follows. In Sec. II, we briefly give the basic definitions of nonequilibrium DMFT. Motivated by

the fact that the mapping on a SIAM in NEQDMFT is simple if the SIAM is in the star geometry, while it is unsolved for the chain geometry, in Sec. III, we compare the entanglement properties for the two cases. As these should not depend on whether Hamiltonian parameters are time dependent or not, we do this for the equilibrium case. Unexpectedly, we find that the star geometry can have much better entanglement properties than the chain geometry. In Sec. IV, we numerically solve the NEQDMFT and analyze the computational resources needed to do so. In Sec. V, we propose a specific extrapolation of the hybridization function that uses time-translational invariance, which is reestablished after a certain relaxation phase after a quench to a time-independent Hamiltonian. In Sec. VI, we conclude the paper.

II. BASICS OF NONEQUILBRIUM DMFT

We aim to describe the real-time evolution of a lattice quantum many-body system such as the single-band Hubbard model

$$H_{\text{Hub}}(t) = -v(t) \sum_{ij\sigma} c_{i\sigma}^{\dagger} c_{j\sigma}$$
$$+ U(t) \sum_{i} \left(n_{i\uparrow} - \frac{1}{2} \right) \left(n_{i\downarrow} - \frac{1}{2} \right), \quad (1)$$

where $c_{i\sigma}^{\dagger}$ ($c_{i\sigma}$) creates (annihilates) an electron with spin σ on site i of the crystal lattice, $n_{i\sigma}$ is the spin-resolved density, $v(t)$ is the hopping energy, and $U(t)$ is the local interaction energy.

The central task of nonequilibrium DMFT based on the Keldysh formalism [21] is to compute the local contour-ordered Green's function

$$G_{\sigma}(t,t') = -i \langle \mathcal{T}_{\mathcal{C}} c_{\sigma}(t) c_{\sigma}^{\dagger}(t') \rangle_{S_{\text{loc}}} \quad (2)$$

of an effective single-site impurity model that approximates the lattice model (1). The time arguments of contour-ordered functions lie on the L-shaped Keldysh contour $\mathcal{C}$, and $\langle T_{\mathcal{C}} \ldots \rangle_{S_{\text{loc}}} \equiv \text{Tr}[T_{\mathcal{C}} e^{S_{\text{loc}}} \ldots] / \text{Tr}[T_{\mathcal{C}} e^{S_{\text{loc}}}]$ denotes the contour-ordered expectation value [7]. For real-time arguments as studied in this paper, though, different orderings on the L-shaped contour simply lead to the familiar definitions of retarded and advanced Green's functions. The action S_{loc} of

the effective model is given by ($\hbar \equiv 1$)

$$
S_{\text{loc}} = -i \int_{\mathcal{C}} dt \left(U(t) \left[n_\uparrow(t) - \frac{1}{2} \right] \left[n_\downarrow(t) - \frac{1}{2} \right] \right.
$$
$$
\left. - \mu \sum_\sigma n_\sigma(t) \right) - i \int_{\mathcal{C}} \int_{\mathcal{C}} dt \, dt'
$$
$$
\times \sum_\sigma c_\sigma^\dagger(t) \Lambda_\sigma(t,t') c_\sigma(t'), \tag{3}
$$

where the first part describes the local energies associated with the impurity (μ denotes the chemical potential), and the second part describes the hybridization of the impurity with a bath of noninteracting fermions. This Gaussian bath is integrated out and by that gives rise to the two-time hybridization function $\Lambda_\sigma(t,t')$. $\Lambda_\sigma(t,t')$ must be determined self-consistently such that the resulting self-energy of the effective impurity model equals the local self-energy of the lattice model. In the simplest case of a Bethe lattice with nearest-neighbor hopping in the limit of infinite coordination number Z, this requirement leads to a self-consistency relation of closed form [22]

$$
\Lambda_\sigma(t,t') = v(t) G_\sigma(t,t') v(t'), \tag{4}
$$

where the hopping matrix elements in Eq. (1) have been rescaled according to $v(t) \to v(t)/\sqrt{Z}$ [1].

A. Hamiltonian representation

The DMFT action S_{loc} in Eq. (3) can also be represented by a time-dependent Anderson model (SIAM) [14]

$$
H(t) = H_{\text{imp}}(t) + H_{\text{bath}}(t) + H_{\text{hyb}}(t),
$$
$$
H_{\text{imp}}(t) = U(t) \left(n_{0\uparrow} - \frac{1}{2} \right) \left(n_{0\downarrow} - \frac{1}{2} \right) - \mu \sum_\sigma n_{0\sigma},
$$
$$
\tag{5}
$$
$$
H_{\text{bath}}(t) = \sum_{l=1}^{L_b} \sum_\sigma \epsilon_{l\sigma} c_{l\sigma}^\dagger c_{l\sigma},
$$
$$
H_{\text{hyb}}(t) = \sum_{l=1}^{L_b} \sum_\sigma (V_{l\sigma}(t) c_{0\sigma}^\dagger c_{l\sigma} + \text{H.c.}),
$$

where the impurity at site 0 is coupled with hopping energies $V_{l\sigma}(t)$ in a star geometry to L_b noninteracting bath orbitals at potentials $\epsilon_{l\sigma}$, which can be chosen to be time independent [14]. The hybridization function of a SIAM is

$$
\Lambda_\sigma^{\text{SIAM}}(t,t') = \sum_{l=1}^{L_b} V_{l\sigma}(t) g(\epsilon_{l\sigma}, t, t') V_{l\sigma}(t')^*, \tag{6}
$$

where

$$
g(\epsilon_{l\sigma}, t, t') = -i[\theta_{\mathcal{C}}(t,t') - f(\epsilon_{l\sigma})] e^{-i\epsilon_{l\sigma}(t-t')} \tag{7}
$$

is the Green's function of an isolated bath orbital, $f(\epsilon) = 1/(e^{\beta\epsilon} + 1)$ denotes the Fermi distribution, and $\theta_{\mathcal{C}}(t,t')$ is the contour step function

$$
\theta_{\mathcal{C}}(t,t') = \begin{cases} 1 & \text{for} \quad t \geqslant_{\mathcal{C}} t', \\ 0 & \text{else.} \end{cases} \tag{8}
$$

B. How to obtain the Hamiltonian parameters?

It remains to solve the following problem: Given the hybridization function $\Lambda_\sigma(t,t') = v(t) G_\sigma(t,t') v(t')$, obtained from the self-consistency condition (4), one needs to determine the Hamiltonian parameters of the SIAM (5) that generate this hybridization function $\Lambda_\sigma^{\text{SIAM}}(t,t') = \Lambda_\sigma(t,t')$ via Eq. (6).

To achieve this [14,23], two distinct baths have to be introduced: the *first* bath $\Lambda_\sigma^{\text{SIAM},-}$ describes initial correlations in the system, whereas the *second* bath $\Lambda_\sigma^{\text{SIAM},+}$ describes the dynamic buildup of correlations. The parameters $V_{l\sigma}(t)$ and $\epsilon_{l\sigma}$ that generate the *first* bath can be directly expressed using the bath spectral function that corresponds to $\Lambda(t,t')$. The parameters for the *second* bath have to be constructed using a matrix factorization of $\Lambda(t,t')$. As in this work, for simplicity, only time evolutions from uncorrelated initial states are considered, $\Lambda_\sigma^{\text{SIAM},-}(t,t') \equiv 0$, and we only recapitulate the construction of the *second* bath $\Lambda_\sigma^{\text{SIAM},+} \equiv \Lambda_\sigma^{\text{SIAM}}$.

In this case, it will be sufficient to consider Green's functions and the hybridization function only for real-time arguments. For real times, rewriting the contour-ordered Green's function (2) using the *greater* and *lesser* Green's function and introducing an analogous definition for the hybridization function leads to

$$
G(t,t') = \theta_{\mathcal{C}}(t,t') G_\sigma^>(t,t') + \theta_{\mathcal{C}}(t',t) G_\sigma^<(t,t'), \tag{9}
$$
$$
\Lambda_\sigma(t,t') = \theta_{\mathcal{C}}(t,t') \Lambda_\sigma^>(t,t') + \theta_{\mathcal{C}}(t',t) \Lambda_\sigma^<(t,t'), \tag{10}
$$

where

$$
G^>(t,t') = -i \langle c(t) c^\dagger(t') \rangle_{S_{\text{loc}}}, \tag{11a}
$$
$$
G^<(t,t') = i \langle c^\dagger(t') c(t) \rangle_{S_{\text{loc}}}. \tag{11b}
$$

This allows us to rewrite the self-consistency (4) as

$$
\Lambda_\sigma^{\gtrless}(t,t') = v(t) G_\sigma^{\gtrless}(t,t') v(t'). \tag{12}
$$

Independent of that, $\Lambda^{\text{SIAM}}(t,t')$ in (6) can be simplified due to a freedom in choice for the bath potentials $\epsilon_{l\sigma}$, which are chosen to have different initial and final constant values [14]. Choosing $\epsilon_{l\sigma} = 0$ for the final value cancels the oscillatory term $e^{-i\epsilon_{l\sigma}(t-t')}$ in Eq. (7). Considering occupied sites with initial potential energy $\epsilon_{l\sigma} < 0$ at $T = 0$, one has $g(\epsilon_{l\sigma}, t, t') = -i[\theta_{\mathcal{C}}(t,t') - 1] = i\theta_{\mathcal{C}}(t',t)$, whereas for unoccupied orbitals with initial $\epsilon_{l\sigma} > 0$ one has $g(\epsilon_{l\sigma}, t, t') = -i\theta_{\mathcal{C}}(t,t')$.

Rewriting Eq. (6) with this choice [14] for the potential energies gives

$$
\Lambda_\sigma^{\text{SIAM}}(t,t') = i\theta_{\mathcal{C}}(t',t) \sum_{l \text{ occ.}} V_{l\sigma}(t) V_{l\sigma}(t')^*
$$
$$
- i\theta_{\mathcal{C}}(t,t') \sum_{l \text{ unocc.}} V_{l\sigma}(t) V_{l\sigma}(t')^*. \tag{13}
$$

Comparison with Eq. (10) then allows us to rewrite the self-consistency for the *greater* and *lesser* hybridization functions

as

$$\Lambda_\sigma^<(t,t') = i \sum_{l=1}^{L_b/2} V_{l\sigma}(t) V_{l\sigma}(t')^*, \tag{14a}$$

$$\Lambda_\sigma^>(t,t') = -i \sum_{l=L_b/2+1}^{L_b} V_{l\sigma}(t) V_{l\sigma}(t')^*, \tag{14b}$$

where we assumed the first half of bath orbitals to be occupied, and the second half to be unoccupied. If one can solve these equations for the couplings $V_{l\sigma}(t)$, the construction of the appropriate SIAM is completed. In the limit $L_b \to \infty$, one can always find functions $V_{l\sigma}(t)$ that allow us to represent the two-time functions $\Lambda_\sigma^{\gtrless}(t,t')$ via Eq. (14). For a finite number of bath sites, this is not guaranteed, and approximation methods have to be used. The method of choice [14] is a Cholesky factorization of the matrices $\pm i \Lambda_\sigma^{\gtrless}(t,t')$ (the two-time function becomes a matrix with two discrete indices upon time discretization) combined with an optimization procedure [14]. Both are standard numerical routines and straightforwardly give the Hamiltonian parameters $V_{l\sigma}(t)$.

C. Equilibrium case

To make the connection with exisiting treatments of DMFT calculations with DMRG [24–32], we give the equations for the equilibrium case. In equilibrium, all relevant two-time functions are time-translationally invariant and become functions of effectively one time argument, e.g.,

$$G_\sigma^R(t,t') = -i\theta(t - t')[G^>(t,t') - G^<(t,t')]$$
$$\equiv G_\sigma^R(t - t') \tag{15}$$

for the retarded component of the Green's function. One can therefore consider the corresponding one-argument Fourier (Laplace) transformed representation of such functions, e.g., $G_\sigma(\omega) = \int dt \, e^{i\omega t} G_\sigma^R(t,0)$, which is analytic in the upper half complex plane $\{\omega | \mathrm{Re}(\omega) > 0; \omega \in \mathbb{C}\}$, or $\Lambda_\sigma(\omega) = \int dt \, e^{i\omega t} \Lambda_\sigma(t,0)$. The analogous self-consistency condition to Eq. (4) then is

$$\Lambda_\sigma(\omega) = v^2 G_\sigma(\omega). \tag{16}$$

The Fourier transform of the hybridization function of the SIAM Eq. (6) is

$$\Lambda_\sigma^{\mathrm{SIAM}}(\omega) = \sum_{l=1}^{L_b} \frac{|V_{l\sigma}|^2}{\omega - \epsilon_{l\sigma}}, \tag{17}$$

with now time-independent hybridization couplings $V_{l\sigma}$.

When solving the self-consistency condition (16) with the help of a Fourier transform of $G_\sigma^R(t,0)$, one has to know $G_\sigma^R(t,0)$ at all times, in particular for $|t| \to \infty$. If $G_\sigma^R(t,0)$ decays quickly to zero, this poses no computational problem. If not, as in the interesting case close to phase transitions, very long times have to be computed, which is a hard problem due to entanglement growth in DMRG [31]. By contrast, the solution of the nonequilibrium self-consistency condition (4) does not *a priori* require us to compute very long times, as it

does not invoke a Fourier transform. Instead, one solves the self-consistency on the time domain starting at short times going successively to longer times. This makes it well suited for a DMRG treatment.

III. ENTANGLEMENT IN THE STAR VERSUS CHAIN GEOMETRY IN EQUILIBRIUM

The DMFT impurity Hamiltonian is not a physical but an effecitve model for which the only requirement is that the bath hybridization function $\Lambda(t,t')$ fulfills a DMFT self-consistency condition. Apart from this, there is no constraint, and one is, e.g., free to choose the geometry of the impurity problem. To our knowledge, up to now, for MPS/DMRG treatments of impurity problems [25–27,29–34], only the *chain* geometry has been considered, which is also used in NRG. This is due to the common belief that long-range interactions make any treament with MPS very inefficient as then *area laws* do not hold true any more. As discussed in the following, the star geometry of an impurity problem can nevertheless be highly suitable for an MPS treatment. For this analysis, we consider different SIAMs in equilibrium, as the fundamental entanglement properties of the geometry should not depend on whether Hamiltonian parameters are time dependent or not. In this section, therefore, Green's and hybridization functions are time-translationally invariant.

A. Star and chain geometry

The Hamiltonians of the SIAM in the star and the chain geometry read as

$$H^{\mathrm{star}} = H_{\mathrm{imp}} + H_{\mathrm{bath}} + H_{\mathrm{hyb}}, \tag{18a}$$

$$H_{\mathrm{imp}} = U \left(n_{0\uparrow} - \frac{1}{2} \right) \left(n_{0\downarrow} - \frac{1}{2} \right), \tag{18b}$$

$$H_{\mathrm{bath}} = \sum_{l=1}^{L_b} \sum_\sigma \epsilon_l c_{l\sigma}^\dagger c_{l\sigma}, \tag{18c}$$

$$H_{\mathrm{hyb}} = \sum_{l=1}^{L_b} \sum_\sigma \left(V_l c_{0\sigma}^\dagger c_{l\sigma} + \mathrm{H.c.} \right), \tag{18d}$$

$$H^{\mathrm{chain}} = H_{\mathrm{imp}} + H_{\mathrm{pot}} + H_{\mathrm{kin}}, \tag{18e}$$

$$H_{\mathrm{pot}} = \sum_{l=1}^{L_b} \sum_\sigma \widetilde{\epsilon}_l c_{l\sigma}^\dagger c_{l\sigma}, \tag{18f}$$

$$H_{\mathrm{kin}} = \sum_{l=0}^{L_b-1} \sum_\sigma \left(\widetilde{V}_l c_{l+1,\sigma}^\dagger c_{l\sigma} + \mathrm{H.c.} \right). \tag{18g}$$

H^{star} is a time-independent version of the representation of the SIAM chosen in the previous section in Eq. (5). The relation of both H^{star} and H^{chain} is a unitary transformation [31,35,36] defined as the matrix of Lanczos vectors that tridiagonalizes H^{star} (and hence maps it on a chain) as recapitulated in Appendix A 2.

The hybridization functions of the SIAM in both geometries in their dependence on the Hamiltonian parameters of Eq. (18)
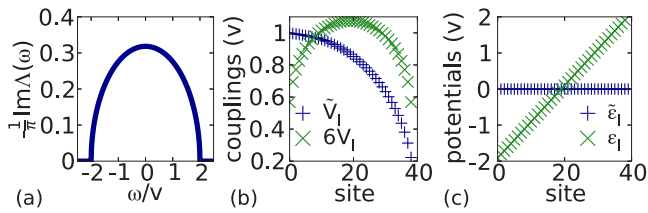
FIG. 1. (Color online) (a) Semielliptic bath spectral function $-\frac{1}{\pi}\text{Im}\Lambda(\omega)$ defined in Eq. (20). (b) Corresponding couplings in the chain ($\widetilde{V}_l$) and the star (V_l) geometry. (c) Corresponding potentials in the chain ($\widetilde{\epsilon}_l$) and the star (ϵ_l) geometry. Parameters are given in units of the hopping v.

are

$$\Lambda^{\text{star}}(\omega) = \sum_{l=1}^{L_b} \frac{|V_l|^2}{\omega - \epsilon_l},$$

$$\Lambda^{\text{chain}}(\omega) = \cfrac{|\widetilde{V}_0|^2}{\omega - \widetilde{\varepsilon}_1 - \cfrac{|\widetilde{V}_1|^2}{\omega - \widetilde{\varepsilon}_2 - \cfrac{\cdots}{\omega - \widetilde{\varepsilon}_{L_b-1} - \cfrac{|\widetilde{V}_{L_b-1}|^2}{\omega - \varepsilon_{L_b}}}}},$$ (19)

where the first line has already been given in Eq. (17).

Consider now the example of a SIAM with a semielliptic bath spectral function, which is given by the imaginary part of the hybridization function $\Lambda(\omega + i0^+)$, where here $\omega \in \mathbb{R}$,

$$-\frac{1}{\pi}\text{Im}\Lambda(\omega + i0^+) = \frac{1}{2v\pi}\sqrt{4 - \left(\frac{\omega}{v}\right)^2}$$ (20)

and shown in Fig. 1(a). In the following, we will omit to specfiy the infinitesimal shift $i0^+$. To find the parameters of the SIAMs that generate this hybridization function via Eq. (19), one discretizes $-\frac{1}{\pi}\text{Im}\Lambda(\omega)$ in a procedure well known from NRG, which is briefly summarized in Appendix A 1 [31,35]. The potentials ϵ_l in the star can therefore be associated with excitations of particles in different energy intervals of the bath spectral function $-\frac{1}{\pi}\text{Im}\Lambda(\omega)$, but have no simple interpretation in the chain geometry. The resulting parameters are shown in Figs. 1(b) and 1(c).

We impose an order on the indices of the star bath states by sorting them according to their potential energy in ascending order [Fig. 1(c)], which maps the star on an *auxiliary chain* which should not be confused with the *chain geometry* introduced before. The decisive difference between the *auxiliary chain* and the *chain geometry* is that the former has long-range interactions while the latter has short-range interactions. We compare the case of the *chain geometry* (i) with two different maps to generate the *auxiliary chain*: (ii) placing the impurity site at the center, and (iii) placing the impurity at the first site. The *auxiliary chain* obtained in case (iii) has long-range interactions at double the range of those that occur in case (ii). One might expect this to lead to very different entanglement properties. All three cases are sketched in Fig. 2.

B. Ground-state properties

Figure 3(a) shows the density distribution in the ground state for the three setups (i)–(iii). In the star geometry, i.e., its
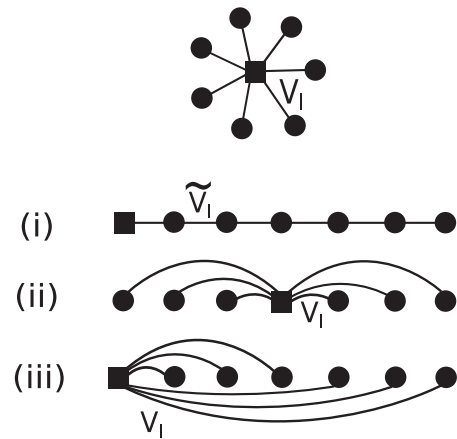

FIG. 2. Sketch of the three setups studied. The star geometry can be mapped with the unitary transform U to the *chain* geometry (i). It can also be mapped to an *auxiliary* chain by sorting the indices ascendingly to their potential energy. If one places the impurity in the center of this chain, one obtains the layout (ii), if one places it on the left edge of the chain, layout (iii) is obtained. Layouts (ii) and (iii) differ by the range over which the couplings V_l couple different lattice sites.

auxiliary chain representations (ii) and (iii), the density distribution resembles the Fermi function, where sites with negative potential energy are occupied and sites with positive energies are unoccupied. By contrast, the homogeneous potential energies of the chain geometry lead to a homogeneous density
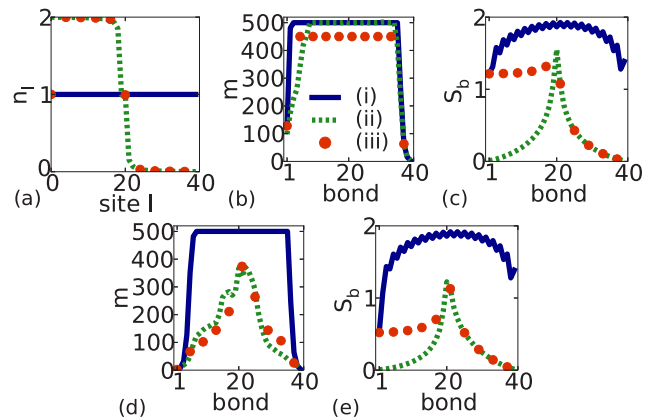
FIG. 3. (Color online) (a)–(c) Properties of the MPS approximation $|E_0\rangle$ of the ground state of a SIAM in the chain (full blue lines) in the three setups sketched in Fig. 2: (i) chain geometry (full blue lines), (ii) and (iii) star geometries with central and edge impurity (dashed green lines and red dotted lines). This is for the semielliptic bath spectral function (20) shown in Fig. 1(a) and for $U/v = 4$. (d), (e) Properties of the initial state $c_{0\sigma}^\dagger|E_0\rangle$ for the time evolution needed to compute the retarded Green's function. (a) Density distribution n_l. (b), (d) Bond dimension m. (c), (e) Bond entanglement entropy S_b. $L_b = 39$ sites are used to approximate the bath. The total chain length is $L = L_b + 1 = 40$. Ground states have been computed with a maximum bond dimension of $m = 500$. In the case of the chain geometry (i) this sufficed to reach a variance of $\langle[(H^{\text{chain}} - E_0)/v]^2\rangle \sim 10^{-4}$, whereas in the case of the star geometry, (ii) and (iii), one could reach $\langle[(H^{\text{star}} - E_0)/v]^2\rangle \sim 10^{-6}$. Here, E_0 denotes the numerical value of the ground-state energy.

distribution. Whereas the wave functions of electrons, which are noninteracting on all but one site of the system, is localized in the strongly inhomogeneous occupied regions in the star geometry, they are completely delocalized in the case of the chain geometry. Localization leads to low entanglement [37] and low bond dimensions, whereas delocalization leads to high entanglement. A similar observation can be made when comparing the momentum representation of free fermions, which is not entangled, with the real-space representation, which is highly entangled. The fact that locality of the ground state in the star geometry transforms to nonlocality in the chain geometry is also obvious from inspection of the concrete unitary transform, which is *not* a Fourier transform, but still associates a superposition of all star bath states with a single chain bath state [see, e.g., Eq. (A2) in Appendix A 2]. *Locality* is therefore not related to the range of interactions in this case. We note that recent progress in exact diagonalization techniques also points out the fact that efficient bath geometries should be designed in a way that avoids partially filled bath geometries [38].

Figures 3(b) and 3(c) show the bond dimensions m in the ground state and the bond entanglement entropies S_b. These support the previous conceptual arguments when taking into account that, in the case of the chain geometry (i), a maximum of $m = 500$ kept states sufficed to reach a variance of $\langle [(H^{\mathrm{chain}} - E_0)/v]^2 \rangle \sim 10^{-4}$, whereas in the case of the star geometry (ii) and (iii), one could reach the much better value of $\langle [(H^{\mathrm{star}} - E_0)/v]^2 \rangle \sim 10^{-6}$.

C. Time evolution

To understand how entanglement grows during time evolution, consider the computation of the *greater* Green's function for the impurity [compare its definition Eq. (11a)]

$$G_\sigma^>(t,t') = -i \langle c_{0\sigma}(t) c_{0\sigma}^\dagger(t') \rangle, \qquad (21)$$

where the expectation value at $T = 0$ is taken in the ground state. In equilibrium, where $G_\sigma^>(t,t') = G_\sigma^>(t - t')$, one can without loss of generality set $t' = 0$ and instead compute

$$G_\sigma^>(t) = -i \langle E_0 | c_{0\sigma} e^{-i(H - E_0)t} c_{0\sigma}^\dagger | E_0 \rangle. \qquad (22)$$

1. Initial state

Applying the creation operator $c_{0\sigma}^\dagger$ to the ground state destroys much of its entanglement, as can be seen by inspecting Figs. 3(d) and 3(e), which show bond dimensions and entanglement in the initial state $c_{0\sigma}^\dagger | E_0 \rangle$ used for the time evolution in Eq. (22). The action of $c_{0\sigma}^\dagger$ on the ground state $|E_0\rangle$ cancels *exactly* all superpositions of Fock states in which the impurity site is occupied, which strongly reduces entanglement. As the impurity site is involved in almost all states in the star geometry, the action $c_{0\sigma}^\dagger$ reduces entanglement in the star geometry dramatically, almost independently of whether the site is located at the center (ii) or at the edge (iii) [Fig. 3(d)]. In the chain geometry, the site does not have such a prominent role and, therefore, reduction of entanglement is much less pronounced [Fig. 3(d)].

2. Entanglement growth

During the real-time evolution needed to compute Eq. (22), we compute each time step $\Delta t = 0.05/v$ with a precision of

$$\epsilon_{\mathrm{err}} = ||\, |\psi(t + \Delta t)\rangle - \exp(-i H \Delta t)|\psi(t)\rangle \,|| < 10^{-6}, \quad (23)$$

and do not limit the growth of bond dimensions needed to guarantee this error. Truncating the initial state down to this precision reduces the original bond dimensions shown in Fig. 3(d) to very small values. These can be seen in the short-time regions of Figs. 4(a)–4(c), where we plot the bond dimensions that occur in the three setups (i), (ii), and (iii), respectively.

In the chain geometry, the growth of the bond dimension m [Fig. 4 (a)] and of the entanglement entropy S_b [Fig. 4 (d)] is associated with the particle that is created at site 0 at time $t = 0$ and subsequently travels across the chain as seen by its density evolution shown in Fig. 4(g). In the regions that have not yet been reached by the particle, almost no change in m and S_b is observed. In the star geometry, by contrast, the particle remains almost localized [Fig. 4(h)] and entropy grows much more locally [Figs. 4(e) and 4(f)]. m_b and S_b are peaked at the center of the system as entanglement builds up only with low-energy states during time evolution. These
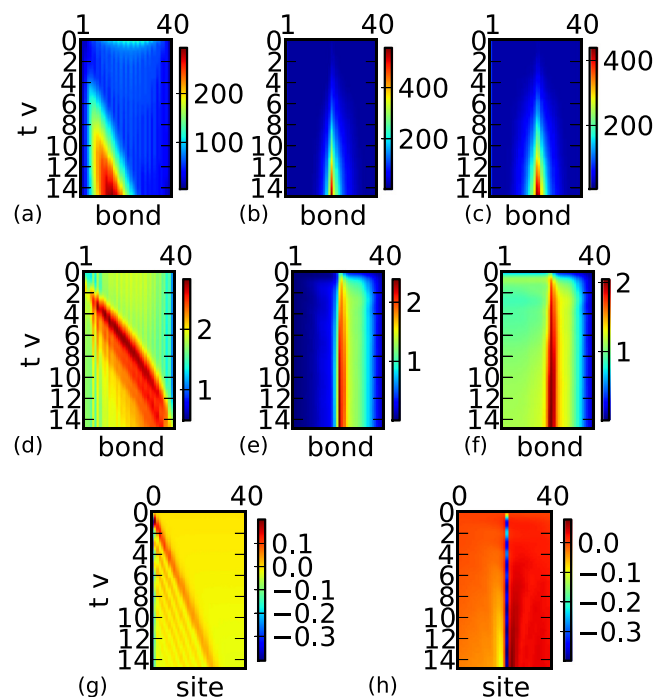
FIG. 4. (Color online) Time evolution of a SIAM with semielliptic bath spectral function (20) at $U/v = 4$ for the three setups (i)–(iii) shown in Fig. 2. The properties of the initial states for the evolution are shown in Fig. 3. Panels (a), (d), and (g) refer to the chain geometry (i), panels (b), (e), and (h) refer to the star geometry with the impurity located at the center (ii), and panels (c) and (f) to the star geometry with the impurity located at the left edge (iii). Panels (a), (b), and (c) show the local bond dimension m plotted versus bond and time, panels (d), (e), and (f) show the bond entanglement entropy S_b, and panels (g) and (h) show the density distribution substracted from its initial value $n_l(t) - n_l(0)$ plotted versus site l and time.
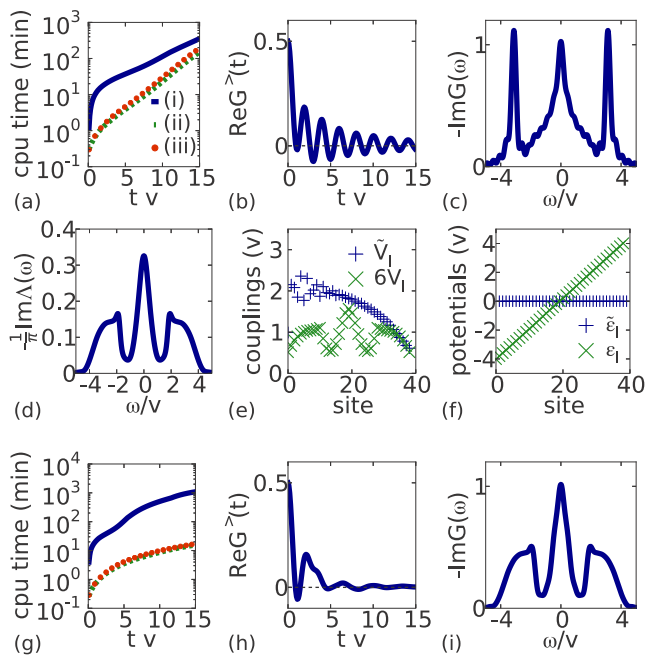
FIG. 5. (Color online) Panels (a)–(c) refer to the computation with semiellipitic bath spectral function [Fig. 1(a)]. Panels (d)–(h) refer to a computation with the self-consistently determined bath spectral function (d) for $U/v = 4$. Panels (a) and (g) show computation time versus physical time. Therein, the blue solid line refers to the chain geometry (i) whereas the green [red] dashed [dotted] line refers to the star geometry with the impurity located at the center (ii) [at the edge (iii)]. Panels (b) and (h) show the time evolution of the greater Green's function and panels (c) and (i) show the Fourier transform of the Green's function, which is the same for all three setups (i)–(iii), and therefore only one curve is shown. The oscillations in the resolution of $-\mathrm{Im}G(\omega)$ in panel (c) can be removed by convolution with a Gaussian or a Lorentzian of small width η. On the (real-) time domain, this would correspond to a slight damping (*windowing*) of $G^>(t)$ with a Gaussian or Lorentzian of large width $1/\eta$ and maximum at $t = 0$. This suppresses contributions for times $t \gtrsim 1/\eta$. Alternatively, one can compute the real-time evolution of the Green's function up to higher times, until it has converged to zero, or use an extrapolation technique such as *linear prediction* [32,39–41].

low-energy bath states are located at the center of the system irrespective of whether the impurity is located there (ii) or at the edge (iii). The buildup of entanglement with high-energy bath states would involve the occupation of these states, which is energetically strongly suppressed.

Figure 5(a) then shows how this affects the computer time needed to reach a certain physical time. The chain geometry (i) is clearly less efficient than the star geometry setups (ii) and (iii). Figures 5(b) and 5(c) show the time evolution of the Green's function and its Fourier transform, which are identical in all three setups (i)–(iii). All of the preceding results are not specific for the SIAM with semielliptic bath spectral function at $U/v = 4$. In all other cases studied by us, they are valid to an even greater extent. Consider the case with a bath spectral function $-\frac{1}{\pi}\mathrm{Im}\Lambda(\omega)$ that is the solution of the DMFT for the Bethe lattice for $U/v = 4$ as shown in Fig. 5(d). The qualitative form of the Hamiltonian parameters,
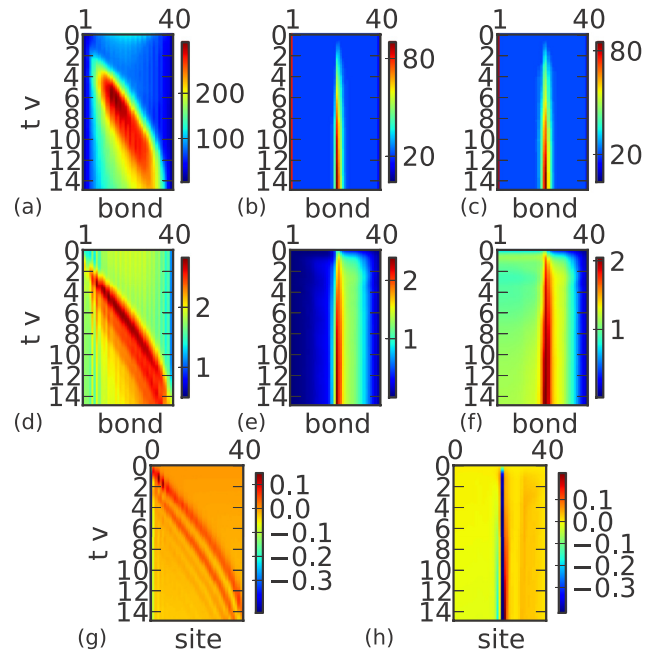

FIG. 6. (Color online) Time evolution for SIAMs in both geometries for a SIAM with self-consistently determined bath spectral function as shown in Fig. 5(d). The definition of panels is analogous to the one of Fig. 4.

shown in Figs. 5(e) and 5(f), is still similar to the previous case (Fig. 1), but the absolute magnitude of couplings and potentials is higher as the support of the bath spectral function is now of the order of $2U = 8v$. This makes the system in the star geometry more inhomogeneous and thus more localized: entanglement between sites of very different energy is disfavored energetically, whereas no such effect occurs in the chain geometry. Therefore, one sees that all computations can be performed with tremendously increased efficiency in the star geometry, which results in computation time reductions of *two orders of magnitude* as shown in Fig. 5(g). Figure 6, which is organized in the same way as Fig. 4, shows that this speedup comes with much lower bond dimensions than in the previous case (Fig. 4).

It remains to consider different values for the interaction U. It turns out that the intermediate value $U/v = 4$ leads to the strongest entanglement growth. For low and high values of the interaction U, all preceding arguments still hold true, but entanglement growth is strongly reduced in the star geometry for two further important reasons. In the noninteracting limit $U = 0$, $c_{0\sigma}^\dagger |E_0\rangle$ is an eigenstate of H. This implies that time evolution does not affect entanglement in the state. By continuity, *close to* the noninteracting limit, only very few entanglement is generated. In the strongly interacting limit $U \gg v$, very low entanglement growth is observed for a different reason. Excitation of high-energy states, i.e., occupation of bath sites with high energy in the star geometry, has to involve hopping across the impurity, where the electron needs to pay the energy for double occupation U. For high values of U, this process is strongly suppressed, and the consequence is again much lower bond dimensions than in the intermediate case $U/v = 4$. In Appendix A 3, these

arguments are supported with numerical data for the bond dimensions (Fig. 12) for all interaction strengths.

D. Nature of long-range interactions

The preceding arguments and observations show that the long-range interactions present in the *auxiliary chain* representation of the *star* geometry do not imply that it is *a priori* less suited for the treatment with MPS than the short-range interacting *chain* geometry. One should realize that the long-range interactions in the *auxiliary chain* are *not physical* interactions as they do *not* occur among *all* sites separated by a certain interaction range. They are *artificial* interactions that occur *exclusively* between the impurity site and each single bath site. If this were not the case, the calculations using the *auxiliary chain* with the impurity at the center (ii) and the left edge (iii) of the system should lead to very different entanglement, as the second case has long-range interactions at double the distance than in the first case. But, as obvious from all examples discussed before [see, e.g., the plots for the computer time in Figs. 5(a) and 5(g)], entanglement is comparable in both setups.

The physical interpretation of the concept of entanglement entropy for these long-range interacting systems is no longer meaningful. There is no physical content in the notions *left subsystem* and *right subsystem* as in the usual line of argumentation when introducing DMRG, for instance, for the case of a Heisenberg spin chain. Still, MPS can be a meaningful representation, but should then simply be interpreted as a certain way to manage and store the coefficients of the superpositions of Fock states $|\alpha_0\alpha_1\alpha_2\ldots\rangle$ where $\alpha_i \in \{0, \uparrow, \downarrow, \uparrow\downarrow\}$ denotes the local quantum state. The corresponding MPS realizes, by computing all contractions of matrices over physical quantum numbers $\{\alpha_i\}$, the subset of all possible 4^L Fock states, whose members have significant weight in a given many-body state $|\psi\rangle$. Independent of whether the underlying Hamiltonian has long-range interactions or not, bond dimensions in a given MPS can be strongly reduced by reducing the number of Fock states with significant weights in $|\psi\rangle$. In the case of the strongly inhomogeneous problem of the star geometry, states that involve occupied sites with high potential and unoccupied sites with low potential have a very small weight. In the case of the homogeneous chain geometry, no such argument applies, and *a priori* the number of Fock states with significant weight can be much higher.

IV. SOLVING NONEQUILIBRIUM DMFT USING MPS

Having motivated the usage of the star geometry of impurity problems for MPS-based algorithms in the previous section, we will now use it to solve NEQDMFT. This point is important as a formulation of NEQDMFT in the chain geometry is highly nontrivial and has not yet been achieved, whereas its formulation in the star geometry has been worked out by Eckstein [23] and Gramsch *et al.* [14].

A. Model definition

In the following, we briefly summarize the benchmark setups studied by Gramsch *et al.* [14] and Balzer *et al.* [20] by means of exact diagonalization and multiconfiguration time-

dependent Hartree. Consider the NEQDMFT for the Hubbard model on the Bethe lattice, i.e., impose the self-consistency condition (4), for an initial preparation of the system in the atomic limit ($v = 0$). The following ramp then rapidly turns on the hopping up to a final value of $v = v_0 \equiv 1$ at time $t_1 > 0$:

$$v(t) = \begin{cases} \frac{1}{2}[1 - \cos(\omega_0 t)] & \text{for} \quad t < t_1, \omega_0 = \frac{\pi}{t_1}, \\ 1 & \text{for} \quad t \geqslant t_1. \end{cases} \quad (24)$$

Since we start from the atomic limit, there are no impurity-bath correlations in the initial state and we only need to consider the *second* bath, as discussed in Sec. II.

The hybridization function $\Lambda(t,t')$ is particle-hole symmetric and spin symmetric ($\Lambda_\uparrow = \Lambda_\downarrow = \Lambda$) in the para-magnetic phase considered here. The initial ground state of the SIAM contains an equal number of empty and doubly occupied bath sites and a singly occupied impurity. In practice, we average over two Green's functions G^α and G^β, where the impurity of system α (β) is populated initially by a single up-spin (down-spin) electron. The full Green's function is then given by

$$G_\sigma(t,t') = \frac{1}{2}\left[G_{0\sigma}^\alpha(t,t') + G_{0\sigma}^\beta(t,t')\right]. \quad (25)$$

Taking the average restores particle-hole symmetry, which is not given for G^α or G^β alone.

The self-consistency condition (4) is solved in the formulation (14) by a matrix decomposition of $-i\Lambda^<(t,t')$ into coupling parameters $V_{l\sigma}(t)$, as explained in detail by Gramsch *et al.* [14]. Knowing the coupling parameters, we compute the real-time impurity Green's functions $G_\sigma^s(t,t') = \theta_C(t,t')G_\sigma^{s,>}(t,t') + \theta_C(t',t)G_\sigma^{s,<}(t,t')$ with respect to the SIAMs $s = \alpha$ and $s = \beta$ by an MPS Krylov time-evolution algorithm

$$G_\sigma^{s,>}(t,t') = -i\langle\psi_0^s|U(0,t)c_{0\sigma}U(t,t')c_{0\sigma}^\dagger U(t',0)|\psi_0^s\rangle,$$

$$G_\sigma^{s,<}(t,t') = i\langle\psi_0^s|U(0,t')c_{0\sigma}^\dagger U(t',t)c_{0\sigma}U(t,0)|\psi_0^s\rangle, \quad (26)$$

$$U(t,t') = \mathcal{T}_t \exp\left(-i\int_{t'}^t ds\, H(s)\right),$$

where $\mathcal{T}_t$ denotes the usual time-ordering operator. For this, we use a simple middle-point approximation to evolve $|\psi\rangle$ one time step Δt further,

$$|\psi(t + \Delta t)\rangle = \exp[-i H(t + \Delta t/2)\Delta t]|\psi(t)\rangle \quad (27)$$

and interpolate the Hamiltonian, i.e., the couplings $V_{l\sigma}(t)$, with standard spline interpolation.

We compute the system's kinetic energy as $E_{\text{kin}}(t) = -i\sum_\sigma \int_C ds\, \Lambda(t,s)G_\sigma(s,t')|_{t=t'}^<$, the density $\langle n(t)\rangle = -i\sum_\sigma G_\sigma^<(t,t)$, which is a conserved quantity, and the double occupation $d(t) = \langle n_{0\uparrow}(t)n_{0\downarrow}(t)\rangle$. All of these quantities are averaged over the SIAMs α and β. The double occupation also gives access to the interaction energy $E_{\text{int}}(t) = U[d(t) - \frac{1}{4}]$ and by that allows us to compute the total energy as $E_{\text{tot}} = E_{\text{kin}} + E_{\text{int}}$.

In Sec. II B, we explained that we choose the bath potentials to be homogeneous. By this, a substantial part of the discussion of Sec. III that was based on the inhomogeneity of the star geometry does not apply to the description of the present setup. There are three arguments, that still motivate the use of the star geometry. (a) The statements about the nature of long-range interactions interactions in Sec. III D remain

still valid and are independent of whether the problem is homogeneous or not. (b) If one does not start from the atomic limit, but has to consider initial correlations in the bath, this will require the representation of the *first* bath referred to in Sec. II. This will again be inhomogeneous, and all of the results of Sec. III will again apply. (c) The formulation of the nonequilibrium problem in the chain geometry is highly nontrivial, whereas in the star geometry, computations can be carried out straightforwardly.

B. Numerical results

Figure 7(a) shows the time evolution of the double occupation $d(t)$ for an interaction energy of $U = 10$. Whereas in exact diagonalization, the maximal treatable bath size was $L_b = 14$ [20], we are able to perform computations for $L_b = 24$ in a numerically controlled way. The error measure for this is the conservation of the total energy $E_{tot}(t)$ shown in the inset of Fig. 7(b). The bath size of $L_b = 24$ allows to reach $t_{max} \sim 7/v_0$, whereas the highest reached time in the literature up to now, for the case $U/v_0 = 10$, is $t_{max} \sim 2.5/v_0$ [14]. The substantial increase of the possible simulation time is related to the reduced approximation error for the hybridization function $\max |\Lambda(t,t') - \Lambda_{Cholesky}(t,t')|$ for large bath sizes as shown in Fig. 8(a).

(a)

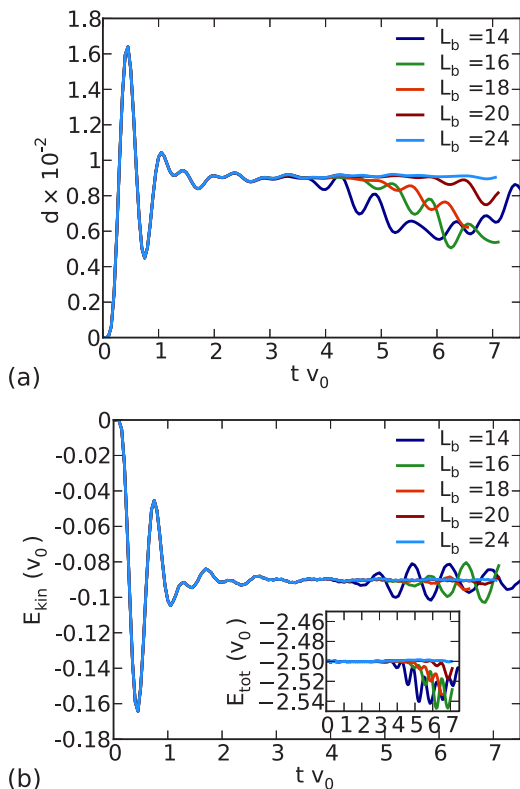(b)

FIG. 7. (Color online) Time evolution of double occupancy $\langle d(t) \rangle$ (a) and kinetic and total energy (b) for $U = 10$ and different bath sizes. For the largest bath shown $L_b = 24$ we could reach a time $t_{max} \sim 7/v_0$ in a controlled way, meaning that the total energy is conserved. We did *not* limit the maximal allowed bond dimension m, but we imposed an upper error bound for the time evolution in single time step of $\Delta t = 0.05/v_0$ of $\epsilon_{err} = 10^{-6}$, as defined in Eq. (23).
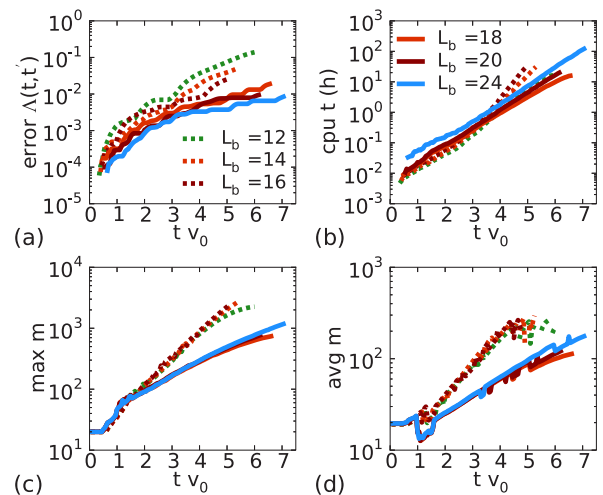

(a)   (b)

(c)   (d)

FIG. 8. (Color online) Solid lines refer to the $U = 10$ case, dashed lines to the $U = 4$ case. Panel (a) shows the error needed to compute one time step in the DMFT scheme of $\Delta t = 0.05/v_0$. Panel (b) shows the computation time $\max |\Lambda(t,t') - \Lambda_{Cholesky}(t,t')|$ of the hybridization function. Panel (c) shows the maximal bond dimension that occurs in set of Krylov states needed to expand $\exp[-iH(t)\Delta t]$. Panel (d) shows the average bond dimension in these states. The average dimension is much lower than the maximal dimension, which can be understood when looking at the spatially resolved bond dimensions that are shown in Figs. 4 and 6 for the equilibrium case, but are typical also for the nonequilibrium case.

In Fig. 8(b), we show the computer time needed to converge one DMFT time slice $\Delta t = 0.05/v_0$ using four DMFT iterations on a slice. The computation uses two cores, one for each SIAM $s = \{\alpha, \beta\}$. Figure 8(c) shows the maximal bond dimension that occurs in the computed states to be around $m \sim 1000$ for the largest bath in the case of $U/v_0 = 10$. The average bond dimension, shown in Fig. 8(d), is much lower, as the distribution of m is strongly inhomogeneous, similarly to the cases studied before [see e.g. Fig. 6(b)]. The storage of MPS with these bond dimensions is easily feasible. The exponentially growing computation time in Fig. 8(b) limits the accessible time scales. The shown accessed times though can still be reached comparatively easily, when realizing that computations on the t-t' grid can be trivially parallelized with a linear speedup (computations on one time slice are independent from each other). In practice, we used 16 cores to compute the time evolution for $L_b = 24$ and $U = 10$. All of the above used the $U(1) \times U(1)$ symmetry of the underlying SIAMs that are associated with particle-number conservation and the S_z total spin. A computation that uses the $U(1) \times SU(2)$ symmetry should strongly increase the computational efficiency. The maximally reachable simulation time should then be around $t_{max} \sim 8/v_0 - 9/v_0$.

Let us now study the much harder case of intermediate interaction strength $U/v_0 = 4$. Figure 9 shows results for the double occupation $d(t)$ and the kinetic and total energies for this case. Entanglement entropy grows much faster than for $U/v_0 = 10$, as mixing between occupied and empty bath orbitals is energetically less suppressed, as discussed in Sec. III C 2. This is reflected in the rapid growth of bond
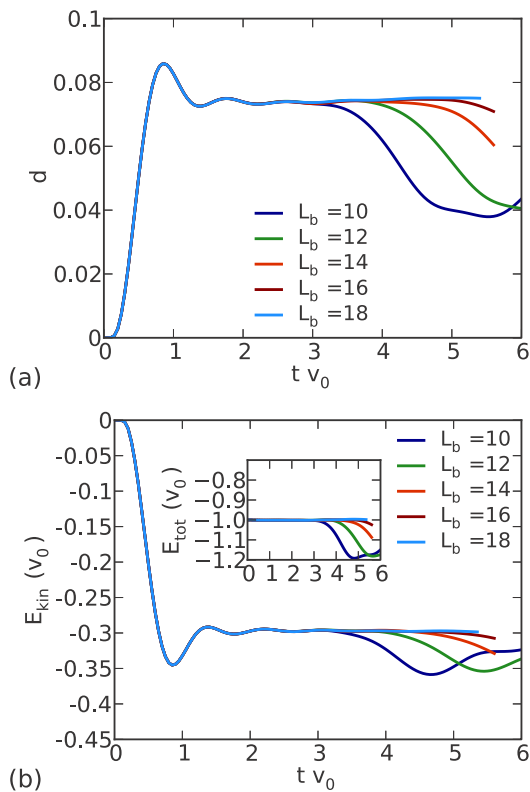
FIG. 9. (Color online) Time evolution of double occupancy $\langle d(t) \rangle$ (a) and kinetic and total energy (b) for $U = 4$ and different bath sizes. For the largest bath shown $L_b = 18$ we could reach a time $t_{\max} \sim 5.5/v_0$ in a controlled way, meaning that the total energy is conserved.

dimensions shown by the dashed lines in Figs. 8(c) and 8(d). Still, the bath sizes treated here are beyond the regime of exact diagonalization and multiconfiguration time-dependent Hartree [20]. While Gramsch *et al.* [14] could reach $t_{\max} \sim 2.8/v_0$ using exact diagonalization, we reach $t_{\max} \sim 5.5/v_0$ by investing the computational resources shown in Fig. 8. Also here, using higher computational resources, and extrapolating the maximal bond dimension shown in Fig. 8(c), would allow us to reach $t_{\max} \sim 6/v_0$ with a maximal $m \sim 10^4$. Again, usage of the SU(2) symmetry can help to substantially increase the computational efficiency and increase the value of $t_{\max} \sim 6/v_0$.

In Appendix B, we study a simple time-dependent impurity problem as done by Balzer *et al.* [20], for which neither a self-consistency DMFT loop has to be iterated nor does time propagation need to be computed in the whole t-t' plane. This reduces computation times by orders of magnitudes, and we could reach higher values of $t_{\max}$. The entanglement growth observed for this example was comparable to the full self-consistent calculation. In Appendix C, we study an inhomogeneous reformulation of the impurity problem, motivated by the results of Sec. III C 2 that showed that strongly inhomogeneous impurity models lead to less entanglement than homogeneous models. This reformulation can be easily achieved by using the local gauge symmetry of the couplings $V_{l\sigma}(t)$, that has already been used to render the bath potentials time independent (see Sec. II B). We found, though, that

the increased driving of the system that is implied by this reformulation exactly compensates the positive effect of the inhomogeneity and, by that, the same entanglement growth is observed in both setups.

V. APPROXIMATED SELF-CONSISTENCY: RELAXATION PHASE AND STEADY PHASE

For a quench to a Hamiltonian that becomes time independent after a certain transition period, one observes that, after a *relaxation phase* that lasts until t_{relax}, the Green's function shows the time-translational invariance that it would fulfill in equilibrium $G(t,t') = G(t - t')$. Putting that differently, it fulfills the symmetry $G(t,t') = G(t + s, t' + s)$ for some intermediate time s if $\min(t,t') > t_{\text{relax}}$, i.e., $G(t + s, t' + s) = \text{const}(t,t')$ can be extrapolated using a constant value. By virtue of the self-consistency condition (4), the same argumentation holds true for the hybridization function, and one can conclude that, as soon as time-translational invariance is restored, one does no longer need to solve the DMFT self-consistency on the whole time slice, but already *knows* the correct $\Lambda(t,t')$ by extrapolation for times $t' > t_{\text{relax}}$. The DMFT iteration needs only to be computed for "small" times on the time slice $t' \in [0, t_{\text{relax}}]$, whereas usually, one has to compute it for $t' \in [0, t]$.

Figure 10(a) shows a typical self-consistently determined hybridization function $i\Lambda^>(t,t')$ for the same setup as studied in the previous section and $U = 4$. We use a bath size $L_b = 12$ here, for which the corresponding results for the double occupation have already been shown in Fig. 9(a). The symmetry $i\Lambda^>(t,t') = i\Lambda^>(t + s, t' + s)$ is obvious already from the color plot in Fig. 10(a). Figure 10(b) then studies a computation based on the extrapolated $\Lambda_{\text{relax}}(t,t')$ for which the self-consistency has only been computed for times $\min(t,t') < t_{\text{relax}} = 1/v_0$. As the difference to the exact computation is not perceivable with the eye, we show a color plot of the difference $i\Lambda^>_{\text{relax}}(t,t') - i\Lambda^>(t,t')$. In particular for times close to the diagonal $t \sim t'$, this difference is almost zero, but also for the off-diagonal elements, it remains small.

Figure 11 shows results for the double occupation and kinetic and total energies that have been computed using the above-described approximation, and considers different values for the relaxation time t_{relax}. Already for the smallest value studied, $t_{\text{relax}} = 1/v_0$, the result for the double occupation is
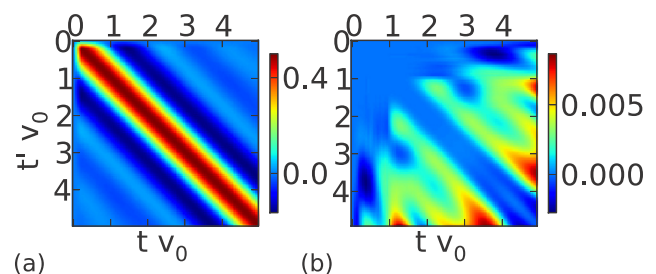

FIG. 10. (Color online) (a) Hybridization function $\Lambda(t,t')$ obtained from a calculation in which the self-consistency has been computed on the "full" t-t' grid. (b) Difference of hybridization functions $\Lambda_{\text{relax}}(t,t') - \Lambda(t,t')$, where for $\Lambda_{\text{relax}}(t,t')$, the self-consistency has only been solved for times $t' < t_{\text{relax}} = 1/v_0$.
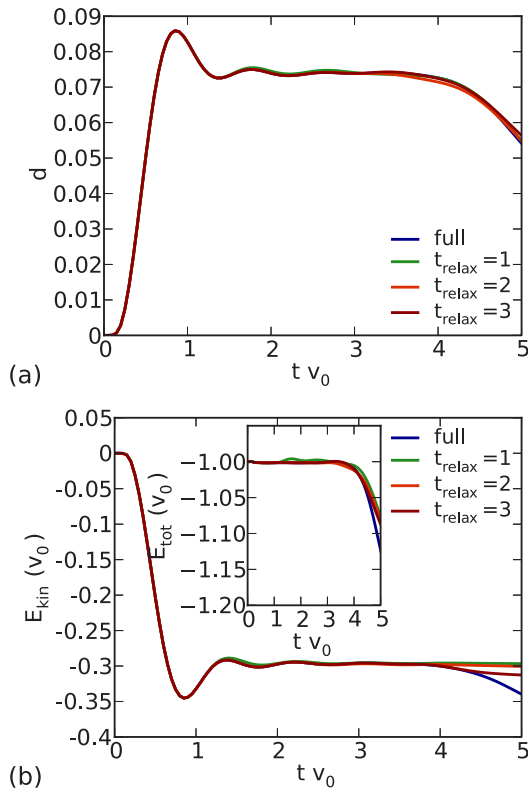
FIG. 11. (Color online) Comparison between calculation based on the approximated $\Lambda(t,t')$, for which self-consistency has only been computed for $\min(t,t') < t_{\text{relax}}$, and the exact calculation.

very close to the computation that solved the full DMFT loop. For higher values of t_{relax}, the approximation converges to the result for which the self-consistency has been solved in the full t-t' plane.

It should be interesting to study theoretically how t_{relax} depends on the initial state, quench setup, and system parameters, as it measures the time the system takes until it restores the equilibrium property of the most fundamental system parametrization, namely, the underlying $\Lambda(t,t')$, although other observables like the double occupation $d(t)$ might not yet have relaxed (compare Figs. 11 and 10). Aside from this theoretical interest, the described extrapolation scheme helps to speed up computations significantly.

The line of argumentation above should not only apply to quenches to constant Hamiltonians. Also, for periodically driven system controlled extrapolations should be possible. In this case, a constant extrapolation is no longer appropriate but, e.g., *linear prediction* can extrapolate regular oscillations with high precision [39].

VI. CONCLUSION

For equilibrium DMFT calculations, up to now, it has been difficult for DMRG/MPS-based methods to reach the computational efficiencies of CTQMC and NRG computations [25–32]. This situation should drastically be improved in view of the results of Sec. III of this paper, where we showed a tremendous speedup of more than two orders of magnitude

(Fig. 5) upon using the star instead of the chain geometry for the DMFT impurity problem. In addition to this speedup, the star geometry has tremendous technical advantages when studying impurity problems with more than two bands. While the chain representation then runs into so-called *normalization* problems for the underlying MPS structure, this is not the case for star geometry. It now seems feasible to attack the first three-band model within DMFT using an MPS-based description.

In nonequilibrium, the situation is very different as there is no such disadvantage in computational efficiency for DMRG/MPS-based calculations. This is due to the fact that parallelization is easily feasible for the DMRG computations and one is not so much interested in the behavior of Green's functions at $t \to \infty$ (compare Sec. II C). CTQMC, by contrast, then has the *phase* problem as a big disadvantage. Although NRG has a time-dependent formulation [42], and despite recent further progress [43], it has not yet been employed to treat NEQDMFT, as is the case for the recent numerical operator method [44].

In this paper, we showed that the performance of MPS-based computations in the star geometry largely exceeds that of exact diagonalization, and bath sizes could be reached that now make it possible to study more complicated setups than quenches from the noncorrelated atomic limit.

APPENDIX A: EQUILBRIUM DMFT: COMPARISON OF STAR AND CHAIN GEOMETRIES

1. Bath discretization

The discrete approximative representation of a SIAM in the star geometry with given bath spectral function $-\frac{1}{\pi}\text{Im}\Lambda(\omega)$ is given by Hamiltonian (18a), where the parameters in H_{bath} and H_{coupl} are [31,35]

$$
\begin{aligned}
V_l^2 &= \int_{I_l} d\omega \left[-\frac{1}{\pi}\text{Im}\Lambda(\omega) \right], \\
\epsilon_l &= \frac{1}{V_l^2} \int_{I_l} d\omega\, \omega \left[-\frac{1}{\pi}\text{Im}\Lambda(\omega) \right].
\end{aligned}
\tag{A1}
$$

Here, the bath discretization intervals are defined as $I_l = [\omega_l, \omega_{l+1}]$, and $\cup_l I_l$ should contain the support of $-\frac{1}{\pi}\text{Im}\Lambda(\omega)$. We use a linear discretization to define $\{\omega_l\}$, but a logarithmic discretization can as well be employed. The creation operators $c_{l\sigma}^\dagger$ in Eq. (18a) can be associated with excitations in a certain energy interval I_l of the bath spectral function $-\frac{1}{\pi}\text{Im}\Lambda(\omega)$.

2. Map from star to chain

Denote the bath orbital (single-particle) states of the star as $|c_l\rangle$. These are associated with the operators $c_{l\sigma}^\dagger$ in Eq. (18a) via $|c_l\rangle = c_{l\sigma}^\dagger |\text{vac}\rangle$ (we dropped the spin index in $|c_l\rangle$). The

first orbital of the chain is then defined as

$$|\widetilde{c}_1\rangle = \frac{1}{\widetilde{V}_0}\sum_{l=1}^{L_b} V_l|c_l\rangle, \quad \widetilde{V}_0 = \sqrt{\sum_l |V_l|^2}. \quad \text{(A2)}$$

It is a superposition of all states in the star. H_{hyb} in (18d) can then be written as $H_{\text{hyb}} = \sum_\sigma \widetilde{V}_0(|c_{0\sigma}\rangle\langle\widetilde{c}_{1\sigma}| + \text{H.c.})$. The Lanczos algorithm constructs a three-diagonal representation of $H_{\text{bath}} + H_{\text{hyb}}$ by representing it in its Gram-Schmidt orthogonalized Krylov basis $\{|\widetilde{c}_n\rangle\}$. H_{hyb} is already diagonal in this basis as by definition it has its single nonzero component for $\langle\widetilde{c}_1|H_{\text{hyb}}|\widetilde{c}_1\rangle$, and can be ignored for the Lanczos recursion:

$$\widetilde{\epsilon}_n = \langle\widetilde{c}_n|H_{\text{bath}}|\widetilde{c}_n\rangle, \quad \text{(A3a)}$$

$$|r_n\rangle = H_{\text{bath}}|\widetilde{c}_n\rangle - \widetilde{\epsilon}_n|\widetilde{c}_n\rangle - \widetilde{V}_{n-1}|\widetilde{c}_{n-1}\rangle, \quad \text{(A3b)}$$

$$\widetilde{V}_n = |\langle r_n|r_n\rangle|^{\frac{1}{2}}, \quad \text{(A3c)}$$

$$|\widetilde{c}_{n+1}\rangle = \frac{1}{\widetilde{V}_n}|r_n\rangle, \quad \text{for } n = 2,\dots,L_b - 1. \quad \text{(A3d)}$$

For $n = 1$, only the definition of $|r_n\rangle$ changes

$$|r_1\rangle = H_{\text{bath}}|\widetilde{c}_1\rangle - \widetilde{\epsilon}_1|\widetilde{c}_1\rangle. \quad \text{(A4)}$$

The above equations are easily solved by multiplying from the left with $\langle c_l|$ and inserting identities $\sum_{l'}|c_{l'}\rangle\langle c_{l'}|$ such that the initial vector can be written as $(\langle c_l|\widetilde{c}_1\rangle)_{l=1}^{L_b} = (V_l)_{l=1}^{L_b}$ and the representation of H_{bath} involved is $\langle c_l|H_{\text{bath}}|c_{l'}\rangle = \epsilon_l\delta_{ll'}$. Due to the numerical instability of the Lanczos algorithm, the recursion has to be computed with high-precision arithmetics.

The unitary transform that connects the two geometries via $U^\dagger(\mathcal{H}_{\text{bath}} + \mathcal{H}_{\text{hyb}})U = \mathcal{H}_{\text{pot}} + \mathcal{H}_{\text{kin}}$, where $(\mathcal{H}_{\text{bath}} + \mathcal{H}_{\text{hyb}})_{ll'} = \langle c_l|H_{\text{bath}} + H_{\text{hyb}}|c_{l'}\rangle$ and $(\mathcal{H}_{\text{pot}} + \mathcal{H}_{\text{kin}})_{nn'} = \langle\widetilde{c}_n|H_{\text{pot}} + H_{\text{kin}}|\widetilde{c}_{n'}\rangle$ is given by

$$(U)_{l,n=1}^{L_b} = ((\langle c_l|\widetilde{c}_n\rangle))_{l,n=1}^{L_b} = \begin{pmatrix} V_1/\widetilde{V}_0 & \langle c_1|\widetilde{c}_1\rangle & \dots \\ V_2/\widetilde{V}_0 & \langle c_2|\widetilde{c}_1\rangle & \dots \\ \vdots & \vdots & \\ V_{L_b}/\widetilde{V}_0 & & \end{pmatrix} \quad \text{(A5)}$$

and relates the two basis sets via $|\widetilde{c}_n\rangle = \sum_l U_{nl}^\dagger|c_l\rangle$.

3. Time evolution for different interaction strengths

In Fig. 12, we study the time evolution of a SIAM with semielliptic bath spectral function (20) for different interaction strengths $U/v \in \{0, 0.5, 4, 10\}$ in the chain geometry (i) and the star geometry (ii), where the detailed setups are sketched in Fig. 2. As discussed in Sec. III C 2, we observe a strongly reduced entanglement growth in the case of the star geometry in both limits of weak and strong interaction.

APPENDIX B: RESULTS FOR A NON-SELF-CONSISTENT IMPURITY PROBLEM

Here, we compute the time evolution of a SIAM with a hybridization function Λ given as

$$\Lambda(t,t') = v(t)g(t,t')v(t'), \quad t,t' \leqslant t_{\text{max}} \quad \text{(B1)}$$
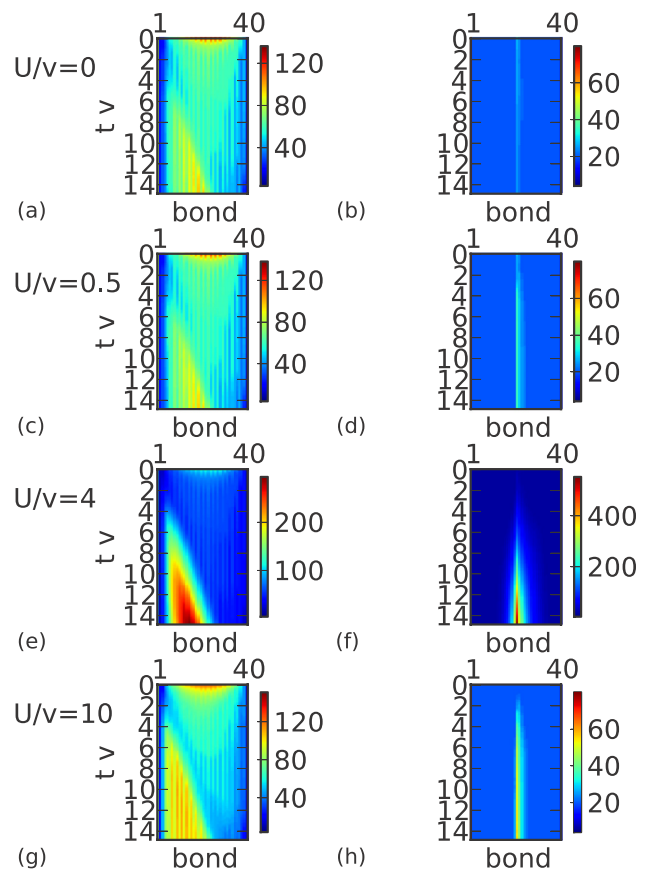
FIG. 12. (Color online) Bond dimension m versus time and bond for different interactions strengths U as given in the figure. We compare the chain geometry (i) (panels (a), (c), (e), (g)) and the star geometry with the impurity located at the center (ii) (panels (b), (d), (f), (h)). The geometries are defined in Fig. 2.

where $g(t,t') = \theta(t,t')g^>(t,t') + \theta(t',t)g^<(t,t')$ with

$$g^{\gtrless}(t,t') = \mp i \int d\omega\, f^{\gtrless}(\omega)A(\omega)e^{-i\omega(t-t')}. \quad \text{(B2)}$$

Here, $f^<(\omega) = f(\omega) = 1/(e^{\beta\omega} + 1)$, $f^>(\omega) = 1 - f(\omega)$, and the semielliptic density of states $A(\omega) = \frac{1}{2\pi}\sqrt{4 - \omega^2}$. We use the temperature $T = 1 = 1/\beta$ and the quench from the atomic limit defined in Eq. (24). This is the same setup as studied by Balzer *et al.* [20].

Figures 13(a) and 13(b) show results for the double occupation $d(t)$ obtained for two different interaction strengths $U/v_0 = 10$ and 4. For the two biggest bath sizes studied, $L_b = 20$ and 22, the value for the double occupation agrees up to times $t \sim 11/v_0$. This has been used by Balzer *et al.* [20] as indicator that the computation is controlled. But, while Balzer *et al.* [20] could only treat bath sizes up to $L_b = 16$, we are able to perform controlled computations with bath sizes up to $L_b = 24$, as has already been shown in Fig. 7, although, for the full self-consistent calculation, accessible times are much lower than here in Fig. 13. Also, we are able to efficiently treat the case $U = 4$, which is much more entangled. This limits the efficiency of multiconfiguration time-dependent Hartree as well as any MPS representation, but seems to be more severe in the former case.

FIG. 13. (Color online) Results for the solution of the impurity model with the hybridization function defined in Eq. (B1) for two interactions $U = 10$ (a) and $U = 4$ (b). This does not involve the solution of a full self-consistent computation.

FIG. 14. (Color online) Time evolution of couplings for the case with homogeneous potential $\epsilon_{l\sigma} = 0$ (full lines) and the case with $\epsilon_{l\sigma} = -2v_0 + l4v_0/L_b$, where l runs over L_b bath sites.

APPENDIX C: REGAUGING POTENTIALS AND COUPLINGS DOES NOT INFLUENCE ENTANGLEMENT

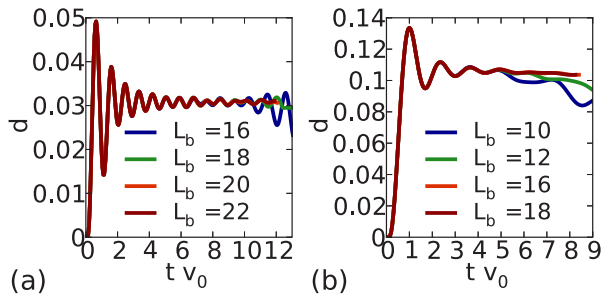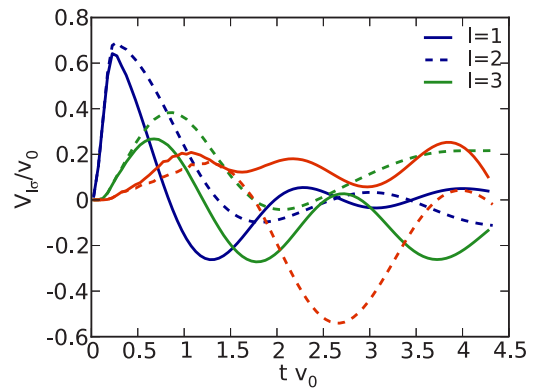In principle, one is free to choose the potentials of the star geometry arbitrarily if at the same time, one rescales the couplings [14]: Instead of the homogeneous star with time-independent potentials ϵ_p, which we considered in the previous sections as was done by Gramsch *et al.* [14] and Balzer *et al.* [20], one can equivalently solve an inhomogeneous star with time-independent potentials ϵ'_p. Instead of reformulating the matrix decomposition with a then oscillating noninteracting Green's function $g(t,t',\epsilon'_p) \propto e^{-i\epsilon'_p(t-t')}$, one can obtain the couplings $V'_p(t)$ that correspond to the inhomogeneous

model by a simple gauge transformation of the couplings that correspond to $\epsilon_p = 0$: $V'_p(t) = V_p(t)\exp(-i\epsilon'_p t)$.

We investigated the question of whether this freedom can be used to influence the entanglement properties of the system, starting from the assumption that the motion of particles in the inhomogeneous system is more constrained than in the homogeneous system. This fact is, however, compensated by the fact that the couplings $V'_p(t)$ then oscillate much slower (see Fig. 14), which leads to a stronger driving of the system. Equivalent entanglement properties result. This could have been expected, as the gauge transformation is a *local* transformation.

[1] W. Metzner and D. Vollhardt, Phys. Rev. Lett. **62**, 324 (1989).

[2] A. Georges and G. Kotliar, Phys. Rev. B **45**, 6479 (1992).

[3] A. Georges, G. Kotliar, W. Krauth, and M. J. Rozenberg, Rev. Mod. Phys. **68**, 13 (1996).

[4] G. Kotliar, S. Savrasov, K. Haule, V. Oudovenko, O. Parcollet, and C. Marianetti, Rev. Mod. Phys. **78**, 865 (2006).

[5] P. Schmidt and H. Monien, arXiv:cond-mat/0202046.

[6] J. K. Freericks, V. M. Turkowski, and V. Zlatić, Phys. Rev. Lett. **97**, 266408 (2006).

[7] H. Aoki, N. Tsuji, M. Eckstein, M. Kollar, T. Oka, and P. Werner, Rev. Mod. Phys. **86**, 779 (2014).

[8] M. Eckstein, M. Kollar, and P. Werner, Phys. Rev. Lett. **103**, 056403 (2009).

[9] M. Eckstein and P. Werner, Phys. Rev. B **82**, 115115 (2010).

[10] M. Eckstein, M. Kollar, and P. Werner, Phys. Rev. B **81**, 115131 (2010).

[11] A. Amaricci, C. Weber, M. Capone, and G. Kotliar, Phys. Rev. B **86**, 085110 (2012).

[12] N. Tsuji and P. Werner, Phys. Rev. B **88**, 165115 (2013).

[13] E. Arrigoni, M. Knap, and W. von der Linden, Phys. Rev. Lett. **110**, 086403 (2013).

[14] C. Gramsch, K. Balzer, M. Eckstein, and M. Kollar, Phys. Rev. B **88**, 235106 (2013).

[15] K. Balzer and M. Eckstein, Phys. Rev. B **89**, 035148 (2014).

[16] U. Schollwöck, Rev. Mod. Phys. **77**, 259 (2005).

[17] U. Schollwöck, Ann. Phys. (NY) **326**, 96 (2011).

[18] F. Verstraete and J. I. Cirac, arXiv:cond-mat/0407066.

[19] G. Vidal, Phys. Rev. Lett. **99**, 220405 (2007).

[20] K. Balzer, Z. Li, O. Vendrell, and M. Eckstein, arXiv:1407.6578.

[21] L. V. Keldysh, Zh. Eksp. Teor. Fiz. **47**, 1515 (1964) [Sov. Phys.– JETP **20**, 1018 (1965)].

[22] M. Eckstein, A. Hackl, S. Kehrein, M. Kollar, M. Moeckel, P. Werner, and F. A. Wolf, Eur. Phys. J. Spec. Topics **180**, 217 (2009).

[23] M. Eckstein, Ph.D. thesis, Uni Augsburg, 2009.

[24] D. J. García, K. Hallberg, and M. J. Rozenberg, Phys. Rev. Lett. **93**, 246403 (2004).

[25] S. Nishimoto and E. Jeckelmann, J. Phys.: Condens. Matter **16**, 613 (2004).

[26] S. Nishimoto, F. Gebhard, and E. Jeckelmann, J. Phys.: Condens. Matter **16**, 7063 (2004).

[27] M. Karski, C. Raas, and G. S. Uhrig, Phys. Rev. B **72**, 113110 (2005).

[28] D. J. García, E. Miranda, K. Hallberg, and M. J. Rozenberg, Phys. Rev. B **75**, 121102 (2007).

[29] M. Karski, C. Raas, and G. S. Uhrig, Phys. Rev. B **77**, 075116 (2008).

[30] M. Ganahl, P. Thunström, F. Verstraete, K. Held, and H. G. Evertz, Phys. Rev. B **90**, 045144 (2014).

[31] F. A. Wolf, I. P. McCulloch, O. Parcollet, and U. Schollwöck, Phys. Rev. B **90**, 115124 (2014).

[32] M. Ganahl, M. Aichhorn, P. Thunström, K. Held, H. G. Evertz, and F. Verstraete, arXiv:1405.6728.

[33] C. Raas, G. S. Uhrig, and F. B. Anders, Phys. Rev. B **69**, 041102 (2004).

[34] M. Nuss, M. Ganahl, E. Arrigoni, W. von der Linden, and H. G. Evertz, arXiv:1409.0646.

[35] R. Bulla, T. Costi, and T. Pruschke, Rev. Mod. Phys. **80**, 395 (2008).

[36] C. Raas, Ph.D. thesis, University of Cologne, 2005.

[37] D. Pekker and B. K. Clark, arXiv:1410.2224.

[38] Y. Lu, M. Höppner, O. Gunnarsson, and M. W. Haverkort, Phys. Rev. B **90**, 085102 (2014).

[39] W. H. Press, S. A. Teukolsky, W. T. Vetterling, and B. P. Flannery, *Numerical Recipes 3rd Edition: The Art of Scientific Computing*, 3rd ed. (Cambridge University Press, New York, 2007).

[40] S. R. White and I. Affleck, Phys. Rev. B **77**, 134437 (2008).

[41] T. Barthel, U. Schollwöck, and S. R. White, Phys. Rev. B **79**, 245101 (2009).

[42] F. B. Anders and A. Schiller, Phys. Rev. Lett. **95**, 196801 (2005).

[43] H. T. M. Nghiem and T. A. Costi, Phys. Rev. B **90**, 035129 (2014).

[44] P. Wang, G. Cohen, and S. Xu, arXiv:1410.1480.

4.2. Non-thermal melting of Neel order in the Hubbard model

The following article (Balzer *et al.*, 2015) studies the mechanism underlying the melting of Neel order in the Hubbard model. It is found in particular that the relaxation behavior for small values of the interaction can be understood in terms of the statistical theory of Kollar, Wolf, and Eckstein (2011): emergent quasi-particles allow to define a generalized Gibbs ensemble. For high values of the interaction, by contrast, the melting can be understood as an energy transfer of charge degrees of freedom to the spin background while local moments and their exchange coupling persists.

▷   *Non-thermal melting of Neel order in the Hubbard model*
     K Balzer, **FA Wolf**, IP McCulloch, P Werner and M Eckstein
     Phys. Rev. X **5**, 031039

Nonthermal Melting of Néel Order in the Hubbard Model

Karsten Balzer,[1] F. Alexander Wolf,[2] Ian P. McCulloch,[3] Philipp Werner,[4] and Martin Eckstein[1,*]

[1]*Max Planck Research Department for Structural Dynamics, University of Hamburg-CFEL,*
22761 Hamburg, Germany
[2]*Department of Physics, Arnold Sommerfeld Center for Theoretical Physics,*
LMU Munich, Theresienstrasse 37, 80333 München, Germany
[3]*Centre for Engineered Quantum Systems, School of Physical Sciences, The University of Queensland,*
Brisbane, Queensland 4072, Australia
[4]*Department of Physics, University of Fribourg, 1700 Fribourg, Switzerland*

We study the unitary time evolution of antiferromagnetic order in the Hubbard model after a quench starting from the perfect Néel state. In this setup, which is well suited for experiments with cold atoms, one can distinguish fundamentally different pathways for melting of long-range order at weak and strong interaction. In the Mott insulating regime, melting of long-range order occurs due to the ultrafast transfer of energy from charge excitations to the spin background, while local magnetic moments and their exchange coupling persist during the process. The latter can be demonstrated by a local spin-precession experiment. At weak interaction, local moments decay along with the long-range order. The dynamics is governed by residual quasiparticles, which are reflected in oscillations of the off-diagonal components of the momentum distribution. Such oscillations provide an alternative route to study the prethermalization phenomenon and its influence on the dynamics away from the integrable (noninteracting) limit. The Hubbard model is solved within nonequilibrium dynamical mean-field theory, using the density-matrix renormalization group as an impurity solver.

I. INTRODUCTION

Ultrafast pump-probe experiments on condensed-matter systems and experiments with cold gases in optical lattices have opened the intriguing possibility of controlling transitions between complex phases on microscopic time scales. This has motivated intensive theoretical efforts to understand fundamental aspects of the dynamics in interacting many-body systems and led to predictions in marked contrast to the naive expectation that interactions imply rapid thermalization [1]: Integrable systems can keep memory of the initial state for all times and relax to a generalized Gibbs ensemble [2,3], but also away from integrability thermalization can be delayed by prethermalizaton [4–7], and one can identify regimes of different dynamical behavior that are clearly separated by nonthermal critical points [8–13].

Of particular interest with respect to complex phases in condensed matter is the dynamics of symmetry-broken states [14–16]. While the relevant relaxation mechanisms after a perturbation are hard to disentangle in a solid, cold atoms in optical lattices provide a versatile platform to investigate isolated quantum systems in ideal situations. The preparation of thermodynamic long-range ordered phases in cold atoms is still a challenge [17,18], but advanced techniques for lattice design have made it possible to prepare an ordered state on a lattice of isolated sites and to probe its dynamics after tunneling between the sites is switched on [19–22]. In the following, we consider such a setup for the Fermi-Hubbard model, a paradigm model for emergent long-range order in condensed matter systems. We simulate the time evolution starting from a classical Néel state in which neighboring lattice sites of a bipartite lattice are occupied with particles of opposite spin.

In general, one can anticipate fundamentally different pathways for melting of long-range antiferromagnetic order in the weakly and strongly interacting Hubbard model: For strong interaction, long-range order arises from antiferromagnetically coupled local moments, which emerge when charge fluctuations are frozen. Magnetic order could thus possibly melt via the destruction of the local moments themselves, through a reduction of the effective exchange interaction [23] (while moments persist), or along a quasithermal pathway, by the transfer of energy from excited quasiparticles (hot electrons) to spins. The latter mechanism is intensively studied in the context of

*[*]martin.eckstein@mpsd.cfel.de

photocarrier relaxation in high-T_c cuprates [24–29], where the investigation of the spin-charge interaction challenges the limits for the time resolution in state-of-the-art pump-probe experiments [30–32]. For weak interaction, on the other hand, quasiparticle states may be important to understand relaxation processes. In the paramagnetic phase the conservation of the quasiparticle momentum occupations imposes constraints on the dynamics, which can lead to prethermalization [4,5,9,33–35]. Prethermalizaton, which was recently observed in a one-dimensional Bose gas [7], has been suggested to be a universal feature of near-integrable systems [6], but previous predictions for the Hubbard model rely on a discontinuity of the momentum distribution which is absent at nonzero temperature and thus experimentally hard to observe. Here, we show that the symmetry-broken initial state provides an alternative perspective to investigate this physics and its breakdown far from integrability.

Quenches from a Néel state have been explored in quantum spin models [10,36–38], and also as a way to prepare ordered states in the Hubbard model [39], but a pure spin model cannot describe the relevant dynamics of charge excitations and local moments. The Hubbard model has been studied in one dimension using the density-matrix renormalization group (DMRG) [40]. For the dynamics of lattice fermion models in more than one dimension, non-equilibrium dynamical mean-field theory (DMFT) [41] is the most promising approach. Quenches within the anti-ferromagnetic phase of the Hubbard model at strong coupling [25] are in line with the "quasithermal" pathway discussed above. The regime of intermediate interactions, where the notion of local moments becomes ambiguous, or weak coupling, where prethermalization may be expected, has been elusive thus far. Previous numerical solutions of the DMFT equations were based on the self-consistent strong-coupling expansion [42] or weak-coupling impurity solvers [13,43,44], which both fail at intermediate coupling, while weak-coupling quantum Monte Carlo studies [9,42] are most efficient for non-interacting initial states and restricted to short times. In this work, we overcome these limitations using a recently developed Hamiltonian-based formulation for the impurity model of nonequilibrium DMFT [45], which has opened the possibility to use wave-function-based techniques to solve the DMFT equations [46,47]. Here, we use DMRG as an impurity solver [47], which allows us to reach sufficiently long times in the evolution to address the above issues.

II. MODEL AND METHODS

Throughout this work we consider the single-band Hubbard model at half filling, with nearest-neighbor hopping J and on-site Coulomb repulsion U. The Hamiltonian is given by

$$H = -J(t) \sum_{\langle ij \rangle \sigma = \uparrow, \downarrow} c_{i\sigma}^{\dagger} c_{j\sigma} + U \sum_{i} \left(n_{i\uparrow} - \frac{1}{2} \right) \left(n_{i\downarrow} - \frac{1}{2} \right),$$

$$(1)$$

where $c_{i\sigma}^{\dagger}$ ($c_{i\sigma}$) are electron creation (annihilation) operators for lattice site i and spin σ, and $n_{i\sigma} = c_{i\sigma}^{\dagger} c_{i\sigma}$. The model is solved using nonequilibrium DMFT [41], for a Bethe lattice in the limit of infinite coordination number Z and hopping $J = J_*/\sqrt{Z}$, where the approach becomes exact [48]. The energy unit is set by $J_* = 1$, and time is measured in inverse energy, i.e., the free density of states is given by $D(\epsilon) = \sqrt{4 - \epsilon^2}/(2\pi)$. To simulate the quench, we choose a time-dependent hopping $J_*(t) = 0$ for $t \leq 0$ and $J_*(t) = 1$ for $t > 0$. For $t \leq 0$, the system therefore consists of a set of isolated lattice sites, which are prepared in a classical Néel state,

$$|\Psi_{\text{Néel}}\rangle = \prod_{i \in A} c_{i\uparrow}^{\dagger} \prod_{j \in B} c_{j\downarrow}^{\dagger} |0\rangle,$$

$$(2)$$

where A and B are sublattices of the bipartite Bethe lattice.

In DMFT, the lattice model is mapped to a set of impurity problems, one for each inequivalent lattice site $j = A, B$, with a time-dependent hybridization function $\Delta_{j\sigma}(t, t')$. (In this expression, time arguments lie on the Keldysh contour; see Ref. [41] for a detailed description of non-equilibrium DMFT and the Keldysh formalism.) For the Bethe lattice, the latter is determined self-consistently by $\Delta_{A(B),\sigma}(t, t') = J_*(t) G_{B(A),\sigma}(t, t') J_*(t')$, where $G_{j\sigma}(t, t') = -i \langle T_{\mathcal{C}} c_{j\sigma}(t) c_{j\sigma}^{\dagger}(t') \rangle$ is the local Green function. To solve the impurity model with a non-time-translationally-invariant hybridization function, we derive an equivalent representation in terms of a time-dependent Anderson impurity Hamiltonian [45] with up to $L = 24$ bath orbitals, from which the time-dependent Green functions are computed using a Krylov time propagation for matrix product states [47]. The Hamiltonian representation of the DMFT impurity model is exact for small times, but an increasing number of bath sites is needed to reach longer times [49]. We verify the convergence of the solution with the bath size L. Up to $L = 12$, the results have also been cross-checked with a Krylov time propagation in the full Hilbert space. For further details of the numerical solution, see Appendix A.

III. RESULTS

Figure 1 shows the time evolution of the antiferromagnetic order parameter $M(t)$ and the double occupation $d(t) = \langle n_{\uparrow}(t) n_{\downarrow}(t) \rangle$ after the quench, for various values of the Coulomb interaction. In order to account for the trivial reduction of the local spin expectation value by virtual charge fluctuations, we define $M(t)$ as the staggered order $M_{\text{stagg}} \equiv \langle n_{A\uparrow}(t) - n_{A\downarrow}(t) \rangle = \langle n_{B\downarrow}(t) - n_{B\uparrow}(t) \rangle$, normalized
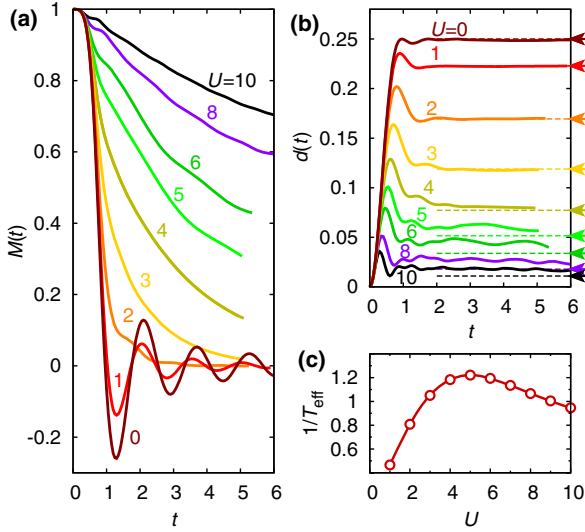
FIG. 1.   (a) Time evolution of the order parameter $M(t) = M_{stagg}/[1 - 2d(t)]$ for different values of the Coulomb repulsion in the range $U = 0$ to $U = 10$. (b) The double occupation $d(t)$ at the same values of U. Arrows indicate the double occupation in a thermalized state at the same total energy as the quenched state (as obtained from equilibrium DMFT, using a quantum Monte Carlo impurity solver [54]). All thermalized states are in the paramagnetic phase; the corresponding inverse temperature $1/T_{eff}$ is plotted in (c).

by the probability P_1 for a site to be singly occupied, $P_1(t) = 1 - 2d(t)$. To test whether the system thermalizes after the quench, we compare to an equilibrium state at the same internal energy (which is zero for the Néel state). The corresponding effective temperature T_{eff} [Fig. 1(c)] lies above the Néel temperature $T_{Néel}$ for all values of U [50]. This implies a paramagnetic state after thermalization.

While $M(t)$ indeed continues to decay throughout the simulated time interval, the double occupancy saturates to a nonthermal value for $U \gtrsim 4$ [arrows in Fig. 1(b) point to the thermalized value $d(T_{eff})$], in agreement with earlier studies on the lifetime of doublons in the paramagnetic Mott regime [51–53]. At a first glance, the relaxation of $M(t)$ and $d(t)$ therefore suggests different mechanisms for small and large values of U, with a rapid and oscillatory decay of $M(t)$, and a long-lived nonthermal state, respectively. In the following, we analyze the two regimes in more detail.

A. Weak coupling: Residual quasiparticles

For quenches to small U the Hamiltonian is close to the integrable point $U = 0$. This suggests to study the relaxation in terms of the momentum occupation $n_k(t) = \langle c_k^\dagger c_k \rangle$, which is conserved at $U = 0$. For a state with translational symmetry breaking, the single-particle density matrix $\rho_{kk'}(t) = \langle c_{k'}^\dagger(t) c_k(t) \rangle$ is no longer diagonal in momentum k. (The discussion holds for a general lattice like the Bethe lattice when k denotes the eigenstates of the translationally invariant hopping matrix.) For nearest-neighbor hopping on a bipartite lattice, eigenstates come in pairs $k, \bar{k}$ with single-particle energy $\epsilon_k = -\epsilon_{\bar{k}}$, where the wave functions for $\bar{k}$ and k differ by a staggered phase $\xi_i = \pm$ for $i \in A(B)$, and $\rho_{k\bar{k}} \neq 0$ if the symmetry between sublattices is broken. At half filling, the system becomes particle-hole symmetric, so that the Fermi surface is located at $\epsilon = 0$ and satisfies a perfect nesting condition. (On the cubic lattice, k and $\bar{k} = k + (\pi, \pi, \ldots)$ are momenta related by the antiferromagnetic nesting vector.) In Fig. 2, we plot the diagonal and off-diagonal components of the single-particle density matrix in terms of the two functions $n(\epsilon_k, t) = \langle c_k^\dagger(t) c_k(t) \rangle$
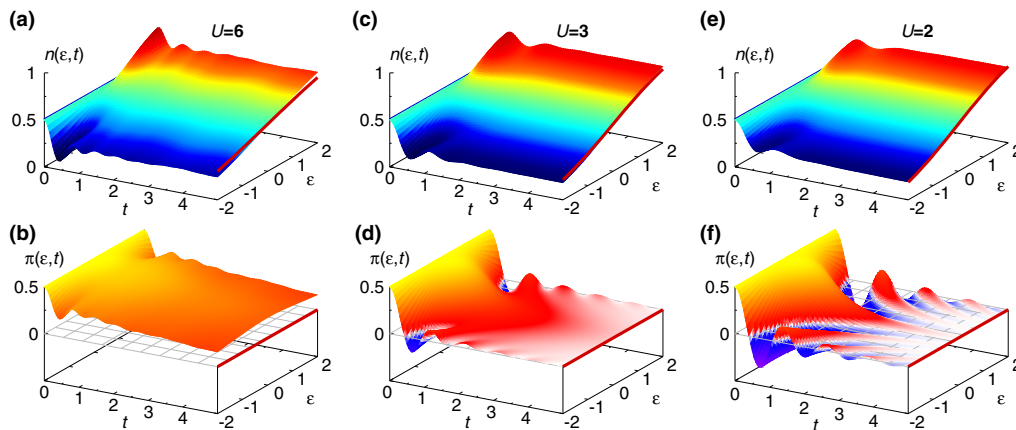
FIG. 2.   Diagonal component $n(\epsilon_k, t) = \langle c_k^\dagger c_k \rangle$ of the momentum occupation [(a), (c), and (e)] and off-diagonal component $\mathrm{Re}\,\pi(\epsilon_k) = \langle c_k^\dagger c_{\bar{k}} \rangle$ [(b), (d), and (f)], where k and $\bar{k}$ are pairs of single-particle states coupled by a staggered potential, plotted for quenches to three different values of U as a function of the energy ϵ_k ranging from -2 to 2 in the band of the Bethe lattice. The bold lines indicate momentum distributions obtained in the (paramagnetic) equilibrium state at the same energy. Note that the symmetry of the curves for $\epsilon \to -\epsilon$ is a consequence of particle-hole symmetry.

and $\pi(\epsilon_k, t) = \langle c_k^\dagger(t) c_{\bar{k}}(t) \rangle$, which depend on k only via ϵ_k due to the locality of the self-energy within DMFT. In the thermalized state, $\pi(\epsilon) = 0$, because the state does not break the sublattice symmetry, while in the localized initial state, $n(\epsilon, t = 0) = \pi(\epsilon, t = 0) = 1/2$. In agreement with the behavior of the double occupancy, $n(\epsilon, t)$ does not thermalize at large U [thermalized values $\pi_{T_{\text{eff}}}(\epsilon)$ and $n_{T_{\text{eff}}}(\epsilon)$ are shown by solid lines]. For $U \leq 2$, however, the differences between $n(\epsilon, t)$ and $n_{T_{\text{eff}}}(\epsilon)$ become tiny. This is in stark contrast to the behavior of the paramagnetic system after a quench from $U = 0$, where prethermalization manifests itself precisely in the difference between $n(\epsilon, t)$ and $n_{T_{\text{eff}}}(\epsilon)$ [5]. Thermalization of $n(\epsilon)$ implies that the kinetic energy E_{kin} thermalizes, which is in analogy to Ref. [5], but in the present case, T_{eff} becomes large for small U, so that the whole functional form of $n_{T_{\text{eff}}}(\epsilon)$ is already determined by E_{kin}. Moreover, around $U = 3$, the relaxation of $\pi(\epsilon, t)$ changes from an oscillatory to a monotonic decay. [In Fig. 2, we plot the real part of $\pi(\epsilon, t)$; the imaginary part shows a similar crossover from oscillatory to nonoscillatory behavior.]

This observation may be explained following the perturbative arguments of Refs. [5,6]. To second order in U, the Hamiltonian (1) is unitarily equivalent to a model $H = \sum_k \tilde{\epsilon}_k \tilde{c}_k^\dagger \tilde{c}_k + \mathcal{O}(U^2)$ that is quadratic in terms of quasiparticle operators $\tilde{c}_k$; we have $c_k = R_k \tilde{c}_k + \text{incoh}$, with a finite residue R_k, where incoh denotes incoherent contributions, i.e., an admixture of particle-hole excitations to higher order in U. Hence, the momentum occupation is given by $n_k(t) = R_k^2 \langle \tilde{c}_k^\dagger(t) \tilde{c}_k(t) \rangle + \text{incoh}$. The term proportional to R_k^2 (the coherent part) is unchanged by the time evolution to second order in U. We transform $n_k(t) = R_k^2 \langle \tilde{c}_k^\dagger(0) \tilde{c}_k(0) \rangle + \text{incoh}$ back to the original basis using the inverse transformation $\tilde{c}_k = R'_k c_k + \cdots$. Assuming that R_k is real, one has $R_k = R'_k$, because $\{\tilde{c}_k, \tilde{c}_{k'}^\dagger\} = \{c_k, c_{k'}^\dagger\} = \delta_{kk'}$. Thus, the backtransformation gives $n_k(t) = R_k^4 n_k(0) + \text{incoh}$, where the incoherent contribution is a smooth function of k. For quenches in the paramagnetic phase, $n_k(t)$ thus preserves the initial discontinuity at the Fermi surface, which can be taken as a measure of prethermalization [5]. In the symmetry broken state, however, $n_k(0)$ is independent of k, and thus $n_k(t)$ does not clearly exhibit the existence of residual quasiparticles. In fact, the numerical results suggest that the incoherent part can accurately be described by a thermal distribution. In contrast, a similar argument for the off-diagonal component shows that $\pi_k(t) = R_k^2 \langle \tilde{c}_k^\dagger(t) \tilde{c}_{\bar{k}}(t) \rangle + \text{incoh} = R_k^4 e^{i 2 \tilde{\epsilon}_k t} \pi(\epsilon, t = 0) + \text{incoh}$, where we use the time evolution of the quasiparticle, $\tilde{c}_{k(\bar{k})}(t) = e^{\mp i \tilde{\epsilon}_k t} \tilde{c}_{k(\bar{k})}(0)$, and $R_k = R_{\bar{k}}$. Hence, we find that the residual quasiparticle dynamics leading to prethermalization close to the integrable point $U = 0$ can be studied very conveniently with the symmetry-broken initial state in

terms of oscillations in the off-diagonal components of the momentum occupation.

Similar to the interaction quench in the paramagnetic phase [9,11], we find that the "prethermalization" regime in which residual quasiparticles dominate the dynamics is limited to small interactions; at large interactions, $\pi(\epsilon, t)$ relaxes to zero monotonically [see the $U = 6$ data in Fig. 2(b)] and the distribution becomes flat over the Brillouin zone. Below, we see that the dynamics at large U can be analyzed in terms of well-defined localized moments. In contrast to the quench in the paramagnetic phase, the crossover between the weak- and strong-coupling regimes is relatively smooth and occurs between $U = 2$ and $U = 3$: In Fig. 3(a), we exemplarily plot $\text{Re}\,\pi(\epsilon, t)$ for fixed $\epsilon = -1.5$ and various U. For $U \lesssim 2$, the curves can be accurately fit (after a transient t_0 needed to reach the prethermalized state) with decaying oscillations $f_1(t) = a \exp[-\Gamma(t - t_0)] \cos(-2\epsilon' t + \phi)$, where, in agreement with the discussion above, the quasiparticle energy $\epsilon' \to \epsilon$, and $\Gamma \sim U^2$ for $U \to 0$ [solid lines in Fig. 3(a), fit parameters in Fig. 3(b)]. For $U \gtrsim 3$, on the other hand, a good fit is a monotonically decaying curve $f_2(t) = b \exp[-c(t - t_0)]$. For $2 \lesssim U \lesssim 3$, there is a crossover between the two behaviors, as evidenced by the dependence of the amplitudes a and b of the monotonic and the oscillating component on U [Fig. 3(b)].

Before discussing the strong-coupling regime, we note that off-diagonal momentum distributions can, in principle, be measured by a modified time-of-flight measurement, if
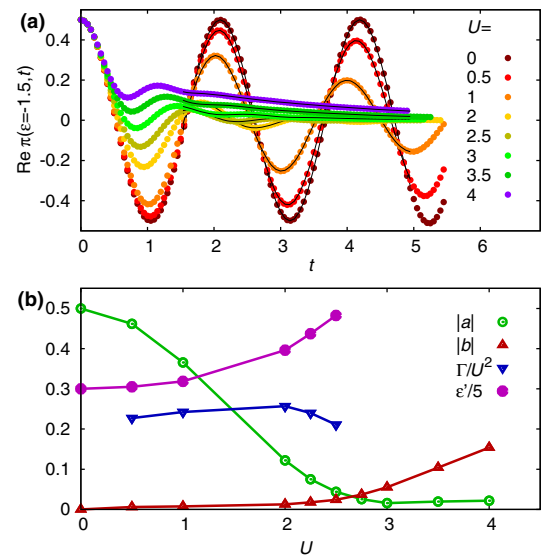
FIG. 3. (a) Line cut of $\pi(\epsilon, t)$ for $\epsilon = -1.5$ and various values of U. Solid lines are fits with the sum of a decaying exponential background and decaying oscillations, $f(t) = b \exp[-c(t - t_0)] + a \exp[-\Gamma(t - t_0)] \cos(2\epsilon' t + \phi)$ for $t > t_0 = 1.5$. (b) Amplitudes of the background b, the oscillations a, the quasiparticle energy ϵ', and the quasiparticle decay rate Γ as a function of U. (Note that Γ and ϵ' are no longer well defined if a becomes small.)

before releasing the cloud one would switch off the interaction and the tunneling (so that $\epsilon_k = 0$), switch on a staggered potential, which is $\pm \Delta$ on the A and B sublattice, respectively, and evolve for a given time t_m. Time of flight measures the regular momentum occupation $n_k = \langle c_k^\dagger c_k \rangle$ after that procedure. In the $k, \bar{k}$ basis, the staggered potential is given by $H = \Delta \sum_k (c_k^\dagger c_{\bar{k}} + \text{H.c.})$, so that $n_k(t + t_m) = n_k(t)\cos^2(t_m\Delta) + n_{\bar{k}}(t)\sin^2(t_m\Delta) + \sin(2t_m\Delta)\text{Im}\pi_k(t)$ after propagation in the pure staggered potential from time t to $t + t_m$, and $\text{Im}\pi_k(t)$ can be extracted.

B. Dynamics of local moments

In a Mott insulator at large U one can expect the existence of well-defined local moments. It is an intriguing question whether these moments persist in the quenched state while the long-range order disappears, and to what extent the crossover in relaxation behavior from weak to strong coupling can be characterized in terms of these local moments. In the following, we propose a simple experiment to distinguish the existence and strength of moments in the quenched state: one spin in the initial Néel state on a given site (the probe site "o") is flipped to the x direction [see Fig. 4(d), inset]. Choosing o on the A sublattice of the Néel state, the initial state [Eq. (2)] of the dynamics is changed to $(|\Psi_{\text{Néel}}, \uparrow\rangle + |\Psi_{\text{Néel}}, \downarrow\rangle)/\sqrt{2}$, where $|\Psi_{\text{Néel}}, \sigma\rangle = c_{o,\sigma}^\dagger c_{o\uparrow} |\Psi_{\text{Néel}}\rangle$. In a perfect local moment picture, the spin should then precess in the exchange field of its neighbors.

The inhomogeneous setup with one probe spin can be solved within DMFT, where it corresponds to a modified impurity problem at site o, while the rest of the lattice is

unchanged (see Appendix A). Figures 4(a)–4(c) show the local spin expectation values $\langle S_z \rangle$, $\langle S_y \rangle$, and $\langle S_x \rangle$ at site o for various values of the interaction. In Fig. 4(d), we show the trajectory of the spin in the S_x-S_y plane, starting from $S_x = 1$, $S_y = 0$ at time $t = 0$. For large U, one can indeed observe a precessional motion in the S_x-S_y plane, as expected for a local moment subject to an exchange field in the z direction. For $U = 0$, on the other hand, the spin dynamics is entirely longitudinal, showing no sign of well-defined local moments. [For $U = 0$, the dynamics can be solved analytically, yielding $S_{x,o} = J_1(t)^2/t^2$, while $S_{o,y} = 0$ for the Bethe lattice at $Z = \infty$, where $J_1(x)$ is the first Bessel function (see Appendix C)]. There is a crossover between the two relaxation regimes.

Although the exchange interaction is, in principle, not an instantaneous interaction on the time scale of the electronic hopping [23], it is illustrative to quantify the precession dynamics in terms of an effective exchange field. For this purpose we follow Refs. [23,55] and define $\boldsymbol{B}_{\text{eff}}$ such that $\langle \boldsymbol{S}(t) \rangle$ satisfies the equation of motion $d/dt\langle \boldsymbol{S}(t) \rangle = \boldsymbol{B}_{\text{eff}} \times \langle \boldsymbol{S}(t) \rangle$. We can assume that $\boldsymbol{B}_{\text{eff}} = B_{\text{eff}}\hat{z}$ acts only in the z direction (parallel to the order parameter M_{stagg} on the neighboring sites) and use the parametrization $B_{\text{eff}} = J_{\text{ex}}M_{\text{stagg}}$ to define an effective exchange interaction J_{ex}; the latter is then given by $J_{\text{ex}} = \dot{\phi}(t)/|M_{\text{stagg}}|$, where $\phi(t) = \arctan[S_y(t)/S_x(t)]$ is the angle of the spin in the x-y plane. The resulting value J_{ex} is plotted in Fig. 4(e). For large U, J_{ex} shows very good agreement with the perturbative value of the exchange in the Hubbard model, $4J_*^2/U$, and is not substantially decreasing with time even for quenches at intermediate
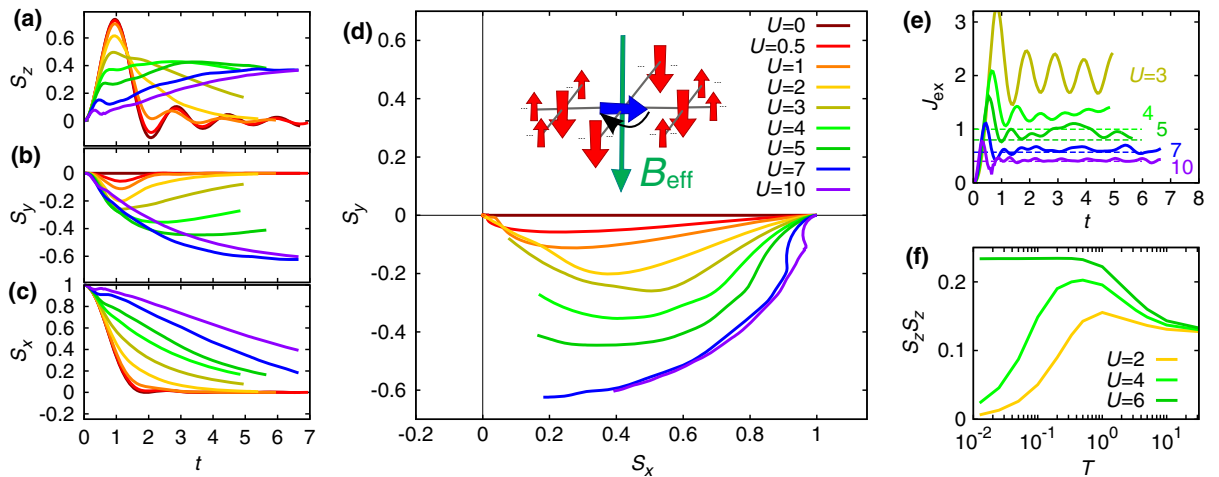
FIG. 4. Dynamics at a probe site o, where the spin is initially flipped to the x direction. (a)–(c) Expectation values $\langle S_z(t) \rangle$, $\langle S_y(t) \rangle$, and $\langle S_x(t) \rangle$ for various values of U [see legend in (d)]. (d) Trajectory of the spin $\langle \boldsymbol{S} \rangle$ in the S_x-S_y plane. The inset illustrates the initial state, with one spin flipped to the x direction, and the effective exchange field. (e) Effective exchange interaction, $d\phi(t)/dt/|M_{\text{stagg}}|$, where $\phi(t) = \arctan(S_y/S_x)$ is the angle in the S_x-S_y plane, for $U = 3, 4, 5, 7, 10$. The dotted lines correspond to the perturbative value of the exchange interaction, $J_{\text{ex}} = 4J_*^2/U$. (f) Temperature-dependent local moment in equilibrium, defined by $(1/\beta) \int_0^\beta d\tau \langle S_z(\tau) S_z(0) \rangle$, obtained using a continuous-time quantum Monte Carlo impurity solver.

interaction ($U \approx 4$) where the order parameter quickly decays to zero (see Fig. 1) [56]. Equilibrium estimates of the local moment in the intermediate-coupling regime [Fig. 4(f)] furthermore show tendencies of moment formation at elevated temperatures, which may explain why some spin precession occurs even for $U = 2$. The combination of these results shows that the melting of long-range order proceeds by the quasithermal pathway discussed in the Introduction, i.e., a disordering of exchange-coupled moments, rather than by a change of the exchange interaction or a destruction of the moments.

C. Strong coupling: Spin-charge interaction

At large U, a quench within a Mott insulator freezes virtual charge fluctuations, leaving behind a certain density n_δ of long-lived mobile carriers [25]. The mechanism for the decay of the antiferromagnetic order is thus expected to be the transfer of energy from excited quasiparticles to the spins, which is currently intensively investigated in condensed-matter pump-probe experiments. Although this mechanism is rather well understood in contrast to the dynamics at intermediate coupling, it is worthwhile to see how it can be investigated in the cold-atom setup, because experiments in solids are very challenging.

To investigate the decay of long-range order systematically, one has to vary the excitation density. Here, we use a quench protocol where, in addition to switching on the hopping at time $t = 0$, the interaction is changed to an intermediate interaction value U_i for a short time $0 \leq t \leq 0.5$ before it is set to the final value U for $t > 0.5$. (Note that various other protocols, such as an intermediate time-dependent modulation of the hopping, would have the same effect.) Small values U_i lead to a larger double occupancy [Fig. 5(a)], and indeed also a more rapid decay of $M(t)$ [Fig. 5(b)]. We also note that an exponential fit $M(t) \sim a e^{-t/\tau} + b$ would be consistent with a threshold behavior in which $M(t)$ extrapolates to a finite value b for small excitation density (U_i close to $U_i = 8$) and to $b = 0$ for large excitation density, consistent with earlier quench studies based on the noncrossing approximation impurity solver [25], but the times are not sufficient to analyze this long-time behavior in detail.

For a quantitative analysis of the short-time behavior, we determine the number n_δ of doublons and hole carriers in the quenched state [Fig. 5(c), inset]. Because of virtual charge fluctuations, n_δ is not exactly given by an instantaneous expectation value $d(t)$ in the Hubbard model, and we compute n_δ from the total weight in the upper Hubbard band (Apprndix B) [57]. For small times, the curves $M(t)$ for various values U_i can then be scaled on top of each other by plotting $[1 - M(t)]/n_\delta$ [Fig. 5(c)]. Such a scaling implies that the number of flipped spins, $1 - M(t)$, is proportional to the number of carriers. This is consistent with the picture that spin flips are inserted by mobile
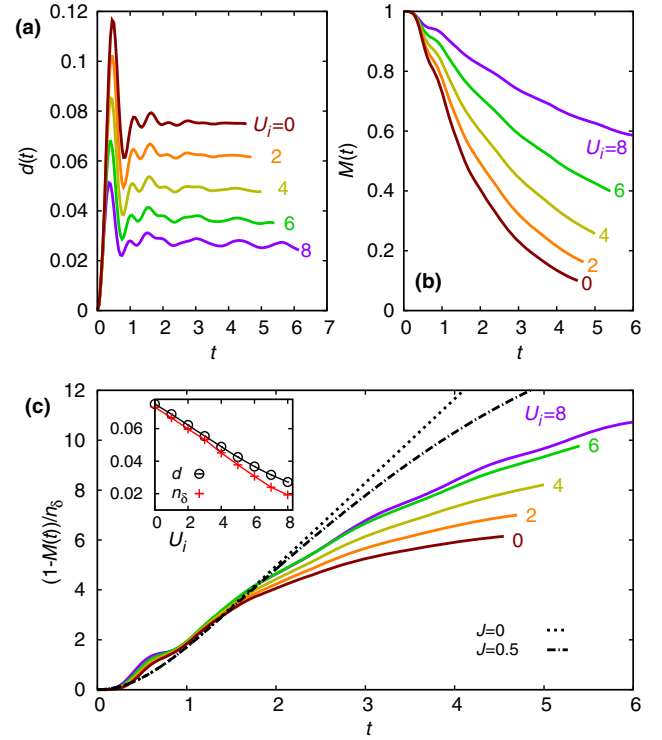
FIG. 5. Data for the following quench protocol: $t < 0$: $J_* = 0$ (Néel state); $0 \leq t < 0.5$: $J_* = 1$, $U = U_i$; $t \geq 0.5$: $J_* = 1$, $U = 8$. The intermediate step controls the excitation density in the final state. (a) Time evolution of the double occupancy or various values of U_i. (b) Time evolution of the order parameter $M(t)$. (c) Number of spin flips per charge-carrier density n_δ, $[1 - M(t)]/n_\delta$, compared to the mean displacement $R(t)$ of the initially localized particle in the t-J_z model for $J_{ex}^* = 0$ and $J_{ex}^* = 0.5$ (dotted and dashed black lines; see text). The inset shows the average of $d(t)$ for $2 \leq t \leq 5$ (open circles), and the density of mobile carriers n_δ, obtained from the integrated weight in the upper Hubbard band (red crosses).

carriers, which are initially localized and thus act independently up to times depending on n_δ. For large times there is a deviation from the scaling due to the gradual melting of the order parameter.

To further corroborate this picture, we analytically compute the spin-flip rate per carrier in the low-density limit from the behavior of a single carrier that is initially localized at a given site 0 in an Ising spin background. Following Ref. [29], we omit the transverse dynamics of the spins, which is on the time scale of J_{ex} and much slower than the hopping, and keep only the z component of the exchange coupling J_{ex} (t-J_z model). The model can then be reduced to a tight-binding model for a single particle on the lattice, with effective Hamiltonian $H = -J_*/\sqrt{Z} \sum_{\langle ij \rangle} c_i^\dagger c_j + J_{ex}^*/2 \sum_j |j| c_j^\dagger c_j$ ($J_{ex}^* \equiv Z J_{ex}$, which is finite for $Z \to \infty$ and $J = J_*/\sqrt{Z}$). The number of flipped spins is simply given by the displacement $|j|$ from the origin, and the second term in the Hamiltonian accounts

for the corresponding exchange energy cost; i.e., the particle is bound to the origin by a linear potential due to the "string" of flipped spins left behind [58]. The dotted line in Fig. 5(c) shows the mean displacement $R(t)$ of the particle in this model, which indeed coincides with the mean number of flipped spins per particle in the numerical DMFT results. As is evident from a comparison of the two curves for $J_{ex} = 0$ and $J_{ex} = 0.5$ [the perturbative value for the Hubbard model at $U = 8$, see also Fig. 4(e)], the effect of J_{ex} becomes important only at longer times (when numerical data already depend on n_δ), because initially the kinetic energy of the carrier is much larger than J_{ex}. In order to measure the effect of J_{ex} on the charge-carrier interaction, one would have to reduce the number of excitations (e.g., by switching on the hopping slowly), which, however, makes an accurate determination of n_δ increasingly difficult.

IV. CONCLUSION

In conclusion, we study the short-time relaxation dynamics of the Néel state in the single-band Hubbard model by means of nonequilibrium DMFT, using DMRG to solve the quantum impurity model. We find qualitatively different relaxation behaviors for weak and strong interactions, separated by a crossover around $U \approx 0.6 \times$ bandwidth: For strong interaction, local magnetic moments persist while their order is destroyed by spin flips due to the hopping of mobile charges. The latter resembles the femtosecond carrier spin interaction, which is relevant for the dynamics of photoinduced states in high-T_c cuprates [32]. To demonstrate the persistence of local moments, we propose a spin-precession experiment, which could be implemented similar to the proposed measurement of dynamic spin-spin correlation functions in equilibrium [59]. At weak interaction, the dynamics of the Néel state is governed by almost conserved quasiparticles, which are also the origin for prethermalization in nearly integrable systems [4,6,7]. In the symmetry-broken state, the breakdown of these quasiparticles away from integrability leads to a crossover from oscillatory to nonoscillatory relaxation behavior, which can provide a clear experimental signature that does not rely on a quantitative comparison to the thermal equilibrium state.

Our simulations within DMFT are exact in the infinite-dimensional limit, and it is thus interesting to compare to recent results for one dimension [40]. Similar to our results, in $d = 1$ one finds a rapid saturation of the double occupancy and a slower dynamics of the order parameter at large U, but the decay of antiferromagnetic order is of a different origin: In large dimensions, the fastest melting processes after the quench take place on the time scale of the hopping due to the strong charge-spin interaction, while the latter is absent in $d = 1$ so that the dynamics happens on the time scale of the exchange interaction [40]. The quasiparticle physics at weak coupling and in the crossover

regime has not been addressed in Ref. [40], but based on the perturbative argument given above, the signatures in the off-diagonal components of the momentum distribution should persist also in lower dimensions. (Also in the paramagnetic case, a long-lived jump in the momentum distribution function is found in $d = 1$ [33,35,60] and $d = 2$ [34,35].)

Quench experiments starting from the Néel state have recently been performed with noninteracting fermions in one dimension [21] and bosons in two dimensions [22]. Hence, this setup should be a feasible approach to study fundamental aspects of the decay of antiferromagnetic long-range order in the paradigmatic Hubbard model. We expect the predictions to be robust for an inhomogeneous trapping potential as long as there is a large half filled region (which is guaranteed by the preparation of the state in the Mott regime). If the tails are not magnetically ordered, they give a contribution to the signal discussed above only on longer time scales that allow for substantial mass transport between different regions of the trap. Moreover, on the numerical side, our work emphasizes the high potential of DMRG as an impurity solver for future applications of nonequilibrium DMFT to explore the intermediate-coupling regime, which is inaccessible by weak- or strong-coupling perturbation theory.

APPENDIX A: DMRG + DMFT SETUP

1. General setup

To simulate the dynamics of a lattice model that is initially in equilibrium at temperature $T = 1/\beta$, we adopt the formulation of dynamical mean-field theory within the Keldysh framework (nonequilibrium DMFT), for an L-shaped time contour $\mathcal{C}$ that extends from initial time $t = 0$ to a maximal time t_{max} along the real-time axis, back to time 0, and along the imaginary time axis to $-i\beta$. For a general description of the formalism, as well as the notation and definition of contour-ordered functions, we refer to Ref. [41]. In this Appendix, we summarize the specific setup for the quench from the Néel state and the solution of the DMFT equations using DMRG.

In DMFT, the lattice model is mapped to a set of impurity problems, one for each inequivalent lattice site j, with time-dependent hybridization functions $\Delta_{j\sigma}(t, t')$. The action of the impurity model is given by

$$S_j = -i \int_{\mathcal{C}} dt U n_\uparrow(t) n_\downarrow(t)$$
$$- i \sum_\sigma \int_{\mathcal{C}} dt_1 dt_2 c_\sigma^\dagger(t_1) \Delta_{j\sigma}(t_1, t_2) c_\sigma(t_2) \quad \text{(A1)}$$

on the Keldysh contour $\mathcal{C}$, which yields the local contour-ordered Green function $G_{j\sigma}(t, t') = -i\text{Tr}[T_{\mathcal{C}} e^{S_j} c_\sigma(t) c_\sigma^\dagger(t')]/\mathcal{Z}$. The hybridization function $\Delta_{j\sigma}(t, t')$ must be defined self-consistently. For the Bethe lattice, one has [61]

$$\Delta_{j\sigma}(t, t') = \sum_l J(t) G_{l\sigma}(t, t') J(t')^*, \quad \text{(A2)}$$

where the sum runs over nearest neighbors of j. In the antiferromagnetic state, all sites on the A and B sublattices are equivalent, respectively. With the additional symmetry $G_{A,\sigma} = G_{B,-\sigma}$, only one impurity model must be solved with $\Delta_\sigma(t, t') = J_*(t) G_{-\sigma}(t, t') J_*(t')$, where we use the scaling $J(t) = J_*(t)/\sqrt{Z}$ with the coordination number Z. For the initial product state with $J_*(t) = 0$ for $t < 0$, $\Delta(t, t') = 0$ if one time argument is on the imaginary branch of $\mathcal{C}$. Furthermore, equivalence under a simultaneous spin and particle-hole transformation implies the symmetry

$$\Delta_\sigma^>(t, t') = \Delta_{-\sigma}^<(t, t')^*. \quad \text{(A3)}$$

To compute the Green function, we follow Ref. [45] and map the impurity model to a time-dependent Anderson Hamiltonian

$$H_{\text{imp}} = U n_\uparrow n_\downarrow + \sum_{p\sigma} \epsilon_{p\sigma} a_{p\sigma}^\dagger a_{p\sigma}$$
$$+ \sum_{p\sigma} [V_{p\sigma}(t) c_\sigma^\dagger a_{p\sigma} + \text{H.c.}], \quad \text{(A4)}$$

in which the impurity is coupled to L bath orbitals ($p = 1, ..., L$). The parameters $V_{p\sigma}(t)$ and ϵ_p are determined such that the local Green functions obtained from Eqs. (A1) and (A4) are identical. As derived in Ref. [45], for $J_*(t < 0) = 0$, one can choose $V_{p\sigma}(t) = 0$ for $t < 0$, and the mapping condition is satisfied by (assuming L even)

$$\Delta_\sigma^<(t, t') = i \sum_{p=1}^{L/2} V_{p\sigma}(t) V_{p\sigma}^*(t'), \quad \text{(A5)}$$

$$\Delta_\sigma^>(t, t') = -i \sum_{p=L/2+1}^{L} V_{p\sigma}(t) V_{p\sigma}^*(t'), \quad \text{(A6)}$$

where $\epsilon_{p\sigma} = 0$, and the bath orbitals $p = 1, ..., L/2$ and $p = L/2 + 1, ..., L$ are initially doubly occupied and

empty, respectively. Equations (A5) and (A6) are solved by a Cholesky fit of the real-time matrix $\Delta(t, t')$, which quickly converges for small times with the number of bath orbitals required [49]. Because of the symmetry [Eq. (A3)], we use

$$V_{p,-\sigma}(t) = V_{L/2+p,\sigma}(t)^* \quad \text{for } p \leq L/2. \quad \text{(A7)}$$

The impurity site is initially occupied with a spin $\sigma = \uparrow$ (for a site on the A sublattice), i.e., the initial state for the impurity model is a product state $|\Psi_{\text{imp},A}\rangle = c_\uparrow^\dagger \prod_{i=1}^{L/2} a_{p\uparrow}^\dagger a_{p\downarrow}^\dagger |0\rangle$, and the Green function is obtained by solving

$$G_{A,\sigma}^<(t, t') = i\langle \Psi_{\text{imp},A} | c_\sigma^\dagger(t') c_\sigma(t) | \Psi_{\text{imp},A} \rangle, \quad \text{(A8)}$$

$$G_{A,\sigma}^>(t, t') = -i\langle \Psi_{\text{imp},A} | c_\sigma(t) c_\sigma^\dagger(t') | \Psi_{\text{imp},A} \rangle, \quad \text{(A9)}$$

where time evolution is determined by Eq. (A4). We use a Krylov time propagation for matrix product states [47] with up to $L = 24$ bath orbitals.

2. Inhomogeneous setup

For the inhomogeneous setup, we assume that in the initial state on the lattice the spin at one site o of the lattice is flipped in the x direction. Without loss of generality, we assume that o is on the A sublattice. From the self-consistency equation (A2), one can see that the hybridization on all other sites differs from the homogeneous case only in order $1/Z$; i.e., for $Z \to \infty$ the backaction of the probe site on the rest of the lattice can be neglected. On the probe site we solve an impurity problem with the same (nonequilibrium) hybridization function Δ_A as on all remaining A sites, i.e., an impurity problem [Eq. (A4)] with the same parameters $V_{p\sigma}$ but with a different initial state:

$$|\Psi_{\text{imp},o}\rangle = \left(c_\uparrow^\dagger \prod_{i=1}^{L/2} a_{p\uparrow}^\dagger a_{p\downarrow}^\dagger |0\rangle + c_\downarrow^\dagger \prod_{i=1}^{L/2} a_{p\uparrow}^\dagger a_{p\downarrow}^\dagger |0\rangle \right)/\sqrt{2}. \quad \text{(A10)}$$

3. Observables

Local observables $\langle \mathcal{O}_j(t) \rangle \equiv \langle \Psi_{\text{imp},j} | \mathcal{O}(t) | \Psi_{\text{imp},j} \rangle$ are directly measured in the impurity model ($j = o, A$), in particular, the density $\mathcal{O} \equiv n_\sigma$, the double occupancy $\mathcal{O} \equiv n_\uparrow n_\downarrow$, and the spin $\mathcal{O} \equiv S_{\alpha = x,y,z} = \frac{1}{2} \sum_{\sigma\sigma'} c_\sigma^\dagger \boldsymbol{\tau}_\alpha c_{\sigma'}$ ($\boldsymbol{\tau}_\alpha$ are the Pauli matrices).

In the translationally invariant case (no probe site), we also determine diagonal and off-diagonal components of the momentum occupations $n(\epsilon, t)$ and $\pi(\epsilon, t)$, which are obtained from the momentum resolved Green function (for the definition of k and $\bar{k}$, see the main text):

$$\boldsymbol{G}_{\epsilon_k}(t,t') = \begin{pmatrix} -i\langle T_{\mathcal{C}} c_k(t) c_k^\dagger(t')\rangle & -i\langle T_{\mathcal{C}} c_k(t) c_{\bar{k}}^\dagger(t')\rangle \\ -i\langle T_{\mathcal{C}} c_{\bar{k}}(t) c_k^\dagger(t')\rangle & -i\langle T_{\mathcal{C}} c_{\bar{k}}(t) c_{\bar{k}}^\dagger(t')\rangle \end{pmatrix}.$$

(A11)

(Here and in the following, bold-faced quantities denote 2×2 matrices and we omit spin indices for simplicity.) The self-energy is local in space but depends on the sublattice and spin; in the $k, \bar{k}$ representation, it thus assumes the (2×2) form

$$\Sigma(t,t') = \frac{1}{2}[\Sigma_A(t,t') + \Sigma_B(t,t')]\mathbf{1}$$
$$+ \frac{1}{2}[\Sigma_A(t,t') - \Sigma_B(t,t')]\boldsymbol{\tau}_x, \qquad (A12)$$

so that $\boldsymbol{G}_\epsilon$ is obtained from the lattice Dyson equation $\boldsymbol{G}_\epsilon = (i\partial_t + \mu - \boldsymbol{\epsilon} - \boldsymbol{\Sigma})^{-1}$, where the dispersion in the $k, \bar{k}$ representation reads $\boldsymbol{\epsilon} = \epsilon\boldsymbol{\tau}_z$ because $\epsilon_k = -\epsilon_{\bar{k}}$. The components Σ_j of the self-energy ($j = A, B$) are obtained from the impurity Dyson equation $(i\partial_t + \mu - \Delta_j - \Sigma_j)^{-1} = G_j$. In praxis, we solve an integral equation $G_j = Z_j + Z_j * \Delta_j * G_j$ for $Z_j = (i\partial_t + \mu - \Sigma_j)^{-1}$. We then have $\boldsymbol{Z} = (i\partial_t + \mu - \boldsymbol{\Sigma})^{-1} = \frac{1}{2}(Z_A + Z_B)\mathbf{1} + \frac{1}{2}(Z_A - Z_B)\boldsymbol{\tau}_x$, and $\boldsymbol{G}_\epsilon$ is obtained from the integral equation $\boldsymbol{G}_\epsilon = \boldsymbol{Z} + \boldsymbol{Z} * \boldsymbol{\epsilon} * \boldsymbol{G}_\epsilon$.

APPENDIX B: MOBILE CARRIER DENSITY IN THE EXCITED STATE

In the Mott insulating phase of the Hubbard model, a well-defined measure for the number of doublon or hole carriers is given by the total occupied spectral weight in the upper Hubbard band and the total unoccupied weight in the lower Hubbard band, respectively. The double occupancy, in contrast, depends on virtual charge fluctuations, which are nonzero also in the insulating ground state. Specifically, we define the occupied density of states as the partial Fourier transform $N_\sigma(t, \omega) = \mathrm{Im} \int_0^t ds \exp(-s^2/2\delta^2) \exp(-is\omega) G_\sigma^<(t - s, t)$, where $G_\sigma^<(s, s') = i\langle c_\sigma^\dagger(s') c_\sigma(s)\rangle$ is the local Green function and $\delta = 1.5$ ensures a smooth cutoff (which does not influence the results unless its inverse width is longer than the inverse of the gap). The spectrum $N_\sigma(\omega, t)$ is plotted in Fig. 6(a) for two different times, for the same quench parameters as in Fig. 5 of the main text. The right-hand panel shows the integrated density $W_\sigma(t) = \int_0^\infty d\omega N_\sigma(\omega, t)$. While the weight in the upper and lower band differs considerably between majority and minority spin, the integrated weight $W_\sigma(t)$ reflects the doublon density and is thus independent of σ. It is interesting to point out that as a function of time spectral weight is redistributed both between the lower Hubbard bands of the two spin components (which reflects the decay of the Néel order) and within the upper Hubbard band (which reflects the change of the kinetic energy of the doublons), while the
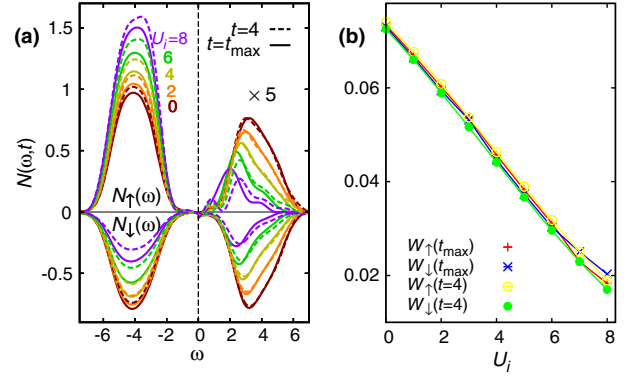
FIG. 6. (a) Occupied density of states $N_\sigma(\omega, t)$ after the quench: $t < 0$: $v = 0$ (Néel state); $0 \leq t < 0.5$: $v = 1$, $U = U_i$; $t \geq 0.5$: $v = 1$, $U = 8$, for various values of U_i; $N_\uparrow(\omega, t)$ and $N_\downarrow(\omega, t)$ refer to majority and minority spin, respectively, and the upper Hubbard band is scaled by a factor of 5. Dashed and solid lines denote time $t = 4$ and the largest simulation time $t = t_{max}$, respectively. (b) Integrated weight in the upper Hubbard band (red crosses and blue stars).

total weight in the upper band is roughly constant (see, e.g., Ref. [25]). For the analysis in the main text, we take $n_\delta = [W_\uparrow(t_{max}) + W_\downarrow(t_{max})]/2$.

APPENDIX C: SOLUTION FOR $U = 0$

For $U = 0$, the time evolution of the Néel state on the Bethe lattice can be obtained analytically by solving the Heisenberg equations of motion for the c operators, which provides a good check for the numerical implementation. For completeness, we provide this solution here. We choose site 0 to be the origin of the Bethe lattice, which is on the A sublattice without loss of generality. One can map the solution of equations of motion on the Bethe lattice to a one-dimensional semi-infinite chain by introducing operators that are invariant under all permutations of the branches of the Bethe lattice [62],

$$C_n = \frac{1}{\sqrt{Z_n}} \sum_{i:|i-0|=n} c_i, \qquad (C1)$$

where $Z_n = \sum_{i:|i-0|=n}$ is the number of sites on the nth nearest-neighbor shell. Then the action of the Hamiltonian is determined by $[H, C_j] = -\sum_{i=0}^\infty h_{ji} C_i$, with

$$h = \begin{pmatrix} 0 & 1 & 0 & 0 & \cdots \\ 1 & 0 & 1 & 0 & \\ 0 & 1 & 0 & 1 & \\ \vdots & & & & \ddots \end{pmatrix}. \qquad (C2)$$

Hence, eigenvectors for the eigenvalue ϵ satisfy the equations

$$\phi(\epsilon)_0 = 1, \tag{C3}$$

$$\phi(\epsilon)_1 = \epsilon, \tag{C4}$$

$$\epsilon\phi(\epsilon)_n = \phi(\epsilon)_{n+1} + \phi(\epsilon)_{n-1}, \tag{C5}$$

and are thus given by the Chebychev polynomials of the second kind [63], $\phi(\epsilon)_n = U_n(\epsilon/2)$ for $-1 \leq \epsilon/2 \leq 1$. The U_n can be conveniently written as

$$U_n[\cos(\theta)] = \frac{\sin[(n+1)\theta]}{\sin(\theta)}, \tag{C6}$$

from which one can also see the orthogonality

$$\int_{-1}^{1} dx w(x) U_n(x) U_m(x) = \delta_{mn}, \tag{C7}$$

with $w(x) = (2/\pi)\sqrt{1-x^2}$. Thus, the solution of the Heisenberg equations of motion for the local c operator [Eq. (C1)],

$$\frac{d}{dt}C_0(t) = i[H, C_0(t)], \qquad C_0(0) = C_0, \tag{C8}$$

is given by

$$C_0(t) = \sum_{n=0}^{\infty} \psi_n(t)C_n, \tag{C9}$$

$$\psi_n = \int_{-1}^{1} dx w(x) e^{-i2xt} U_n(x). \tag{C10}$$

This can be transformed to

$$\begin{aligned}
\psi_n &= \frac{2}{\pi}\int_{-1}^{1} d[\cos(\theta)]\sin(\theta)e^{-i2\cos(\theta)t}\frac{\sin[(n+1)\theta]}{\sin(\theta)} \\
&= \frac{2}{\pi}\int_0^{\pi} d\theta \sin[(n+1)\theta]\frac{1}{2it}\partial_\theta e^{-i2\cos(\theta)t} \\
&= \frac{i}{\pi t}\int_0^{\pi} d\theta e^{-i2\cos(\theta)t}\partial_\theta \sin[(n+1)\theta] \\
&= \frac{i(n+1)}{\pi t}\int_0^{\pi} d\theta e^{-i2\cos(\theta)t}\cos[(n+1)\theta] \\
&= \frac{i(n+1)}{\pi t}\int_0^{\pi} d\theta e^{i2\cos(\theta)t}\cos[(n+1)\theta](-1)^{n+1} \\
&= (-i)^n(n+1)\frac{J_{n+1}(2t)}{t}. \tag{C11}
\end{aligned}$$

The second-to-last line is a variable transformation $\theta \to \pi - \theta$, and in the last line we use the integral representation of the Bessel function [63],

$$J_n(z) = \frac{(-i)^n}{\pi}\int_0^{\pi} d\theta \cos(n\theta)e^{iz\cos(\theta)}. \tag{C12}$$

The explicit form of the C operators can be used to obtain local observables,

$$\langle\Psi|c_\sigma^\dagger(t)c_{\sigma'}(t)|\Psi\rangle = \sum_{n,m}\psi_n^*(t)\psi_m(t)\langle\Psi|C_{n\sigma}^\dagger C_{m\sigma'}|\Psi\rangle \tag{C13}$$

$$= \sum_n |\psi_n(t)|^2\langle\Psi|C_{n\sigma}^\dagger C_{n\sigma'}|\Psi\rangle, \tag{C14}$$

where the expectation values are simple initial state values. We start by evaluating the time evolution of the magnetic order, $n_\uparrow - n_\downarrow$, at site 0, in the classical Néel state. For the latter, we have

$$\langle\Psi_{\text{Néel}}|C_{n\uparrow}^\dagger C_{n\uparrow} - C_{n\downarrow}^\dagger C_{n\downarrow}|\Psi_{\text{Néel}}\rangle = (-1)^n, \tag{C15}$$

and hence,

$$\langle\Psi_{\text{Néel}}|n_\uparrow(t) - n_\downarrow(t)|\Psi_{\text{Néel}}\rangle = \sum_{n=0}^{\infty}(-1)^n\frac{(n+1)^2 J_{n+1}(2t)^2}{t^2} \tag{C16}$$

(where the summation index has been shifted by one). We can now use Gegenbauer's addition theorem for Bessel functions [63] to obtain the final result,

$$\langle\Psi_{\text{Néel}}|n_\uparrow(t) - n_\downarrow(t)|\Psi_{\text{Néel}}\rangle = \frac{J_1(4t)}{2t}, \tag{C17}$$

which fits the numerics.

Next, we compute site 0 expectation values on the probe site. Now the initial state is a superposition:

$$|\Psi\rangle = (|\Psi_{\text{Néel}}, \uparrow\rangle + |\Psi_{\text{Néel}}, \downarrow\rangle)/\sqrt{2}, \tag{C18}$$

$$|\Psi_{\text{Néel}}, \sigma\rangle = c_{0,\sigma}^\dagger c_{0,\uparrow}|\Psi_{\text{Néel}}\rangle. \tag{C19}$$

We evaluate the cross-spin expectation values:

$$\begin{aligned}
\langle S_0^+(t)\rangle &= \langle\Psi|c_{0\uparrow}^\dagger(t)c_{0\downarrow}(t)\Psi\rangle \\
&= \sum_n |\psi_n(t)|^2\langle\Psi|C_{n\uparrow}^\dagger C_{n\downarrow}|\Psi\rangle. \tag{C20}
\end{aligned}$$

Spin-flip expectation values are only nonzero in the initial state at site 0, where we have

$$\langle S_0^+(t) \rangle = |\psi_0(t)|^2 \langle \Psi | c_{0\uparrow}^\dagger c_{0\downarrow} | \Psi \rangle \tag{C21}$$

$$= \frac{J_1(2t)^2}{2t^2}. \tag{C22}$$

Hence, $S_0^+(t)$ is purely real, so that the dynamics is entirely longitudinal in the S_x-S_y plane:

$$\langle S_0^x(t) \rangle = \frac{J_1(2t)^2}{2t^2}, \tag{C23}$$

$$\langle S_0^y(t) \rangle = 0. \tag{C24}$$

---

[1] A. Polkovnikov, K. Sengupta, A. Silva, and M. Vengalattore, *Colloquium: Nonequilibrium Dynamics of Closed Interacting Quantum Systems*, Rev. Mod. Phys. **83**, 863 (2011).

[2] M. Rigol, V. Dunjko, V. Yurovsky, and M. Olshanii, *Relaxation in a Completely Integrable Many-Body Quantum System: An Ab Initio Study of the Dynamics of the Highly Excited States of 1D Lattice Hard-Core Bosons*, Phys. Rev. Lett. **98**, 050405 (2007).

[3] T. Langen, S. Erne, R. Geiger, B. Rauer, Th. Schweigler, M. Kuhnert, W. Rohringer, I. E. Mazets, Th. Gasenzer, and J. Schmiedmayer, *Experimental Observation of a Generalized Gibbs Ensemble*, Science **348**, 207 (2015).

[4] J. Berges, Sz. Borsányi, and C. Wetterich, *Prethermalization*, Phys. Rev. Lett. **93**, 142002 (2004).

[5] M. Moeckel and S. Kehrein, *Interaction Quench in the Hubbard Model*, Phys. Rev. Lett. **100**, 175702 (2008).

[6] M. Kollar, F. A. Wolf, and M. Eckstein, *Generalized Gibbs Ensemble Prediction of Prethermalization Plateaus and Their Relation to Nonthermal Steady States in Integrable Systems*, Phys. Rev. B **84**, 054304 (2011).

[7] M. Gring, M. Kuhnert, T. Langen, T. Kitagawa, B. Rauer, M. Schreitl, I. Mazets, D. Adu Smith, E. Demler, and J. Schmiedmayer, *Relaxation and Prethermalization in an Isolated Quantum System*, Science **337**, 1318 (2012).

[8] C. Kollath, A. M. Läuchli, and E. Altman, *Quench Dynamics and Nonequilibrium Phase Diagram of the Bose-Hubbard Model*, Phys. Rev. Lett. **98**, 180601 (2007).

[9] M. Eckstein, M. Kollar, and P. Werner, *Thermalization after an Interaction Quench in the Hubbard Model*, Phys. Rev. Lett. **103**, 056403 (2009).

[10] P. Barmettler, M. Punk, V. Gritsev, E. Demler, and E. Altman, *Relaxation of Antiferromagnetic Order in Spin-1/2 Chains Following a Quantum Quench*, Phys. Rev. Lett. **102**, 130603 (2009).

[11] M. Schiró and M. Fabrizio, *Time-Dependent Mean Field Theory for Quench Dynamics in Correlated Electron Systems*, Phys. Rev. Lett. **105**, 076401 (2010).

[12] B. Sciolla and G. Biroli, *Quantum Quenches and Off-Equilibrium Dynamical Transition in the Infinite-Dimensional Bose-Hubbard Model*, Phys. Rev. Lett. **105**, 220401 (2010).

[13] N. Tsuji, M. Eckstein, and P. Werner, *Nonthermal Antiferromagnetic Order and Nonequilibrium Criticality in the Hubbard Model*, Phys. Rev. Lett. **110**, 136404 (2013).

[14] P. Beaud *et al.*, *A Time-Dependent Order Parameter for Ultrafast Photoinduced Phase Transitions*, Nat. Mater. **13**, 923 (2014).

[15] H. Ehrke, R. I. Tobey, S. Wall, S. A. Cavill, M. Först, V. Khanna, T. Garl, N. Stojanovic, D. Prabhakaran, A. T. Boothroyd, M. Gensch, A. Mirone, P. Reutler, A. Revcolevschi, S. S. Dhesi, and A. Cavalleri, *Photoinduced Melting of Antiferromagnetic Order in $La_{0.5}Sr_{1.5}MnO_4$ Measured Using Ultrafast Resonant Soft X-Ray Diffraction*, Phys. Rev. Lett. **106**, 217401 (2011).

[16] H. Ichikawa, Sh. Nozawa, T. Sato, A. Tomita, K. Ichiyanagi, M. Chollet, L. Guerin, N. Dean, A. Cavalleri, Sh. Adachi, T. Arima, H. Sawa, Y. Ogimoto, M. Nakamura, R. Tamaki, K. Miyano, and Sh. Koshihara, *Transient Photoinduced 'Hidden' Phase in a Manganite*, Nat. Mater. **10**, 101 (2011).

[17] D. Greif, Th. Uehlinger, G. Jotzu, L. Tarruell, and T. Esslinger, *Short-Range Quantum Magnetism of Ultracold Fermions in an Optical Lattice*, Science **340**, 1307 (2013).

[18] R. A. Hart, M. Duarte, P. T. Yang, X. Liu, Th. Paiva, E. Khatami, R. T. Scalettar, N. Trivedi, D. A. Huse, and R. G. Hulet, *Observation of Antiferromagnetic Correlations in the Hubbard Model with Ultracold Atoms*, Nature (London) **519**, 211 (2015).

[19] S. Trotzky, Y-A. Chen, A. Flesch, I. P. McCulloch, U. Schollwöck, J. Eisert, and I. Bloch, *Probing the Relaxation towards Equilibrium in an Isolated Strongly Correlated One-Dimensional Bose Gas*, Nat. Phys. **8**, 325 (2012).

[20] M. Schreiber, S. S. Hodgman, P. Bordia, H. P. Lüschen, M. H. Fischer, R. Vosk, E. Altman, U. Schneider, and I. Bloch, *Observation of Many-Body Localization of Interacting Fermions in a Quasi-Random Optical Lattice*, Science **349**, 842 (2015).

[21] D. Pertot, A. Sheikhan, E. Cocchi, L. A. Miller, J. E. Bohn, M. Koschorreck, M. Köhl, and C. Kollath, *Relaxation Dynamics of a Fermi Gas in an Optical Superlattice*, Phys. Rev. Lett. **113**, 170403 (2014).

[22] R. C. Brown, R. Wyllie, S. B. Koller, E. Goldschmidt, M. Foss-Feig, and J. V. Porto, *2D Superexchange Mediated Magnetization Dynamics in an Optical Lattice*, Science **348**, 540 (2015).

[23] J. H. Mentink and M. Eckstein, *Ultrafast Quenching of the Exchange Interaction in a Mott Insulator*, Phys. Rev. Lett. **113**, 057201 (2014).

[24] M. Mierzejewski, L. Vidmar, J. Bonča, and P. Prelovšek, *Nonequilibrium Quantum Dynamics of a Charge Carrier Doped into a Mott Insulator*, Phys. Rev. Lett. **106**, 196401 (2011).

[25] P. Werner, N. Tsuji, and M. Eckstein, *Nonthermal Symmetry-Broken States in the Strongly Interacting Hubbard Model*, Phys. Rev. B **86**, 205101 (2012).

[26] J. Kogoj, Zala Lenarčič, D. Golež, M. Mierzejewski, P. Prelovšek, and J. Bonča, *Multistage Dynamics of the Spin-Lattice Polaron Formation*, Phys. Rev. B **90**, 125104 (2014).

[27] M. Eckstein and P. Werner, *Ultrafast Separation of Photo-doped Carriers in Mott Antiferromagnets*, Phys. Rev. Lett. **113**, 076405 (2014).

[28] M. Eckstein and Ph. Werner, *Ultra-Fast Photo-Carrier Relaxation in Mott Insulators with Short-Range Spin Correlations*, arXiv:1410.3956.

[29] D. Golež, J. Bonča, M. Mierzejewski, and L Vidmar, *Mechanism of Ultrafast Relaxation of a Photo-Carrier in Antiferromagnetic Spin Background*, Phys. Rev. B **89**, 165118 (2014).

[30] H. Okamoto, T. Miyagoe, K. Kobayashi, H. Uemura, H. Nishioka, H. Matsuzaki, A. Sawa, and Y. Tokura, *Ultrafast Charge Dynamics in Photoexcited* Nd_2CuO_4 *and* La_2CuO_4 *Cuprate Compounds Investigated by Femtosecond Absorption Spectroscopy*, Phys. Rev. B **82**, 060513 (2010).

[31] H. Okamoto, T. Miyagoe, K. Kobayashi, H. Uemura, H. Nishioka, H. Matsuzaki, A. Sawa, and Y. Tokura, *Photo-induced Transition from Mott Insulator to Metal in the Undoped Cuprates* Nd_2CuO_4 *and* La_2CuO_4, Phys. Rev. B **83**, 125102 (2011).

[32] S. Dal Conte *et al.*, *Snapshots of the Retarded Interaction of Charge Carriers with Ultrafast Fluctuations in Cuprates*, Nat. Phys. **11**, 421 (2015).

[33] S. A. Hamerla and G. S. Uhrig, *Dynamical Transition in Interaction Quenches of the One-Dimensional Hubbard Model*, Phys. Rev. B **87**, 064304 (2013).

[34] S. A. Hamerla and G. S. Uhrig, *Interaction Quenches in the Two-Dimensional Fermionic Hubbard Model*, Phys. Rev. B **89**, 104301 (2014).

[35] N. Tsuji, P. Barmettler, H. Aoki, and P. Werner, *Non-equilibrium Dynamical Cluster Theory*, Phys. Rev. B **90**, 075117 (2014).

[36] P. Barmettler, M. Punk, V. Gritsev, E. Demler, and E. Altman, *Quantum Quenches in the Anisotropic Spin-1/2 Heisenberg Chain: Different Approaches to Many-Body Dynamics Far from Equilibrium*, New J. Phys. **12**, 055017 (2010).

[37] W. Liu and N. Andrei, *Quench Dynamics of the Anisotropic Heisenberg Model*, Phys. Rev. Lett. **112**, 257204 (2014).

[38] M. Heyl, *Dynamical Quantum Phase Transitions in Systems with Broken-Symmetry Phases*, Phys. Rev. Lett. **113**, 205701 (2014).

[39] M. Ojekhile, R. Höppner, H. Moritz, and L. Mathey, *Sudden and Slow Quenches into the Antiferromagnetic Phase of Ultracold Fermions*, arXiv:1308.5680.

[40] A. Bauer, F. Dorfner, and F. Heidrich-Meisner, *Temporal Decay of Néel Order in the One-Dimensional Fermi-Hubbard Model*, Phys. Rev. A **91**, 053628 (2015).

[41] H. Aoki, N. Tsuji, M. Eckstein, M. Kollar, T. Oka, and P. Werner, *Nonequilibrium Dynamical Mean-Field Theory and Its Applications*, Rev. Mod. Phys. **86**, 779 (2014).

[42] M. Eckstein and P. Werner, *Nonequilibrium Dynamical Mean-Field Calculations Based on the Noncrossing Approximation and Its Generalizations*, Phys. Rev. B **82**, 115115 (2010).

[43] M. Eckstein and P. Werner, *Damping of Bloch Oscillations in the Hubbard Model*, Phys. Rev. Lett. **107**, 186406 (2011).

[44] N. Tsuji and P. Werner, *Nonequilibrium Dynamical Mean-Field Theory Based on Weak-Coupling Perturbation Expansions: Application to Dynamical Symmetry Breaking in the Hubbard Model*, Phys. Rev. B **88**, 165115 (2013).

[45] Ch. Gramsch, K. Balzer, M. Eckstein, and M. Kollar, *Hamiltonian-Based Impurity Solver for Nonequilibrium*

[46] *Dynamical Mean-Field Theory*, Phys. Rev. B **88**, 235106 (2013).

[46] K. Balzer, Zheng Li, O. Vendrell, and M. Eckstein, *Multi-configuration Time-Dependent Hartree Impurity Solver for Nonequilibrium Dynamical Mean-Field Theory*, Phys. Rev. B **91**, 045136 (2015).

[47] F. A. Wolf, I. P. McCulloch, and U. Schollwöck, *Solving Nonequilibrium Dynamical Mean-Field Theory Using Matrix Product States*, Phys. Rev. B **90**, 235131 (2014).

[48] W. Metzner and D. Vollhardt, *Correlated Lattice Fermions in* $d = \infty$ *Dimensions*, Phys. Rev. Lett. **62**, 324 (1989).

[49] K. Balzer and M. Eckstein, *Auxiliary Hamiltonian Representation of the Nonequilibrium Dyson Equation*, Phys. Rev. B **89**, 035148 (2014).

[50] The maximum Néel temperature in equilibrium is $T_{\text{Néel}} = 0.2$, around $U = 4$; see A. Koga and P. Werner, *Low-Temperature Properties of the Infinite-Dimensional Attractive Hubbard Model*, Phys. Rev. A **84**, 023638 (2011).

[51] K. Winkler, G. Thalhammer, F. Lang, R. Grimm, J. H. Denschlag, A. J. Daley, A. Kantian, H. P. Büchler, and P. Zoller, *Repulsively Bound Atom Pairs in an Optical Lattice*, Nature (London) **441**, 853 (2006).

[52] R. Sensarma, D. Pekker, E. Altman, E. Demler, N. Strohmaier, D. Greif, R. Jördens, L. Tarruell, H. Moritz, and T. Esslinger, *Lifetime of Double Occupancies in the Fermi-Hubbard Model*, Phys. Rev. B **82**, 224302 (2010).

[53] M. Eckstein and P. Werner, *Thermalization of a Pump-Excited Mott Insulator*, Phys. Rev. B **84**, 035122 (2011).

[54] P. Werner, A. Comanac, L. de Medici, M. Troyer, and A. J. Millis, *Continuous-Time Solver for Quantum Impurity Models*, Phys. Rev. Lett. **97**, 076405 (2006).

[55] J. H. Mentink, K. Balzer, and M. Eckstein, *Ultrafast and Reversible Control of the Exchange Interaction in Mott Insulators*, Nat. Commun. **6**, 6708 (2015).

[56] Note that in Ref. [23] a modification of the J_{ex} was observed after photodoping. However, a quantitative comparison to the current setup up to a few percent is not meaningful, because exchange interactions defined by the spin response are expected to depend both weakly on the canting angle of the spin with respect to its neighbors (non-Heisenberg-like terms play a role for large angles) and on time.

[57] In a cold-atom experiment, one could switch off the hopping slowly compared to the Mott gap, in order to adiabatically reduce the quantum fluctuations.

[58] E. Dagotto, *Correlated Electrons in High-Temperature Superconductors*, Rev. Mod. Phys. **66**, 763 (1994).

[59] M. Knap, A. Kantian, T. Giamarchi, I. Bloch, M. D. Lukin, and E. Demler, *Probing Real-Space and Time-Resolved Correlation Functions with Many-Body Ramsey Interferometry*, Phys. Rev. Lett. **111**, 147205 (2013).

[60] Götz S. Uhrig, *Interaction Quenches of Fermi Gases*, Phys. Rev. A **80**, 061602 (2009).

[61] A. Georges, G. Kotliar, W. Krauth, and M. J. Rozenberg, *Dynamical Mean-Field Theory of Strongly Correlated Fermion Systems and the Limit of Infinite Dimensions*, Rev. Mod. Phys. **68**, 13 (1996).

[62] G. D. Mahan, *Energy Bands of the Bethe Lattice*, Phys. Rev. B **63**, 155110 (2001).

[63] M. Abramowitz and I. Stegun, *Handbook of Mathematical Functions* (Dover Publications, New York, 1965).

5. Related technical results

5.1. Spectral functions and time evolution from the Chebyshev recursion

The study of Wolf *et al.* (2014a) left several open questions regarding computations using the Chebyshev expansion: in particular whether the MPS represented Chebyshev expansion would be more strongly entangled than its Fourier counterpart. Furthermore: it was unclear under which conditions *linear prediction* could be applied. The following article (Wolf *et al.*, 2015b), settles these questions (i) by investigating the convergence behavior of sequences of expansion coefficients, and (ii) by showing that in a certain limit, the Chebyshev expansion becomes equivalent to the Fourier expansion.

▷ *Spectral functions and time evolution from the Chebyshev recursion*
  FA Wolf, JA Justiniano, IP McCulloch, and U Schollwöck
  Phys. Rev. B **91** 115144 (2015)

Spectral functions and time evolution from the Chebyshev recursion

F. Alexander Wolf,[1] Jorge A. Justiniano,[1] Ian P. McCulloch,[2] and Ulrich Schollwöck[1]

[1]*Department of Physics, Arnold Sommerfeld Center for Theoretical Physics, LMU Munich, Theresienstrasse 37, 80333 München, Germany*
[2]*Centre for Engineered Quantum Systems, School of Physical Sciences, The University of Queensland, Brisbane, Queensland 4072, Australia*

We link linear prediction of Chebyshev and Fourier expansions to analytic continuation. We push the resolution in the Chebyshev-based computation of $T = 0$ many-body spectral functions to a much higher precision by deriving a modified Chebyshev series expansion that allows to reduce the expansion order by a factor $\sim \frac{1}{6}$. We show that in a certain limit the Chebyshev technique becomes equivalent to computing spectral functions via time evolution and subsequent Fourier transform. This introduces a novel recursive time-evolution algorithm that instead of the group operator e^{-iHt} only involves the action of the generator H. For quantum impurity problems, we introduce an adapted discretization scheme for the bath spectral function. We discuss the relevance of these results for matrix product state (MPS) based DMRG-type algorithms, and their use within the dynamical mean-field theory (DMFT). We present strong evidence that the Chebyshev recursion extracts less spectral information from H than time evolution algorithms when fixing a given amount of created entanglement.

I. INTRODUCTION

Expanding the spectral density $A(\omega)$ of an operator H in the monomes ω^n via the moments

$$\mu_n^{\mathrm{mon}} = \int d\omega \, A(\omega) \omega^n$$

is a tool that originates in the early days of quantum mechanics [1]. Computing these moments iteratively though is numerically unstable [2,3] and one replaced expansions in ω^n by expansions in such polynomials $p_n(\omega)$ of degree n that can be stably computed [4,5]. A prominent example for $p_n(\omega)$ are Chebyshev polynomials, whose associated three-term recursion is stable as it does not admit a so-called *minimal* [2] solution.

After the development of stable recursions, the next step in the mid 1990s was the introduction of kernels that damp the erroneous *Gibbs oscillations* of truncated polynomial expansions of discontinuous functions [6–8], which lead to the *kernel polynomial approximation*. It deals with redefined series expansions that represent the convolution of the expanded function with a *broadening kernel*, like a Gaussian or Lorentzian. This technique has been reviewed in Ref. [1] and more recently in Ref. [9] from a numerical linear algebra perspective.

In this paper, we drop the idea of such *broadening* kernels in frequency space or the equivalent *damping* or *windowing* kernels in the associated Fourier or Chebyshev expansions. Instead, we employ the fundamentally different technique of *linear prediction* [10]. Linear prediction is a *linear* recursive reformulation (Appendix C) of the *nonlinear* problem to fit the surrogate function

$$g(t) = \sum_i \alpha_i e^{i\omega_i t}, \quad \alpha_i, \omega_i \in \mathbb{C}, t \in \mathbb{R}, \quad (1)$$

to given numerical data $\{t_n, g_n\}$. Due to linearity, linear prediction is able to treat superpositions of hundreds of terms, and by that reliably extracts much information about an underlying function from its *local* knowledge $\{t_n, g_n\}$. In

order for this to be meaningful, the underlying function, e.g., a Green's function, must be compatible with (1).

In particular, we note that Eq. (1) can serve as an ansatz for *analytic continuation* of a zero-temperature Green's function

$$G(t) = -i\langle \psi_0 | e^{-i(H-E_0)t} | \psi_0 \rangle, \quad (2)$$

where $|\psi_0\rangle$ is a single-particle excitation of the ground state $|E_0\rangle$ of H, for example, the creation of a fermion $|\psi_0\rangle = c^\dagger |E_0\rangle$. Note that in the case of fermions, Eq. (2) describes only the $t > 0$ contribution [usually more precisely denoted $G^>(t)$] of the *full* fermionic Green's function. $G(t)$ is analytic everywhere in the complex plane except for $t \to i\infty$ and thereby allows for an analytic continuation of $G(t)$ from a local description $\{t_n, G(t_n)\}$ to the domain $[t_0, \infty)$. This analytic continuation is highly different from the ill-conditioned problem of continuing the frequency-space represented Green's function from a domain in the complex plane (e.g., the imaginary-frequency axis or a parallel of the real-frequency axis) to the real-frequency axis, where the frequency-space Green's function has poles.

In the context of Green's functions, linear prediction has for the first time been used to extrapolate the time evolution of the *spin structure factor* in the one-dimensional Heisenberg model [11,12]. While for the spin-1 model it was clear that the ansatz (1) is justified as the time evolution is dominated by a small number of *magnons* whose excitation energies correspond directly to the frequencies ω_i in Eq. (1) [11], this was not the case for the spin-$\frac{1}{2}$ model [12]. In the latter, *spinons* dominate, which lead to a (infinitely) high number of poles on the real-frequency axis, and the *direct* correspondence of pole energies and frequencies ω_i in Eq. (1) is lost. Still, the ansatz works [12] in an approximate sense by extracting effective frequencies.

For the computation of spectral functions, the use of linear prediction for the time evolution of Green's functions provides a highly attractive alternative approach to the usual *damping* or *windowing* in real-time or *broadening* in frequency space: an approach that *enhances* resolution in frequency space. Up to now, it is not entirely clear in which cases this is controlled. On

the other hand, the approach of *damping* the truncated series expansion cannot be considered controlled, too: although a broadened function $f_\eta(\omega)$, which is for Gaussian broadening given by $f_\eta(\omega) = \frac{1}{\eta\sqrt{2\pi}} \int d\omega' e^{-(\omega'-\omega)^2/2\eta^2} f(\omega')$, converges uniformly to the underlying original function $f(\omega)$ for $\eta \to 0$, extraction of information (*deconvolution*) from $f_\eta(\omega)$ about $f(\omega)$ is uncontrolled as it corresponds to the problem of analytic continuation from a domain in the complex plane to the real axis.

Recently, Ref. [13] suggested to extrapolate the Chebyshev expansion of a spectral function using linear prediction, albeit only justified by the empirical success. In the remainder of this introduction, we place these results in the context of the preceding discussion, and by that put this approach on more firm grounds.

A. Chebyshev and Fourier transformation basics

The Chebyshev polynomials of the first kind

$$T_n(x) = \cos(n \arccos(x)) \tag{3}$$

can be generated by the recursion

$$T_n(x) = 2x T_{n-1}(x) - T_{n-2}(x), \quad T_1 = x, \quad T_0 = 1, \tag{4}$$

which is numerically stable if $|x| \leqslant 1$. Chebyshev polynomials are orthonormal with respect to the weighted inner product

$$\int_{-1}^{1} dx \, w_n(x) T_m(x) T_n(x) = \delta_{nm}, \tag{5a}$$

$$w_n(x) = \frac{2 - \delta_{n0}}{\pi \sqrt{1 - x^2}}. \tag{5b}$$

Any integrable function $f(x)|_{x \in [-1,1]}$ can be expanded in $T_n(x)$:

$$f(x) = \sum_{n=0}^{\infty} w_n(x) \mu_n T_n(x), \tag{6a}$$

$$\mu_n = \int_{-1}^{1} dx \, T_n(x) f(x), \tag{6b}$$

where the definition of the so-called *Chebyshev moments* μ_n via the *nonweighted* inner product (6b) follows when applying $\int_{-1}^{1} dx \, T_m(x) \dots$ to both sides of (6a).

Analogously, any integrable function $f(\omega)|_{\omega \in [-\frac{a}{2}, \frac{a}{2}]}$, where $a \in \mathbb{R}$, can be expanded in a Fourier series:

$$f(\omega) = \frac{1}{2a\pi} \sum_{n=-\infty}^{\infty} e^{i\omega t_n} f(t_n), \tag{7a}$$

$$f(t_n) = \int_{-a/2}^{a/2} d\omega \, e^{-i\omega t_n} f(\omega), \quad t_n = \frac{n}{a}, \tag{7b}$$

which represents a *Fourier transform* for $a \to \infty$.

B. Expansion of a spectral function

Consider now the expansion of the spectral function $A(\omega)$ of a Hamilton operator H with respect to a reference energy

E_{ref} and a state $|\psi_0\rangle$ as in Eq. (2):

$$A(\omega) = \langle \psi_0 | \delta(\omega - (H - E_{\mathrm{ref}})) | \psi_0 \rangle. \tag{8}$$

The spectral function is related to the Green's function of (2) via its Fourier transform: $A(\omega) = -\frac{1}{\pi} \mathrm{Im} \, G(\omega + i0^+)$.

The coefficients of the Fourier expansion can be computed by inserting an identity of eigenstates $\sum_i |E_i\rangle\langle E_i|$ in the integral over the delta function $\delta(\omega - (H - E_{\mathrm{ref}}))$:

$$f(t_n) = \int_{-a/2}^{a/2} d\omega \, e^{-i\omega t_n} A(\omega) = \langle \psi_0 | \psi(t_n) \rangle, \tag{9a}$$

$$|\psi(t_n)\rangle = e^{-i(H - E_{\mathrm{ref}})t_n} |\psi_0\rangle, \quad t_n = \frac{n}{a}. \tag{9b}$$

In order for (9) to hold true, a must be chosen large enough so that the support of $A(\omega)$ is contained in $[-\frac{a}{2}, \frac{a}{2}]$. A sufficient condition for that is $\mathrm{spec}(H - E_{\mathrm{ref}}) \subset [-\frac{a}{2}, \frac{a}{2}]$, which is possible as we consider operators H with bounded spectra. Equation (9b) makes it obvious that a has the meaning of an inverse time step.

To compute the coefficients for the Chebyshev expansion, we need to consider a spectral function whose support is contained in $[-1, 1]$. For this, introduce a rescaled and shifted version of H with appropriately chosen constants a and b:

$$\mathcal{H}_{a,b} = \frac{H - E_{\mathrm{ref}}}{a} + b, \quad x = \frac{\omega}{a} + b, \tag{10}$$

where a can again be considered an "inverse time step" and $\mathcal{H}$ is dimensionless. Note that in Ref. [14], the definition of b differed from the one here by a factor a. Then

$$\mathcal{A}_{a,b}(x) = \langle \psi_0 | \delta(x - \mathcal{H}_{a,b}) | \psi_0 \rangle \tag{11}$$

yields the original spectral function via $A(\omega) = \frac{1}{a} \mathcal{A}(\frac{\omega}{a} + b)$, where we omitted to specify the indices a, b, as in most of the rest of this paper. The Chebyshev moments for $\mathcal{A}(x)$ can be computed analogously to the Fourier coefficients (9):

$$\mu_n = \int_{-1}^{1} dx \, \mathcal{A}(x) T_n(x) = \langle \psi_0 | \psi_n \rangle, \tag{12a}$$

$$|\psi_n\rangle = T_n(\mathcal{H}) |\psi_0\rangle. \tag{12b}$$

Inserting the recursive definition (4) of $T_n(\mathcal{H})$ in the definition (12b) of $|\psi_n\rangle$, one obtains a practical calculation scheme for the power series expansion of $T_n(\mathcal{H})$, and by that for the *Chebyshev states* $|\psi_n\rangle$ in Eq. (12):

$$|\psi_n\rangle = 2\mathcal{H}|\psi_{n-1}\rangle - |\psi_{n-2}\rangle, \quad |\psi_1\rangle = \mathcal{H}|\psi_0\rangle. \tag{13}$$

C. Analytic continuation

A comparison of (9b) and (12b) clarifies why linear prediction is an equally justified approach for Chebyshev and Fourier expansions.

Rewriting the "evolution operators" that appear in Eq. (9b) and (12b) as

$$\exp(-in\mathcal{H}_{a,b=0}) \quad \text{and} \quad \cos(n \arccos(\mathcal{H}_{a,b})) \tag{14}$$

makes it clear that we deal with *analytic* functions of n if we consider n as a continuous complex variable. Using (9a) and (12a), this makes the Fourier and the Chebyshev coefficients $f(t_n)$ and μ_n analytic functions of n, too. In addition,

Re $\exp(-in\mathcal{H}_{a,b}) = \cos(n\mathcal{H}_{a,b})$ shows that the real part of the functional dependence of the time-evolution operator on n is the same as for the "Chebyshev evolution operator," when neglecting a redefinition of oscillation frequencies. As this redefinition can be accounted for by the fitting procedure, the particular form of the surrogate function $g(t)$ in Eq. (1) is equally suited to analytically continue both types of expansions. A fundamental theorem from complex analysis then tells us that if linear prediction provides us with a function $g(t)$ that *locally agrees* with $f(t_n)$ or μ_n, we know that this function globally agrees with $f(t_n)$ or μ_n. Of course, in practice these arguments are to be taken with care, as we will never numerically find a function $g(t_n)$ that *agrees exactly* with the local data $\{g_n, t_n\}$.

D. Outline of the paper

We will first study the convergence properties of the Chebyshev expansion of discontinuous (spectral) functions in the thermodynamic limit. This allows to derive a new scheme for a Chebyshev series definition that leads to an exponential convergence and allows to reduce expansion orders in practical calculations by a factor $\sim\frac{1}{6}$ (Sec. II). We then apply these results to the computation of spectral functions for finite systems (Sec. III), and discuss the relevance for matrix product state (MPS) based computations (Sec. IV). After that, we describe the approximate equivalence of the Chebyshev recursion to time evolution and show how this leads to a time-evolution algorithm (Sec. V). Finally, we conclude the paper (Sec. VI).

II. SPECTRAL FUNCTIONS IN THE THERMODYNAMIC LIMIT

A spectral function for a system of finite size L has a *finite-size peak* structure due to an agglomeration of eigenvalues that is not present in the thermodynamic limit. In a weakly interacting system, this agglomeration happens around the positions of the eigenvalues of the corresponding noninteracting (single-particle) system. This argument gives us the best, though still very rough, estimate W_{single}/L for the spacing of finite-size peaks, where W_{single} is the single-particle bandwidth. At a much smaller spacing than that, spectral functions have an underlying delta-peak structure, as is obvious from definition (8), which can be rewritten as

$$A(\omega) = \sum_i W_i \, \delta(\omega - (E_i - E_{\text{ref}})), \qquad (15)$$

with weights $W_i = |\langle\psi_0|E_i\rangle|^2$. The delta-peak structure merges to a (sectionwise) smooth function only in the thermodynamic limit.

Expanding the spectral function of a finite-size system in orthogonal polynomials is a very efficient way to *not* resolve either finite-size peaks or the delta-peak structure, but to extract only the smooth function of the thermodynamic limit, as, e.g., discussed in Ref. [14]. It is this function of the thermodynamic limit that we are interested in, and for which we start our discussion.

A. Discontinuity of spectral functions

The state $|\psi_0\rangle$ and the energy E_{ref} in Eq. (15) are generally associated to the ground state of a certain symmetry sector

N of H, which for fermions is typically a particle number. The reference energy for $|\psi_0\rangle = c^\dagger|E_0\rangle$ then is the Fermi energy, which is the ground-state energy $E_{\text{ref}} = E_0^{N-1}$ of the contiguous symmetry sector of $|\psi_0\rangle$ (or $E_{\text{ref}} = E_0^{N+1}$ for a hole excitation). The weights $W_i = |\langle\psi_0|E_i\rangle|^2$ in the spectral function (15) can be nonzero only for eigenstates $|E_i\rangle$ and eigenvalues E_i from the sector N. The particular meaning of E_{ref} as a ground-state energy then implies that even if the global spectral function

$$A_{\text{global}}(\omega) = \sum_i \delta(\omega - (E_i - E_{\text{ref}})) \qquad (16)$$

is smooth, the weights W_i generally introduce a discontinuity at $\omega = 0$ (we use the term *global* here, as $|\psi_0\rangle$ usually is a *local* excitation associated with a certain quantum number).

B. Convergence of Chebyshev series expansions

The convergence of the Chebyshev moments $\mu_n \to 0$ of a function $f(x)$ *in the limit* $n \to \infty$ can be characterized by the degree of differentiability of $f(x)$, similar to a Fourier expansion [15]. Let k denote the highest integer for which the kth derivative of $f(x)$ is integrable; if $f(x)$ is smooth ($k = \infty$), the envelope of μ_n converges exponentially to zero with respect to n; if $f(x)$ is a step function ($k = 1$), the envelope converges algebraically with $\frac{1}{n}$; and if $f(x)$ is a delta function, the envelope remains constant. In general, the order of convergence is *at least* $\frac{1}{n^k}$. Although in Ref. [15], this is stated for moments computed with the *weighted* inner product (5b), it also holds for moments computed using (6b) (see Appendix A). In practice, we are not interested in the limit $n \to \infty$, but rather in intermediate values of n: but also here, the degree of differentiability of $A(\omega)$ helps us to learn something about the convergence of μ_n.

Consider a typical discontinuous spectral function $A^>(\omega)$ as shown in the top panel of Fig. 1. Its corresponding Chebyshev moments $\mu_n^>$ are computed by numerically integrating (6b) and shown in the bottom panel of Fig. 1 as blue circles. The blue line in the inset shows the envelope of $\mu_n^>$, which evidently decreases algebraically to zero.

Now note that continuity of $A^>(\omega)$ at $\omega = 0$ can easily be restored by defining

$$\widetilde{A}^>(\omega) = A^>(\omega) - A^>(0). \qquad (17)$$

The green crosses (lines) in the bottom panel of Fig. 1 show that the Chebyshev moments $\widetilde{\mu}_n^>$ of $\widetilde{A}^>(\omega)$ converge exponentially for the values of n considered in the plot, i.e., *qualitatively* differently than $\mu_n^>$. This is observed although $\widetilde{A}^>(\omega)$ is not smooth, but only once differentiable (kink in first derivative at $\omega = 0$).

While the construction of $\widetilde{A}^>(\omega)$ is completely general, for the particular case of a fermionic spectral function, another way of constructing a continuous function from $A^>(\omega)$ has been favored; in the appendix of Ref. [17], it was mentioned that the Chebyshev expansion of the *full* spectral function

$$A(\omega) = A^>(\omega) + A^<(-\omega),$$
$$A^{\gtrless}(\omega) = \langle\psi_0^{\gtrless}|\,\delta(\omega - (H - E_0))|\psi_0^{\gtrless}\rangle, \qquad (18)$$
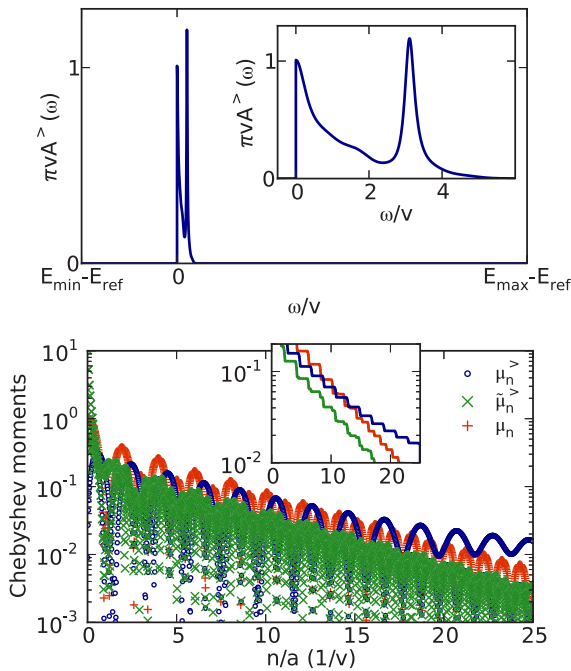
FIG. 1. (Color online) (Top) Typical example of a discontinuous spectral function due to the restriction to a given symmetry sector. In this case, this is the particle contribution of the spectral function of the single-impurity Anderson model (SIAM) with semielliptic bath density of states of half-bandwidth $2v$ and interaction $U/v = 4$ [16], taken from Ref. [14]. The spectral function is given by (8) using $|\psi_0\rangle = c^\dagger |E_0\rangle$, where $|E_0\rangle$ denotes the half-filled ground state and E_{ref} is the Fermi energy E_0. Here, only the shape of the scalar function is of importance, therefore we postpone the model definition to (30). The same spectral function is obtained for the local density of states of the first site for spinless fermions hopping on a semi-infinite chain with tunneling v and an interaction of $U/v = 4$ that acts only on the first site. (Bottom) Comparison of convergence of the Chebyshev moments of $A^>(\omega)$ with its redefinitions $\widetilde{A}^>(\omega)$ and $A(\omega)$, giving rise to moments $\mu_n^>$, $\widetilde{\mu}_n^>$, and μ_n, respectively. The full spectral function (18) for this example is $A(\omega) = A^>(\omega) + A^>(-\omega)$ as here, $A^<(\omega) = A^>(\omega)$ due to particle-hole symmetry. All of this is for the setup $b = 0$ using a rescaling of $a = 100v$ in Eq. (10).

obtained by summing over particle ($>$) and hole ($<$) contributions, is much better suited for a Chebyshev expansion than $A^{\gtrless}(\omega)$, as it lacks the discontinuity. In Ref. [13], it was then pointed out that the *full* $A(\omega)$ is *smooth* and therefore, Chebyshev moments should decrease exponentially, which would allow us to use linear prediction. In general, it is *not* true that $A(\omega)$ is smooth, due to the possibility of *van Hove singularities*, as appear, e.g., for the $U = 0$ case of the spectral function of the single impurity Anderson model (SIAM) (see Appendix B, Fig. 11). Still, $A(\omega)$ is likely to be smooth, and for the present example, it is. The bottom panel of Fig. 1 therefore shows that the Chebyshev moments μ_n for $A(\omega)$ decrease at the same exponential rate as the moments $\widetilde{\mu}_n^>$ of $\widetilde{A}^>(\omega)$. The statements about the qualitatively different convergence behaviors of $A^>(\omega)$, $\widetilde{A}^>(\omega)$, and $A(\omega)$ are confirmed for further typical examples in Appendix B.

C. Comparison of setups $b = 0$ and $b \simeq -1$

In Ref. [14], we pointed out that the choice $b = 0$ in Eq. (10) is computationally much less efficient than the choice $b \simeq -1$ (called "$b \simeq -a$" in Ref. [14]). Whereas constructing a Chebyshev expansion of the *full* spectral function $A(\omega)$ *requires* choosing $b = 0$, this is not the case for $\widetilde{A}(\omega)$. For $\widetilde{A}(\omega)$, we can therefore use the exponential rate of convergence to quantify the amount of spectral information that the Chebyshev recursion extracts from H in the setups $b = 0$ and $b \simeq -1$, and by that understand the observations of Ref. [14] quantitatively.

The key observation to make is that the integral

$$\mu_n^> = \int_{-1}^{1} dx\, \mathcal{A}_{a,b}^>(x) T_n(x) \qquad (19)$$

extracts a highly different amount of information about the structure of $A^>(\omega)$ depending on how a and b in Eq. (10) are chosen when generating $\mathcal{A}_{a,b}^>(x)$.

Throughout the whole paper, we keep $a = 100v$ fixed to guarantee the numerical stability of the Chebyshev recursion for the typical system sizes of around $L \geqslant 80$ that are large enough to display "thermodynamic limit behavior." If we chose a smaller, we could only stably compute "small" systems or we would have to resort to the technique of *energy truncation*, which is strongly prone to errors [17]. Furthermore, in the MPS context, it is important to compare only computations in which a is kept constant: constant a means constant effective hopping energies $\frac{v}{a}$ in $\mathcal{H}$, and by that a constant amount of entanglement production in a single iteration step of (13). The parameter b, by contrast, can be chosen freely without affecting the numerical stability, and in principle, without affecting the entanglement production in MPS computations.

The top panels of Fig. 2 show the convolution of $\mathcal{A}_{a,b}^>(x)$ with Chebyshev polynomials $T_n(x)$ of different degree n for the two setups $b = 0$ and $b = -0.995 \simeq -1$. The highly increased oscillation frequency that is evident in the setup $b = -0.995$ can be understood by looking at the natural stretching of the frequency scale of Chebyshev polynomials close to the boundaries of $[-1,1]$. Expressing the integral (19) by substituting $x = \cos\theta$

$$\mu_n^> = -\int_{\pi}^{0} d\theta\, \mathcal{A}_{a,b}^>(\cos\theta) \cos(n\theta) \sin\theta, \qquad (20)$$

one arrives at a convolution with the regularly oscillating $\cos(n\theta)$. Consider now the interval of width 0.05 on $[-1,1]$, which corresponds to the (single-particle) support of $\mathcal{A}_{a,b}^>(x)$ in the example of Fig. 2. By computing the integral widths under the map $x = \cos\theta$, one learns that placing the support in the "boundary region" $[-0.995, -0.95]$, as results for $b = -0.995$, increases the resolution by a factor ~ 6.4 compared to placing it in the "center region" $[0, 0.05]$, as results for $b = 0$. These effects are well-known boundary effects of the Chebyshev polynomials that are exploited also in the solution of differential equations [15].

The bottom panel of Fig. 2 shows the Chebyshev moments obtained in the $b = -0.995$ setup, for $A^>(\omega)$ (blue circles)
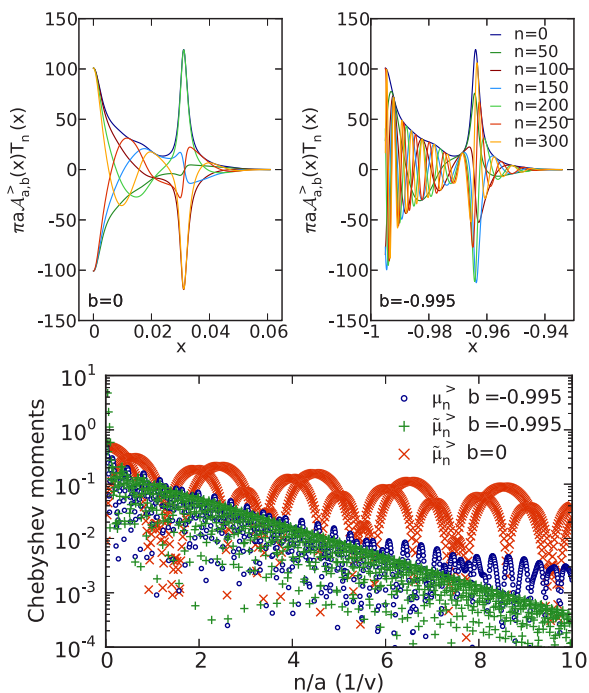
FIG. 2. (Color online) (Top) Integrand for computation of moments for the spectral function shown in Fig. 1 in the two setups $b = 0$ (left) and $b = -0.995$ (right). (Bottom) Comparison of convergence of moments computed with the integrands shown in the top panels. In all of that, $a = 100v$.

and for $\widetilde{A}^>(\omega)$ (green pluses). As mentioned before, for this setup, no Chebyshev expansion of the *full* spectral function $A(\omega)$ is possible. Instead, we compare the $b = -0.995$ results to the $b = 0$ results, depicted as red crosses. It is evident that the Chebyshev expansion in the $b = -0.995$ setup converges much faster than the one in the $b = 0$ setup. After $n = 1000$ iterations, the magnitude differs by more than 100.

This difference directly appears in the error of the Chebyshev series, as stated by the following general rule: the order of the error ε of a Chebyshev (or Fourier) series representation of a function that is truncated at $n = N$ can be estimated by (see Ref. [15, Chap. 2.12])

$$\varepsilon = \mathcal{O}(\mu_N) \quad \text{if } \mu_n \text{ converges exponentially,} \tag{21a}$$

$$\varepsilon = \mathcal{O}(N\mu_N) \quad \text{if } \mu_n \text{ converges algebraically.} \tag{21b}$$

D. Linear prediction for the Chebyshev expansion

The main motivation for studying the convergence of different Chebyshev expansions in the previous sections lies in the possibility to extrapolate exponentially decreasing sequences with *linear prediction*. As discussed in the introduction, the latter allows an extremely high gain in resolution, if its application is justified. For details on linear prediction, see Appendix C.

In what follows, we compare the known approach of using linear prediction for the Chebyshev expansion of $A(\omega)$, as suggested in Ref. [13], with the approach of extrapolating the Chebyshev expansion of $\widetilde{A}^>(\omega)$.

We first compute the Chebyshev moments of the step function that has the discontinuity of $A^>(\omega)$ at $\omega = 0$, which

transforms to $x = -b$ for $\mathcal{A}^>(x)$, as

$$\mu_n^{\text{step}} = \int_{-b}^1 dx \, T_n(x)$$
$$= \frac{1}{2} \left\{ \frac{\cos[(n+1)\arccos x]}{n+1} \right.$$
$$\left. - \frac{\cos[(n-1)\arccos x]}{n-1} \right\} \Bigg|_{-b}^1 . \tag{22}$$

The Chebyshev moments of $\widetilde{A}^>(x)$ are then given by

$$\widetilde{\mu}_n^> = \mu_n^> - A^>(0)\mu_n^{\text{step}} \tag{23}$$

and are accessible by linear prediction, as they decrease exponentially.

The core problem in this new approach is that the value $A^>(0)$ of the spectral function is, in general, unknown *prior* to linear prediction. However, it fulfills the following self-consistency problem, which can be iteratively solved; choosing a start value $A_0^>(0)$ for $A^>(0)$, we compute $\widetilde{\mu}_n$, extrapolate the sequence up to convergence, and then use the extrapolated sequence to reconstruct $A^>(\omega)$, which provides us with a new value $A_1^>(0)$. We repeat the procedure until the new and the old version $A_i^>(0)$ and $A_{i+1}^>(0)$ agree. This procedure is found to converge stably and quickly for all examples studied (see also Appendix B).

Figure 3 compares the approach of reconstructing the *full* spectral function $A(\omega)$ from $A^>(\omega)$, using linear prediction for the expansion of $A(\omega)$ in the $b = 0$ setup, with the approach of using linear prediction of $\widetilde{A}^>(\omega)$ in the $b = -0.995$ setup. We take the function of Fig. 1 as input function that shall be reconstructed. In the top panels of Fig. 3, we compare both setups for $N = 200$ computed moments that are then extrapolated to $N \gg 1000$ until they converge to a value of 10^{-6}. We choose this comparatively small number of computed moments, as in MPS algorithms the number of moments that can be computed in a controlled way is strongly limited [14].

The upper left panel of Fig. 3 shows that already for $N = 200$, our approach (dashed red line) allows a very good reconstruction of the input function. In the upper right panel, we show the error of this reconstruction, which becomes maximal at the second peak of the input function and is of order 10^{-2}, i.e., a relative error of a few percent. The situation is very different for the extrapolation scheme of the full $A(\omega)$ that uses the $b = 0$ setup. For $N = 200$ computed moments, large errors are observed in both top panels of Fig. 3.

In the bottom panel of Fig. 3, we plot the maximal error, defined as $\max_{\omega \geq 0} |A_{\text{reconst}}(\omega) - A_{\text{input}}(\omega)|$, versus different values of the number of computed moments N. An orders of magnitude reduction of the error is seen upon using our over the previous approach. If one compares the expansion order N for which an error of 5×10^{-3} is reached ($N \sim 250$ in the $b \simeq -1$ setup, and $N = 1200$ in the $b = 0$ setup), one recovers the factor ~ 6 that has been derived in the previous section.

Only at very high expansion orders, which in practice can often not be reached by MPS computations, the original approach allows to reach smaller error levels for the presently studied generic example. More examples are studied in Appendix B.
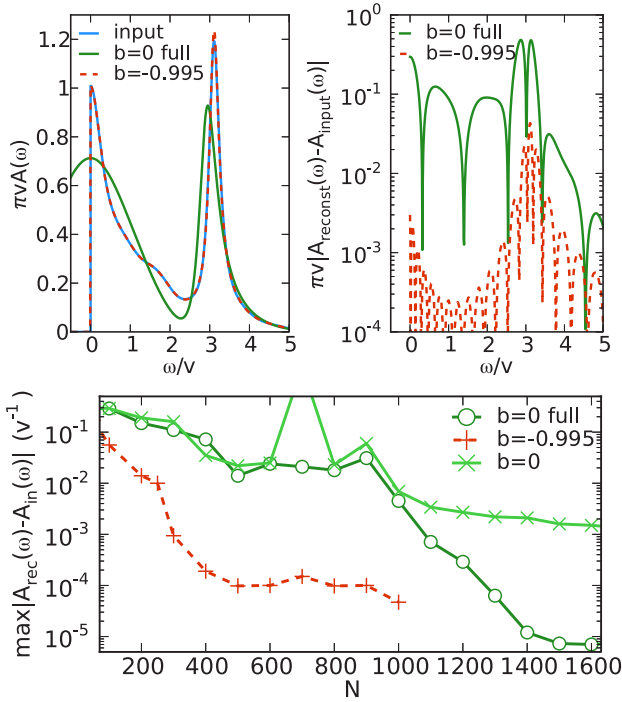
FIG. 3. (Color online) (Top) Input spectral function and reconstructed spectral functions using linear prediction for $N = 200$ computed Chebyshev moments. We compare our proposal with the original proposal [13], where for the $b = 0$ setup the expansion of the *full* spectral function was extrapolated. (Left) In the first case, we use the Chebyshev expansion of $\widetilde{A}^{>}(\omega)$ in the $b = -0.995$ setup (red dashed lines), and in the second, we use the Chebyshev expansion of the *full* spectral function $A(\omega)$ in the $b = 0$ setup (solid green line). (Right) Error of these functions $|A_{\text{reconst}}(\omega) - A_{\text{input}}(\omega)|$ for both setups. (Bottom) The error $\max_{\omega \geqslant 0} |A_{\text{reconst}}(\omega) - A_{\text{input}}(\omega)|$ vs number N of computed Chebyshev moments. Here, we also show results for using the Chebyshev expansion of $\widetilde{A}^{>}(\omega)$ in the $b = 0$ setup (light green crossed line). This is different from using the *full* spectral function $A(\omega)$ in the $b = 0$ setup. Lower error levels only occur for much higher expansion orders than shown in the panel.

III. SPECTRAL FUNCTIONS FOR FINITE SYSTEMS

Let us now study the case of finite systems, where a discretized representation of the spectral function is used for reconstruction. The general previous arguments are still valid, but several technical details have to be taken into account. In particular, we suggest a new discretization scheme suited for reconstruction with Chebyshev expansions. Such a discretization scheme can be used for problems that allow to manipulate the discretization of the spectral function. This is, e.g., the case for impurity models, for which the discretization of the input bath spectral function determines the discretization of the spectral function. Still, the following discussion is also relevant to, e.g., finite lattice models for which the discretization is physically constrained.

To construct a discrete representation of a continuous function $A(\omega)$, we employ the scheme that is used to discretize the *hybridization function* of impurity models in the numerical renormalization group [18]. This proceeds as follows. For L given discretization intervals $[\omega_l, \omega_{l+1}]$, $l = 1, \ldots, L$, we

compute discrete weights V_l^2 and eigenvalue positions ϵ_l by

$$V_l^2 = \int_{\omega_l}^{\omega_{l+1}} d\omega \, A(\omega),$$

$$\epsilon_l = \frac{1}{V_l^2} \int_{\omega_l}^{\omega_{l+1}} d\omega \, \omega A(\omega). \tag{24}$$

The first line associates a weight and the second line a representative energy with an interval of energies $[\omega_l, \omega_{l+1}]$. For the energy, one could, e.g., take [9] the simple average $\frac{1}{2}(\omega_l + \omega_{l+1})$. Equation (24), by contrast, produces an average using the weighting function $\frac{1}{V_l^2} A(\omega)$, which attributes more weight to peaks of $A(\omega)$.

We choose the left boundary of the first interval ω_1 and the right boundary of the last interval ω_{L+1} such that the distance $\omega_{L+1} - \omega_1$ is minimized but [14]

$$\int_{\omega_1}^{\omega_{L+1}} d\omega \, A(\omega) \geqslant 0.999 \int_{-\infty}^{\infty} d\omega \, A(\omega), \tag{25}$$

where the integrand is non-negative, which guarantees that $[\omega_1, \omega_{L+1}]$ contains almost the complete support of $A^{>}(\omega)$, but minimizes *finite-size* effects. The intermediate values of the discretization intervals $\{\omega_2, \ldots, \omega_L\}$ can be chosen using a logarithmic discretization, as done in NRG [18]. However, if an *unbiased* resolution is wanted, one usually chooses a linear discretization [13,14]

$$\omega_l = (l - 1)\Delta\omega + \omega_1, \quad l = 2, \ldots, L,$$

$$\Delta\omega = \frac{1}{L}(\omega_{L+1} - \omega_1). \tag{26}$$

As Chebyshev polynomials do *not* show an *unbiased* energy resolution as they oscillate much quicker at the boundaries of $[-1, 1]$ than in the center, the linear discretization will first resolve the finite-size (discrete) structure close to the boundaries of $[-1, 1]$. We suggest to adapt the discretization to account for the cosine mapping (20) of the energy scale that is responsible for this phenomenon.

Let us study the case of even L (for odd L, see Appendix D) and assume without loss of generality that we want as many intervals $\{\omega_l, \omega_{l+1}\}$ on the positive half-axis as on the negative half-axis, which implies

$$\omega_{L/2} = 0. \tag{27}$$

As we already know ω_{L+1} from (25), we only have to fix the intermediate interval boundaries $\{\omega_{L/2+1}, \ldots, \omega_L\}$. We define

$$\omega_{L/2+l} = a(\cos(\theta_{L/2} + l\Delta\theta) - b), \quad l = 1, \ldots, L/2,$$

$$\Delta\theta = \frac{2}{L}(\theta_{L+1} - \theta_{L/2}),$$

$$\theta_{L/2} = \arccos b,$$

$$\theta_{L+1} = \arccos\left(b + \frac{\omega_{L+1}}{a}\right). \tag{28}$$

Using these definitions, a discrete representation $A_{\text{discr}}(\omega)$ of $A(\omega)$ [in the sense that $A_{\text{discr}}(\omega) \to A(\omega)$ for $L \to \infty$] is given by

$$A_{\text{discr}}(\omega) = \langle\psi_0|\delta(\omega - H)|\psi_0\rangle,$$

$$H_{ll'} = \epsilon_l\delta_{ll'}, \quad l, l' = 1, \ldots, L, \tag{29}$$
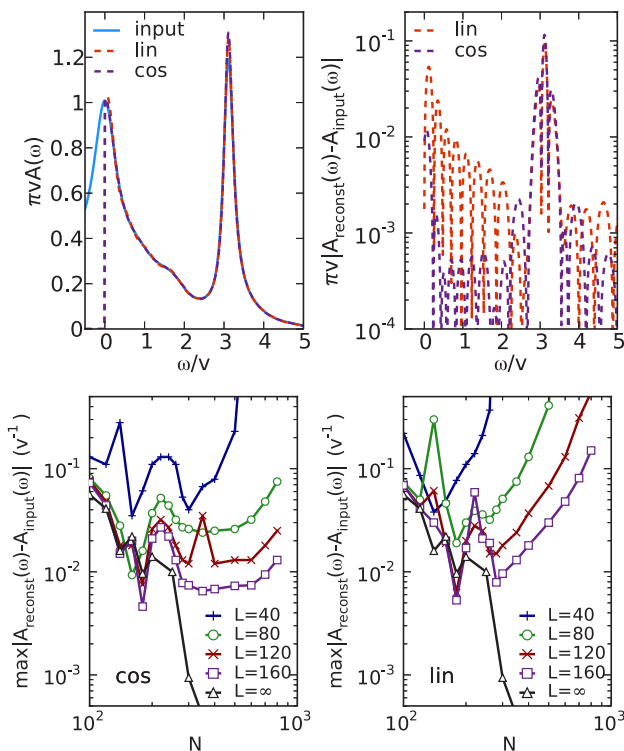
$$|\psi_0\rangle_l = V_l,$$

FIG. 4. (Color online) Reconstruction of the spectral function of Fig. 1 represented by the discrete Hamiltonian (29). (Top left) Input function and reconstructed functions using $L = 80$, $N = 200$, $a = 100v$, $b = -0.995$. We compare the linear discretization (26) with the cosine (28) discretization. (Top right) Difference of input and reconstructed functions of the top left panel. (Bottom left) The error $\max_{\omega \geqslant 0} |A_{\text{reconst}}(\omega) - A_{\text{input}}(\omega)|$ vs number N of computed Chebyshev moments using a cosine discretization. (Bottom right) Error for linear discretization.

where $H \in \mathbb{R}^{L \times L}$ and $|\psi_0\rangle \in \mathbb{R}^L$, and the parameters ϵ_l and V_l are given in Eq. (24). This is consistent with definition (8) if we realize that this is a single-particle Hamiltonian for a particle that is in any of the ϵ_l energy states with probability V_l^2. The reference energy would be the ground-state energy of the vacuum $E_{\text{ref}} = 0$. To obtain the step function behavior of $A^>(\omega)$, we project out the positive energy contributions from the initial state $|\psi_0\rangle$.

In Fig. 4, we show the reconstruction of spectral functions based on the linear prediction of the moments computed for $\tilde{A}^>_{\text{discr}}(\omega)$ using the operator-valued Chebyshev expansion presented in Sec. I B for the "Hamiltonian" defined in Eq. (29). This is analogous to the top left panel of Fig. 3, which treated the thermodynamic limit.

For the finite-size system, the specific choice of discretization is important and we compare the linear and the cosine discretization in the top panels of Fig. 4 for the expansion order $N = 200$ and a system size $L = 80$. From the large error at $\omega = 0$ for the linear discretization (red dashed line) seen in the right top panel of Fig. 4, which was not present in the thermodynamic limit (red dashed line in right top panel of Fig. 3), we conclude that the linear discretization starts resolving finite-size features close to $\omega = 0$ already for $N = 200$. The lower panels then show how the error

behaves as a function of the number of computed moments for different system sizes L. While the cosine discretization follows the error of the thermodynamic limit quite closely for low values of N and lattice sizes of $L \geqslant 80$, it almost saturates in a plateau for higher expansion orders, and only starts increasing slightly for very high expansion orders. For the linear discretization, neither the close correspondence with the thermodynamic limit is observed, nor does the error only moderately depends on the expansion order: instead, the error increases exponentially for high values of N, as then, finite-size features are inhomogeneously resolved. Both features make it difficult to determine the value of N for which the computation of Chebyshev moments should be stopped in order to obtain a minimal error.

IV. IMPLICATIONS FOR MPS REPRESENTATIONS

What is the relevance of the previous results for matrix product state (MPS) based computations of the spectral function for a given matrix product operator (MPO) H [19]? Repeated MPO operations on MPS create entanglement, which eventually makes manipulating and storing MPS computationally very costly. Manipulations, such as applying H to states $|t_n\rangle$ in the recursion (13), or performing subsequent time-evolution steps $e^{-iH\Delta t}$, can therefore only be carried out up to a certain recursion order n or time t, before hitting an *exponential wall* in computation cost. For time-evolution algorithms, this has long been known [20,21], but this also limits computations using the Chebyshev recursion [14].

In the following, we show that the method introduced in the previous sections outperforms the previous approach [13]: it extracts more spectral information from H when creating the same amount of entanglement or, which is equivalent up to technical details of the algorithm, using the same computation time.

As an example, we compute the spectral function of the single impurity Anderson model (SIAM), which serves as a common benchmark [13,14,16,22,23] and is highly relevant as it is at the core of dynamical mean-field theory (DMFT) [24–27].

The Hamiltonian of the SIAM is given as

$$H^{\text{SIAM}} = H_{\text{imp}} + H_{\text{bath}} + H_{\text{hyb}},$$

$$H_{\text{imp}} = U\left(n_{0\uparrow} - \frac{1}{2}\right)\left(n_{0\downarrow} - \frac{1}{2}\right),$$

$$H_{\text{bath}} = \sum_{l=1}^{L_b} \sum_{\sigma} \epsilon_l c_{l\sigma}^\dagger c_{l\sigma},$$

$$H_{\text{hyb}} = \sum_{l=1}^{L_b} \sum_{\sigma} (V_l c_{0\sigma}^\dagger c_{l\sigma} + \text{H.c.}). \tag{30}$$

By a unitary transform effected by Lanczos tridiagonalization, this can be mapped on the so-called *chain* geometry. However, as this leads to higher entanglement, we simply order bath states by their potential energy, which directly gives a one-dimensional array that can be treated with MPS [23]. We solve

the model for the semielliptic bath density of states

$$-\frac{1}{\pi}\text{Im}\Lambda(\omega) = \frac{1}{2v\pi}\sqrt{4 - \left(\frac{\omega}{v}\right)^2}, \qquad (31)$$

which is discretized according to the procedure discussed in Sec. III, and then yields the parameters ϵ_l and V_l. It is important to realize that here, we discretize the *bath hybridization* function whereas in Sec. III, we discretized the *spectral function*. While Sec. III did this to illustrate the effect of discretization for a toy model for which the spectral function was known from the beginning, in the present case, a true many-body computation is involved. In the present case, the relevant discretization parameter is the bath size $L_b = L - 1$, and no longer the system size [14].

We compute the spectral function (18) of the impurity Green's function, where the initial states are single-particle excitations of the ground state: $|\psi_{0\sigma}^{>}\rangle = c_{0\sigma}^{\dagger}|E_0\rangle$ and $|\psi_{0\sigma}^{<}\rangle = c_{0\sigma}|E_0\rangle$. As we consider the particle-hole and spin-symmetric case of (30), we only need to compute one Chebyshev recursion; to be precise, $|\psi_0\rangle = c_{0\uparrow}^{\dagger}|E_0\rangle$. We compare our results with the dynamic DMRG results from Ref. [16], which are believed to be highly reliable. In particular, we compare computations in the formerly suggested setup [13,17] that uses the Chebyshev recursion for $b = 0$ in Eq. (10) and reconstructs the *full* spectral function $A(\omega)$ using linear prediction [13], and the one suggested here that uses $b = -0.995$ and reconstructs the *shifted* spectral function $\widetilde{A}(\omega)$ using linear prediction.

In the top left panel of Fig. 5, we show computations of the spectral function of the SIAM for $L = 80$ for $N = 260$ in the $b = -0.995$ setup, and $N = 900$ in the $b = 0$ setup and compare it with the result of Ref. [16]. We choose these two expansion orders, as they lead to a comparable maximum error, as shown in the top right panel of Fig. 5. In the $b = -0.995$ setup, this maximum error is slightly smaller. Around $\omega = 0$, by contrast, the error in the $b = -0.995$ setup is much smaller. If we compare the computation time that is needed to reach this precision ($\max|A_{\text{reconst}}(\omega) - A_{\text{input}}| \simeq 0.015/v$), we find that the $b = -0.995$ setup required $\sim$145 min whereas the $b = 0$ setup required $\sim$434 min. If one makes this comparison for a slightly larger error ($\max|A_{\text{reconst}}(\omega) - A_{\text{input}}| \simeq 0.025/v$), realized for expansion order $N = 120$ for the $b = -0.995$ setup, and for expansion order $N = 200$ for the $b = 0$ setup, the comparison in computation times reads $\sim$12 min versus $\sim$160 min.

When studying the convergence of the maximum error with respect to expansion order N in the lower left panel of Fig. 5, we see that this is, after a sharp decrease for low expansion orders, not monotonously decreasing. The previously mentioned choices, $N = 260$ in the $b = -0.995$ setup and $N = 900$ in the $b = 0$ setup, both correspond to a minimum in the oscillations, as seen when inspecting the green solid (dashed) lines for the $b = -0.995$ ($b = 0$) setup. The nonmonotonicity makes general comparisons for the speedup difficult. But the lower right panel of Fig. 5 still shows that with only a few exceptions, the solid ($b = -0.995$) lines are always clearly below the dashed ($b = 0$) lines. The logarithmic abscissa therefore indicates a high speedup.
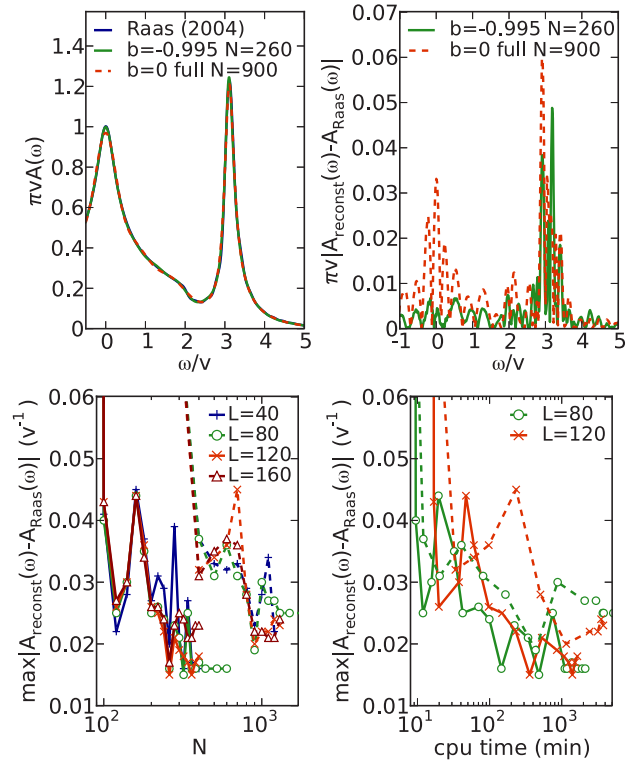
FIG. 5. (Color online) Comparison of MPS computed spectral functions in the two setups studied in the previous sections, with data by Raas *et al.* [16]. Solid lines refer to the method that uses $\widetilde{A}(\omega)$, dashed lines refer to the method that uses the *full* spectral function $A(\omega)$. (Top left) For $L = 80$ and two exemplary expansion orders. (Top right) Errors of comparison in top left panel. (Bottom left) Plot of the maximum error vs expansion order N. (Bottom right) Plot of the maximum error vs computer time.

V. COMPARISON TO TIME EVOLUTION

It is interesting to compare the efficiency of the available MPS algorithms to extract spectral information from H. The candidates are, aside from the dynamic DMRG [28], which is believed to be computationally highly costly, time-evolution and recursive algorithms. The latter are, in particular, expansions in Chebyshev polynomials [17] and the Lanczos algorithm [29,30]. Lanczos is numerically unstable as the basis that it spans looses its orthogonality for high numbers of iterations [31]. This seems to disqualify Lanczos as a high-performing candidate. Therefore the main question is whether the Chebyshev recursion can more efficiently extract spectral information from H than time-evolution algorithms.

To answer this question, in the following, we exploit the fact that for $b = 0$ in the limit $a \to \infty$, the Chebyshev expansion becomes a Fourier expansion, and the Chebyshev states directly describe the time evolved system. This is different from the procedure of computing the time dependence of a Green's function via a Fourier transform of its spectral function [17,32–34]. For comparison, we summarize the latter technique in Appendix E.

The approximate equivalence of the Chebyshev recursion to time evolution can be used as a novel time-evolution algorithm. This is interesting as for long-range interacting

Hamiltonians H, the MPO representation of e^{-iHt} is not available, or only approximately [35]. Although it is possible to use the so-called Krylov algorithms for such problems, this requires some programming effort, and is in general believed to be numerically rather inefficient as compared to other time-evolution algorithms. Long-range interacting problems appear, e.g., if mapping a two-dimensional system on a one-dimensional chain, or in the solution of a SIAM using a *star* geometry [23] as in Eq. (30).

A. Statement of approximate equivalence

The time evolution of a state $|\psi_0\rangle$

$$|\psi(t)\rangle = \exp(-iHt)|\psi_0\rangle, \tag{32}$$

can be approximately linked to the sequence of Chebyshev vectors generated by starting from $|\psi_0\rangle$ as follows.

Choose a reference energy $E_{\rm ref}$ in Eq. (10) that is characteristic for the initial state of the time evolution and the Chebyshev recursion. When computing the time evolution of the Green's function with $|\psi_0\rangle = c^\dagger|E_0\rangle$, one chooses $E_{\rm ref} = E_0$, if $|\psi_0\rangle$ is not an eigenstate, we choose $E_{\rm ref} = \langle\psi_0|H|\psi_0\rangle$.

Then define $|\phi(t)\rangle = \exp(iE_{\rm ref}t)|\psi(t)\rangle$ and $\mathcal{H} = (H - E_{\rm ref})/a$ as in Eq. (10) in the $b = 0$ setup. Here, a has the meaning of an inverse time step of unit energy. With these definitions, (32) reads as

$$\begin{aligned} |\phi(t)\rangle &= \exp(-ia\mathcal{H}t)|\psi_0\rangle \\ &= (\cos(a\mathcal{H}t) - i\sin(a\mathcal{H}t))|\psi_0\rangle \\ &\equiv |\phi_{\cos}(t)\rangle - i|\phi_{\sin}(t)\rangle. \end{aligned} \tag{33}$$

Let us discretize time by defining $t_n = \frac{n}{a}$, then

$$|\phi_{\cos}(t_n)\rangle = \cos(n\mathcal{H})|\psi_0\rangle, \tag{34a}$$

$$|\phi_{\sin}(t_n)\rangle = \sin(n\mathcal{H})|\psi_0\rangle. \tag{34b}$$

We now want to compute the action of $\cos(n\mathcal{H})|\psi_0\rangle$ on $|\psi_0\rangle$ using a recursion that only involves the action of $\mathcal{H}$. This is not possible with the standard recursion for the cosine function, as shown in Appendix F 1.

Let us instead consider the action of the Chebyshev polynomials

$$T_n(\mathcal{H}) = \cos(n\arccos(\mathcal{H})) \tag{35}$$

on $|\psi_0\rangle$. This action approximately reproduces the action of the plane cosine function, if we consider every fourth iteration, i.e., introduce the new index $n' = 4n$, $n \in \mathbb{N}$:

$$\begin{aligned} T_{n'}(\mathcal{H})|\psi_0\rangle &= \cos\left[n'\left(\frac{\pi}{2} - \mathcal{H}\right)\right]|\psi_0\rangle + \epsilon(n')|\psi_0\rangle \\ &= \cos(n'\mathcal{H})|\psi_0\rangle + \epsilon(n')|\psi_0\rangle. \, n' = 0,4,8,\ldots \end{aligned} \tag{36}$$

In the first line, we used the Taylor expansion $\arccos(\mathcal{H}) = \frac{\pi}{2} - \mathcal{H} + \frac{1}{6}\mathcal{H}^3 + \cdots$, that leads to the error function $\epsilon(n')$ (Appendix F 5), and in the second line, we used $n'\frac{\pi}{2} = 2\pi n$, $n \in \mathbb{N}$, which obviously drops out of the argument of the cosine (also see Appendix F 2).

The error $\epsilon(n')$ is bounded by (F16)

$$|\epsilon(t_{n'})| = \frac{t}{t_{\rm err}} \quad \text{if} \quad t < t_{\rm err},$$

$$t_{\rm err} = \frac{a^2}{\sigma^3}, \tag{37}$$

where σ is the spectral width of the initial state $|\psi_0\rangle \equiv |\psi_0\rangle$ around $E_{\rm ref}$,

$$\sigma = \max_{|E_k\rangle \in |\psi_0\rangle} |E_k - E_{\rm ref}|, \tag{38}$$

where "$|E_k\rangle \in |\psi_0\rangle$" refers to the decomposition of the initial state in eigenstates $|E_k\rangle$ of $\mathcal{H}$

$$|\psi_0\rangle = \sum_k c_k|E_k\rangle. \tag{39}$$

The "spectral width" σ is usually small compared to reasonably high values of the inverse time step a. If one is unsure of whether a was chosen large enough, one reruns a calculation with a higher value of a and checks convergence.

We can now compute the time evolution

$$\begin{aligned} |\phi_{\cos}(t_{n'})\rangle &= |\phi_{\rm cheb}(t_{n'})\rangle + \epsilon(t_{n'})|\psi_0\rangle, \\ |\phi_{\rm cheb}(t_{n'})\rangle &= T_{n'}(\mathcal{H})|\psi_0\rangle, \quad n' = 0,4,8,\ldots \end{aligned} \tag{40}$$

via the recursion (13):

$$\begin{aligned} |\phi_{\rm cheb}(t_n)\rangle &= 2\mathcal{H}|\phi_{\rm cheb}(t_{n-1})\rangle - |\phi_{\rm cheb}(t_{n-2})\rangle, \\ |\phi_{\rm cheb}(t_1)\rangle &= \mathcal{H}|\psi_0\rangle, \quad n = 0,1,2,\ldots. \end{aligned} \tag{41}$$

B. Numerical examples

1. Single-particle computation for SIAM

Figure 6 shows the numerically exact time evolution of a single particle created on the first site $|\psi_0\rangle = c_0^\dagger|E_0\rangle$ of a chain of 100 lattice sites. The spectral width therefore is $\sigma = 2v$. The left panel of Fig. 6 plots the Chebyshev moments $\mu_n = \langle\psi_0|t_n\rangle$ obtained with $a = 100v$ and the time evolution of the corresponding Green's function $iG^>(t) = e^{iE_0t}\langle\psi_0|\psi(t)\rangle$ for the time step $\frac{4}{a}$. Every fourth Chebyshev moment agrees with a value of the Green's function. In the right panel, we show the long-time behavior of $G^>(t)$ and the difference $G^>(4n/a) - \mu_{4n}$. The difference is seen to be clearly below the conservative upper bound (37), it remains of the order of $\sigma^3/a^2 = 8 \times 10^{-4}$ up to very high times that correspond to 100 hopping processes ($t = 100/v$).

2. MPS computation for SIAM

We now study the time evolution of the SIAM (7) in the star geometry [23] for the single-particle excitation $|\psi_0\rangle = c_{0\uparrow}^\dagger|E_0\rangle$ of the half-filled ground state $|E_0\rangle$. The left panel shows the time evolution of the corresponding Green's function, computed with an MPS Krylov algorithm that imposes the error bound:

$$\||\psi(t + \Delta t)\rangle - \exp(-iH\Delta t)|\psi(t)\rangle\| < \varepsilon_{\rm kry},$$

for a time step of $\Delta t = \frac{4}{a}$. An error bound of $\varepsilon_{\rm kry} = 5 \times 10^{-4}$ suffices to reliably compute times up to $15/v$.

In the MPS implementation of the Chebyshev recursion, we fix the global truncation error per iteration step, as discussed
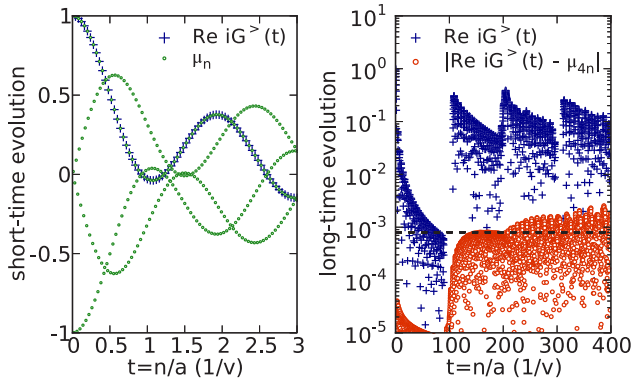
FIG. 6. (Color online) (Left) Time evolution of a particle created on the first site of a chain of length $L = 100$ with hopping $v = 1$, that is, $|\psi_0\rangle = c_0^\dagger|\text{vac}\rangle$. We compare the time evolution of the Green's function $iG^>(t) = e^{iE_0t}\langle\psi_0|\psi(t)\rangle$ (shown as blue crosses) with the Chebyshev moments $\mu_n = \langle\psi_0|\psi_n\rangle$ (shown as green dots) obtained when computing the recursion $|\psi_n\rangle = 2H/a|\psi_{n-1}\rangle - |\psi_n - 2\rangle$. Hopping amplitudes v_l are obtained from the discretization of the spectral function of Fig. 1. A qualitatively equivalent behavior is obtained for a chain with homogeneous hopping $v_l = v$. (Right) Long-time evolution of the Green's function (blue crosses), and difference of the Green's function and the Chebyshev moments (red dots). The horizontal dashed line marks the prefactor of the error estimate (37), which is computed as $\sigma^3/a^2 = 8 \times 10^{-4}$.

in Ref. [14]:

$$\||t_n\rangle - (2\mathcal{H}|t_{n-1}\rangle - |t_{n-2}\rangle)\| < \varepsilon_{\text{che}}. \tag{42}$$

To achieve this, two options are available. If during the variational compression of $(2\mathcal{H}|t_{n-1}\rangle - |t_{n-2}\rangle)$, the truncation error exceeds ε_{che}, even when choosing a better and better guess state, one can either directly increase the bond dimension, or reduce the truncated weight *per bond*, which indirectly increases the bond dimension. While for the setup in Ref. [14], there were reasons to choose the former option, here we choose the latter as our Krylov algorithm uses a similar adaption.

We compare the results of the Krylov algorithm with the Chebyshev algorithm (40). In the top left panel of Fig. 7, we plot the Green's function $iG^>(t) = e^{iE_0t}\langle\psi_0|\psi(t)\rangle$. If imposing the same error tolerance $\varepsilon_{\text{che}} = \varepsilon_{\text{kry}}$, we obtain agreement of both algorithms only for short times. Only a much smaller tolerance for the Chebyshev algorithm $\varepsilon_{\text{che}} = \frac{1}{10}\varepsilon_{\text{kry}}$ leads to agreement also for long times. We conclude that error accumulation in the Chebyshev recursion is much worse conditioned than in the time-evolution algorithm, and even worse than what could be expected from the four "auxiliary steps" made in Eq. (41) between each "physical time step:" imposing a tolerance $\varepsilon_{\text{che}} = \frac{1}{4}\varepsilon_{\text{kry}}$ for the Chebyshev recursion is not sufficient to produce comparable results.

The reduced error tolerance $\varepsilon_{\text{che}} = \frac{1}{10}\varepsilon_{\text{kry}}$ for the Chebyshev recursion comes at the price of an order of magnitude increase in the bond dimension compared to the Krylov algorithm, as shown in the top right panel of Fig. 7. However, for $\varepsilon_{\text{che}} = \varepsilon_{\text{kry}}$, the Chebyshev recursion needs higher bond dimensions than the Krylov algorithm. The lower left panel compares the overlap of the Chebyshev-evolved and the Krylov-evolved states by plotting $|1 - \langle\psi_{\text{cheb}}|\psi_{\text{kry}}\rangle/\langle\psi_{\text{cheb}}|\psi_{\text{cheb}}\rangle|$. With only few exceptions, this quantity is bounded by the theoretical
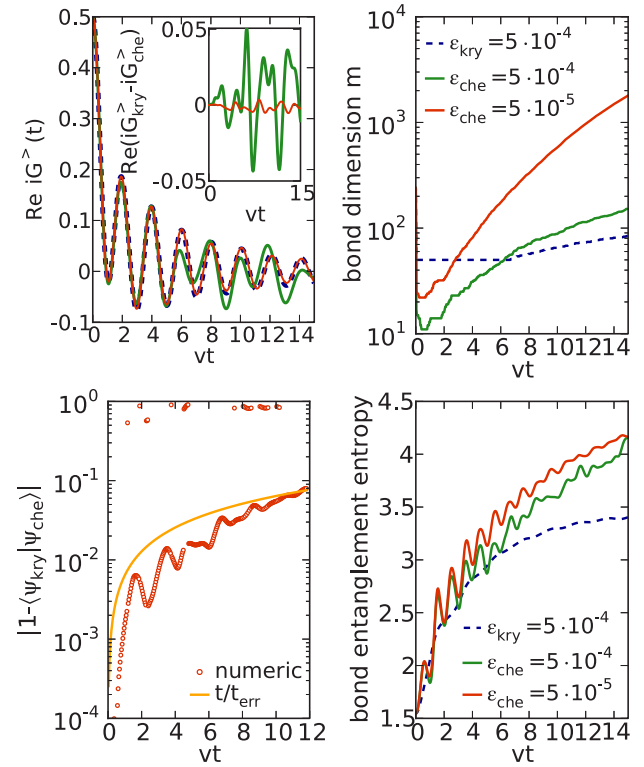

FIG. 7. (Color online) Time evolution of the single-particle excitation $c_{0\uparrow}^\dagger|E_0\rangle$ in the half-filled single-impurity Anderson model (30) with semielliptic density of states of half-bandwidth $2v$ and interaction $U/v = 4$ for $L = 40$. Computations using an MPS Krylov algorithm with error tolerance $\varepsilon_{\text{kry}} = 5 \times 10^{-4}$ and the Chebyshev recursion (40) for different error tolerances $\varepsilon_{\text{che}} = 5 \times 10^{-4}$ and $\varepsilon_{\text{che}} = 5 \times 10^{-5}$. (Top left) Time evolution of Greens's function. Both algorithms produce the same result upon using the smaller error tolerance for the Chebyshev algorithm. The legend is found in the top right panel. (Top right) Maximal bond dimension, located at the central bond. The Krylov time evolution leads to a much smaller maximal bond dimension, as its computation produces a faithful result already with the relatively high error tolerance of $\varepsilon_{\text{kry}} = 5 \times 10^{-4}$, for which the Chebyshev algorithm shows strong errors in the Green's function. (Bottom left) Difference of overlap of Chebyshev and Krylov evolved states, comparing the $\varepsilon_{\text{che}} = 5 \times 10^{-5}$ with the $\varepsilon_{\text{kry}} = 5 \times 10^{-4}$ computation. The difference of overlap is bounded by the analytical prediction of (37), except for few exceptions that lie above it. These exceptions are of purely numerical origin as they are not visible in any other quantity. For the highest times shown, truncation errors have accumulated so much that the analytical prediction starts to fail. (Bottom right) Bond entanglement entropy at center bond.

prediction of (37), when setting $\sigma = 4v = U$. The exceptions are artifacts of the detailed implementation of the algorithms as the key observable $G^>(t)$ is correctly computed, but still their existence suggest that the implementation can be improved. Ignoring these exceptions, we see that the normalized overlap $\langle\psi_{\text{cheb}}|\psi_{\text{kry}}\rangle$ deviates from one only by a few percent even for long times. However, these few percent come with a considerable growth of the entanglement entropy, as can be concluded by inspecting the lower right panel of Fig. 7. There, already the $\varepsilon_{\text{che}} = \varepsilon_{\text{kry}}$ case shows a considerably increased entropy.

Aside from the two preceding fundamental reasons (different error accumulation, small difference of states), the increased bond dimensions in the Chebyshev algorithm can also be related to a purely technical question: the variational compression [19] in each Chebyshev iteration produces a state that fulfills (42), but might be a state with unnecessarily high bond dimension m. Similarly to the DMRG ground-state optimization algorithm, also variational compression can get stuck in *local minima*. Currently, we use White's *mixing factor* [36] to avoid this. A recent publication suggests an even better strategy and explains these problems concisely [37].

In general, the subspace of the Hilbert space that is needed to be faithfully described in order to measure the spectral function can be spanned using different basis states. In principle, the most efficient spanning would be provided by the Lanczos algorithm, as the latter provides *orthogonal* states. However, it is impractical due to numerical instability. The basis states provided by time evolution or the Chebyshev recursion are not orthogonal to each other, but can be stably generated. The numerical evidence discussed in the previous paragraphs indicates that the Chebyshev recursion generates a much more entangled basis of this subspace than a time-evolution algorithm: it extracts less spectral information when fixing a maximal entanglement entropy. However, these arguments directly hold only for the "$b = 0$ setup" of the Chebyshev recursion, in which it is transparently comparable with a time-evolution algorithm as there is a one-to-one correspondence of time-evolution steps and iterations of the recursion.

Sections II–IV of this paper showed that the $b = 0$ setup is the computationally least favorable setup of the Chebyshev recursion, and a $b \simeq -1$ setup much better. Still, the gains in computation time of the $b \simeq -1$ setup over the $b = 0$ setup shown in the bottom right panel of Fig. 5 seem not to be sufficient to compensate the clear inferiority of the Chebyshev method shown in the upper right panel of Fig. 7. A definitive statement is difficult due to the nonmonotonic behavior of the error in Fig. 5 and due to the fact that such a comparison is strongly affected by the details of the implementation of the algorithms, and not only by the principle nature of how strongly entangled its resulting basis states are. For this reason, the discussion on the most efficient method for computing spectral functions using MPS cannot be generally considered settled.

3. Expansion in Hubbard model

Finally, we study the time evolution of the one-dimensional Hubbard model

$$H^{\text{Hubbard}} = U \sum_l \left(n_{l\uparrow} - \frac{1}{2} \right) \left(n_{l\downarrow} - \frac{1}{2} \right)$$
$$- v \sum_{l\sigma} (c_{l\sigma}^{\dagger} c_{l+1\sigma} + \text{H.c.}), \qquad (43)$$

starting from a product state with doubly occupied sites in the center of the system, and evolving this state at interaction $U/v = 4$, as shown in Fig. 8. We obtain very good agreement of the Krylov and the Chebyshev algorithm, although there is no rigorous *a priori* reason, for which the initial product state should have a narrow spectral width, i.e., small σ in the sense of (38), as was the case for the single-particle excited initial state. On the other hand, for example, in the many studies
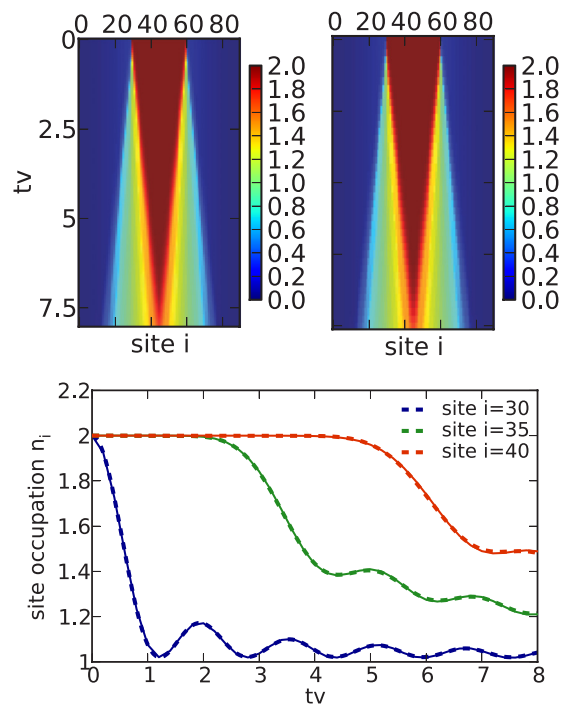
FIG. 8. (Color online) Time evolution of a one-dimensional fermionic Hubbard model on $L = 90$ sites, with an interaction of $U/v = 4$ and nearest-neighbor hopping v starting from a product state (double occupation in the center of the system). (Left) Chebyshev computation using $\varepsilon_{\text{che}} = 0.0001$. (Right) Krylov computation using $\varepsilon_{\text{kry}} = \varepsilon_{\text{che}}$. (Bottom) Detailed comparison for the occupation of specific sites. Chebyshev results are shown as dashed lines, Krylov results are shown as solid lines. Deviations are smaller than 1%.

on the *eigenstate thermalization hypothesis* [38,39], it is a frequently met assumption that for typical initial states the energy distribution around its mean value is extremely narrow, with a width of the order of the single-particle energy scale (see, e.g., Ref. [40] Fig. 3(b)).

VI. CONCLUSION

We started by linking *linear prediction* to *analytic continuation*, which explains why linear prediction is a reasonable method to extrapolate both Fourier and Chebyshev expansions of spectral functions. In order to apply linear prediction, we introduced a new method to avoid the algebraic convergence of Chebyshev moments (expansion coefficients) of generic steplike spectral functions. This amounts to a particular redefinition of the series expansion that is based on a subtraction of the Chebyshev moments of a self-consistently determined step function.

We then showed that this allows to reduce the expansion order by a factor $\frac{1}{6}$ as compared to the existing method [13]. For linearly scaling algorithms, as in exact diagonalization [1,9], this means a reduction of computation time of the same factor. Also for matrix product state computations high speedups are obtained. Furthermore, we showed how to adapt the discretization of hybridization functions of impurity models to the Chebyshev method.

Finally, we showed the approximate equivalence of the Chebyshev recursion to time evolution in a certain limit. This led to a novel time-evolution algorithm and allowed to transparently compare standard time evolution and the Chebyshev recursion in how efficient they extract spectral information from an operator H. For exact representations, the Chebyshev recursion is superior to time evolution as the latter is equivalent to the least favorable setup of the Chebyshev expansion, which can be improved by the previously mentioned factor $\frac{1}{6}$. For matrix product state representations, our results indicate that the Chebyshev expansion is inferior: we observe a much higher entanglement production in the Chebyshev recursion than in standard time evolution. We identify as the main reason for this an unfavorable error accumulation in the Chebyshev recursion that requires computations at higher accuracy. So while in the history of the solution of differential equations for non-periodic problems, Chebyshev expansions replaced Fourier expansions in the course of time [15], in the matrix product state context, such a transition now seems unlikely. Still, the Chebyshev recursion provides an easy-to-implement and straightforward way to compute spectral functions.

Relevant applications of the results of this paper are the computation of conductivities [41], the computation of time evolution of long-range interacting systems [35], and in particular, the challenging solution of dynamical mean-field theory [13,14]. For example, the latter can usually not be accessed by combining analytical and numeric techniques as recently done for the Hubbard model in Ref. [42].

APPENDIX A: CONVERGENCE SPEED

Analogously to Ref. [15, Chap. 2.9], we give the argument for the speed of convergence of the Chebyshev sequence, computed with the nonweighted inner product of (6b)

$$\mu_n = \int_{-1}^{1} dx\, f(x) T_n(x)$$
$$= \int_{0}^{\pi} d\theta\, f(\cos\theta) \cos(n\theta) \sin\theta$$
$$= \mathrm{Re} \int_{0}^{\pi} d\theta\, \widetilde{f}(\cos\theta) e^{in\theta}, \qquad (A1)$$

where $\widetilde{f}(\theta) = f(\cos\theta)\sin\theta$. We can then do k partial integrations, if $\widetilde{f}(\theta)$ is k times differentiable,

$$\mu_n = \mathrm{Re}\left\{ -\sum_{j=1}^{k} \left[\left(\frac{i}{n}\right)^j e^{in\theta} \widetilde{f}^{(j-1)}(\theta) \Big|_0^\pi \right] \right.$$
$$\left. + \left(\frac{i}{n}\right)^k \int_0^\pi d\theta\, \widetilde{f}^{(k)}(\theta) e^{in\theta} \right\}, \qquad (A2)$$

where $\widetilde{f}^{(j)}(\theta)$ denotes the jth derivative of $\widetilde{f}(\theta)$. If $\widetilde{f}^{(j)}(0) = \widetilde{f}^{(j)}(\pi) = 0$ for $j = 0, \ldots, k-1$, which is fulfilled for typical single-particle spectral functions as in Fig. 2, and if $\widetilde{f}^{(k)}(\theta)$ is integrable, (A2) constitutes an upper bound $\mathcal{O}(\frac{1}{n^k})$ for the sequence μ_n.

APPENDIX B: EXAMPLES FOR LINEAR PREDICTION OF CHEBYSHEV EXPANSIONS

In Sec. II, we compared the reconstruction of a spectral functions using its extrapolated (linearly predicted) Chebyshev expansion. We focused on a typical example for this discussion, given by the $U/v = 4$ spectral function of the half-filled SIAM with semielliptic bath density of states, which is shown in the top panel of Fig. 1.

In this Appendix, we support the arguments of Sec. II by showing further generic examples. Starting from a steplike input function $A^>(\omega)$, we again compare the two reconstructions based on (i) linearly predicting the "subtracted" spectral function $\widetilde{A}^>(\omega)$ of (17) and (ii) linearly predicting the "full"
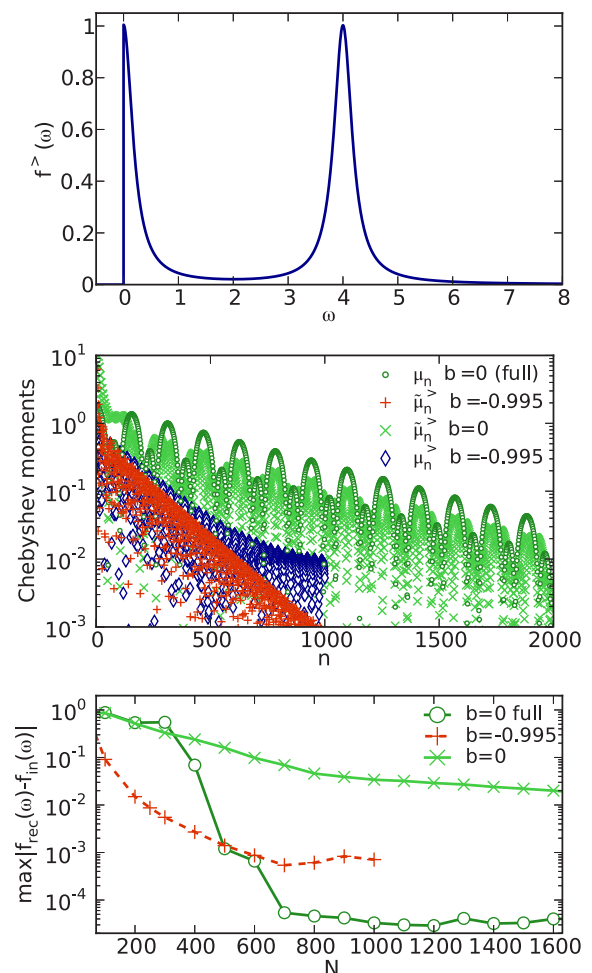

FIG. 9. (Color online) (Top) Test function consisting of two Lorentzians (B1). (Center) Corresponding Chebyshev moments in the three different setups $\mu^>$, $\widetilde{\mu}^>$, and μ, analogously to the bottom panel of Fig. 2. (Bottom) Error of reconstructed spectral function, analogously to the bottom panel of Fig. 3. All of this is for $a = 100$.
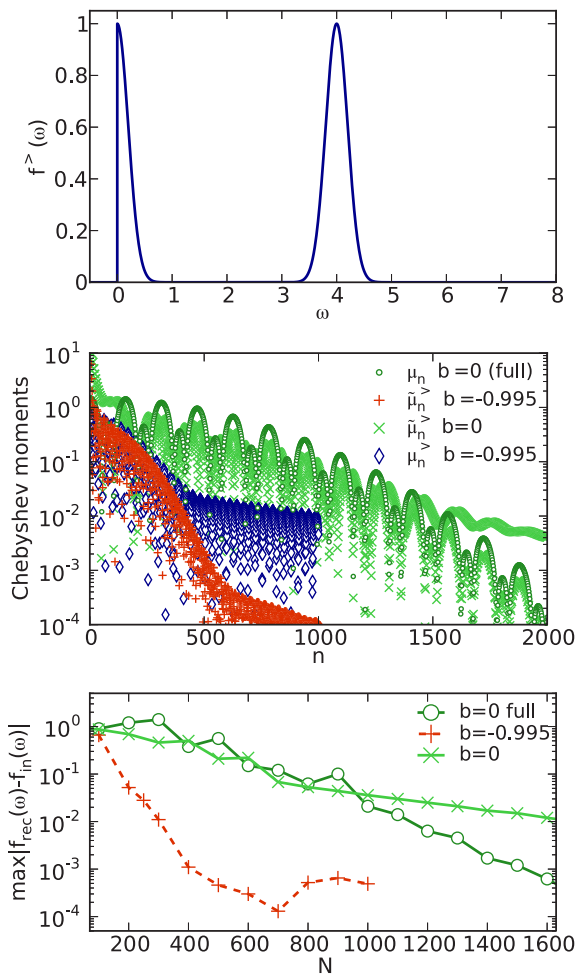
FIG. 10. (Color online) (Top) Test function consisting of two Gaussians (B1). (Center) Corresponding Chebyshev moments in the three different setups $\mu^>$, $\tilde{\mu}^>$, and μ, analogously to the bottom panel of Fig. 2. (Bottom) Error of reconstructed spectral function, analogously to the bottom panel of Fig. 3. All of this is for $a = 100$.

FIG. 11. (Color online) (Top) Particle spectral function of half-filled noninteracting SIAM. (Center) Corresponding Chebyshev moments in the three different setups $\mu^>$, $\tilde{\mu}^>$, and μ, analogously to the bottom panel of Fig. 2. (Bottom) Error of reconstructed spectral function, analogously to the bottom panel of Fig. 3.

(summed particle and hole contributions) spectral function $A(\omega)$ of (18).

To consider generic cases, we study functions that show "features" at $\omega = 0$ and at some distance, of order of the single-particle bandwidth, away from it. The most natural choice for constructing such functions are superpositions of (non-normalized) Lorentzians and Gaussians

$$f^>(\omega) = \begin{cases} 0 & \text{for } \omega < 0 \\ \sum_{\omega_0 \in \{0,4\}} h(\omega, \omega_0) & \text{else,} \end{cases}$$

$$h_l(\omega, \omega_0) = \frac{\eta^2}{(\omega - \omega_0)^2 + \eta^2}, \qquad \text{(B1)}$$

$$h_g(\omega, \omega_0) = e^{-\frac{(\omega - \omega_0)^2}{2\eta^2}}.$$

The function $f^>(\omega)$ is plotted for both choices in the top panels of Figs. 9 and 10 for $\eta = 0.2$.

Based on the same argument as is the basis for Sec. V in this paper (approximate equivalence of Fourier and Chebyshev expansion), Ref. [14] showed the decrease of Chebyshev moments for superpositions of Lorentzians and Gaussians, to

be approximately exponential and $\propto e^{-\alpha n^2}$, respectively. This behavior is observed in both center panels of Figs. 9 and 10. For high values of n, in Fig. 10, the decrease $\propto e^{-\alpha n^2}$ transitions into an exponential decrease, which is not in contradiction with the result of Ref. [14]. In Sec. V, we discuss intermediate values of n.

In the bottom panels of Figs. 9 and 10, we then show the error obtained for the different methods of reconstruction. Linearly predicting $\tilde{A}^>(\omega)$ yields considerably lower errors than linearly predicting the "full" spectral function $A(\omega)$. Only in the case of Lorentzians (lower panel of Fig. 9), using $A(\omega)$ leads to lower errors for values of n.

Finally, in Fig. 11, we show results for the spectral function of the half-filled noninteracting SIAM with semielliptic bath density of states, which itself is semielliptic,

$$A^>(\omega) = \begin{cases} 0 & \text{for } \omega < 0, \\ 0 & \text{for } \omega > 2v, \\ \frac{1}{2v\pi}\sqrt{4 - \left(\frac{\omega}{v}\right)^2} & \text{else.} \end{cases} \qquad \text{(B2)}$$

$A^>(\omega)$ has a kink at $\omega = 2v$, as can be seen in the top panel of Fig. 11. Therefore the Chebyshev moments decrease only algebraically, as seen in the center panel of Fig. 11.

If we consider the error of the linear-prediction-based reconstructed $A^>(\omega)$, shown in the bottom panel of Fig. 11, we see that this yields much better results than the estimate (21) gives for a plain truncation of an algebraically decreasing series. Concerning the comparison between the two methods of reconstructing $\widetilde{A}^>(\omega)$ and the full $A(\omega)$, we observe that $\widetilde{A}^>(\omega)$ yields to smaller errors throughout.

We finally note that studying the spectral function of the noninteracting SIAM with a constant bath density of states as in Refs. [17,13], does not constitute a more general case. The analytic expression for this is very close to a single Lorentzian.

APPENDIX C: LINEAR PREDICTION

In the context of time-evolution, *linear prediction* has been long established in the DMRG community [11,12], but it has only recently been applied to the computation of Chebyshev moments [13,14]. The optimization problem for the sequence μ_n becomes linear, if the sequence can be defined *recursively*:

$$\tilde{\mu}_n = -\sum_{i=1}^{p} a_i \mu_{n-i}, \qquad (C1)$$

which is easily found to be equivalent to (1) [12]. The strategy is then as follows. Compute N_c Chebyshev moments, and predict moments for higher values of n using (C1).

The coefficients a_i are optimized by minimizing the least-square error $\sum_{n \in \mathcal{N}_{\text{fit}}} |\tilde{\mu}_n - \mu_n|^2$ for a subset $\mathcal{N}_{\text{fit}} = \{N_c - n_{\text{fit}}, \ldots, N_c - 1, N_c\}$ of the computed data. We confirmed $n_{\text{fit}} = N_c/4$ to be a robust choice, (i) small enough to go beyond complicated low-order (short-time) behavior and (ii) large enough to have a good statistics for the fit. Earlier [14], we chose $n_{\text{fit}} = N_c/2$, which leads to a better statistics for the fit. However, this improvement is not important, as we do not deal with stochastic data. Minimization yields

$$R\boldsymbol{a} = -\boldsymbol{r}, \quad \boldsymbol{a} = -R^{-1}\boldsymbol{r},$$
$$R_{ji} = \sum_{n \in \mathcal{N}_{\text{fit}}} \mu_{n-j}^* \mu_{n-i}, \qquad (C2)$$
$$r_j = \sum_{n \in \mathcal{N}_{\text{fit}}} \mu_{n-j}^* \mu_n.$$

Linear prediction is more prone to *overfitting* if choosing p to be very high. Therefore one should restrict the number of coefficients to $p = \min(n_{\text{fit}}/2, 100)$. Furthermore, one adds a small constant $\delta = 10^{-6}$ to the diagonal of R in order to enable the inversion of the singular matrix R. Defining [12]

$$M = \begin{pmatrix} -a_1 & -a_2 & -a_3 & \ldots & -a_p \\ 1 & 0 & 0 & \ldots & 0 \\ 0 & 1 & 0 & \ldots & 0 \\ \vdots & \ddots & \ddots & \ddots & \vdots \\ 0 & 0 & \ldots & 1 & 0 \end{pmatrix},$$

one obtains the predicted moments $\tilde{\mu}_{N_c+n} = (M^n \boldsymbol{\mu}_{N_c})$, where $\boldsymbol{\mu}_{N_c} = (\mu_{N_c-1} \ \mu_{N_c-2} \ \ldots \ \mu_{N_c-p})^T$. The matrix M might have eigenvalues with absolute value larger than 1, either due to numerical inaccuracies or due to the fact that linear prediction

cannot be applied as μ_n rather increases than decreases on the training subset $\mathcal{N}_{\text{fit}}$. In order to obtain a convergent prediction, we set the weights that correspond to these eigenvalues to zero measuring the ratio of the associated discarded weight compared to the total weight. If this ratio is higher than a few percent, we conclude that linear prediction cannot be applied. One can then restart the computation to increase the number of computed moments N_c, and try applying linear prediction for a higher number of moments.

APPENDIX D: DISCRETIZATION FOR ODD L

In the case of odd L we cannot equate the central interval boundary with 0 as in Eq. (27). Instead we have to choose the correct width for the "central interval" by choosing the neighboring boundaries $\omega_{(L+1)/2}$ and $\omega_{(L+1)/2+1}$ correctly. This is achieved by subtracting an offset Δw from each of the positive boundaries defined in Eq. (28), such that for $l = 1, 2, \ldots$

$$\omega_{(L+1)/2+l} = a(\cos(\theta_{(L+1)/2+1} + l\Delta\theta) - b - \Delta\omega),$$
$$\Delta\theta = \frac{2}{L}(\theta_{L+1} - \theta_{(L+1)/2+1}),$$
$$\theta_{(L+1)/2+1} = \arccos b,$$
$$\theta_{L+1} = \arccos\left(b + \frac{\omega_{L+1}}{a}\right),$$
$$\Delta\omega = \frac{1}{2}(\cos(\theta_{(L+1)/2+1} + \Delta\theta) - b). \qquad (D1)$$

For negative boundaries, $\Delta\omega$ has to be added instead of subtracted.

APPENDIX E: TIME EVOLUTION BY FOURIER TRANSFORM

Given the Chebyshev expansion in frequency space,

$$A^>(\omega) = \frac{1}{a}\mathcal{A}^>\left(\frac{\omega}{a} + b\right),$$
$$\mathcal{A}^>(x) = \sum_n w_n(x)\mu_n T_n(x), \qquad (E1)$$

we can obtain the time evolution of a *single* Green function, but not for the whole system state, by Fourier transforming

$$\begin{aligned}
G^>(t) &= \int_{-\infty}^{\infty} d\omega \, A^>(\omega) e^{i\omega t} \\
&= \frac{1}{a} \int_{-\infty}^{\infty} d\omega \, \mathcal{A}^>\left(\frac{\omega}{a} + b\right) e^{i\omega t} \\
&= \int_{-\infty}^{\infty} dx \, \mathcal{A}^>(x) e^{ia(x-b)t} \\
&= \int_{-\infty}^{\infty} dx \sum_n w_n(x)\mu_n T_n(x) e^{ia(x-b)t} \\
&= \sum_n \mu_n \int_{-\infty}^{\infty} dx \, w_n(x) T_n(x) e^{ia(x-b)t} \\
&= e^{-iabt} \sum_n (2 - \delta_{n0})(-i)^n \mu_n J_n(at), \qquad (E2)
\end{aligned}$$

where the last step (interchanging sum and integral) is only possible if the sum is absolutely convergent, or finite. The Fourier transform can be looked up in a handbook on integrals,

$$\int_{-\infty}^{\infty} dx \, w_n(x) T_n(x) e^{ia(x-b)t}$$

$$= (2 - \delta_{n0}) e^{-iabt} \int_{-\infty}^{\infty} dx \, \frac{T_n(x) e^{iaxt}}{\pi \sqrt{1-x^2}}$$

$$= (-i)^n (2 - \delta_{n0}) e^{-iabt} J_n(at). \tag{E3}$$

APPENDIX F: COMPARISON TO TIME EVOLUTION

1. Standard recursion for cosine

As usual for a vector space of orthogonal polynomials, the space of cosine functions $\{\cos(nx)\}$, where $n \in \mathbb{N}, x \in \mathbb{R}$, can be generated using a three-term recursion formula:

$$\cos(nx) = 2\cos(x)\cos((n-1)x) - \cos((n-2)x), \tag{F1}$$

which can be proven using addition theorems.

Rewriting this in the operator-valued form for the argument $\mathcal{H}$, and acting on $|\psi_0\rangle$ yields for the definition of $|\phi_{\cos}(t_n)\rangle$ in Eq. (34),

$$|\phi_{\cos}(t_n)\rangle = 2\cos\mathcal{H}|\phi_{\cos}(t_{n-1})\rangle - |\phi_{\cos}(t_{n-2})\rangle. \tag{F2}$$

However, this provides no solution for our problem as the action of $\cos\mathcal{H}$ on $|\phi_{\cos}(t_{n-1})\rangle$ is not known.

2. Shifted cosine

Using an addition theorem

$$\cos\left(n\left(\frac{\pi}{2} - \alpha\right)\right)$$

$$= \cos\left(n\frac{\pi}{2}\right)\cos(n\alpha) + \sin\left(n\frac{\pi}{2}\right)\sin(n\alpha)$$

$$= \begin{cases} \cos(n\alpha) & \text{if } \frac{n}{4} \in \mathbb{N} \\ \sin(n\alpha) & \text{if } \frac{n+2}{4} \in \mathbb{N} \\ \frac{1}{\sqrt{2}}(\cos(n\alpha) + \sin(n\alpha)) & \text{else} \end{cases} \tag{F3}$$

Equation (36) follows if setting $\alpha = \mathcal{H}$.

3. Sine term

Changing the initial conditions of (F4a) generates the polynomials $T_n' = \sin(n \arccos(x))$

$$T_n'(x) = 2x T_{n-1}'(x) - T_{n-2}'(x), \tag{F4a}$$

$$T_1'(x) = \sqrt{1-x^2}, \quad T_0'(x) = 0, \tag{F4b}$$

which approximates the sine function, in the same way as (36) approximates the cosine

$$T_n'(\mathcal{H}) \simeq \sin(n\mathcal{H}) \text{ if } n/4 \in \mathbb{N}. \tag{F5}$$

4. Bound for Arccos

Bounding the Arccos works as follows:

$$\arccos(x) = \frac{\pi}{2} - \sum_{n=0}^{\infty} \frac{\binom{2n}{n} x^{2n+1}}{4^n(2n+1)}$$

$$= \frac{\pi}{2} - x - r(x)$$

$$r(x) = x^3 \left[\frac{1}{6} + \left|\sum_{n=2}^{\infty} \frac{\binom{2n}{n} x^{2n-2}}{4^n(2n+1)}\right|\right]. \tag{F6}$$

Using $\arcsin(1) = \sum_{n=0}^{\infty} \frac{\binom{2n}{n}}{4^n(2n+1)} = \frac{\pi}{2}$ we can bound

$$|r(x)| = |x^3| \left[\frac{1}{6} + \left|\sum_{n=2}^{\infty} \frac{\binom{2n}{n} x^{2n-2}}{4^n(2n+1)}\right|\right]$$

$$< |x^3| \left[\frac{1}{6} + \left|\sum_{n=2}^{\infty} \frac{\binom{2n}{n}}{4^n(2n+1)}\right|\right]$$

$$= |x^3| \left(\frac{1}{6} + \frac{\pi}{2} - 1 - \frac{1}{6}\right)$$

$$= |x^3| \left(\frac{\pi}{2} - 1\right)$$

$$< \frac{2}{3}|x^3|. \tag{F7}$$

5. Error computation

The approximation in Eq. (36) is based on the Taylor expansion

$$\arccos(\mathcal{H}) = \frac{\pi}{2} - \mathcal{H} + \frac{1}{6}\mathcal{H}^3 + \mathcal{O}(\mathcal{H}^5),$$

$$\mathcal{H} = \frac{H - E_{\text{ref}}}{a}, \tag{F8}$$

which reflects the fact that the arcus cosine is well approximated already by the leading linear term around $x = 0$.

The approximation of $|\phi(t_n)\rangle$ that has been generated in this way, is good if a is large enough and becomes exact for $a \to \infty$. However, how large does one have to choose a in practice in order for $\epsilon(t_{n'})$ to be bounded by the wished accuracy?

Consider the decomposition of the initial state in eigenstates $|E_n\rangle$ of $\mathcal{H}$

$$|\psi_0\rangle = \sum_k c_k |E_k\rangle, \tag{F9}$$

and, defining $\omega_k = \frac{E_k - E_{\text{ref}}}{a}$, therefore

$$T_n(\mathcal{H})|\psi_0\rangle = \sum_k c_k T_n(\omega_k)|E_k\rangle. \tag{F10}$$

We are now only interested in indices n' that are multiples of $4n$, as only those have the interpretation of a time-evolved

state. Therefore

$$
\begin{aligned}
T_{n'}(\omega_k) &= \cos(n' \arccos(\omega_k)) \\
&= \cos(n'\omega_k - n'r_k) \quad \text{as } n' = 4n, \text{ see Eq. (F3)}, \\
&= \cos(n'\omega_k)\cos(n'r_k) + \sin(n'\omega_k)\sin(mr_k) \\
&= \cos(n'\omega_k) + \epsilon_k(n'), \\
\epsilon_k(n') &= \cos(n'\omega_k)(\cos(mr_k) - 1) \\
&\quad + \sin(n'\omega_k)\sin(mr_k).
\end{aligned}
$$

Up to here everything was exact.

Now we can strictly bound the absolute value of the error term using $|\sin(r_k)| < |r_k|$ and $|\cos(r_k) - 1| < \frac{r_k^2}{2}$ and trivially bounding $\cos(n'\omega_k)$ and $\sin(n'\omega_k)$ by one,

$$
|\epsilon_k(n')| < \tfrac{1}{2}n'^2 r_k^2 + n'|r_k|. \tag{F11}
$$

Let us now define the energy eigenvector $|E_{\max}\rangle$ for which the error ϵ_k becomes maximal, which is the one for which $\omega_{\max}$ is maximal, i.e.,

$$
\omega_{\max} = \max_{|E_k\rangle \in |\psi_0\rangle} \omega_k \tag{F12}
$$

with which we compute $r_{\max}$ and $\epsilon_{\max}$. We can then simplify further

$$
\sum_k c_k \epsilon_k(n') |E_k\rangle < \epsilon_{\max}(n') \sum_k c_k |E_k\rangle = \epsilon_{\max}(n')|\psi_0\rangle.
$$

We therefore arrive at

$$
T_{n'}(\mathcal{H})|\psi_0\rangle = \cos(n'\mathcal{H})|\psi_0\rangle + \epsilon(n')|\psi_0\rangle \tag{F13}
$$

The value of $\omega_{\max}$ is determined by the cutoff of the distribution of eigenvectors $|E_k\rangle$ in $|\psi_0\rangle$. This can be a strict cutoff or a few standard deviations of Gaussian distribution, beyond which no contributions with numerically measurable weight occur. Let denote this cutoff or width σ and define it analogously

to $\omega_{\max}$, i.e.,

$$
\sigma = \max_{|E_k\rangle \in |\psi_0\rangle} |E_k - E_{\text{ref}}| \Rightarrow \omega_{\max} = \frac{\sigma}{a}. \tag{F14}
$$

If, e.g., $|\psi_0\rangle$ is constructed by applying a single-particle operator to an eigenstate (e.g., the ground state) of H, σ is the single-particle bandwidth W_{single} times a small factor of order 1.

Finally, we need to bound the error term r_k (Appendix F 4)

$$
r_k = \tfrac{1}{6}\omega_k^3 + \mathcal{O}(\omega_k^5), \quad |r_k| < \tfrac{2}{3}|\omega_k^3|. \tag{F15}
$$

Using the definition of σ, let us now bound $\epsilon(n')$:

$$
\begin{aligned}
|\epsilon(n')| &< |\epsilon_{\max}(n')| \\
&< \frac{1}{2}n'^2 r_{\max}^2 + n'|r_{\max}| \\
&< \frac{1}{2}n'^2 \left(\frac{2}{3}\right)^2 \omega_{\max}^6 + n'\frac{2}{3}|\omega_{\max}^3| \\
&= \frac{1}{2}n'^2 \left(\frac{2}{3}\right)^2 \left(\frac{\sigma}{a}\right)^6 + n'\frac{2}{3}\left(\frac{\sigma}{a}\right)^3 \\
&< \frac{3}{2}n'\frac{2}{3}\left(\frac{\sigma}{a}\right)^3 \quad \text{if} \quad n' < n'_{\text{ref}} \\
&= \frac{n'}{n'_{\text{ref}}}, \quad n'_{\text{ref}} = \left(\frac{a}{\sigma}\right)^3.
\end{aligned}
$$

Or expressing this in units of time,

$$
\begin{aligned}
|\epsilon(t_{n'})| &= \frac{t}{t_{\text{err}}} \quad \text{if} \quad t < t_{\text{err}}, \\
t_{\text{err}} &= \frac{a^2}{\sigma^3}. \tag{F16}
\end{aligned}
$$

Inserting typical values, where v is a hopping energy for a single-particle process: $\sigma = 2v$, $a = 100v$, one finds $t_{\text{err}} = \frac{1250}{v}$. The accumulated error $\epsilon(t_{n'})$ therefore remains smaller than 10^{-2} if $t < 12.5\frac{1}{v}$.

---

[1] A. Weiße, G. Wellein, A. Alvermann, and H. Fehske, Rev. Mod. Phys. **78**, 275 (2006).

[2] W. Gautschi, SIAM Rev. **9**, 24 (1967).

[3] W. Gautschi, Math. Comp. **22**, 251 (1968).

[4] W. Gautschi, Math. Comp. **24**, 245 (1970).

[5] R. A. Sack and A. F. Donovan, Numer. Math. **18**, 465 (1971).

[6] R. N. Silver and H. Röder, Int. J. Mod. Phys. C **05**, 735 (1994).

[7] L.-W. Wang, Phys. Rev. B **49**, 10154 (1994).

[8] L.-W. Wang and A. Zunger, Phys. Rev. Lett. **73**, 1039 (1994).

[9] L. Lin, Y. Saad, and C. Yang, arXiv:1308.5467.

[10] W. H. Press, S. A. Teukolsky, W. T. Vetterling, and B. P. Flannery, *Numerical Recipes: The Art of Scientific Computing*, 3rd ed. (Cambridge University Press, New York, 2007).

[11] S. R. White and I. Affleck, Phys. Rev. B **77**, 134437 (2008).

[12] T. Barthel, U. Schollwöck, and S. R. White, Phys. Rev. B **79**, 245101 (2009).

[13] M. Ganahl, P. Thunström, F. Verstraete, K. Held, and H. G. Evertz, Phys. Rev. B **90**, 045144 (2014).

[14] F. A. Wolf, I. P. McCulloch, O. Parcollet, and U. Schollwöck, Phys. Rev. B **90**, 115124 (2014).

[15] J. B. Boyd, *Chebyshev and Fourier Spectral Methods* (Dover Publications, Mineola, New York, 2001).

[16] C. Raas, G. S. Uhrig, and F. B. Anders, Phys. Rev. B **69**, 041102 (2004).

[17] A. Holzner, A. Weichselbaum, I. P. McCulloch, U. Schollwöck, and J. von Delft, Phys. Rev. B **83**, 195115 (2011).

[18] R. Bulla, T. Costi, and T. Pruschke, Rev. Mod. Phys. **80**, 395 (2008).

[19] U. Schollwöck, Ann. Phys. **326**, 96 (2011).

[20] D. Gobert, C. Kollath, U. Schollwöck, and G. Schütz, Phys. Rev. E **71**, 036102 (2005).

[21] J. Eisert and T. J. Osborne, Phys. Rev. Lett. **97**, 150404 (2006).

[22] M. Ganahl, M. Aichhorn, P. Thunström, K. Held, H. G. Evertz, and F. Verstraete, arXiv:1405.6728.

[23] F. A. Wolf, I. P. McCulloch, and U. Schollwöck, Phys. Rev. B **90**, 235131 (2014).

[24] W. Metzner and D. Vollhardt, Phys. Rev. Lett. **62**, 324 (1989).

[25] A. Georges and G. Kotliar, Phys. Rev. B **45**, 6479 (1992).

[26] A. Georges, G. Kotliar, W. Krauth, and M. J. Rozenberg, Rev. Mod. Phys. **68**, 13 (1996).

[27] G. Kotliar, S. Savrasov, K. Haule, V. Oudovenko, O. Parcollet, and C. Marianetti, Rev. Mod. Phys. **78**, 865 (2006).

[28] E. Jeckelmann, Phys. Rev. B **66**, 045114 (2002).

[29] D. J. García, K. Hallberg, and M. J. Rozenberg, Phys. Rev. Lett. **93**, 246403 (2004).

[30] P. E. Dargel, A. Wöllert, A. Honecker, I. P. McCulloch, U. Schollwöck, and T. Pruschke, Phys. Rev. B **85**, 205119 (2012).

[31] P. Arbenz, *Numerical Methods for Solving Large Scale Eigenvalue Problems*, Lecture Notes (ETH, Zürich, 2012).

[32] H. Tal-Ezer and R. Kosloff, J. Chem. Phys. **81**, 3967 (1984).

[33] C. Leforestier, R. Bisseling, C. Cerjan, M. Feit, R. Friesner, A. Guldberg, A. Hammerich, G. Jolicard, W. Karrlein, H.-D. Meyer *et al.*, J. Comp. Phys. **94**, 59 (1991).

[34] J. C. Halimeh, F. Kolley, I. P. McCulloch, and U. Schollwöck, (unpublished).

[35] M. P. Zaletel, R. S. K. Mong, C. Karrasch, J. E. Moore, and F. Pollmann, arXiv:1407.1832.

[36] S. R. White, Phys. Rev. B **72**, 180403 (2005).

[37] C. Hubig, I. P. McCulloch, U. Schollwöck, and F. A. Wolf, [Phys. Rev. B (to be published)], arXiv:1501.05504.

[38] J. M. Deutsch, Phys. Rev. A **43**, 2046 (1991).

[39] M. Srednicki, Phys. Rev. E **50**, 888 (1994).

[40] M. Rigol, V. Dunjko, and M. Olshanii, Nature (London) **452**, 854 (2008).

[41] J. H. García, L. Covaci, and T. G. Rappoport, Phys. Rev. Lett. **114**, 116602 (2015).

[42] L. Seabra, F. H. L. Essler, F. Pollmann, I. Schneider, and T. Veness, Phys. Rev. B **90**, 245127 (2014).

5.2. Strictly single-site DMRG algorithm with subspace expansion

Motivated by a visit of the authors of Dolgov and Savostyanov (2014) and Savostyanov, Dolgov, Werner, and Kuprov (2014) at LMU Munich, we (Hubig, McCulloch, Schollwöck, and Wolf, 2015) started thinking about implementing the ideas of Dolgov and Savostyanov (2014), which concern the "perturbation" of a DMRG optimization to avoid trapping in local minima. For the application of DMFT, the demanding form of the Hamiltonian (global energy landscape) always necessitates to use the perturbation technique of White (2005).[1] The following paper (Hubig *et al.*, 2015) combines ideas of White (2005) and Dolgov and Savostyanov (2014) to develop a computationally less costly perturbation algorithm.

▷ *Strictly single-site DMRG algorithm with subspace expansion*
C Hubig, IP McCulloch, U Schollwöck, and **FA Wolf**
Phys. Rev. B **91** 155115 (2015)

---

[1]See also the discussion in the appendix of Wolf *et al.* (2015a) in Sec. 3.2.

Strictly single-site DMRG algorithm with subspace expansion

C. Hubig,[1,*] I. P. McCulloch,[2] U. Schollwöck,[1] and F. A. Wolf[1]

[1]*Department of Physics and Arnold Sommerfeld Center for Theoretical Physics, Ludwig-Maximilians-Universität München,*
Theresienstrasse 37, 80333 München, Germany
[2]*Centre for Engineered Quantum Systems, School of Physical Sciences, The University of Queensland, Brisbane, Queensland 4072, Australia*

We introduce a strictly single-site DMRG algorithm based on the subspace expansion of the alternating minimal energy (AMEn) method. The proposed new MPS basis enrichment method is sufficient to avoid local minima during the optimization, similar to the density matrix perturbation method, but computationally cheaper. Each application of $\hat{H}$ to $|\Psi\rangle$ in the central eigensolver is reduced in cost for a speed-up of $\approx (d+1)/2$, with d the physical site dimension. Further speed-ups result from cheaper auxiliary calculations and an often greatly improved convergence behavior. Runtime to convergence improves by up to a factor of 2.5 on the Fermi-Hubbard model compared to the previous single-site method and by up to a factor of 3.9 compared to two-site DMRG. The method is compatible with real-space parallelization and non-Abelian symmetries.

　　PACS number(s): 05.10.Cc, 02.70.−c, 71.27.+a

I. INTRODUCTION

Since its introduction in 1993 [1,2], the density matrix renormalization group method (DMRG) has seen tremendous use in the study of one-dimensional systems [3,4]. Various improvements such as real-space parallelization [5], the use of Abelian and non-Abelian symmetries [6], and multigrid methods [7] have been proposed. Most markedly, the introduction [8] of density matrix perturbation steps allowed the switch from two-site DMRG to single-site DMRG in 2005, which provided a major speed-up and improved convergence in particular for systems with long-range interactions.

Nevertheless, despite some progress [9–11], (nearly) two-dimensional systems, such as long cylinders, are still a hard problem for DMRG. The main reason for this is the different scaling of entanglement due to the area law [12,13]: in one dimension, entanglement and hence matrix dimensions in DMRG are essentially size-independent for ground states of gapped systems, whereas in two dimensions, entanglement grows linearly and matrix dimensions roughly exponentially with system width.

As a result, the part of the Hilbert space considered by DMRG during its ground state search increases dramatically, resulting mainly in three problems as follows. First, the DMRG algorithm becomes numerically more challenging as the sizes of matrices involved grow [we will assume matrix-matrix multiplications to scale as $O(m^3)$ throughout the paper]. Second, the increased search space size makes it more likely to get stuck in local minima. Third, while sequential updates work well in one-dimensional (1D) chains with short-range interactions, nearest-neighbor sites in the 2D lattice can be separated much farther in the DMRG chain. Therefore, improvements to the core DMRG algorithm are still highly worthwhile.

In this paper, we will adopt parts of the AMEn method [14] developed in the tensor train/numerical linear algebra community to construct a strictly single-site DMRG algorithm that works without accessing the (full) reduced density

matrix. Compared to the existing *center matrix wave function formalism* (CWF) [15], we achieve a speed-up of $\approx (d+1)/2$ during each application of $\hat{H}$ to $|\Psi\rangle$ in the eigensolver during the central optimization routine, where d is the dimension of the physical state space on each site.

The layout of this paper is as follows. Section II will establish the notation. Section III will recapitulate the density matrix perturbation method and the CWF. Section IV will introduce the subspace expansion method and the heuristic expansion term with a simple two-spin example. The strictly single-site DMRG algorithm (DMRG3S) will be presented in Sec. V alongside a comparison with the existing CWF. As both the original perturbation method and the heuristic subspace expansion require a *mixing factor* α [8], Sec. VI describes how to adaptively choose α for fastest convergence. Numerical comparisons and examples will be given in Sec. VII.

II. DMRG BASICS

The notation established here closely follows the review article in Ref. [4]. Consider a state $|\Psi\rangle$ of a system of l sites. Each site has a physical state dimension d_i, e.g., $\forall i : d_i = 3$, $l = 50$ for a system of 50 $S = 1$ spins:

$$|\Psi\rangle = \sum_{\sigma_1 \dots \sigma_l} c_{\sigma_1 \dots \sigma_l} |\sigma_1 \dots \sigma_l\rangle. \quad (1)$$

In practice, the dimension of the physical basis is usually constant, $\forall i : d_i = d$, but we will keep the subscript to refer to one specific basis on site i where necessary.

It is then possible to decompose the coefficients $c_{\sigma_1, \dots, \sigma_l}$ as a series of rank-3 tensors $M_1, \dots, M_l$ of size (d_i, m_{i-1}, m_i), respectively, with $m_0 = m_l = 1$. The coefficient $c_{\sigma_1, \dots, \sigma_l}$ can then be written as the matrix product of the corresponding matrices in $M_1, \dots, M_l$:

$$|\Psi\rangle = \sum_{\sigma_1 \dots \sigma_l} \underbrace{M_1^{\sigma_1} \cdots M_l^{\sigma_l}}_{c_{\sigma_1 \dots \sigma_l}} |\sigma_1 \dots \sigma_l\rangle. \quad (2)$$

The maximal dimension $m = \max_i\{m_i\}$ is called the *MPS bond dimension*. In typical one-dimensional calculations, $m = 200$, but for, e.g., 32×5 cylinders, $m > 5000$ is often

*c.hubig@physik.uni-muenchen.de

necessary. It is in these numerically demanding cases that our improvements are of particular relevance.

Similarly, a Hamiltonian operator can be written as a *matrix product operator* (MPO), where each tensor W_i is now of rank 4, namely (d_i, d_i, w_{i-1}, w_i):

$$\hat{H} = \sum_{\substack{\sigma_1 \ldots \sigma_l \\ \tau_1 \ldots \tau_l}} W_1^{\sigma_1 \tau_1} \cdots W_l^{\sigma_l \tau_l} |\sigma_1 \ldots \sigma_l\rangle \langle \tau_1 \ldots \tau_l|. \quad (3)$$

$w = \max_i \{w_i\}$ is called the *MPO bond dimension*. We will usually assume that for most i, $m_i = m$ and $w_i = w$. In practice, this holds nearly everywhere except at the ends of the chain, where the m_i grow exponentially from 1 to m. The basis of M_i (W_i) of dimension m_{i-1} (w_{i-1}) is called the left-hand side (LHS) basis, whereas the basis of dimension m_i (w_i) is the right-hand side (RHS) basis of this tensor. For simplicity, m_i, d_i, and w_i can also refer to the specific basis (and not only its dimension) when unambiguous.

Instead of M_i, we will also write A_i (B_i) for a left (right) normalized MPS tensor:

$$\sum_{\sigma_i} A_i^{\sigma_i \dagger} A_i^{\sigma_i} = \mathbb{I}, \quad (4)$$

$$\sum_{\sigma_i} B_i^{\sigma_i} B_i^{\sigma_i \dagger} = \mathbb{I}. \quad (5)$$

If we then define the contractions

$$l_i = \left(A_1^{\sigma_1} \cdots A_{i-1}^{\sigma_{i-1}} M_i^{\sigma_i} \right) \in (d_1, \ldots, d_i, m_i), \quad (6)$$

$$r_i = \left(M_i^{\sigma_i} B_{i+1}^{\sigma_{i+1}} \cdots B_l^{\sigma_l} \right) \in (m_{i-1}, d_i, \ldots, d_l), \quad (7)$$

we can rewrite $|\Psi\rangle$ from (2) as

$$|\Psi\rangle = \sum_{\sigma_1 \ldots \sigma_l} l_i r_{i+1} |\sigma_1 \ldots \sigma_i\rangle \otimes |\sigma_{i+1} \ldots \sigma_l\rangle. \quad (8)$$

That is, when only considering one specific bond $(i, i + 1)$, the left and right MPS bases at this bond are built up from the states generated by the MPS tensor chains to the left and right of the bond. Individual elements of an MPS basis are therefore called "state."

Furthermore, define $L_0 = 1$ and $L_i = L_{i-1} A_i^\dagger W_i A_i$ with summation over all possible indices. Similarly, $R_{l+1} = 1$ and $R_i = R_{i+1} B_i^\dagger W_i B_i$. With these contractions, it is possible to write

$$\langle \Psi | \hat{H} | \Psi \rangle = L_{i-1} M_i^\dagger W_i M_i R_{i+1} \quad (9)$$

for any $i \in [0, l]$.

DMRG then works by *sweeping* over the system multiple times. During each sweep, each site tensor M_i is sequentially *updated* once with each update consisting of one optimization step via, e.g., a sparse eigensolver and possibly one *enrichment* step during which the left or right MPS basis of M_i is changed in some way. Depending on the exact implementation, updates may work on one (single-site DMRG) or two sites (two-site DMRG) at a time. The enrichment step may be missing or implemented via density matrix perturbation or subspace expansion.

III. PERTURBATION STEP AND CENTER MATRIX WAVE FUNCTION FORMALISM (CWF)

A. Convergence problems of single-site DMRG

During single-site DMRG, only a single MPS tensor M_i on site i is optimized at once. Compared to two-site DMRG, the search space is reduced by a factor of $d \approx 2 \ldots 5$, leading to a speed-up of at least $O(d)$ per iteration [8]. However, since the left and right bases of the tensors M_i are fixed and defined by the environment (l_{i-1} and r_{i+1}), this approach is likely to get stuck. While also occurring if there are no symmetries implemented on the level of the MPS, this issue is most easily visible if one considers $U(1)$ symmetries [4]: assume that all basis states to the right of the RHS bond of M_i transform as some quantum number s_z. If we now target a specific sector, e.g., $S_z = 0$ overall, then on the LHS of this bond (i.e., from the left edge up to and including M_i), all states must transform as $-s_z$. In this configuration, it is impossible for a local change of M_i to add a new state that transforms as, say, s_z', to its right basis states, as there would be no corresponding state $-s_z'$ to the right of that bond, rendering the addition of the state moot from the perspective of the local optimizer, as its norm will be zero identically. A concrete example of this issue is given in Sec. VII A.

DMRG is a variational approach on the state space available to MPS of a given bond dimension. As such, the algorithm must converge into either the global or a local minimum of the energy in this state space. Hence, we will call all cases where DMRG converges on an energy substantially higher than the minimal energy achievable with the allowed MPS bond dimension cases where DMRG is stuck in *local minima*.

B. Density matrix perturbation

This convergence problem has been solved by White [8]. In the following, we will assume a left-to-right sweep; sweeping in the other direction works similarly, but on the left rather than right bonds. After the local optimization of the tensor M_i, the reduced density matrix

$$\rho_{i,R} = l_{i-1} M_i M_i^\dagger l_{i-1}^\dagger \quad (10)$$

is built on the next bond. This is the reduced density matrix resulting from tracing out the part of the system to the left of bond $(i, i + 1)$.

$\rho_{i,R}$ is then perturbed as

$$\rho_{i,R} \rightarrow \rho_{i,R}' = \rho_{i,R} + \alpha \operatorname{Tr}(L_i \rho_{i,R} L_i^\dagger). \quad (11)$$

The new $\rho_{i,R}'$ is then used to decide on a new set of basis states on the RHS of M_i, with the inverse mapping from the new to the old basis being multiplied into each component of B_{i+1}. The mixing factor α is a small scalar used to control the perturbation. A new scheme to find the optimal choice of α is discussed in Sec. VI.

C. Center matrix wave function formalism (CWF)

In a standard single-site DMRG calculation, the reduced density matrix $\rho_{i,R}$ is never used. More importantly, even building $\rho_{i,R}$ on a given bond $(i, i + 1)$ will not yield a density matrix that can be used in (11), as it only contains the m_i states

existing on that bond already without knowledge of the m_{i-1} states on the bond one step to the left. In other words, it is not possible to choose the optimal set $\widetilde{m_i}$ based only on m_i; rather, one requires also d_i and m_{i-1}.

The center matrix wave function formalism [15] was developed to cope with this problem. Given a site tensor $M_i \in (d_i,m_{i-1},m_i)$ on a left-to-right sweep, it introduces a "center matrix" $C_{i,R} \in (d_i m_{i-1},m_i)$ and replaces the original site tensor as

$$M_i \rightarrow A_i \in (d_i,m_{i-1},d_i m_{i-1}) \text{ so that } M_i = A_i C_{i,R}. \quad (12)$$

A_i is constructed to be left orthogonal and is essentially an identity matrix mapping the left basis m_{i-1} and the physical basis d_i onto a complete basis containing all $d_i m_{i-1}$ states on its right. The new basis is "complete" in the sense that all states reachable from the left bond basis m_{i-1} and the local physical basis d_i are contained within it.

The contents of M_i are placed in $C_{i,R}$ accordingly and the original state remains unchanged. The reduced density matrix is then $\rho_{i,R} = C_{i,R} C_{i,R}^{\dagger}$ and has access to all $d_i m_{i-1}$ states, as required above. A perturbation of $\rho_{i,R}$ according to (11) hence allows the introduction of new states.

The DMRG optimization step can work on $C_{i,R}$ alone, with L_i built prior to optimization of $C_{i,R}$ from the expanded A_i. During each eigensolver step, the effective Hamiltonian on site i has to be applied onto $C_{i,R}$. The application is done by contraction of $L_i \in (w,d_i m_{i-1},d_i m_{i-1})$, $R_{i+1} \in (w,m_i,m_i)$, and $C_{i,R} \in (d_i m_{i-1},m_i)$ at cost $O(w(d^2 + d)m^3)$ per step. After optimization, the perturbation is added. Its computational cost is dominated by the calculation of $\alpha \operatorname{Tr}\{L_i \rho_{i,R} L_i^{\dagger}\}$ at $O(wd^3 m^3)$. The bond between A_i and $C_{i,R}$ can then be truncated down to m using $\rho_{i,R}'$ and the remaining parts of $C_{i,R}$ are multiplied into B_{i+1} to the right.

The resulting algorithm converges quickly for one-dimensional problems and performs reasonably well for small cylinders. However, both the cost of the applications of $\hat{H}$ to $|\Psi\rangle$ as $O(w(d^2 + d)m^3)$ as well as the large density matrix $\rho \in (dm,dm)$ cause problems if m and w become large.

IV. SUBSPACE EXPANSION

The idea of using *subspace expansion* instead of density matrix perturbation originates [14,16] in the tensor train/numerical linear algebra community. There, a stringent proof was given regarding the convergence properties of this method when the local tensor Z_i of the residual

$$|Z\rangle \equiv \hat{H}|\Psi\rangle - E|\Psi\rangle = \sum_{\sigma_1 \ldots \sigma_l} Z_1^{\sigma_1} \cdots Z_l^{\sigma_l} |\sigma_1 \ldots \sigma_l\rangle \quad (13)$$

is used as the expansion term. Here, we will only use the method of subspace expansion and substitute a numerically much more cheaply available expansion term.

The following section is divided into three parts as follows. First, we will explain the concept of subspace expansion acting on two neighboring MPS tensors M_i, M_{i+1}. Second, the expansion term employed in DMRG3S is introduced and motivated. Third, a simple example is described.

A. Subspace expansion with an arbitrary expansion term

In the following, we will describe subspace expansion of the RHS basis of the current working tensor, as it would occur during a left-to-right sweep.

Assume a state $|\Psi\rangle$ described by a set of tensors $\{A_1, \ldots, A_{i-1}, M_i, B_{i+1}, \ldots, B_l\}$. At the bond $(i,i+1)$, we can then decompose the state as a sum over left and right basis states as in Eq. (8).

Now we *expand* the tensor $M_i \in (d,m_{i-1},m_i)$ by some expansion term $P_i \in (d,m_{i-1},m_{P_i})$ for each individual physical index component:

$$M_i^{\sigma_i} \rightarrow \tilde{M}_i^{\sigma_i} = \begin{bmatrix} M_i^{\sigma_i} & P_i^{\sigma_i} \end{bmatrix}. \quad (14)$$

This effectively expands the RHS MPS basis of M_i from m_i to $m_i + m_{P_i}$. Similarly, expand the components of $B_{i+1} \in (d,m_i,m_{i+1})$ with zeros:

$$B_{i+1}^{\sigma_{i+1}} \rightarrow \tilde{B}_{i+1}^{\sigma_{i+1}} = \begin{bmatrix} B_{i+1}^{\sigma_{i+1}} \\ 0 \end{bmatrix}. \quad (15)$$

The appropriately sized block of zeros only multiplies with the expansion term $P_i^{\sigma_i}$. In terms of a decomposition as in (8), this is equivalent to

$$|\Psi\rangle = \sum_{\sigma_1, \ldots, \sigma_l} [l_i \ p] \begin{bmatrix} r_{i+1} \\ 0 \end{bmatrix} |\sigma_1 \ldots \sigma_i\rangle \otimes |\sigma_{i+1}, \ldots, \sigma_l\rangle \quad (16)$$

where p is the result of multiplying l_{i-1} and P_i, with the zero in the second expression similarly resulting from the zero in B_{i+1}. While the state $|\Psi\rangle$ remains unchanged, the local optimizer on the new site B_{i+1} can now choose the initially zero components differently if so required: the necessary flexibility in the left/right basis states to escape local minima has been achieved without referring to the density matrix.

Note that while orthonormality of B_{i+1} is lost, we do not need it between the enrichment step on site i and the optimization step on site $i + 1$. The orthonormality of M_i can be restored via singular value decomposition as usual. Furthermore, it is usually necessary to truncate the RHS basis of $\tilde{M}_i$ down from $m_i + m_{P_i}$ to m immediately following the expansion: this preserves the most relevant states of the expansion term while avoiding an exponential explosion of bond dimensions.

When sweeping from right to left, the left rather than right MPS basis of the current working tensor is expanded, with the left tensor A_{i-1} being zero padded as opposed to the right tensor B_{i+1}:

$$M_i^{\sigma_i} \rightarrow \tilde{M}_i^{\sigma_i} = \begin{bmatrix} M_i^{\sigma_i} \\ P_i^{\sigma_i} \end{bmatrix}, \quad (17)$$

$$A_{i-1}^{\sigma_{i-1}} \rightarrow \tilde{A}_{i-1}^{\sigma_{i-1}} = \begin{bmatrix} A_{i-1}^{\sigma_{i-1}} & 0 \end{bmatrix}. \quad (18)$$

B. Expansion term

Using the exact residual as the expansion term is computationally expensive: the term $\hat{H}|\Psi\rangle$ can be updated locally and is mostly unproblematic, but the subtraction of $E|\Psi\rangle$ and subsequent reorthonormalization is costly and has to be done after each local optimization, as the current value of E changes. This exact calculation is hence only possible for $m \approx 100$, which is far too small to tackle difficult two-dimensional problems.

Instead, we propose the very cheaply available terms

$$P_i = \alpha L_{i-1} M_i W_i \in (d_i, m_{i-1}, w_i m_i) \qquad (19)$$

to be used during left-to-right sweeps and $P_i = \alpha R_{i+1} M_i W_i$ for use during right-to-left sweeps with some scalar mixing factor α. In the regime where the exact residual can be computed, these terms work essentially equally well.

This expression for P_i can be heuristically motivated as follows: Eq. (19) is equivalent to the partial projection of $H|\Psi\rangle$ onto $|\Psi\rangle$ to the left of the current bond. Hence, in the ground state and ignoring numerical errors, the RHS basis of this P_i is identical to that of M_i. Truncation from $m_i + m_{P_i}$ to m_i is then possible without inducing errors.

Numerically, it seems possible to choose α arbitrarily large without hindering convergence or perturbing the state too much in simple (one-dimensional) problems. However, if the chosen maximal bond dimension m is insufficient to faithfully capture the ground state of the given system, α has to be taken to zero eventually to allow convergence. Otherwise, P_i will continuously add new states and disturb the result of the eigensolver, which is optimal at this specific value of m but not an eigenstate of $\hat{H}$ yet.

The cost of a single subspace expansion is $O(wdm^3 + w^2d^2m^2)$ for the calculation of P_i, potentially $O(2dwm^2)$ for the addition to M_i and B_{i+1}, respectively, and $O(dw^2m^3 + d^2m^2)$ for the SVD of an (dm, wm) matrix formed from $\tilde{M}_i$. If we restrict the SVD to m singular values, then the resulting matrices will be of dimension (dm, m), (m, m), and (m, wm), respectively. The first can be reformed into $\tilde{A}_i$ at cost $O(dm^2)$ and the second and third multiplied into B_{i+1} at cost $O(m^3dw + m^3d)$. The total cost of this step is dominated by the cost of the SVD at $O(dw^2m^3)$, which is still cheaper than the calculation of the perturbation term in (11), not considering the other costs associated to using the density matrix for truncation.

C. Subspace expansion at the example of a $d = l = 2$ spin system

In the following, we will demonstrate and illustrate the method of subspace expansion at the simple example of a system of two spins with $S = \frac{1}{2}$ from $m = 1$ to $m = 2$ as it would occur during a left-to-right sweep.

Assume the Hamiltonian

$$H = S_x^1 S_x^2 + S_y^1 S_y^2 + S_z^1 S_z^2 \qquad (20)$$

$$= \frac{1}{2}\{S_+^1 S_-^2 + S_-^1 S_+^2\} + S_z^1 S_z^2 \qquad (21)$$

with MPO components

$$W_1 = \left[\frac{1}{\sqrt{2}} S_+ \quad \frac{1}{\sqrt{2}} S_- \quad S_z \right], \qquad (22)$$

$$W_2 = \left[\frac{1}{\sqrt{2}} S_- \quad \frac{1}{\sqrt{2}} S_+ \quad S_z \right]^T. \qquad (23)$$

Let the initial state be an $m = 1$ MPS, described by components

$$A_1^\uparrow = [a], \quad A_1^\downarrow = [\sqrt{1-a^2}], \qquad (24)$$

$$B_2^\uparrow = [b], \quad B_2^\downarrow = [\sqrt{1-b^2}], \qquad (25)$$

where square brackets denote matrices in the MPS bond indices. Due to the standard normalization constraints, there are only two free scalar variables here, a and b.

Subspace expansion of A_1 is straightforward (keep in mind that $L_0 \equiv 1$ for convenience):

$$P_1^{\tau_1} = \sum_{\sigma_1} W_1^{\tau_1 \sigma_1} A_1^{\sigma_1}, \qquad (26)$$

$$P_1^\uparrow = W_1^{\uparrow\uparrow} A_1^\uparrow + W_1^{\uparrow\downarrow} A_1^\downarrow \qquad (27)$$

$$= \left[\frac{\sqrt{1-a^2}}{\sqrt{2}} \quad 0 \quad a \right], \qquad (28)$$

$$P_1^\downarrow = W_1^{\downarrow\uparrow} A_1^\uparrow + W_1^{\downarrow\downarrow} A_1^\downarrow \qquad (29)$$

$$= \left[0 \quad \frac{a}{\sqrt{2}} \quad -\sqrt{1-a^2} \right], \qquad (30)$$

resulting in A_1' and B_2' directly after the expansion:

$$A_1'^\uparrow = \left[a \quad \frac{\sqrt{1-a^2}}{\sqrt{2}} \quad 0 \quad a \right], \qquad (31)$$

$$A_1'^\downarrow = \left[\sqrt{1-a^2} \quad 0 \quad \frac{a}{\sqrt{2}} \quad -\sqrt{1-a^2} \right], \qquad (32)$$

$$B_2'^\uparrow = \begin{bmatrix} b \\ 0 \\ 0 \\ 0 \end{bmatrix}, \quad B_2'^\downarrow = \begin{bmatrix} \sqrt{1-b^2} \\ 0 \\ 0 \\ 0 \end{bmatrix}. \qquad (33)$$

Normalizing A_1' via a singular-value decomposition as $A_1' \rightarrow A_1'' SV^\dagger$ and multiplying $SV^\dagger B_2' \rightarrow B_2''$ gives

$$A_1''^\uparrow = [1 \quad 0], \qquad (34)$$

$$A_1''^\downarrow = [0 \quad 1], \qquad (35)$$

$$SV^\dagger = \begin{bmatrix} a & \frac{\sqrt{1-a^2}}{\sqrt{2}} & 0 & a \\ \sqrt{1-a^2} & 0 & \frac{a}{\sqrt{2}} & -\sqrt{1-a^2} \end{bmatrix}, \qquad (36)$$

$$B_2''^\uparrow = \begin{bmatrix} ab \\ \sqrt{1-a^2}b \end{bmatrix}, \qquad (37)$$

$$B_2''^\downarrow = \begin{bmatrix} a\sqrt{1-b^2} \\ \sqrt{1-a^2}\sqrt{1-b^2} \end{bmatrix}. \qquad (38)$$

As expected, the final state $|\psi\rangle = \sum_{\sigma_1 \sigma_2} A_1''^{\sigma_1} B_2''^{\sigma_2}$ is still entirely unchanged, but there is now a one-to-one correspondence between the four entries of B_2'' and the coefficients $c_{\{\uparrow,\downarrow\},\{\uparrow,\downarrow\}}$ in the computational basis, making the optimization towards $c_{ii} = 0, c_{i \neq j} = \frac{1}{\sqrt{2}}$ trivial.

V. STRICTLY SINGLE-SITE DMRG

We can now combine standard single-site DMRG (e.g., Ref. [4], p. 67) with the subspace expansion method as a way to enrich the local state space, leading to a strictly single-site DMRG implementation (DMRG3S) that works without referring to the density matrix at any point.

With the notation from Sec. II, the steps follow mostly standard single-site DMRG. In an outermost loop, the algorithm sweeps over the system from left-to-right and right-to-left until convergence is reached. Criteria for convergence are, e.g., diminishing changes in energy or an overlap close to 1 between the states at the ends of subsequent sweeps.

The inner loop sweeps over the system, iterating over and updating the tensors on each site sequentially. Each local update during a left-to-right sweep (right-to-left sweeps work analogously) consists of the following steps.

(1) Optimize the tensor M_i: use an eigensolver targeting the smallest eigenvalue to find a solution $(M_i^\star, \lambda^\star)$ to the eigenvalue problem

$$L_{i-1} R_{i+1} W_i M_i = \lambda M_i. \tag{39}$$

$\lambda^\star$ is the new current energy estimate. This first step dominates the computational cost.

(2) Build αP_i according to (19) using $M_i^\star$. Build an appropriately sized zero block 0_{i+1} after the dimensions of P_i are known.

(3) Subspace-expand $M_i^\star \to \tilde{M}_i^\star$ with αP_i and B_{i+1} with 0_{i+1}.

(4) Apply a SVD to $\tilde{M}_i^\star$ and truncate its right basis to m_i again, resulting in $\tilde{A}_i^\star$.

(5) Multiply the remainder of the SVD ($SV^\dagger$) into $B_{i+1} \to \tilde{B}_{i+1}$.

(6) Build L_i from $\tilde{A}_i^\star$, L_{i-1}, and W_i.

(7) Calculate a new energy value after truncation based on L_i, $\tilde{B}_{i+1}$, W_{i+1}, and R_{i+1}. Use this energy value and $\lambda^\star$ to adapt the current value of α (cf. Sec. VI).

(8) Continue on site $i + 1$.

Of these, steps (2) and (3) implement the actual subspace expansion, whereas all others are identical to standard single-site DMRG.

It is important to note that the only change from standard single-site DMRG is the addition of an enrichment step via subspace expansion. Therefore, this method does not interfere with, e.g., real-space parallelized DMRG [5,17], the use of non-Abelian symmetries [6,15], or multigrid methods [7].

To analyze the computational cost, we have to take special care to ensure optimal ordering of the multiplications during each eigensolver iteration in (39). The problem is to contract $L_{i-1} R_{i+1} W_i M_i$, with L_{i-1} and $R_{i+1} \in (w, m, m)$, $W_i \in (d, d, w, w)$, and $M_i \in (d, m, m)$. The optimal ordering is then $(((L_{i-1} M_i) W_i) R_{i+1})$ as follows.

(1) Contract L_{i-1} and M_i over the left MPS bond at cost $O(mw \cdot m \cdot dm = m^3 wd)$.

(2) Multiply in W_i over the physical bond of M_i and the left MPO bond at cost $O(m^2 \cdot wd \cdot dw = m^2 d^2 w^2)$.

(3) Finally contract with R_{i+1} over the right MPO and MPS bonds at cost $O(md \cdot wm \cdot m = m^3 dw)$.

The total cost of this procedure to apply $\hat{H}$ to $|\Psi\rangle$ is $O(2m^3 wd + d^2 m^2 w^2)$. Assuming large $d^2 w/m$ is small, this gives a speed-up in the eigensolver multiplications of $(d + 1)/2$ over the CWF approach, which takes $O(m^3 wd(d + 1))$.

In addition to this speed-up, the subspace expansion is considerably cheaper than the density matrix perturbation. Since the perturbation/truncation step can often take up to 30% of total computational time, improvements there also have a high impact. At the same time, the number of sweeps at large m

needed to converge does not seem to increase compared to the CWF approach (cf. Sec. VII) and sometimes even decreases.

VI. ADAPTIVE CHOICE OF MIXING FACTOR

Both density matrix perturbation and subspace expansion generally require some small mixing factor α to moderate the contributions of the perturbation terms. The optimal choice of this α depends on the number of states available and those required to represent the ground state, as well as the current speed of convergence. Too large values for α hinder convergence by destroying the improvements made by the local optimizer, whereas too small values lead to the calculation being stuck in local minima with vital states not added for the reasons given in Sec. III B. The correct choice of α hence affects calculations to a large degree, but is also difficult to estimate before the start of the calculation.

Figure 1 displays the individual steps within a single update from the energy perspective: let ΔE_O denote the gain in energy during the optimization step and let ΔE_T denote the subsequent rise in energy during the truncation following the enrichment step. $\Delta E_T \neq 0$ only occurs if some enrichment (either via density matrix perturbation or subspace expansion) has occurred; otherwise, there would be no need for any sort of truncation. We can hence control the approximate value of ΔE_T via α, which leads to a simple adaptive and computationally cheap algorithm.

If ΔE_T was very small or even negative (after changing the optimized state by expansion of its right basis) during the current update, we can increase α during the next update step on the next site. If, on the other hand, $|\Delta E_T| \approx |\Delta E_O|$, that is, if the error incurred during truncation nullified the gain in energy during the optimization step, we should reduce the value of α at the next iteration to avoid making this mistake again.

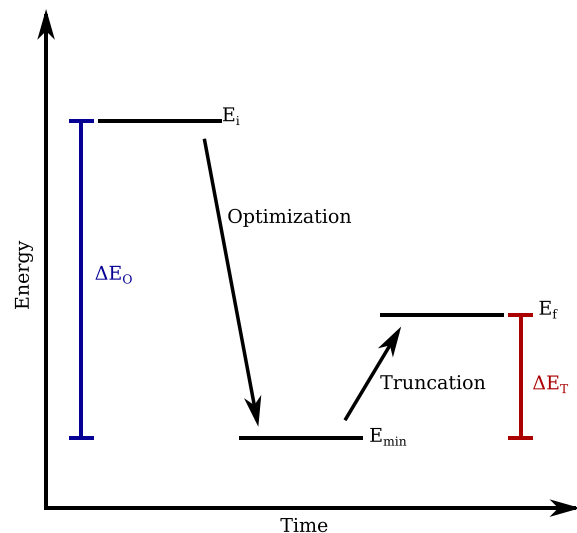

FIG. 1. (Color online) Energies of the state at different points during a single update: before optimization, the state has some initial energy E_i. Local optimization via the eigensolver takes this energy down by ΔE_O to $E_{\min}$. Subsequent truncation causes a rise in energy by ΔE_T with the final value at the end of this update being E_f.

In practice, it seems that keeping $\Delta E_T \approx -0.3 \Delta E_O$ gives the fastest convergence. Given the order-of-magnitude nature of α, it is furthermore best to increase/decrease it via multiplication with some factor greater/smaller than 1 as opposed to adding or subtracting fixed values.

Some special cases for very small ΔE_O (stuck in a local minimum or converged to the ground state?) and $\Delta E_T > 0$ or $\Delta E_T < \Delta E_O$ have to be considered, mostly depending on the exact implementation.

It is unclear whether there is a causal relation between the optimal choice of α and the ratio of $\Delta E_T / \Delta E_O$ or whether both simply correlate with a proceeding DMRG calculation: at the beginning, gains in energy are large and α is optimally chosen large, whereas later on, energy decreases more slowly and smaller values of α are more appropriate.

It is important to note that this is a tool to reach convergence more quickly. If one is primarily interested in a wave function representing the ground state, the calculation of a new α at each iteration comes at essentially zero cost. If, however, the aim is to extrapolate in the truncation error during the calculation, then a fixed value for α is of course absolutely necessary.

VII. NUMERICAL EXAMPLES

A. DMRG stuck in a local minimum

In this subsection, we will give a short example of how DMRG can get stuck in a local minimum even on a very small system. Consider $20 S = \frac{1}{2}$ spins with isotropic antiferromagnetic interactions and open boundary conditions. The $U(1)$ symmetry of the system is exploited on the MPS basis, with the overall S_z forced to be zero. The initial state is constructed from 20 linearly independent states, all with three sites on the very right at $S_z = 0.5$ and $m = 20$ in total. The quantum number distribution at each bond is plotted in Fig. 2 as black circles.

DMRG3S is run with subspace expansion disabled, i.e., $\alpha = 0$, throughout the calculation. The algorithm "converges" to some high-energy state at $E^{\alpha=0} = -6.35479$. The resulting quantum number distribution (red squares in Fig. 2) shows clear asymmetry both between the left and right parts of the system and the $+S_z$ and $-S_z$ sectors at any given bond. It is also visible that while some states are removed by DMRG3S without enrichment, it cannot add new states: the red squares only occur together with the black filled circles from the input state.

If we enable enrichment via subspace expansion, i.e., take $\alpha \neq 0$, DMRG3S quickly converges to a much better ground state at $E^{\alpha\neq0} = -8.6824724$. The quantum numbers are now evenly distributed between the left and right parts of the system and $\pm S_z$ symmetry is also restored.

B. Application to physical systems

In the following subsections, we will compare the two single-site DMRG algorithms CWF and DMRG3S when applied to four different physical systems: a $S = 1$ Heisenberg spin chain with periodic boundary conditions, a bosonic system with an optical lattice potential, a Fermi-Hubbard model at $U = 1$ and quarter-filling, and a system of free fermions at half-filling.
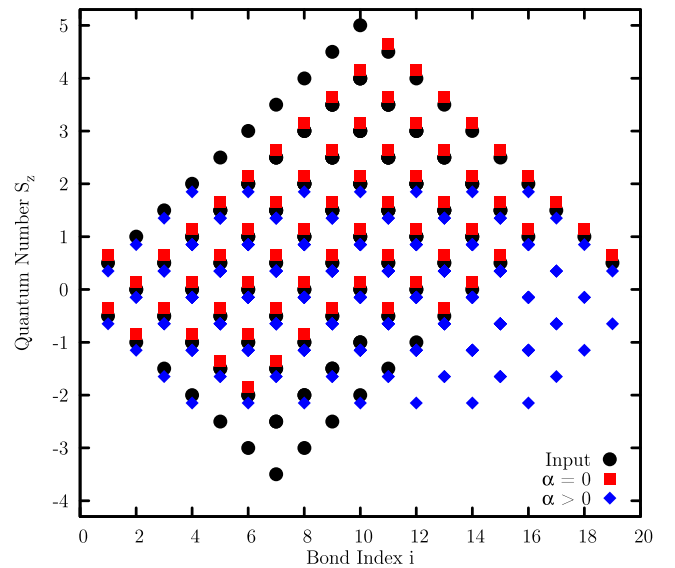

FIG. 2. (Color online) Quantum number distribution as counted from the right at each bond of a $l = 20$ system with $S = \frac{1}{2}$ and $S_z^{\text{total}} = 0$. The artificial input state is shown with black circles. Two DMRG calculations have then been done on this input state, once with no enrichment term ($\alpha = 0$, red squares) and once with subspace expansion enabled ($\alpha \neq 0$, blue diamonds). It is clearly visible that without enrichment, DMRG3S can reduce some weights to zero, but cannot add new states—red only occurs together with black. As soon as enrichment is enabled, DMRG3S restores $\pm S_z$ symmetry and reflective symmetry over the 10th bond and finds a much better ground state.

Each algorithm is run at three different values of $m = m_{\max}, m_{\max}/2, m_{\max}/4$ from the same initial state and run to convergence. This way, it is possible to observe the behavior of the methods at both low and high accuracies.

The usual setup in DMRG calculations of starting at small m and increasing m slowly while the calculation progresses makes it unfortunately very difficult to compare between the three methods. This is because different methods require different configurations to converge optimally. We therefore restrict ourselves to fixed m throughout an entire calculation, even though all methods could be sped up further by increasing m slowly during the calculation.

Errors in energy compared to a numerically exact reference value E_0 are plotted as a function of sweeps and CPU time. It should be stressed that this error in energy is not directly comparable to the truncation error traditionally used in two-site DMRG or the variance $\langle \hat{H}^2 \rangle - \langle \hat{H} \rangle^2$ sometimes considered in single-site DMRG. Even small differences in energy can lead to vastly different physical states and reaching maximal accuracy in energy is crucial to ensure that the true ground state has been reached.

Furthermore, a traditional two-site DMRG (2DMRG) calculation without perturbations is done and its error in energy and runtime to convergence is compared to the two single-site algorithms. Here, *convergence* is defined as a normalized change in energy less than 10^{-9} (for $m = m_{\max}$) (10^{-8}) (for $m < m_{\max}$). The *runtime to convergence* is the CPU time used
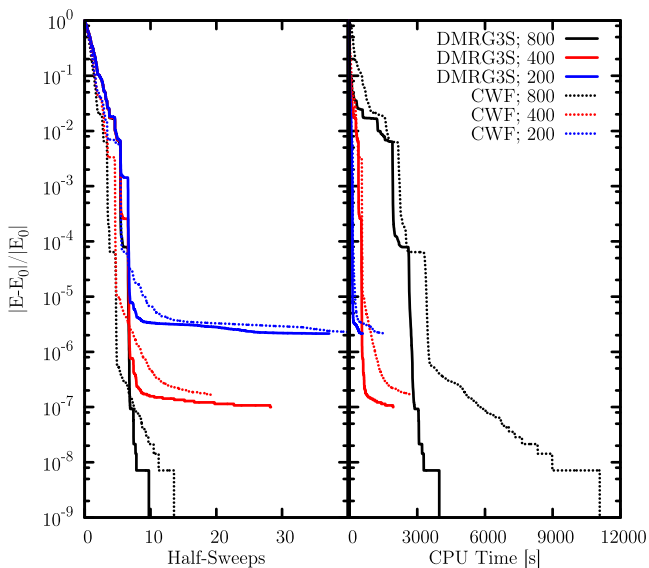
FIG. 3. (Color online) Spin chain Eq. (40): normalized error in energy as a function of sweeps (left) and CPU time used (right) of the two single-site algorithms at different $m = 200, 400, 800$. DMRG3S shows both a speed-up and an improved convergence per sweep compared to CWF, with a long tail of slow convergence very visible for CWF at high accuracies.

until that energy was output by the eigensolver for the first time.

All calculations were performed on a single core of a Xeon E5-2650.

1. $S = 1$ *Heisenberg chain*

First, we consider a $S = 1$ Heisenberg spin chain with $l = 100$ sites and periodic boundary conditions implemented on the level of the Hamiltonian as a simple link between the first and last site:

$$\hat{H} = \sum_{i=1}^{100} \hat{S}_i \cdot \hat{S}_{(i+1)\%100}. \qquad (40)$$

$U(1)$ symmetries are exploited and the calculations are forced in the $S_z = 0$ sector.

This system is of particular interest as, first, it is one of the standard benchmarking systems with well-known analytic values for the ground-state energy. Second, it is a one-dimensional system where the case of periodic boundary conditions can still be tackled by DMRG. The larger MPO bond dimension resulting from these PBC similarly arises during the simulation of quasi-two-dimensional systems as cylinders. The same applies to the non-nearest-neighbor interactions in this system (between the first and last site) and cylindrical systems.

Figure 3 compares the error in energy with respect to the reference value $E_0 = -140.148\,404$ for DMRG3S and CWF for $m = 200, 400, 800$ as a function of sweeps and computation time.

During the first three to four sweeps, DMRG3S exhibits a smaller convergence rate per sweep; however, compared to the first sweeps of CWF, they also cost negligible CPU time. Afterwards, DMRG3S offers comparable (at medium

TABLE I. Spin chain Eq. (40): normalized error in energy at convergence and runtime to convergence of all three methods. DMRG3S is consistently faster than CWF, whereas the energies provided by 2DMRG are not comparable in accuracy.

	$m = 200$	$m = 400$	$m = 800$
DMRG3S energy error	2.1×10^{-6}	1.0×10^{-7}	7.1×10^{-9}
CWF energy error	2.8×10^{-6}	1.7×10^{-7}	7.1×10^{-9}
2DMRG energy error	1.1×10^{-5}	8.6×10^{-7}	1.0×10^{-7}
DMRG3S runtime	583 s	1935 s	3990 s
CWF runtime	1519 s	2695 s	11133 s
2DMRG runtime	762 s	3181 s	21963 s

accuracies) or much improved (at high accuracies) convergence rate per sweep as compared to CWF together with a still reduced average runtime per sweep. Combined, these effects lead to a speed-up of 2.6, 1.3, and 2.7 for $m = 200, 400$, and 800, respectively, between CWF and DMRG3S when considering the runtime to convergence.

In comparison, the 2DMRG algorithm does not handle the periodic boundary conditions well and yields energies higher than the single-site algorithms with perturbations (cf. Table I). Runtime to convergence is hence not comparable.

2. *Dilute bosons on an optical lattice*

We carry on to study bosons in a modulated potential of 10 unit cells, each with 16 sites. The cutoff for local occupation numbers is $n_{max} = 5$, resulting in a local site dimension of $d = 6$. The Hamiltonian is given as

$$\hat{H} = +\sum_{i=1}^{160} \hat{n}_i \left\{ \cos^2\left(2\pi\frac{i-0.5}{16}\right) + (\hat{n}_i - 1)\right\}$$
$$- \sum_{i=1}^{159} \{\hat{c}_i^\dagger \hat{c}_{i+1} + \text{H.c.}\}. \qquad (41)$$

This system should be fairly easy for DMRG to handle, as there are only nearest-neighbor interactions. However, the large-scale order due to the modulated potential and a very small energy penalty paid for an uneven distribution of bosons was observed to cause badly converged results [7]. Manual checks of the states returned by each method hence done to ensure a proper, equal distribution of bosons throughout the whole system.

The state is initialized with $n = 80$ bosons in total. We allow $m = 50, 100, 200$ states and use the energy reference value $E_0 = -103.646\,757$. All algorithms converge to this value at $m = 200$.

Figure 4 compares CWF and DMRG3S, whereas Table II additionally lists 2DMRG. Since the bond dimensions are relatively small, we do not expect a speed-up from faster numerical operations. Instead, the improved convergence behavior per sweep is responsible for the speed-up of 2 of DMRG3S over CWF at small m. At larger m, CWF converges better, but numerical operations also become cheaper for DMRG3S for a speed-up of 2 again.

As there are no long-range interactions, 2DMRG also fares well with regard to energy accuracy. However, it takes longer
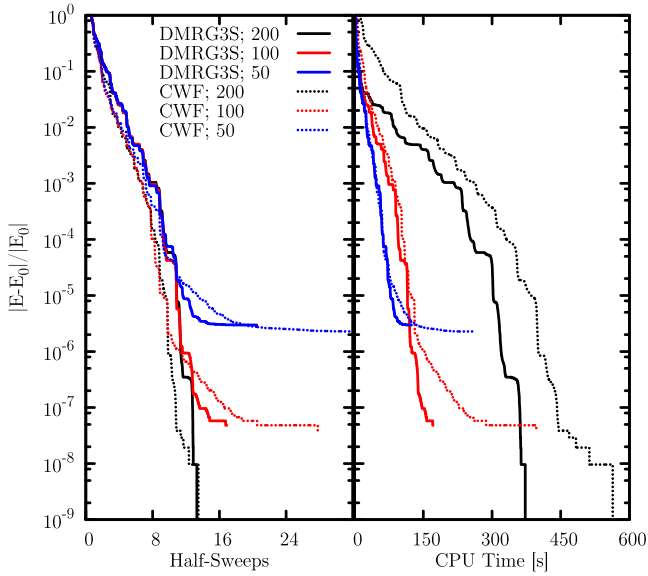
FIG. 4. (Color online) Bosonic system Eq. (41): normalized error in energy from CWF and DMRG3S as a function of sweeps (left) and CPU time used (right) for $m = 50, 100, 200$. Again, an improved convergence behavior at high accuracies can be observed, in particular at smaller values of m. The small bond dimensions lead to a smaller speed-up due to faster numerical operations, which only becomes visible at $m = 200$.
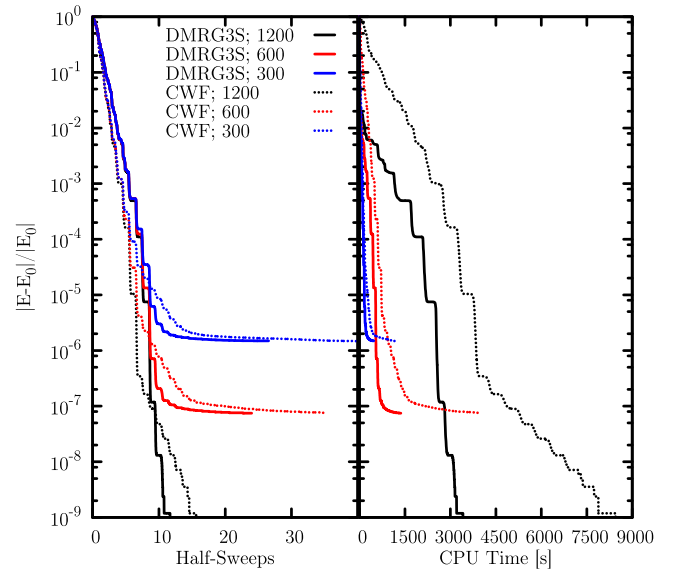

FIG. 5. (Color online) Fermi-Hubbard Eq. (42): normalized error in energy from DMRG3S and CWF as a function of sweeps (left) and CPU time used (right) for different bond dimensions $m = 300, 600, 1200$. The same basic behavior as for the previous systems is repeated, with both improved convergence behavior at high accuracies and faster numerical operations.

to converge than the single-site methods especially at large m, mainly because the eigenvalue problem in two-site DMRG is of dimension d larger than in single-site DMRG. A comparison between DMRG3S and 2DMRG leads to a speed-up of up to 3.3 for the case of $m = 200$.

3. Fermi-Hubbard model

As a third example, substantially more expensive calculations are carried out for a substantially stronger entangled Fermi-Hubbard model of 100 sites with Hamiltonian

$$\hat{H} = \sum_{i=1}^{100} \left\{ -\sum_{\sigma=\uparrow,\downarrow} [\hat{c}_{i,\sigma}^\dagger \hat{c}_{i+1,\sigma} + \text{H.c.}] + \hat{n}_{i,\uparrow}\hat{n}_{i,\downarrow} \right\}. \quad (42)$$

Both $U(1)_{\text{charge}}$ and $U(1)_{\text{Sz}}$ symmetries are employed, with 50 fermions and $S_z^{\text{total}} = 0$ enforced through the choice of initial state. Together with the free fermions from the next

section, we can use this system to study how criticality and increased entanglement affect the three methods.

Calculations are done for $m = 300, 600, 1200$. All methods converge to the same value $E_0 = -84.2555254$ at large m.

Figure 5 compares the two single-site methods, while Table III summarizes all three DMRG implementations. Since the system only exhibits local interactions, 2DMRG fares well and all methods generally provide comparable energies. The difference is therefore in the runtime needed to achieve these energies. Compared to CWF, DMRG3S achieves a speed-up of ≈ 2.6 consistently at all m, as the smallest $m = 300$ is already large enough to justify the assumption $d^2 w \ll m$ in the speed-up of numerical operations. In particular, it continues to converge quickly at high accuracies, whereas CWF develops a long tail of slow convergence. The speed-up compared to 2DMRG is smaller at lower values of m, but increases to 3.9 at $m = 1200$.

TABLE II. Bosonic system Eq. (41): normalized error in energy at convergence and run time to convergence of all three methods. DMRG3S is again the fastest method with a very constant speed-up of 2 over CWF and up to 3.3 over 2DMRG.

	$m = 50$	$m = 100$	$m = 200$
DMRG3S energy error	2.9×10^{-6}	4.8×10^{-8}	$<10^{-9}$
CWF energy error	2.3×10^{-6}	3.9×10^{-8}	$<10^{-9}$
2DMRG energy error	1.9×10^{-6}	2.8×10^{-8}	$<10^{-9}$
DMRG3S runtime	124 s	171 s	469 s
CWF runtime	260 s	397 s	951 s
2DMRG runtime	210 s	462 s	1550 s

TABLE III. Fermi-Hubbard Eq. (42): normalized error in energy at convergence and runtime to convergence of all three methods. Accuracies are comparable between the different methods, but runtimes vary greatly.

	$m = 300$	$m = 600$	$m = 1200$
DMRG3S energy error	1.5×10^{-6}	7.5×10^{-8}	$<10^{-9}$
CWF energy error	1.5×10^{-6}	7.6×10^{-8}	$<10^{-9}$
2DMRG energy error	1.3×10^{-6}	6.4×10^{-8}	$<10^{-9}$
DMRG3S runtime	474 s	1367 s	3955 s
CWF runtime	1215 s	3917 s	10122 s
2DMRG runtime	727 s	2950 s	15596 s

TABLE IV. Free fermions Eq. (43): normalized error in energy at convergence and runtime to convergence of all three methods.

	$m = 300$	$m = 600$	$m = 1200$
DMRG3S energy error	5.0×10^{-6}	2.8×10^{-7}	$< 10^{-9}$
CWF energy error	3.8×10^{-6}	2.8×10^{-7}	$< 10^{-9}$
2DMRG energy error	3.7×10^{-6}	2.6×10^{-7}	$< 10^{-9}$
DMRG3S runtime	533 s	1452 s	4643 s
CWF runtime	863 s	2590 s	9586 s
2DMRG runtime	794 s	4584 s	29698 s

4. Free fermions

Finally, we consider a model of free fermions on a chain of 100 sites with Hamiltonian

$$\hat{H} = -\sum_{i=1}^{100} \sum_{\sigma=\uparrow,\downarrow} [\hat{c}_{i,\sigma}^{\dagger} \hat{c}_{i+1,\sigma} + \text{H.c.}]. \tag{43}$$

The maximally delocalized wave function found in the ground state of this system is notoriously difficult for MPS formats in general to reproduce faithfully. At the same time, most other parameters are identical (d, l, m) or very close (w) to those in the Fermi-Hubbard model from Sec. VIIB3. The calculation is done using $U(1)_{\text{charge}}$ and $U(1)_{\text{Sz}}$ symmetries at half-filling with $N = 100$ fermions and $S_z^{\text{total}} = 0$. The choice of m is the same as for the Fermi-Hubbard system, namely $m = 300, 600, 1200$. We used $E_0 = -126.602\,376$ as the reference value, since all methods converged to this ground-state energy at $m = 1200$.

The results in Table IV and Fig. 6 mostly follow previous results for locally interacting systems: accuracies of all methods are essentially identical, whereas time to convergence varies between the methods. At small m, there are some speed-ups of DMRG3S over CWF, largely due to better convergence behavior per sweep, whereas a significant advantage of DMRG3S becomes visible at larger m, when numerical operations become cheaper compared to the CWF method. Correspondingly, the speed-up from CWF to DMRG3S increases from 1.6 at $m = 300$ to 2 at $m = 1200$.

Similarly, the larger numerical cost of two-site DMRG becomes more noticeable at larger m, with the speed-up between 2DMRG and DMRG3S increasing from 1.5 at $m = 300$ to more than 6 at $m = 1200$.

Compared to the noncritical Fermi-Hubbard system from Sec. VIIB3, we observe larger errors in energy at fixed m, as expected. Correspondingly, as more eigenvalues contribute significantly, convergence of both the eigenvalue solver and the singular value decompositions becomes slower, leading to a slow-down of all three methods.
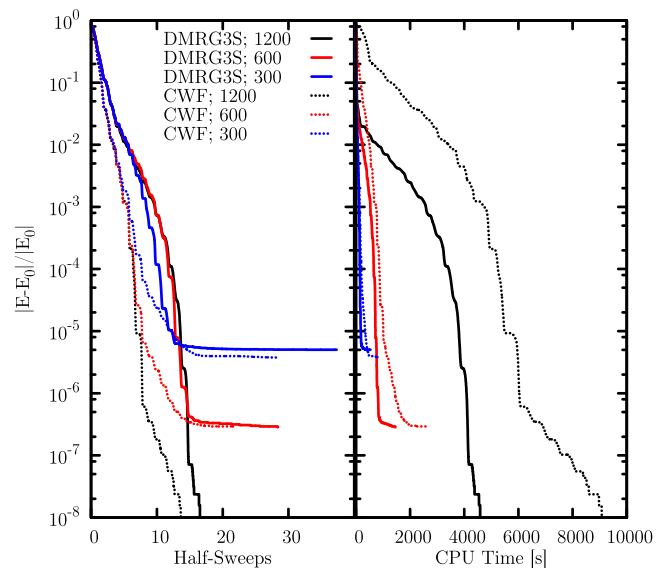

FIG. 6. (Color online) Free fermions Eq. (43): normalized error in energy from CWF and DMRG3S as a function of sweeps (left) and CPU time used (right) at $m = 300, 600, 1200$. CWF again exhibits a long tail of slow convergence, while DMRG3S converges quickly at all m and all accuracies.

VIII. CONCLUSIONS

The new strictly single-site DMRG (DMRG3S) algorithm results in a theoretical speed-up of $\sim (d + 1)/2$ during the optimization steps compared to the center matrix wave function formalism (CWF), provided that $d^2 w/m$ is small. Further, convergence rates per sweep are improved in the important and computationally most expensive high-accuracy/large-m phase of the calculation. In addition, auxiliary calculations (enrichment, normalization, etc.) are sped up and memory requirements are relaxed.

Numerical experiments confirm a speed-up within the theoretical expectations compared to the CWF method. The efficiency of single-site DMRG in general compared to the traditional two-site DMRG was substantiated further by a large speed-up at comparable accuracies in energy.

[1] S. R. White, Phys. Rev. Lett. **69**, 2863 (1992).
[2] S. R. White, Phys. Rev. B **48**, 10345 (1993).
[3] U. Schollwöck, Rev. Mod. Phys. **77**, 259 (2005).
[4] U. Schollwöck, Ann. Phys. (NY) **326**, 96 (2011).
[5] E. M. Stoudenmire and S. R. White, Phys. Rev. B **87**, 155137 (2013).
[6] I. P. McCulloch and M. Gulácsi, Europhys. Lett. **57**, 852 (2002).
[7] M. Dolfi, B. Bauer, M. Troyer, and Z. Ristivojevic, Phys. Rev. Lett. **109**, 020604 (2012).
[8] S. R. White, Phys. Rev. B **72**, 180403 (2005).
[9] S. Yan, D. A. Huse, and S. R. White, Science **332**, 1173 (2011).

[10] S. Depenbrock, I. P. McCulloch, and U. Schollwöck, Phys. Rev. Lett. **109**, 067201 (2012).

[11] E. Stoudenmire and S. R. White, Annu. Rev. Condens. Matter Phys. **3**, 111 (2012).

[12] G. Vidal, J. I. Latorre, E. Rico, and A. Kitaev, Phys. Rev. Lett. **90**, 227902 (2003).

[13] J. Eisert, M. Cramer, and M. B. Plenio, Rev. Mod. Phys. **82**, 277 (2010).

[14] S. Dolgov and D. Savostyanov, SIAM J. Sci. Comput. **36**, A2248 (2014).

[15] I. P. McCulloch, J. Stat. Mech. (2007) P10014.

[16] S. V. Dolgov and D. V. Savostyanov, Lect. Notes Comput. Sci. Eng. **103**, 335 (2015).

[17] S. Depenbrock, Ph.D. thesis, Ludwig-Maximilians-Universität München, 2013.

5.3. How to discretize a quantum bath for real-time evolution

In the framework of an MPS solution to DMFT based on time evolution algorithms on the real-time axis (Ganahl *et al.*, 2014b; Wolf *et al.*, 2014b) or on Chebyshev (Weiße *et al.*, 2006; Holzner *et al.*, 2011; Wolf *et al.*, 2014a, 2015b) or Lanczos (Gagliano and Balseiro, 1987; Hallberg, 1995; García *et al.*, 2004; Dargel *et al.*, 2012) algorithms, it is a highly important question whether an intelligent discretization technique allows to use smaller bath sizes, and by that reduce computational cost significantly. The following paper (de Vega *et al.*, 2015) shows that this is not possible in general, except for the non-interacting case. For this latter case, we show that a quadrature-rule based strategy, which is well known in the literature (Burkey and Cantrell, 1984), reproduces the numerically exact time evolution of the continuous system up to a time $t_{\max}$, for which we give a simple expression. The result is not only relevant for strongly correlated quantum many body systems, but also in the context of open quantum systems.

▷　　*How to discretize a quantum bath for real-time evolution*
　　　I de Vega, U Schollwöck and **FA Wolf**
　　　Phys. Rev. B **92**, 155126

How to discretize a quantum bath for real-time evolution

Inés de Vega, Ulrich Schollwöck, and F. Alexander Wolf

Department of Physics and Arnold Sommerfeld Center for Theoretical Physics, Ludwig-Maximilians-Universität München,
Theresienstr. 37, 80333 Munich, Germany

Many numerical techniques for the description of quantum systems that are coupled to a continuous bath require the discretization of the latter. To this end, a wealth of methods has been developed in the literature, which we classify as (i) direct discretization, (ii) orthogonal polynomial, and (iii) numerical optimization strategies. We recapitulate strategies (i) and (ii) to clarify their relation. For quadratic Hamiltonians, we show that (ii) is the best strategy in the sense that it gives the numerically exact time evolution up to a maximum time $t_{\max}$, for which we give a simple expression. For nonquadratic Hamiltonians, we show that no such best strategy exists. We present numerical examples relevant to open quantum systems and strongly correlated systems, as treated by dynamical mean-field theory (DMFT).

I. INTRODUCTION

Quantum systems coupled to a continuous bath appear in different fields of physics, such as open quantum systems (OQS), strongly correlated many-body physics, and spectroscopy and scattering problems. In the context of OQS [1,2], for instance, a quantum system like an atom or a quantum dot is linearly coupled to a continuous bath like a phononic, electronic, or photonic reservoir, which produces dissipation and decoherence in the system. In the context of strongly correlated many-body physics, the Anderson impurity model [3] and its generalizations, which describe clusters of electronic impurities coupled to a continuous conduction band of electrons, are an important field of study. In addition, they are the basis for dynamical mean-field theory (DMFT) [4–6], which is the most widely used numerical method to describe strongly correlated systems in dimensions higher than one in physics [7,8] and is popular also in quantum chemistry [9]. A discrete system coupled to a continuum appears also in spectroscopy or scattering problems [10], leading to a *resonance* or state with a complex energy that due to the imaginary energy component decays in time.

The dynamics of a system that is strongly coupled to a continuous environment cannot be described using analytic weak-coupling approaches [1,2], and requires the use of numerical techniques such as exact diagonalization (ED), the density matrix renormalization group (DMRG), and the numerical renormalization group (NRG). However, all of these numerical techniques are restricted to treating *discrete* Hamiltonians, and cannot *directly* deal with a Hamiltonian that involves a continuous bath. Therefore it is necessary to construct a discrete approximation to the continuous Hamiltonian.

In this paper, we analyze the problem of constructing the discrete Hamiltonian that best approximates the time evolution produced by the continuous Hamiltonian with the smallest possible number N_b of discrete degrees of freedom. As the many-body Hilbert space grows exponentially with N_b, this question is highly relevant, and its solution would allow to tackle systems with a complexity that is otherwise out of reach. We will show that this problem can only be solved for quadratic Hamiltonians. For nonquadratic Hamiltonians, we show that

no *best discrete approximation* exists, and instead, heuristic arguments have to be used to construct an approximation, as already found frequently in the literature [11–18].

Let us consider a general setup consisting of a system with Hamiltonian H_{sys} expressed in terms of system operators $d^{\dagger}$ and d (e.g., in the quadratic case $H_{\text{sys}} = \epsilon_0 d^{\dagger} d$), which is linearly coupled to a continuous harmonic oscillator bath characterized by a Hamiltonian H_{bath},

$$H = H_{\text{sys}} + H_{\text{bath}} + H_{\text{coupl}}, \tag{1a}$$

$$H_{\text{bath}} = \int_a^b dx\, x\, a_x^{\dagger} a_x, \tag{1b}$$

$$H_{\text{coupl}} = \int_a^b dx\, V(x) d^{\dagger} a_x + \text{H.c.}, \tag{1c}$$

via a "coupling function" $V(x)$. Here, $a_x^{\dagger}$ (a_x) create (annihilate) an occupation of a bath level with energy x. This defines the bath spectral density $J(x)$ as [1,19]

$$J(x) = \int_a^b dx'\, |V(x')|^2 \delta(x - x') = |V(x)|^2. \tag{2}$$

This spectral density, which depends on the continuous bath variable x, fully characterizes the influence of the bath on the system. Similarly, a system linearly coupled to a discrete harmonic oscillator bath is characterized by a Hamiltonian

$$H^{\text{discr}} = H_{\text{sys}} + H_{\text{bath}}^{\text{discr}} + H_{\text{coupl}}^{\text{discr}}, \tag{3a}$$

$$H_{\text{bath}}^{\text{discr}} = \sum_{n=1}^{N_b} x_n c_n^{\dagger} c_n, \tag{3b}$$

$$H_{\text{coupl}}^{\text{discr}} = \sum_{n=1}^{N_b} V_n d^{\dagger} c_n + \text{H.c.} \tag{3c}$$

The bath spectral density is a comb of delta peaks and not a continuous function as in Eq. (2) [19],

$$J^{\text{discr}}(x) = \sum_{n=1}^{N_b} |V_n|^2 \delta(x - x_n). \tag{4}$$

For $N_b \to \infty$, one can find an H^{discr} that is equivalent to H [20,21]. For $N_b < \infty$, the discrete Hamiltonian (3) can only serve as an approximation of the continuous Hamiltonian (1a). We classify the strategies for constructing such an approximation as follows. (i) Direct discretization, in which bath energies x_n and couplings V_n are obtained by a discretization of the integration interval $[a,b]$ in (1a). This technique is standard in the context of NRG [21] and frequently used in the context of DMRG [11–18]. (ii) Orthogonal polynomials [22], with which the bath energies x_n are obtained as the zeros of a polynomial that is associated with a quadrature rule for the integration over the *continuous bath energies x*. This has been used in different contexts from DMRG to quantum chemistry [20,23–30]. (iii) Numerical optimization, which consists in choosing the parameters x_n and V_n by minimizing a cost function [31–33].

As strategy (iii) cannot be used to discretize the spectral representation of a bath (see Appendix A), we restrict ourselves to strategies (i) and (ii), which we recapitulate in Secs. II A and II B, respectively. In Sec. II, we clarify the relation of strategies (i) and (ii), which has hitherto been missing from the literature. In Sec. III, we show that strategy (ii) best describes the time-evolution for quadratic Hamiltonians, and that for nonquadratic Hamiltonians, there is no such best strategy. Section IV presents numerical examples and in Sec. V, we draw the main conclusions of the paper.

II. RELATION OF DIFFERENT DISCRETIZATION STRATEGIES

Let us introduce the analytic continuation of the bath spectral density (2) to the complex plane, the *hybridization function* [19] (see Appendix B)

$$\Lambda(z) = \int_a^b dx \, \frac{J(x)}{z - x}, \quad z \in \mathbb{C} \tag{5}$$

with $J(x) = |V(x)|^2$. By the Sokhotski-Plemelj theorem, this implies

$$J(x) = -\frac{1}{\pi} \text{Im} \Lambda(x + i0). \tag{6}$$

The hybridization function does not contain more information than $J(x)$ since its real and imaginary parts are related by the Kramers-Kronig relation, $\text{Re}[\Lambda(x)] = \int dx \frac{\text{Im}[\Lambda(x)]}{x - x'} = -\frac{1}{\pi} \int dx \frac{J(x)}{x - x'}$. Using the discrete bath spectral density $J^{\text{discr}}(x)$ of (4) to evaluate (5), one obtains

$$\Lambda^{\text{discr}}(z) = \sum_{n=1}^N \frac{|V_n|^2}{z - x_n}. \tag{7}$$

A. Direct discretization strategies

Let us consider the approach of Ref. [25] and rephrase the problem of discretizing the Hamiltonian as that of discretizing the integral in (5). The simplest approximation for an integral is obtained by using a trapezoidal integration rule

$$\Lambda(z) = \int_a^b dx \, \frac{|V(x)|^2}{z - x} \simeq \sum_n \frac{|V(x_n)|^2 \Delta x_n}{z - x_n} = \Lambda^{\text{discr}}(z), \tag{8}$$

where x_n are linearly spaced node points with spacing Δx_n. Using this rule to generate an approximation $\Lambda^{\text{discr}}(z)$, i.e., demanding the last equality of the preceding equation to hold, it is possible to identify the couplings as

$$|V_n|^2 = |V(x_n)|^2 \Delta x_n \tag{9}$$

and the node points x_n as bath energies of (3).

The strategy using the trapezoidal rule can be improved as follows. Instead of generating a discrete weight $|V_n|^2$ simply by multiplying the function $|V(x_n)|^2$ with the width of the associated interval Δx as in (9), compute the weight $|V_n|^2$ as an integral of $|V(x)|^2$ over an interval I_n, and the bath energies x_n as weighted averages over this interval:

$$|V_n|^2 = \int_{I_n} dx \, |V(x)|^2, \tag{10a}$$

$$x_n = \frac{1}{|V_n|^2} \int_{I_n} dx \, x \, |V(x)|^2. \tag{10b}$$

This requires to define intervals $I_n \subset [a,b]$, $n = 1, \ldots, N_b$, with $I_n \cap I_m = \emptyset$ for $n \neq m$ and $[a,b] \subset \bigcup_n I_n$. For a linear discretization, this generates intervals of equal width as in the trapezoidal rule (8). But in general, the intervals I_n can have arbitrary widths, and one can, e.g., define a logarithmic discretization, for which the interval widths decrease exponentially for $|x| \to 0$. This guarantees *energy scale separation*, which is required for NRG [21]. ED and DMRG, by contrast, allow for any discretization. Within DMRG, for instance, aside from the linear [12,14,15] and logarithmic discretizations [11,12], it is possible to consider combinations of both discretizations [16], combinations of different logarithmic discretizations [13], or a cosine-spaced discretization [17]. Also, a parabolic discretization has been proposed [18].

Within the direct discretization strategy, the discrete bath operators $c_n^\dagger$ in (3) are interpreted as averages of the continuous bath operators $a_x^\dagger$ in (1a) over the energy interval I_n:

$$c_n^\dagger = \frac{1}{V_n} \int_{I_n} dx \, V(x) a_x^\dagger. \tag{11}$$

The map $a_x^\dagger \mapsto c_n^\dagger$ retains the (anti-)commutation relation of the continuous operators $[a_x, a_{x'}^\dagger]_\pm = \delta(x - x')$ as discretization intervals do not overlap and are normalized:

$$[c_n, c_m^\dagger]_\pm = \frac{1}{V_m^* V_n} \int_{I_n} dx \int_{I_m} dx' \, V^*(x) \, V(x') [a_x, a_{x'}^\dagger]_\pm = \delta_{nm}.$$

In the context of direct discretization strategies, we point out that the discrete representation (3) is typically referred to as the *star representation* of the discrete Hamiltonian. This representation is, via a standard mapping [21], unitarily equivalent to a one-dimensional tight-binding chain, i.e., a *chain representation* (see Appendix C). This mapping is valid independently of the discretization strategy and can even be formally defined to map the continuous star Hamiltonian into a chain with infinite length [26]. This issue will be further discussed in Sec. II B 3. Finally, we note that in the chain representation, the logarithmic discretization leads to next-neighbor couplings that decay exponentially with the distance to the impurity.

1. New proposals

To improve the accuracy of the discretization of previous strategies [11–18,21], it seems reasonable to consider a node distribution that uses more nodes in regions where the bath spectral weight is larger. Based on this heuristic argument, we propose two different variants of direct discretization strategies.

In the first one, which we refer here simply as the *mean method*, we compute the first bath energy as an average over the full support of $J(x)$:

$$x_1 = \frac{1}{|V_{\text{tot}}|^2} \int_a^b dx \, x \, J(x),$$

$$|V_{\text{tot}}|^2 = \int_a^b dx \, J(x). \tag{12}$$

In the next step, we compute x_2 as an average over the interval $[a, x_1]$ and x_3 as an average over the interval $[x_1, b]$. The following steps are repeated in a similar way until obtaining N_b energies. Finally, the weights $|V_n|^2$ are obtained as integrals

$$|V_n|^2 = \int_{(x_{n-1}+x_n)/2}^{(x_n+x_{n+1})/2} dx \, J(x), \tag{13}$$

where for the first ($n = 1$) and the last ($n = N_b$) integral, we replace the lower limit by a, and the upper limit by b, respectively.

Similarly, we define the *equal weight method*. Here, in the first step, we define a weight per bath energy $\frac{1}{N_b} \int_a^b dx \, J(x)$. Then, we define the first interval $I_1 = [a, a_1]$ via

$$\int_a^{a_1} dx \, J(x) = \frac{1}{N_b} \int_a^b dx \, J(x), \tag{14}$$

and the corresponding first bath energy and weight is computed as in (10). The rest of parameters x_n and V_n are obtained analogously.

2. Limits of the direct discretization strategy

The direct discretization strategies considered in this section are based on producing nonequally spaced discretization intervals to minimize the error of the approximation $\Lambda(z) \simeq \Lambda^{\text{discr}}(z)$ for certain values of $z = x + i0^+$, i.e., for certain values of the bath energy x.

The logarithmic discretization, e.g., minimizes the error in the low-energy limit $|x| \to 0$. This discretization then forms a quasicontinuum in a neighborhood of $x = 0$, and therefore the discretized version of the hybridization in such region is a numerically exact approximation to the continuous one. However, such a good approximation for low energies comes at the price that for higher energies the discretization becomes crude, and the logarithmic approximation is therefore not appropriate to describe the time evolution of the system at short and intermediate time scales. Thus NRG, which uses a logarithmic discretization, allows to describe the low-energy physics of a system numerically *exactly*, but gives a very rough approximation of high-energy excitations of the bath. The proposals described in Sec. II A 1, on the other hand, provide a good approximation in those energy regions where the spectral density is larger in magnitude, which may not necessarily coincide with low energies.

In general, *none* of the direct discretization strategies reliably describes the system at all energy scales. More precisely, a safe use of these strategies (i.e., unbiased with respect to energy) to describe time evolution at short and intermediate times scales, requires to consider a relatively high number of bath sites ($N_b = 30$ up to 200, depending on the problem [11,13–18]).

B. Orthogonal polynomial strategy

In order to construct a discrete representation of the integral (5), which is valid for all bath energies x in $[a, b]$, it is necessary to use a discretization method in which each discretized energy value x_n is computed with information of the integrand (5) over the whole integration support $[a, b]$. As will be described in the following, this can be achieved by using Gauss-Christoffel type of quadrature rules to represent the integral (5), which to our knowledge has for the first time been proposed in Ref. [22].

1. Gaussian quadrature

Let us re-express the z-dependent integral (5) in terms of the product of a weight function $w(x)$ ($w(x) \geqslant 0$) and a function $f(x,z)$ (see Ref. [34] for an excellent review on the subject),

$$\Lambda(z) = \int_a^b dx \, \frac{J(x)}{z - x} = \int_a^b dx \, w(x) f(x,z). \tag{15}$$

Now consider a polynomial interpolant $f_N(x,z)$ of $f(x,z)$ with degree $N - 1$ (here and in the following, the degree is with respect to the argument x, which is the integration variable), which is unique and matches $f(x,z)$ at N node points x_n,

$$f(x,z) = f_N(x,z) + r_N(x,z),$$

$$f_N(x,z) = \sum_{n=1}^N f(x_n,z) l_n(x), \quad l_n(x_m) = \delta_{nm}, \tag{16}$$

where $l_n(x)$ can be defined as the $(N-1)$-th order polynomial $l_n(x) = \prod_{m \neq n}(x - x_m) / \prod_{m \neq n}(x_n - x_m)$ and $r_N(x,z)$ is a remainder. Clearly, if the degree of $f(x,z)$ is $N - 1$, one can achieve $r_N(x,z) = 0$ if choosing the N node points x_n *intelligently*, and

$$\Lambda(z) = \int_a^b dx \, w(x) f(x,z) = \sum_{n=1}^N W_n f(x_n,z) + R_N(z),$$

$$W_n = \int_a^b dx \, w(x) l_n(x), \tag{17}$$

is an *exact* representation of the integral, i.e., $R_N(z) = 0$. We refer to W_n as Christoffel weights. It can be shown that $R_N(z) = 0$ holds even if $f(x,z)$ has a degree smaller or equal than $2N - 1$, although then $r_N(x,z) \neq 0$. The integration rule is then of *degree of exactness* $2N - 1$. The higher the degree of exactness, the smaller is the error term $R_N(z)$ for the function $f(x,z)$, even if the latter has degree higher than $2N - 1$.

To obtain the highest possible degree of exactness $2N - 1$, Posse and Christoffel showed in 1877 that the previously referred *intelligent choice* of the nodes x_n is to consider them as the roots of the monic polynomial $p_N(x)$ of degree N that

pertains to the family of orthogonal polynomials obeying

$$\int_a^b dx \, w(x) p_n(x) p_m(x) = \delta_{nm}. \tag{18}$$

Such polynomials can be generated using the recurrence [35]

$$p_{n+1}(x) = (x - \alpha_n) p_n(x) - \beta_n p_{n-1}(x),$$
$$p_0(x) = 1, \qquad p_{-1}(x) = 0, \quad n = 0, \ldots, N-1, \tag{19}$$

where $\beta_0 = 0$ and

$$\gamma_n = \int_a^b dx \, p_n^2(x) w(x), \tag{20a}$$

$$\alpha_n = \frac{1}{\gamma_n} \int_a^b dx \, x \, p_n^2(x) w(x), \quad n = 0, \ldots, N-1 \tag{20b}$$

$$\beta_n = \gamma_n / \gamma_{n-1}, \quad n = 1, \ldots, N-1. \tag{20c}$$

It is easy to see [36] that the roots of p_N can be obtained by diagonalizing the $N \times N$ matrix M [37]:

$$M = \begin{pmatrix} \alpha_0 & \sqrt{\beta_1} & 0 & \cdots \\ \sqrt{\beta_1} & \alpha_1 & \sqrt{\beta_2} & \ddots \\ 0 & \sqrt{\beta_2} & \alpha_2 & \ddots \\ \vdots & \ddots & \ddots & \ddots \end{pmatrix}. \tag{21}$$

In addition, denoting the nth eigenvector of M as v_n, the Christoffel weights in Eq. (17) are given by the square of its first element:

$$W_n = v_{n1}^2. \tag{22}$$

If the inner product (18) is not normalized, one has to multiply the right-hand side of this equation with the norm $\int_a^b dx \, w(x)$.

2. Discrete Hamiltonian representation

Let us now discuss in more detail how to obtain a discrete Hamiltonian with N_b bath sites from the N roots x_n, and Christoffel weights W_n that appear in the Gaussian quadrature rule for the integral (15). We discuss two cases (a) $w(x) = J(x)$ and (b) $w(x) = 1$. Case (a) is, to our knowledge, the only one considered in the literature [20,22–28], whereas case (b) makes the most simple choice for the weight function. (a) The choice $w(x) = J(x)$ and $f_z(x) = \frac{1}{z-x}$ leads to polynomials that are orthogonal with respect to $J(x)$, which we therefore call bath-spectral-density-orthogonal (BSDO). Combining (15) and (17) we find

$$\Lambda(z) \approx \sum_{n=1}^{N_b} \frac{W_n}{z - x_n} = \Lambda^{\text{discr}}(z), \tag{23}$$

which allows to identify the Christoffel weights computed via (22) with the weights $|V_n|^2$ of the discrete bath degrees of freedom:

$$|V_n|^2 = W_n. \tag{24}$$

(b) The choice $w(x) = 1$ and $f_z(x) = \frac{J(x)}{z-x}$. This is the case of Legendre polynomials and one obtains

$$\Lambda(z) \approx \sum_{n=1}^{N_b} \frac{W_n J(x_n)}{z - x_n} = \Lambda^{\text{discr}}(z), \tag{25}$$

and the Christoffel weights W_n relate to the weights of the discrete bath via $|V_n|^2 = W_n J(x_n)$.

The next question is, which of these cases leads to a better approximation? Equations (23) and (25) derived from (17) do not hold exactly: in both cases (a) and (b), $f_z(x)$ contains a pole $\frac{1}{z-x}$ and hence it can not be *exactly* represented by a polynomial of degree $2N_b - 1$. Indeed, a pole is highly difficult to approximate with polynomials and it is quite irrelevant, whether one has an additional factor $J(x)$ that multiplies this pole as in case (b), if this factor $J(x)$ does not exhibit a severe nonregular behavior. This argument is confirmed by the numerical examples discussed in Sec. IV.

3. Relationship to chain mappings

In this section, we show that the orthogonal polynomial method with the weight function chosen as $w(x) = J(x)$ [case (a) above], is equivalent to the *chain mapping* proposed in Refs. [20,26,38], and recently modified in Ref. [28] to tackle temperature environments in an alternative way. It is also equivalent to the chain mapping derived in the Appendix of Ref. [24]. The chain representation of the discrete *star* Hamiltonian obtained by considering $w(x) = J(x)$, can be written as

$$H_{\text{chain}}^{\text{discr}} = H_{\text{sys}} + V_{\text{tot}}(d^\dagger e_0 + e_0^\dagger d)$$
$$+ \sum_{n=0}^{N_b-1} \alpha_n e_n^\dagger e_n + \sum_{n=0}^{N_b-2} \sqrt{\beta_{n+1}} (e_{n+1}^\dagger e_n + e_n^\dagger e_{n+1}), \tag{26}$$

where $|V_{\text{tot}}|^2 = \int_a^b dx \, J(x)$ was defined in (12) and α_n and β_n were defined in the recurrence relation (19). In the limit $N_b \to \infty$, $H_{\text{chain}}^{\text{discr}}$ becomes unitarily equivalent to the continuous H in (1a), and thus provides an *exact* representation of H.

For finite N_b, the unitary transformation that takes (26) back to its star representation (3), is equivalent to a diagonalization of the matrix (21) formed by the recurrence coefficients. As described above, such a transformation leads to the same weights and nodes as the ones obtained with the Gauss-Christoffel (BSDO quadrature). In other words, computing the system dynamics with a chain Hamiltonian (26) is equivalent to computing the system dynamics with a star Hamiltonian (3) where nodes x_n and weights V_n are computed with the BSDO quadrature. Regarding the important application of DMRG calculations: in contrast to what had been commonly believed, it was only recently shown that the star representation can be much less entangled than the chain representation [39].

Within the *direct discretization strategy*, the creation operators $c_n^\dagger$ of the discrete Hamiltonian in the star geometry (3) were obtained as an average over the continuous bath degrees of freedom $a_x^\dagger$ in a small interval I_n, as defined in (11). Within the *orthogonal polynomial* strategy described in the current section, the discrete operators in the chain Hamiltonian (26)

are related to the continuous operators via

$$e_n^\dagger = \int_a^b dx \, U_n(x) a_x^\dagger, \tag{27}$$

where $U_n(x) = \sqrt{J(x)} p_n(x)$. Therefore they correspond to a weighted average over the total support of the spectral function $J(x)$. Note that due to orthogonality and normalization of $p_n(x)$, the transformation is unitary $\int_a^b dx \, U_n^*(x) U_m(x) = \int_a^b dx \, w(x) p_n(x) p_m(x) = \delta_{nm}$ and thereby retains the (anti-) commutation relation of $a_x^\dagger$.

4. Relationship to the Lanczos algorithm

The measure $\omega(x) = J(x)$ is commonly known as Stiltjes measure, and the three-term recursion (19) of the associated BSDO polynomials is equivalent to the Lanczos algorithm for the continuous bath Hamiltonian H_{bath} in (1a) [35] (see Appendix C). The environment discretization then is a consequence of truncating the infinite recurrence relation [and therefore the matrix (21)] at a finite $N = N_b$. The implementation of the algorithm on a computer is though impossible, as there is no direct matrix representation for the continuous H_{bath}.

By contrast, the Lanczos algorithm is a standard procedure to tridiagonalize a *given discrete* bath Hamiltonian $H_{\mathrm{bath}}^{\mathrm{discr}}$ as in (3), to obtain its unitarily equivalent chain representation. In order to do so, one has to come up with a discrete Hamiltonian in the first place, which then has to be constructed using a *direct discretization* strategy.

III. TIME EVOLUTION

Let us now study the time evolution of the hybridization function, which describes the time evolution of the bath, and the time evolution of the Green's function of the system, from which we can construct the time evolution of all system observables. The Green's function is given by

$$G(t) = -i \langle \psi_0 | e^{-i(H-E_0)t} | \psi_0 \rangle, \quad |\psi_0\rangle = d^\dagger |E_0\rangle$$
$$= \int_{-\infty}^{\infty} dx \, A(x) e^{-ixt}, \tag{28}$$

where the initial state is the excitation of the system H_{sys} through occupation with a particle, and the spectral density of the system is

$$A(x) = \sum_n |\langle \psi_0 | E_n \rangle|^2 \delta(x - (E_n - E_0)), \tag{29}$$

where the sum is over all eigenstates $|E_n\rangle$ and eigenenergies E_n of the full Hamiltonian (1a). For a quadratic (single-particle)

Hamiltonian, without loss of generality, one can consider $E_0 = 0$ and $|E_0\rangle = |\mathrm{vac}\rangle$ and therefore only has to study the time-evolution of a *single* particle that is initially in the system and starts interacting with the bath at nonzero times.

Analogously to (28), we define the time evolution of the hybridization function as

$$\Lambda(t) = \int_{-\infty}^{\infty} dx \, J(x) e^{-ixt}. \tag{30}$$

For a discrete Hamiltonian H^{discr}, one obtains

$$G^{\mathrm{discr}}(t) = \int_{-\infty}^{\infty} dx \, A^{\mathrm{discr}}(x) e^{-ixt}, \tag{31}$$

$$\Lambda^{\mathrm{discr}}(t) = \sum_{n=1}^{N_b} |V_n|^2 e^{-ix_n t}. \tag{32}$$

In the following, it is shown that the *orthogonal polynomial* strategy yields the best description of the short- and intermediate-time evolution of the continuous Hamiltonian, if the latter is quadratic. It will then become clear why none of the discretization strategies can be considered the *best* or the *optimal* one if the Hamiltonian is nonquadratic (has higher order interactions). In particular, (1) Sec. III A shows that the best approximation of (30) is obtained using the orthogonal polynomial strategy as described in Sec. II B. (2) Section III B 1 shows that the Lanzos algorithm for the full H generates a matrix $\mathcal{H}_N$, which gives the nodes and the weights that approximates the Green's function (28) with a polynomial quadrature rule. (3) Section III B 2 shows that if H_{sys} is quadratic, $\mathcal{H}_N = \mathcal{H}^{\mathrm{discr}}$, where $\mathcal{H}^{\mathrm{discr}}$ is obtained by Lanczos tridiagonalization of H_{bath}. Also, as it was shown in Sec. II B 4, a Lanczos tridiagonalization of H_{bath} is equivalent to a bath discretization using the orthogonal polynomial strategy of Sec. II B. Hence the orthogonal polynomial strategy leads to a quadrature rule also for the Green's function (28). (4) Section III C shows that if H_{sys} is nonquadratic, then $\mathcal{H}_N \neq \mathcal{H}^{\mathrm{discr}}$, and nothing can be concluded about the optimality of any particular discretization method. An overview of these steps is provided in Table I.

A. Time evolution of the bath

In Sec. II B, we learned that polynomial quadrature rules provide us with the highest *degree of exactness* for computing integral (17). In the following, we will see that this also helps us to understand in which cases (32) provides a good approximation of the Fourier type integral such as (30), and how to choose the parameters of the bath in order to obtain the best approximation. To this end, let us define the error term

TABLE I. Lanczos algorithm and orthogonal-polynomial strategy for real-time evolution.

Lanczos algorithm	Quadratic H_{sys}	Nonquadratic H_{sys}
For continuous H_{bath} [Eq. (1b)]	$\mathcal{H}^{\mathrm{discr}}$ [Eq. (40)] is obtained formally [Appendix (C1)], and numerically (Sec. II B 4)	Same as for quadratic H_{sys}
For continuous H [Eq. (1a)]	$\mathcal{H}_N$ [Eq. (38)] is obtained formally (Appendix C1 and Sec. III B 1 for first steps of algorithm).	Not possible
Is Lanczos for H equal to Lanczos for H_{bath}?	Sec. III B 2: Yes, $\mathcal{H}_N = \mathcal{H}^{\mathrm{discr}}$ for orthogonal polynomial strategy	Sec. III C: No, in general $\mathcal{H}_N \neq \mathcal{H}^{\mathrm{discr}}$

$R_{N_b}(t)$ and write

$$\Lambda(t) = \int_{-\infty}^{\infty} dx\, J(x)e^{-ixt} = \sum_{n=1}^{N_b} |V_n|^2 e^{-ix_n t} + R_{N_b}(t). \quad (33)$$

We see that if we set $w(x) = J(x)$ to construct orthogonal polynomials via (19) and choose x_n to be the roots of the degree N_b polynomial and $|V_n|^2 = W_n$ to be the Christoffel weights (22), then (33) has the form of a Gaussian quadrature rule as in (17) with $f(x,z=t) = e^{-ixt}$.

That is, only if we choose $|V_n|^2$ and x_n according to the orthogonal polynomial strategy with $w(x) = J(x)$, our discrete Hamiltonian corresponds to evaluating the Fourier transform (33) to *degree of exactness* $2N_b - 1$. Otherwise, the degree of exactness will be lower. What does this mean in practice?

For a fixed time t, let us expand the part e^{-ixt} of the integrand $J(x)e^{-ixt} = w(x)e^{-ixt}$ in (33) that cannot be absorbed in a weight function in orthogonal polynomials $q_n(x)$, which are orthogonal with respect to $v(x)$ [$v(x) \geqslant 0$ is an arbitrary weight function], according to

$$e^{-ixt} = \sum_{n=0}^{N} c_n q_n(x) + \sum_{n=N+1}^{\infty} c_n q_n(x),$$

$$c_n = \int_{a}^{b} dx\, v(x)e^{-ixt}q_n(x). \quad (34)$$

Let us furthermore assume the family of polynomials $q_n(x)$ to be chosen optimally for the fixed time t. The optimal choice generates the most quickly converging sequence $c_n \to 0$ and by that minimizes the remainder $r_N = \sum_{n=N+1}^{\infty} c_n q_n(x)$ at each order of N. Of course, we do not know which polynomials these are, but this is not relevant. The only property we need is that the coefficients become zero for values high values of n: $c_n \simeq 0$ for $n > N'(t)$, where $N'(t) = \frac{1}{2}(b-a)t$ (this is shown in Appendix D).

The important observation to make is that choosing x_n and $|V_n|^2 = W_n$ according to the orthogonal polynomial strategy of Sec. II B, corresponds to integrating the first term with $N = 2N_b - 1$ in (34) exactly. Any other choice, will lead to an exact integration of the term only at a *lower* order, or will *not* integrate it exactly at *any* order. Combining this observation with the fact that $c_n \simeq 0$ for $n > \frac{1}{2}(b-a)t$, we conclude that the orthogonal polynomial strategy reproduces basically the *exact* time evolution of the hybridization function for $t < t_{\max}$, with

$$t_{\max} = 2\frac{2N_b - 1}{b - a}. \quad (35)$$

This result is confirmed in the numerical experiments in Sec. IV. We have therefore shown that the best approximation of (30) is given by a orthogonal polynomial strategy as described in Sec. II B.

B. Time evolution of the system

The Green's function of the system as defined in (28) can be rewritten as follows:

$$G(t) = \int_{-\infty}^{\infty} dx\, A(x)e^{-ixt} = \sum_{n=1}^{\infty} |\langle \psi_0 | E_{n-1}\rangle|^2 e^{-iE_{n-1}t}$$

$$= \sum_{n=1}^{N} |\langle \psi_0 | X_n\rangle|^2 e^{-iX_n t} + R_N(t), \quad (36)$$

where $|E_n\rangle$ are eigenstates and E_n eigenenergies of the exact, continuous Hamiltonian (1a), and $R_N(t)$ is a remainder. The problem is therefore again to choose the states $|X_n\rangle$ and the nodes X_n, such as to make (36) a quadrature rule, which we just showed (Sec. III A) to yield the best approximation of Fourier type integrals.

1. Lanczos for quadratic Hamiltonian

For quadratic Hamiltonians, we will show in the following, that the orthogonal polynomial strategy (19) generates a quadrature rule for (36), and X_n and $|X_n\rangle$ become, respectively, the eigenenergies and eigenstates of the discrete Hamiltonian H^{discr}. If either one does not use the orthogonal polynomial strategy, or the Hamiltonian is not quadratic, one *never* generates a quadrature rule in (36).

To this end, let us compute the first steps of the standard Lanczos tridiagonalization algorithm recapitulated in Appendix C. Here, we do it for the full continuous quadratic Hamiltonian (1a), and not for the bath and coupling part of the discrete Hamiltonian (3), as usually done in the context of *chain mappings*.

Assume $H_{\text{sys}} = \varepsilon_0 d^\dagger d$ quadratic. Let us take as initial Lanczos vector the state $|f_0\rangle = |d\rangle = d^\dagger |\text{vac}\rangle = |\psi_0\rangle$. Denoting the single-particle states of the bath as $|a_x\rangle = a_x^\dagger |\text{vac}\rangle$, we have following (C1):

$$\widetilde{\alpha}_0 = \langle f_0 | H | f_0 \rangle = \varepsilon_0,$$

$$|r_0\rangle = H|f_0\rangle - \widetilde{\alpha}_0|f_0\rangle = \int_{a}^{b} dx\, V(x)|a_x\rangle,$$

$$\langle r_0 | r_0 \rangle = \int_{a}^{b} dx\, |V(x)|^2 = |V_{\text{tot}}|^2 = \widetilde{\beta}_1^2, \quad (37)$$

$$|f_1\rangle = \frac{1}{V_{\text{tot}}} \int_{a}^{b} dx\, V(x)|a_x\rangle.$$

Continuing the algorithm up to order N produces a truncated representation of H, which is a $N \times N$ matrix,

$$\mathcal{H}_N = \begin{pmatrix} \varepsilon_0 & V_{\text{tot}} & 0 & \cdots & \\ V_{\text{tot}} & \widetilde{\alpha}_1 & \sqrt{\widetilde{\beta}_2} & 0 & \cdots \\ 0 & \sqrt{\widetilde{\beta}_2} & \widetilde{\alpha}_2 & \sqrt{\widetilde{\beta}_3} & \ddots \\ 0 & 0 & \sqrt{\widetilde{\beta}_3} & \widetilde{\alpha}_3 & \ddots \\ \vdots & \ddots & \ddots & \ddots & \end{pmatrix}. \quad (38)$$

As discussed in Appendix C, there is a set of orthogonal polynomials $q_n(x)$ that are orthogonal with respect to $w(x) = A(x)$ [$A(x)$ is the spectral density of the full Hamiltonian H] associated with the preceding Lanczos algorithm. Therefore

diagonalization of (38) yields roots X_n and Christoffel weights $W_n = |\langle f_0 | X_n \rangle|^2 = |\langle \psi_0 | X_n \rangle|^2$. Hence the Lanczos algorithm evaluated for the continuous quadratic Hamiltonian H with initial state $|f_0\rangle = |\psi_0\rangle$ generates the nodes and weights that make the approximation (36) a quadrature rule. Note that $X_n \neq E_n$, since E_{n-1} are true eigenvalues of H, and X_n are the eigenvalues of the truncated tridiagonal representation $\mathcal{H}_N$ of H.

However, how does this relate to the parametrization for a discrete Hamiltonian H^{discr} that we obtain from the orthogonal polynomial strategy (19) for the weight function $w(x) = J(x)$?

2. Equivalence with orthogonal polynomial strategy

The discrete quadratic Hamiltonian H^{discr}, which has dimension $(N_b + 1) \times (N_b + 1)$, generates the following approximation to the time evolution of the Green's function of the continuous system:

$$G(t) = \int_{-\infty}^{\infty} dx\, A(x) e^{-ixt}$$
$$= \sum_{n=1}^{N_b+1} \left| \langle \psi_0 | E_{n-1}^{\text{discr}} \rangle \right|^2 e^{-i E_{n-1}^{\text{discr}} t} + R_{N_b}^{\text{discr}}(t), \qquad (39)$$

where $|E_n^{\text{discr}}\rangle$ are eigenstates and E_n^{discr} eivenvalues of H^{discr}. Also, H^{discr} can be represented in the chain geometry (26) as

$$\mathcal{H}^{\text{discr}} = \begin{pmatrix} \varepsilon_0 & V_{\text{tot}} & 0 & \cdots & \\ V_{\text{tot}} & \alpha_0 & \sqrt{\beta_1} & 0 & \cdots \\ 0 & \sqrt{\beta_1} & \alpha_1 & \sqrt{\beta_2} & \ddots \\ 0 & 0 & \sqrt{\beta_2} & \alpha_2 & \ddots \\ \vdots & \ddots & \ddots & \ddots & \end{pmatrix}. \qquad (40)$$

As $|\psi_0\rangle = |d\rangle$, this representation of H^{discr} directly yields the weights and energies in (39).

In the following, we will show that the matrix (40) equals the matrix (38) that generates the quadrature rule, only if we compute the parameters of the discrete Hamiltonian using the orthogonal polynomial strategy (19) with $w(x) = J(x)$. Only then, also (39) is a quadrature rule.

To this end, let us further evaluate the Lanczos algorithm for the continuous H. Using the results of (37), we can represent the terms in (1a) as

$$H_{\text{sys}} = \varepsilon_0 |f_0\rangle \langle f_0|,$$
$$H_{\text{coupl}} = V_{\text{tot}}(|f_0\rangle \langle f_1| + \text{H.c.}),$$
$$H_{\text{bath}} = \int_a^b dx\, x |a_x\rangle \langle a_x|.$$

As the Lanczos basis is orthogonal, we see that in subsequent Lanczos steps, only H_{bath} can contribute: H_{sys} and H_{coupl} only have contributions in the subspace spanned by $|f_0\rangle$ and $|f_1\rangle$. We therefore have to evaluate a single next Lanczos step using the full H, and from then on can iterate using only H_{bath}. Now note that the Lanczos vector $|f_1\rangle$ in (37), which is the starting vector for subsequent Lanczos steps, equals the state $|e_0\rangle$ in (C4), which is the initial state for a tridiagonalization of the bath. We already know the latter to be equivalent to the orthogonal polynomial strategy. The Lanczos recursion for the

full H therefore generates the coefficients of the orthogonal polynomial strategy. Let us check this for the next step,

$$\widetilde{\alpha}_1 = \langle f_1 | H | f_1 \rangle = \langle f_1 | H_{\text{bath}} | f_1 \rangle.$$
$$|\widetilde{r}_1\rangle = H|f_1\rangle - \widetilde{\alpha}_1 |f_1\rangle - V_{\text{tot}}|f_0\rangle$$
$$= H_{\text{bath}}|f_1\rangle - \widetilde{\alpha}_1 |f_1\rangle.$$

Evidently, $\widetilde{\alpha}_1 = \alpha_0$ and $|\widetilde{r}_1\rangle = |r_0\rangle$ as $|f_1\rangle = |e_0\rangle$ such that this equals the parameters of (C5) and (19). Hence the matrices (40) and (38) are equivalent, and the time evolution computed with the discrete Hamiltonian is a quadrature rule. For any other choice of H^{discr}, which is not parametrized using (19), we would *not* obtain an equivalent representation to (38), and therefore, (39) would not be a quadrature rule.

The estimate (35) for the maximal time t_{max} yields, as the quadrature rule now uses a polynomial of degree $N_b + 1$,

$$t_{\text{max}} = 2 \frac{2N_b + 1}{b - a}. \qquad (41)$$

C. Impossibility of optimal choice for nonquadratic Hamiltonians

If H_{sys} is *not* quadratic, but has higher-order interaction terms, we cannot obtain a representation of H^{discr} in terms of single-particle states, and hence as a $(N_b + 1) \times (N_b + 1)$ matrix. Rather, any representation of H^{discr} then has an exponential dimension, e.g., $2^{N_b+1} \times 2^{N_b+1}$ for spinless fermions, and dimension $D^{N_b+1} \times D^{N_b+1}$ for bosons with a local basis truncated at a dimension D. The summation over the discrete time evolution of (39) then involves an exponential number of terms. By dimensionality, this summation can never correspond to a quadrature rule with N_b parameters, which gives rise to N_b roots. The time evolution of the bath hybridization function, which always is a single-particle evolution, is not affected by this argument and is still best described using the parameters provided by the orthogonal polynomial strategy.

In summary, for nonquadratic Hamiltonians, even if we have a good approximation of the bath hybridization function up to t_{max}, the dynamics of the system, given by the Green function (39) will no longer be exact up to this time.

IV. NUMERICAL EXAMPLES

A. Spin-boson model

Let us consider the Hamiltonian of an OQS with H_{sys} coupled to a continuous bosonic reservoir:

$$H = H_{\text{sys}} + \int_0^{k_{\text{max}}} dk\, \tilde{g}(k)\,(b(k)\sigma^+ + \sigma^- b(k)^\dagger)$$
$$+ \int_0^{k_{\text{max}}} dk\, \omega(k) b(k)^\dagger b(k), \qquad (42)$$

where $\tilde{g}(k)$ are the coupling strengths, and $b(k)$ $(b(k)^\dagger)$ are harmonic oscillator operators with commutation relations $[b(k), b(k')^\dagger] = \delta(k - k')$. Here, the index k labels the modes, which have a maximum momentum k_{max}. In the frequency representation, and provided that the environment is initially

in a Gaussian state, this Hamiltonian can be rewritten as

$$H = H_{sys} + \int_0^{\omega_{max}} d\omega g(\omega) (b(\omega)\sigma^+ + b(\omega)^\dagger \sigma^-)$$
$$+ \int_0^{\omega_{max}} d\omega \, b(\omega)^\dagger b(\omega), \tag{43}$$

where ω_{max} is determined by k_{max}, and we have defined $g(\omega) = \sqrt{J(\omega)}$, where $J(\omega) = \tilde{g}^2(\omega)\rho_{DOS}(\omega)$ is the spectral density of the environment, and $\rho_{DOS}(\omega)$ is the environment density of states. Hence, Hamiltonian (43) acquires the form (1a), obviously once interpreting the continuous variable x as ω, and $d = \sigma^-$. We also note that the above Hamiltonian corresponds to a simplified version of the spin-boson model, as it assumes a rotating wave approximation to discard *fast rotating* terms of the form $b^\dagger(k)\sigma^+$, and $b(k)\sigma^-$. Such an approximation, which is particularly valid in quantum optics, leads to a Hamiltonian that conserves the number of particles. This simplifies considerably the numerical treatment, particularly at zero temperature.

In order to characterize the environment, let us consider a spectral density of the Caldeira and Leggett type [40,41],

$$J(\omega) = \alpha\omega^s \omega_c^{1-s} e^{-\omega/\omega_c}, \tag{44}$$

which constitute a very general description that allows to describe many different types of reservoirs, depending on the choice of the parameter s. The exponential factor in this model provides a smooth regularization for the spectral density, being modulated by the frequency ω_c. Environments with $0 < s < 1$ are considered as *subohmic*, while those corresponding to $s = 1$ and $s > 1$ are known as *Ohmic* and *super-Ohmic*, respectively. The constant α describes the coupling strength of the system and the environment. In the following, we will focus on a sub-Ohmic spectral density with $s = 1/2$. Sub-Ohmic spectral densities describe the frequency dependence of photonic bands in photonic band gap materials [27,42,43], as well as the dominant noise sources in solid state devices at low temperatures such as superconducting qubits [44], nanomechanical oscillators [45], and quantum dots [46].

Considering zero temperature, the OQS dynamics can be easily solved by exact diagonalization (ED), since there is only one excitation involved in the problem (it is a single-particle problem with a quadratic Hamiltonian). In this context, Fig. 1 shows results for the population

$$P(t) = \langle \sigma^+(t)\sigma^-(t) \rangle, \tag{45}$$

$$\mathcal{E}(t) = |P(t) - P^{discr}(t)|, \tag{46}$$

where $P(t)$ is computed with the continuous environment, and $P^{discr}(t)$ is the population computed with the discretized environment. $\mathcal{E}(t)$ is the error made by using the discretized environment. We compare results obtained using the linear discretization as an example for a *direct discretization strategy* with the *orthogonal polynomial* strategy that uses (19) with the weight function $w(x) = J(x)$ generating BSDO polynomials. Clearly, the BSDO strategy leads to an error that is at least two orders of magnitude smaller than the one of the linear discretization with the same number of modes until reaching
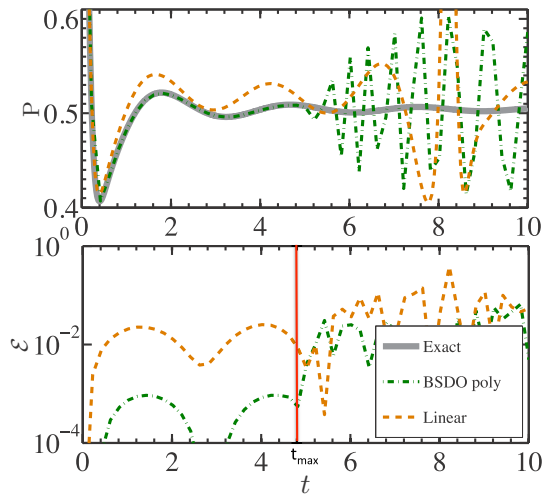

FIG. 1. (Color online) Time evolution of the population of the upper level for $N_b = 65$ (top) and error $\mathcal{E}$ according to (46) in logarithmic scale (bottom). In both cases, different discretization schemes are considered. Dot-dashed green and dashed orange curves correspond respectively to polynomial and linear methods. The linear black curve in the upper panel corresponds to the exact solution. The curves and error of the mean and the equal weight method of Sec. II A 1 are not shown, but have a similar behavior as the ones of the linear method. The red line below shows the time t_{max} at which the error of the polynomial method increases two orders of magnitude, which coincides with the exact formula (41) (see also Fig. 3). We have considered $\omega_s = 0.5$, $\alpha = 1$, $s = 0.5$, $\omega_c = 10$, and a maximum frequency in the spectrum $\omega_{max} = 50$.

a time t_{tmax}, when the discretized system fails to accurately describe the continuous system. Physically, such a failure can be interpreted as a revival of the system dynamics, which occurs when the emitted excitation hits the chain extreme and bounces back into the system. We note that the results obtained with the heuristic approaches described in Sec. II A 1 (not shown) are found to achieve a similar level of accuracy as the linear discretization strategy.

Figure 2 compares two orthogonal-polynomial based strategies: one generated with (19) using the weight function $w(x) = J(x)$ (BSDO quadrature) and one using $w(x) = 1$ (Legendre quadrature). The figure confirms the statement made after Eq. (25) that both strategies yield basically the same accuracy if the bath spectral density does not show a severe nonregular behavior. Also, as shown in Fig. 3, t_{max} is linearly related to the number of node points considered in the quadrature rule. This follows from Eq. (41). We note that also in the finite temperature case, studied within the second-order weak coupling master equation, we can recover the result that the BSDO strategy is optimal up to the time t_{max} (see Appendix E).

B. Single-impurity Anderson model

The single-impurity Anderson model (SIAM) has the form of Hamiltonian (1a), with the impurity and bath operators being
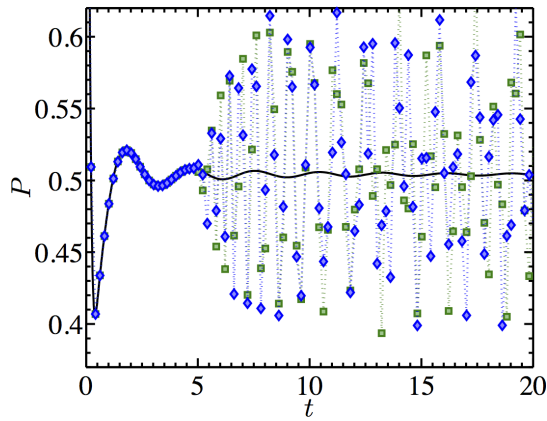
FIG. 2. (Color online) Evolution of the upper level considering the quadrature method with different polynomial classes for $N_b = 65$ nodes. Blue diamonds, and green squares correspond, respectively, to the Gaussian quadrature rule (with Legendre polynomials), and to the Gauss-Christoffel quadrature with BSDO polynomials [i.e., polynomials obeying the relation (18) with $w(x) = J(x)$].

spin-dependent fermionic creation and annihilation operators,

$$H_{sys} = U\left(d_\uparrow^\dagger d_\uparrow - \frac{1}{2}\right)\left(d_\downarrow^\dagger d_\downarrow - \frac{1}{2}\right),$$

$$H_{bath} = \sum_\sigma \int_a^b dx\, x\, a_{x\sigma}^\dagger a_{x\sigma}, \qquad (47)$$

$$H_{coupl} = \sum_\sigma \int_a^b dx\, V(x)(d_\sigma^\dagger a_{x\sigma} + \text{H.c.}).$$

In a grand-canonical picture this corresponds to the half-filled case obtained for chemical potential $\mu = -U/2$. The physics
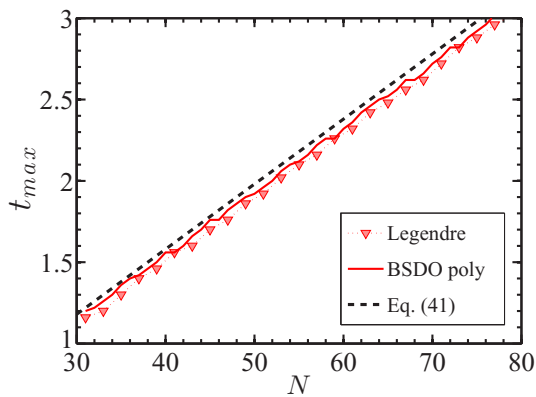

FIG. 3. (Color online) Maximum time at which the error between the evolution with discretization with N nodes, and the exact (continuous) one is below a certain threshold chosen as 0.004. The maximum frequency in the spectrum is $\omega_{max} = 100$. Blue diamonds and green circles correspond, respectively, to the Gaussian quadrature rule (with Legendre polynomials), and to the Gauss-Christoffel quadrature (with BSDO polynomials). System parameters are the same as in Fig. 1, except for the fact that we are now considering $s = 1.5$. The figure shows approximately the same slope as the one predicted by Eq. (41).
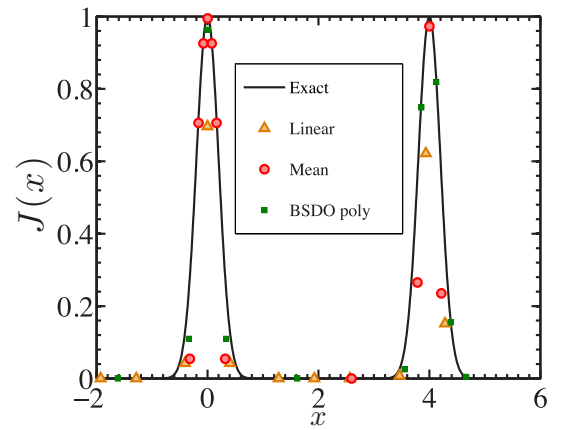

FIG. 4. (Color online) The generic bath spectral density (48) and its discretized versions. To plot the discrete spectral function $J^{discr}(x)$, we replace the delta function by a rescaled indicator function $\delta(x - x_n) \to \chi(x - x_n)/\Delta x_n$, where Δx_n is the width of $I_n = [(x_n + x_{n-1})/2, (x_{n+1} + x_n)/2]$. This rescaling accounts for the fact that for comparisons with the continuous spectral density, the discrete spectral function should be interpreted as a *probability density* defined on the energy interval (a,b) that associates a weight (an excitation probability) to an *energy interval*, and not as a *probability mass function* that associates a weight to a *value* of x_n.

of this case shows generic features. Clearly, for $U \neq 0$, H_{sys} describes a nonquadratic interaction.

The generic case of interest for the physics of strongly-correlated electron systems is best captured by a bath spectral density of the form

$$J(x) = \sum_{x_0 \in \{-4,0,4\}} e^{-\frac{(x-x_0)^2}{2\eta^2}} \text{ for } x \in [-5,5] \qquad (48)$$

outside of the interval $[-5,5]$ we set $J(x) = 0$. This bath spectral density is a superposition of three Gaussian peaks that produces "gapped" regions where $J(x)$ is practically zero. Figure 4 shows the continuous and the discretized version of this $J(x)$. The peak at zero frequency corresponds to low-energy excitations in the bath, as they are present in a metal. The two other peaks correspond to high-energy excitations that become relevant when the interaction U generates low- (single occupation) and high- (double or zero occupation) energy states. In a Mott insulator, there is no low-energy physics any more and the interaction created a gap in the excitation spectrum. The most exciting physics happens in the intermediate regime where the quantum Mott-Insulator phase transition occurs.

Let us first study the noninteracting case $U = 0$, which only involves a quadratic Hamiltonian. In this case, we confirm the results of the previous section. Figure 5 shows the time evolution of the overlap of the initial state [the Green's function $iG(t) = \langle \psi_0 | e^{-i(H-E_0)t} | \psi_0 \rangle$ defined in (28)], that consists in placing a spin-up electron on the impurity $|\psi(t=0)\rangle = d_\uparrow^\dagger | E_0 \rangle$, with its time evolution. Evidently, the linear discretization yields the worst results, and the Gauss-Christoffel (BSDO) strategy yields a numerically exact result up to time 6.

Let us now turn to the interacting case where U is nonzero and the Hamiltonian is no longer quadratic. Figure 6 confirms
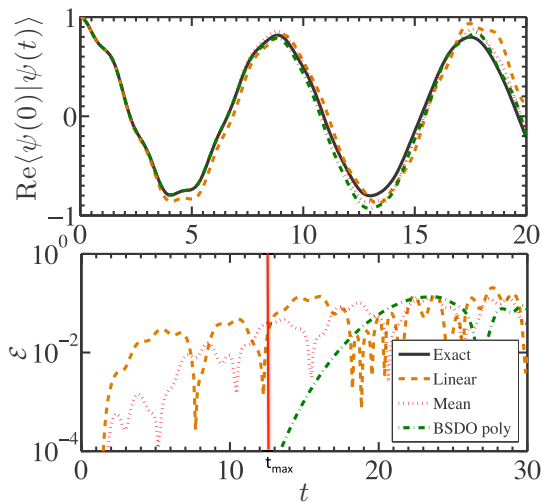
FIG. 5. (Color online) Time evolution of the SIAM (47) for $U = 0$. (Top) Time evolution for $N_b = 15$. (Bottom) Error for $N_b = 31$. The maximal time (red vertical line) until which the BSDO polynomial discretization yields the exact description can be computed using (41), and yields for $a = -5$, $b = 5$, and $N_b = 31$ the value $t_{max} = 12.6$.

the result of Sec. III that BSDO polynomials do no longer give optimal results as they no longer generate a Gaussian quadrature rule. Now the heuristic *mean* method produces the best results, leading to errors that are at least a factor 2 smaller than the BSDO strategy. The mean method directly uses the fact that one can ignore gapped regions in the bath spectral density. This is important in the computation of strongly correlated materials. In both cases described in Figs. 5 and 6, the equal weight method of Sec. II A 1 performs qualitatively similar to the mean method, and therefore it has not been shown for the shake of clarity in the figure.
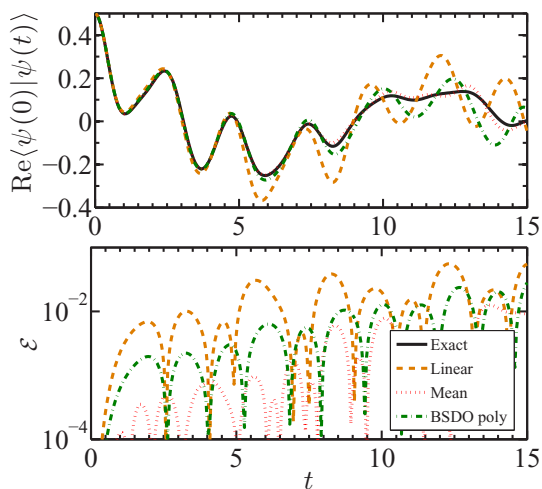

FIG. 6. (Color online) Time evolution of the SIAM (47) for $U = 4$. (Top) Time evolution for $N_b = 15$. (Bottom) Error for $N_b = 31$.

V. CONCLUSIONS

In this paper, we have analyzed a OQS coupled to a bosonic environment characterized by a Caldeira and Leggett type of spectral density, and a quantum impurity model consisting on an impurity coupled to a fermionic bath. We considered *direct discretization strategies* and *orthogonal polynomial* quadrature based strategies. We have shown that when using orthogonal polynomials, the choice of the polynomial class does not affect considerably the error in the resulting system dynamics. In addition, we have shown that the Gauss-Christoffel quadrature rule (which is based on the choice of a particular family of polynomials here denoted as BSDO), correspond to the chain mapping approach proposed by Refs. [26,47]. Such chain mapping leads effectively to a discrete chain representation, which when transformed back to a diagonal form, leads to environment eigenvalues that precisely correspond to the nodes of the Gauss-Christoffel (BSDO) quadrature rule.

Finally, we have shown that in a noninteracting system (i.e., with quadratic Hamiltonian), the polynomial quadrature method is exact at short times. Nevertheless, for nonquadratic Hamiltonians (like an an impurity with nonzero interaction term) this is no longer the case. This means that the notion of optimality that is associated with an optimal representation of the continuous integral of $J(x)$ by a finite number of points breaks down if we consider nonquadratic Hamiltonians. In other words, the nonlinear problem that is encoded in such nonquadratic Hamiltonian obviously will no longer be well described by just considering a polynomial quadrature rule on the integral. It is noted that, although we have presented a scheme (the mean method) that performs better than Gauss Christoffel quadrature in this case, we showed that a general statement *cannot* be made.

Note added in proof. Dynamical error bounds on expectation values of system observables for a Hamiltonian discretised using orthogonal polynomials have recently been derived in Ref. [48].

APPENDIX A: NUMERICAL OPTIMIZATION

Numerical optimization can be formulated in a straightforward way for the hybrdization function $\Lambda(z)$, defined in (5), evaluated on a grid of imaginary frequencies $z = i\omega_k$,

$$\chi^2 = \sum_k |\Lambda(i\omega_k) - \Lambda^{discr}(i\omega_k)|^2, \qquad (A1)$$

using standard numerical minimization techniques [31,49,50]. On the real axis, the equivalent cost function can be formally defined as $\chi^2 = \sum_k |\Lambda(\omega_k + i0^+) - \Lambda^{discr}(\omega_k + i0^+)|^2$, but

is of no use as the difference of a continuous function and a singular function is always infinite. Therefore we *cannot* use numerical optimization to discretize the spectral representation of the continuous bath, i.e., the hybridization function evaluated on the real axis via $J(x) = -\frac{1}{\pi} \text{Im} \Lambda(\omega + i0^+)$.

If one carries out the optimization on the imaginary axis via (A1), one obtains a set of parameters $\{x_n, V_n\}$ for the discrete bath and an associated hybridization function $\Lambda^{\text{discr}}(z)$, which gives a quantitatively precise approximation to $\Lambda(z)$ *only* when evaluated on the imaginary frequency axis. On the real-frequency axis, the approximation is very rough and can only be considered qualitatively correct. This follows already from the fact that only relatively small numbers of bath sites $N_b \lesssim 15$ can be stably optimized. Still the approach is valid if one is satisfied with the much lower precision on the real axis and does not strive to describe real-time evolution as in this paper. The preceding statements are, e.g., discussed, among several other results, in Ref. [51], where the goal was not to describe real-time evolution but "thermodynamic" properties.

We note that one *can* define a meaningful cost function on the real axis, if one allows for non-Hermitian Hamiltonians with complex bath energies, or an equivalent description in terms of Lindbladt operators [32]. We further note that one can also construct an *optimal* discrete representation of the "second bath" that appears within nonequilibrium DMFT [33]. However, this only suffices to describe situations in which the system and bath are initially not entangled [33]. As nonequilibrium DMFT is a promising approach to describe the nonequilibrium dynamics of strongly correlated materials, it is desirable to extend the promising DMRG calculations for situations with a nonentangled initial state [39,52] to the general case of entangled initial states. However, then one also has to discretize the "first" bath, which incorporates the spectral information of H and which is equivalent to the bath that is the subject of the present paper. For the first bath, one again faces the problem that a cost function cannot be meaningfully defined.

APPENDIX B: SYSTEM GREEN'S FUNCTION

The retarded system Green's function is defined in terms of the general retarded Green's function (system and bath)

$$G(x) = \frac{1}{x + i0 - (H - E_0)} \tag{B1}$$

by taking expectation values with respect to the system states [19], e.g., $|\psi_0\rangle = d^\dagger |E_0\rangle$,

$$G_{\text{sys}}(x) = \langle \psi_0 | G(x) | \psi_0 \rangle. \tag{B2}$$

For the system Hamiltonian $H_{\text{sys}} = \epsilon_0 d^\dagger d$ [19], it can be evaluated as

$$G_{\text{sys}}(x) = \frac{1}{x + i0 - \epsilon_0 + \Lambda(x)}, \tag{B3}$$

where $\Lambda(x)$ is defined in (5).

APPENDIX C: LANCZOS ALGORITHM

1. General Lanczos algorithm and relation to orthogonal polynomials

The Lanczos algorithm constructs a three-diagonal matrix representation of any Hermitian operator H by representing it in its Gram-Schmidt orthogonalized Krylov basis $\{|f_n\rangle\}$: given a start vector $|f_0\rangle$ that has nonzero overlap with all eigenstates of H, one orthogonalizes the vector $|f_n\rangle$ with respect to all previous vectors $|f_{n'}\rangle$ with $n' < n$. This results in

$$\begin{aligned}
\alpha_n &= \langle f_n | H | f_n \rangle, \\
|r_n\rangle &= H|f_n\rangle - \alpha_n |f_n\rangle - \sqrt{\beta_n}|f_{n-1}\rangle, \\
\beta_{n+1} &= |\langle r_n | r_n \rangle|, \quad \beta_0 = 0, \\
|f_{n+1}\rangle &= \frac{1}{\sqrt{\beta_{n+1}}}|r_n\rangle, \quad \text{for } n = 0, \dots, N-1.
\end{aligned} \tag{C1}$$

One can show that the Lanczos algorithm implicitly constructs a family of polynomials $q_n(x)$ that are orthogonal with respect to an inner product weighted with the spectral density $A(x)$ of the operator H [35,53]:

$$w(x) = \sum_{n=1}^{\dim(H)} |\langle E_n | f_0 \rangle|^2 \, \delta(E - E_n) = A(x).$$

The proof is as follows. Let us define the polynomial $q_n(x)$ of degree n via

$$|f_n\rangle = q_n(H)|f_0\rangle, \tag{C2}$$

and then show that they are orthogonal with respect to $A(x)$. We note that (C2) can always be fulfilled as $|f_n\rangle$ is constructed by applying H n times to the initial state $|f_0\rangle$. Furthermore,

$$\begin{aligned}
\int_a^b dx\, A(x) q_k(x) q_l(x) &= \sum_{n=1}^{N_b} \langle f_0 | E_n \rangle q_k(E_n) q_l(E_n) \langle E_n | f_0 \rangle \\
&= \langle f_0 | q_k(H) q_l(H) | f_0 \rangle = \langle f_k | f_l \rangle = \delta_{kl},
\end{aligned}$$

which completes the proof.

2. Chain mapping

In the following, we show how to use the Lanczos algorithm to tridiagonlize the star Hamiltonians H in (1a) and H^{discr} in (3). This amounts to using the general algorithm (C1) for the bath Hamiltonians H_{bath} and $H_{\text{bath}}^{\text{discr}}$, respectively. The bath Hamiltonians are quadratic and therefore simple to treat. They have the spectral densities $J(x)$ and $J^{\text{discr}}(x)$ as defined in (2) and (4), respectively. Already from this we can conclude from the argument of Sec. C 1, that the Lanczos algorithm applied for the continuous H_{bath}, yields the same set of orthogonal polynomials as the recurrence (19), and is therefore equivalent to it.

In practice, the algorithm is usually used to obtain representations of the discrete bath and coupling Hamiltonians $H_{\text{bath}}^{\text{discr}}$ and $H_{\text{coupl}}^{\text{discr}}$. We will lay out the procedure for the discrete case, and note differences to the continuous case where necessary.

Let us denote the (single-particle) bath orbital states of the discrete star representation (3) as $|c_n\rangle$. These are associated with the operators $c_n^\dagger$ via $|c_n\rangle = c_n^\dagger |\text{vac}\rangle$. Analogously, define

the bath orbitals of the chain representation (26) as $|e_n\rangle$, where $|e_n\rangle = e_n^\dagger |\text{vac}\rangle$. The first orbital of the chain representation then is

$$|e_0\rangle = \frac{1}{V_{\text{tot}}} \sum_{n=1}^{N_b} V_n |c_n\rangle,$$

$$|V_{\text{tot}}|^2 = \sum_{n=1}^{N_b} |V_n|^2 = \int_a^b dx\, J(x), \tag{C3}$$

in the discrete case, and

$$|e_0\rangle = \frac{1}{V_{\text{tot}}} \int_a^b dx\, V(x)|a_x\rangle, \quad |a_x\rangle = a_x^\dagger|\text{vac}\rangle, \tag{C4}$$

in the continuous case, in agreement with (27). In both cases, it is a superposition of all states in the star. The coupling Hamiltonians $H_{\text{coupl}}^{\text{discr}}$ in (3) can then be written as $H_{\text{coupl}}^{\text{discr}} = V_{\text{tot}}(|d\rangle\langle e_0| + \text{H.c.})$, where $|d\rangle$ is associated with the system operator $d^\dagger$. The same equation holds in the continuous case.

One then uses the Lanczos algorithm to construct a three-diagonal representation of $H_{\text{bath}}^{\text{discr}}$:

$$\alpha_n = \langle e_n | H_{\text{bath}}^{\text{discr}} | e_n \rangle,$$
$$|r_n\rangle = H_{\text{bath}}^{\text{discr}}|e_n\rangle - \alpha_n|e_n\rangle - \sqrt{\beta_n}|e_{n-1}\rangle$$
$$\beta_{n+1} = |\langle r_n|r_n\rangle|, \quad \beta_0 = 0, \tag{C5}$$
$$|e_{n+1}\rangle = \frac{1}{\sqrt{\beta_{n+1}}}|r_n\rangle, \quad \text{for } n = 0, \dots, N_b - 1.$$

or analogously, for the continuous case. The parameters α_n and β_n in the recursion are the parameters of the Hamiltonian (26), and with that the map is complete.

In practice we note that we *cannot* find a direct matrix representation of the continuous Hamiltonian (1a) that we could use on a computer to compute (C5). In the discrete case, on the other hand, the preceding equations are easily solved by generating a matrix representation by multiplying from the left with $\langle c_{n'}|$ and inserting identities $\sum_{n'} |c_{n'}\rangle\langle c_{n'}|$ such that the initial vector can be written as $(\langle c_n|e_0\rangle)_{n=1}^{N_b} = (V_n)_{n=1}^{N_b}$ and the representation of $H_{\text{bath}}^{\text{discr}}$ involved is $\langle c_n|H_{\text{bath}}|c_{n'}\rangle = x_n\delta_{nn'}$.

Due to the numerical instability of the Lanczos algorithm, the recurrences (C5) and (19) have to be computed with high-precision arithmetics when exceeding $N_b \sim 40$ or using the stabilized implementation of Ref. [35].

APPENDIX D: ESTIMATE THE ERROR IN TIME EVOLUTION

As Chebyshev polynomials are *almost optimal*, they will result in a sequence c_n, which is very close to the sequence produced by an optimal choice of polynomials, in the sense of the discussion of (34).

For Chebyshev polynomials $[v(x) = \tilde{v}(x') = \frac{1}{\pi}(1 - x')^{-\frac{1}{2}}$ and $q_n(x) = \tilde{q}_n(x') = \arccos(n\cos(x'))$ with $x' = 2\frac{x-a}{b-a} - 1$, $x = \frac{1}{2}(b-a)x' + \frac{1}{2}(b+a)]$, we can evaluate the coefficients
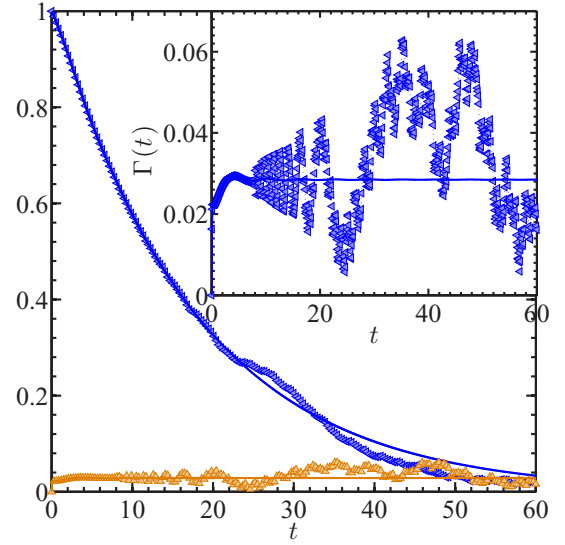

FIG. 7. (Color online) Blue curves represent the master equation solution for the atomic population $\langle\sigma^\dagger(t)\sigma(t)\rangle$, with quasicontinuous spectrum (plain solid curve) and Gauss-Christoffel (BSDO) quadrature with $N = 100$ nodes (curve with triangles). Orange curves (see also inset) represent the evolution of $\Gamma(t) = \int_0^t \alpha_T(\tau)e^{i\omega_S\tau}$ for the same two cases. The spectral density, as well as all system parameters are the same as in Fig. 1, except for the coupling that now is considered to be weak, $\alpha = 0.01$.

in (34) explicitly,

$$c_n = \frac{2}{b-a} e^{-\frac{i}{2}(b+a)t} \int_{-1}^1 dx'\, \tilde{v}(x') e^{-\frac{i}{2}(b-a)t} \tilde{q}_n(x)$$
$$= \frac{2(-i)^n}{b-a} e^{-\frac{i}{2}(b+a)t} J_n\left(\frac{1}{2}(b-a)t\right), \tag{D1}$$
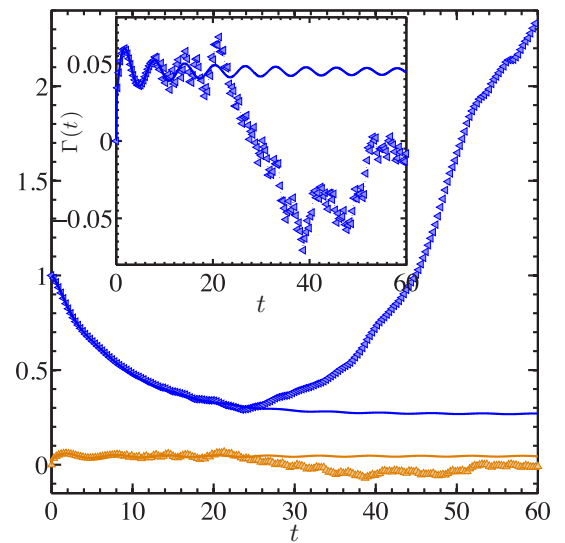

FIG. 8. (Color online) Same as in Fig. 7, but considering finite temperature ($\beta = 1$).

where $J_n(t')$ are Bessel functions of the first kind. For all practical purposes, $J_n(t') \simeq 0$ if $n > t'$. More concretely, the asymptotic form for high values of n reads $n \gg t'^2 - 1$, $J_n(t') \sim \frac{1}{(n+1)!}(\frac{t'}{2})^n$ [54], and shows that this decreases as a faculty.

APPENDIX E: OPEN QUANTUM SYSTEM IN THE PRESENCE OF A THERMAL ENVIRONMENT

Let us now consider $d = d^\dagger = \sigma_x$ in (1a), and a finite temperature in the environment. We study this case within a standard approximate scheme, namely, a master equation (ME) up to second order in the system-environment coupling parameter g [1],

$$\frac{d\rho_s(t)}{dt} = -i[H_{\text{sys}},\rho_s(t)] + \int_0^t d\tau \alpha_2^*(t-\tau)[d^\dagger,\rho_s(t)d(\tau-t)]$$

$$+ \int_0^t d\tau \alpha_2(t-\tau)[d^\dagger(\tau-t)\rho_s(t),d]$$

$$+ \int_0^t d\tau \alpha_1(t-\tau)[d(\tau-t)\rho_s(t),d^\dagger]$$

$$+ \int_0^t d\tau \alpha_1^*(t-\tau)[d,\rho_s(t)d(\tau-t)^\dagger] + \mathcal{O}(g^3), \quad \text{(E1)}$$

with $\alpha_1(t-\tau) = \sum_k g_k^2(n_k+1)e^{-i\omega_k(t-\tau)}$, $\alpha_2(t-\tau) = \sum_\lambda g_k^2 n_k e^{i\omega_k(t-\tau)}$, and $d(t) = e^{iH_{\text{sys}}t}de^{-iH_{\text{sys}}t}$.

As it can be seen in Fig. 7, for zero temperature, and in Fig. 8, for finite temperature, the polynomial Gauss-Christoffel (BSDO) quadrature is still extremely accurate at short times. Nevertheless, just as in the zero temperature case, after a certain time $t_{\max}$, the discretization procedure starts to fail. Such a failure is originated from the fact that the polynomial quadrature rule starts to reproduce inaccurately the integrals $\Gamma(t) = \int_0^t \alpha_T(\tau)e^{i\omega_S\tau}$, with $\alpha_T(t) = \alpha_1(t) + \alpha_2^*(t)$, entering in the master equation.

Indeed, as seen in the inset of both figures, small deviations of this quantity due to an inaccurate discretization, produce large deviations in the dynamics with respect to the reference (corresponding to the solution with a quasicontinuous spectrum), and this deviation is particularly large at finite temperatures.

[1] H. Breuer and F. Petruccione, *The theory of Quantum Open Systems* (Oxford University Press, Oxford, 2002).

[2] A. Rivas and S. F. Huelga, *Open Quantum Systems. An Introduction* (Springer, Heidelberg, 2011).

[3] P. W. Anderson, Phys. Rev. **124**, 41 (1961).

[4] W. Metzner and D. Vollhardt, Phys. Rev. Lett. **62**, 324 (1989).

[5] A. Georges and G. Kotliar, Phys. Rev. B **45**, 6479 (1992).

[6] A. Georges, G. Kotliar, W. Krauth, and M. J. Rozenberg, Rev. Mod. Phys. **68**, 13 (1996).

[7] G. Kotliar, S. Savrasov, K. Haule, V. Oudovenko, O. Parcollet, and C. Marianetti, Rev. Mod. Phys. **78**, 865 (2006).

[8] T. Maier, M. Jarrell, T. Pruschke, and M. Hettler, Rev. Mod. Phys. **77**, 1027 (2005).

[9] D. Zgid and G. K.-L. Chan, J. Chem. Phys. **134**, 094115 (2011).

[10] W. Domcke, Phys. Rep. **208**, 97 (1991).

[11] F. Heidrich-Meisner, A. E. Feiguin, and E. Dagotto, Phys. Rev. B **79**, 235336 (2009).

[12] R. Peters, Phys. Rev. B **84**, 075139 (2011).

[13] F. Guettge, F. B. Anders, U. Schollwoeck, E. Eidelstein, and A. Schiller, Phys. Rev. B **87**, 115115 (2013).

[14] M. Ganahl, P. Thunström, F. Verstraete, K. Held, and H. G. Evertz, Phys. Rev. B **90**, 045144 (2014).

[15] F. A. Wolf, I. P. McCulloch, O. Parcollet, and U. Schollwöck, Phys. Rev. B **90**, 115124 (2014).

[16] A. Weichselbaum, F. Verstraete, U. Schollwöck, J. I. Cirac, and J. von Delft, Phys. Rev. B **80**, 165117 (2009).

[17] F. A. Wolf, J. A. Justiniano, I. P. McCulloch, and U. Schollwöck, Phys. Rev. B **91**, 115144 (2015).

[18] M. Zwolak, J. Chem. Phys. **129**, 101101 (2008).

[19] A. C. Hewson, *The Kondo Problem to Heavy Fermions* (Cambridge University Press, Cambridge, 2003).

[20] A. W. Chin, S. F. Huelga, and M. B. Plenio, in *Semiconductors and Semimetals*, edited by U. Wurfel, M. Thorwart, E. R. Weber, and C. Jagadish (Academic Press, Amsterdam, Netherlands, 2011).

[21] R. Bulla, T. A. Costi, and T. Pruschke, Rev. Mod. Phys. **80**, 395 (2008).

[22] R. S. Burkey and C. D. Cantrell, J. Opt. Soc. Am. B **1**, 169 (1984).

[23] A. K. Kazansky, J. Phys. B **30**, 1401 (1997).

[24] M. Karski, C. Raas, and G. S. Uhrig, Phys. Rev. B **77**, 075116 (2008).

[25] N. Shenvi, J. R. Schmidt, S. T. Edwards, and J. C. Tully, Phys. Rev. A **78**, 022502 (2008).

[26] J. Prior, A. W. Chin, S. F. Huelga, and M. B. Plenio, Phys. Rev. Lett. **105**, 050404 (2010).

[27] J. Prior, I. de Vega, A. W. Chin, S. F. Huelga, and M. B. Plenio, Phys. Rev. A **87**, 013428 (2013).

[28] I. de Vega and M.-C. Banuls, arXiv:1504.07228.

[29] Florian A. Y. N. Schröder, Alex W. Chin, and Richard H. Friend, arXiv:1507.02202.

[30] Inés de Vega, Phys. Rev. A **90**, 043806 (2014).

[31] M. Caffarel and W. Krauth, Phys. Rev. Lett. **72**, 1545 (1994).

[32] A. Dorda, M. Nuss, W. von der Linden, and E. Arrigoni, Phys. Rev. B **89**, 165105 (2014).

[33] C. Gramsch, K. Balzer, M. Eckstein, and M. Kollar, Phys. Rev. B **88**, 235106 (2013).

[34] W. Gautschi, *A Survey of Gauss-Christoffel Quadrature Formulae* (Birkhauser Verlag, Basel, 1981), pp. 72–147.

[35] W. Gautschi, J. Comput. Appl. Math. **178**, 215 (2005).

[36] W. H. Press, S. A. Teukolsky, W. T. Vetterling, and B. P. Flannery, *Numerical Recipes: The Art of Scientific Computing*, 3rd ed. (Cambridge University Press, New York, NY, USA, 2007).

[37] G. H. Golub and J. H. Welsch, Math. Comp. **23**, 221 (1969).

[38] M. P. Woods, R. Groux, A. W. Chin, S. F. Huelga, and M. B. Plenio, J. Math. Phys. **55**, 032101 (2014).

[39] F. A. Wolf, I. P. McCulloch, and U. Schollwöck, Phys. Rev. B **90**, 235131 (2014).

[40] A. O. Caldeira and A. J. Leggett, Physica A **121**, 587 (1983).

[41] U. Weiss, *Quantum Dissipative Systems*, Series in Modern Condensed Matter Systems (World Scientific, Singapore, 2008).

[42] M. Florescu and S. John, Phys. Rev. A **64**, 033801 (2001).

[43] I. de Vega, D. Alonso, and P. Gaspard, Phys. Rev. A **71**, 023812 (2005).

[44] A. Shnirman, Y. Makhlin, and G. Schön, Phys. Scr. **2002**, T102 (2002).

[45] C. Seoanez, F. Guinea, and A. H. C. Neto, Europhys. Lett. **78**, 60002 (2007).

[46] N.-H. Tong and M. Vojta, Phys. Rev. Lett. **97**, 016802 (2006).

[47] A. W. Chin, J. Prior, S. F. Huelga, and M. B. Plenio, Phys. Rev. Lett. **107**, 160601 (2011).

[48] Mischa P. Woods and Martin B. Plenio, arXiv:1508.07354.

[49] A. Go and A. J. Millis, Phys. Rev. Lett. **114**, 016402 (2015).

[50] A. Liebsch and H. Ishida, J. Phys.: Condens. Matter **24**, 053201 (2012).

[51] F. A. Wolf, A. Go, I. P. McCulloch, A. J. Millis, and U. Schollwöck, arXiv:1507.08650.

[52] K. Balzer, F. A. Wolf, I. P. McCulloch, P. Werner, and M. Eckstein, Phys. Rev. X **5**, 031039 (2015).

[53] J. A. Justiniano, Bachelor's Thesis, LMU Munich, 2015.

[54] *Handbook of Mathematical Functions*, edited by M. Abramowitz and I. A. Stegun (Dover, New York, 1965).

6. Conclusion and outlook

Let us first briefly conclude this thesis, and then give an outlook on methods and applications.

Conclusion

Both spectral resolution and entanglement are strongly dependent on whether one solves the DMFT self-consistency equation on the real-frequency or the imaginary-frequency axis.

1. *Imaginary-frequency axis*: The imaginary-time MPS (itMPS) impurity solver of Wolf *et al.* (2015a) proofed to be able to treat complex models, not easily accessible with other methods, at modest computational cost. This development, for the first time, establishes DMRG as a flexible low-coast impurity solver for realistic problems, such as encountered in the study of strongly-correlated materials. The crucial advance stems from the fact that imaginary-time evolution does not create entanglement, and hence allows to compute Green's functions numerically exactly, provided a ground state calculation is feasible.

2. *Real-frequency axis*: Computations on the real axis lead to a much higher spectral resolution as compared to the imaginary axis, at the price of a much higher computational cost (Wolf *et al.*, 2015a). Advancements (Wolf *et al.*, 2014a,b, 2015b) still enabled results for interesting models, such as a two-site dynamical cluster approximation for the single-band Hubbard model. Therefore, for relatively simple models and — of course — in non-equilibrium this remains the method of choice.

Outlook: methods and technology

Let us first give an outlook on prospects for further methodological and technical improvements.

1. *Entanglement:* One does *not* fully understand the different entanglement of different representations of impurity (cluster) problems. Thereby one does not understand the computational complexity of its solution. Can one devise a rigorous method that constructs the *least-entangled representation* of an impurity problem? The considerations of Wolf *et al.* (2014b) that refer to the different entanglement in the star and the chain representation might be just the starting point for such an investigation.

2. *Subspaces for reducing the size of the Hilbert space:* One could use techniques from quantum chemistry that construct subspaces of the Hilbert space, by e.g. systematically constructing particle-hole excitations as a basis for an effective representation of H (Zgid *et al.*, 2012; Lu *et al.*, 2014; Lin and Demkov, 2013a,b). That such ideas can be combined with MPS has been demonstrated (Ma and Ma, 2013).

3. *Reduced dynamics formalism:* Compute the reduced dynamics of the impurity in a quantum impurity-bath problem (Cohen *et al.*, 2013) instead of the dynamics of the full system. This then involves time evolution with a Liouvillian operator.

4. *Can we use the fact that bath sites are non-interacting?* Construct some kind of hybrid MPS – single-particle wavefunction? In CTQMC this fact is exploited by integrating out the bath degrees of freedom analytically.

5. *Finite temperature:* Use finite temperature calculations similar to the impressing results of Savostyanov *et al.* (2014).

6. *Give Lanczos a second chance?* A Lanczos algorithm that measures off-diagonal elements can be parallelized efficiently. This kills one the considerable disadvantage of high computation time mentioned in Sec. 2.3. If one then improves the evaluation of the Hamiltonian in the *crooked* basis, one might devise a stable method. The fact that the basis is non-orthogonal is no problem as such: Chebyshev expansions and the time evolution algorithm produce non-orthogonal basis states, too. Also, errors do not seem to matter too much when computing on the imaginary axis, as far as much experience from the ED+DMFT community tells, see e.g. the work of Capone *et al.* (2007). On the imaginary axis, therefore, it might even be viable to simply ignore the non-orthogonality of the Lanczos basis. Mathematically, this seems less convincing though.

7. *Mathematically prove the most efficient algorithm to extract spectral information from an operator H.* The discussion of Wolf *et al.* (2015b) is for sure not the end of this story. Is the question meaningful in the sense that there might be significant differences using different algorithms? That is, will the entanglement of different sets of basis states to span the relevant subspace of the Hilbert space differ significantly? Wolf *et al.* (2015b) seems to suggest this for the example of a Chebyshev and Fourier expansion. What about the Lanczos algorithm in this context?

8. *Choose the most efficient discretization of the hybridization function?* That is, try to reduce the number of needed bath sites significantly by devising a better discrete approximation to the continuous impurity problem. After the result of de Vega *et al.* (2015), this is the only point where there seems little further hope. Improvements could merely concern the bath fitting procedure of Caffarel and Krauth (1994) or the suggestions of Dorda *et al.* (2014) for computations using the Lindbladt formalism.

Outlook: applications and concepts

There are chances that MPS+DMFT can become much more powerful than CTQMC in the long run. In quantum chemistry,[1] one always deals with the kind of highly coupled Hamiltonians that are generated when mapping many correlated sites and bath sites to an effective one-dimensional geometry as in DMFT. The rule of thumb is that DMRG calculations in quantum chemistry can treat up to $L = 50$ sites. The computations within this thesis still stayed far away from this limit, which makes hope for more.

A fully realistic model for the iron pnictide superconductors, for example, would involve a still higher complexity than the one studied by Wolf *et al.* (2015a). Current studies in this direction either use single-site approximations for five (Werner *et al.*, 2012) or three band models (Stadler *et al.*, 2015). A non-local theory should involve five bands and at least two momentum patches. Such models though are not only relevant for the iron pnictide superconductors, but also for many other complex materials.

As a second application, systems with artificial gauge fields should be a promising application. These are inaccessible to QMC due to the phase problem.

Another path to follow is to use the entanglement of the impurity problem with the bath to distinguish different phases. Almost nothing has been done in this direction and only recently, Udagawa and Motome (2015) performed a cluster DMFT analysis to study entanglement, albeit using CTQMC. In the context of impurity models though, already more work exists (Lee *et al.*, 2015).

---

[1]See e.g. the CheMPS2 package of Wouters *et al.* (2014).

Equilibrium properties of correlated materials are related to the relaxation dynamics of photo-excited states. To understand the interplay of optical electronic excitations with other degrees of freedom is a promising experimental route to understand the mechanism behind high temperature superconductivity (Conte *et al.*, 2015). Aside from this highly interesting question for non-equilibrium DMFT, there are many interesting purely conceptual questions concerning the mechanisms that govern the dynamic behavior of quantum many-body systems in non-equilibrium.

Finally, it would conceptually also be highly interesting to understand the relation of DMFT to the density matrix embedding theory (Knizia and Chan, 2012). This should be relatively straight forward using e.g. computations of entanglement spectra, as both can be evaluated using DMRG.

A. Green's functions

While most conventions on notation have been clarified in the appendices of the journal articles of the previous sections of this thesis, we summarize here the Green's function formalism at zero temperature that is employed throughout this thesis.

Denote the ground state $|E_0\rangle$ with energy E_0 for a given Hamiltonian $H = H_{\text{internal}} - \mu \hat{N}$, where μ is a chemical potential and $\hat{N}$ measures the total particle number. We are interested in spectral and Green's functions that are associated with either single-particle $|\psi_0^>\rangle = d^\dagger|E_0\rangle$ or single-hole excitations $|\psi_0^<\rangle = d|E_0\rangle$, where $d^\dagger$ (d) creates (annihilates) a fermion,

$$G^{\gtrless}(z) = \langle\psi_0^{\gtrless}|\frac{1}{z \mp (H - E_0)}|\psi_0^{\gtrless}\rangle, \quad z \in \mathbb{C} \tag{A.1a}$$

$$A^{\gtrless}(z)(\omega) = \langle\psi_0^{\gtrless}|\delta(\omega \mp (H - E_0))|\psi_0^{\gtrless}\rangle$$
$$= \sum_n |\langle\psi_0^{\gtrless}|E_n\rangle|^2 \delta(\omega \mp (E_n - E_0)). \tag{A.1b}$$

Using the Sokhotski-Plemelj theorem, one finds $A^{\gtrless}(\omega) = -\frac{1}{\pi}\text{Im}\, G^{\gtrless}(\omega + i0^+)$. As $|E_0\rangle$ is the ground state in the grand-canonical ensemble, $A^{\gtrless}(\omega) = 0$ for $\omega \lessgtr 0$.

The central objects of all computations are the *greater* and the *lesser* correlation functions $\widetilde{G}$, which we define for imaginary time $\tau \in \mathbb{R}$ as

$$\widetilde{G}^{\gtrless}(\tau) = \langle\psi_0^{\gtrless}|e^{\mp(H-E_0)\tau}|\psi_0^{\gtrless}\rangle. \tag{A.2}$$

If we evaluate these functions for real-time $t = i\tau$, $t \in \mathbb{R}$, we obtain the usual real-time evolution of a single-particle excitation

$$\widetilde{G}^{\gtrless}(it) = \langle\psi_0^{\gtrless}|e^{\mp i(H-E_0)t}|\psi_0^{\gtrless}\rangle. \tag{A.3}$$

On the imaginary axis, equation (A.2) defines the Fourier transform $G^{\text{mat}}(\tau)$ of the Matsubara Green's function $G^{\text{mat}}(i\omega_n) = \int_{-\infty}^{\infty} d\tau\, G^{\text{mat}}(\tau)e^{i\omega_n\tau}$ as superpositions of a forward-evolution ($\tau > 0$) of the greater and a backward evolution ($\tau < 0$) of the lesser correlation functions

$$G^{\text{mat}}(\tau) = -\theta(\tau)\widetilde{G}^>(\tau) + \theta(-\tau)\widetilde{G}^<(\tau),$$
$$G^{\text{mat}}(i\omega_n) = G^>(i\omega_n) + G^<(i\omega_n). \tag{A.4}$$

Evidently, $G^{\gtrless}(i\omega_n) = G^{\gtrless}(z)|_{z=i\omega_n}$ have the form of the definition (A.1a), with Fourier transforms $G^>(\tau) = -\theta(\tau)\widetilde{G}^>(\tau)$ and $G^<(\tau) = \theta(-\tau)\widetilde{G}^<(\tau)$. The Matsubara frequencies are defined (for fermions) as $\omega_n = (2n+1)\pi/\beta$ and become dense at zero temperature $\beta \to \infty$.

On the real axis, the Fourier transforms of the *zero-temperature* and the *retarded* Green's function are again superpositions of the greater and lesser correlation functions $\widetilde{G}$ evaluated at real time $t = i\tau$ as in (A.3)

$$G^{\text{zero}}(t) = -i\theta(t)\widetilde{G}^>(it) + i\theta(-t)\widetilde{G}^<(it), \tag{A.5a}$$

$$G^{\text{ret}}(t) = -i\theta(t)\widetilde{G}^>(it) - i\theta(t)\widetilde{G}^<(it). \tag{A.5b}$$

Evaluating the Fourier transform $f(\omega) = \int_{-\infty}^{\infty} dt\, f(t)e^{i\omega t}$ yields,[1] upon adding an infinitesimal

---

[1]The backtransform therefore is $f(t) = \int_{-\infty}^{\infty} \frac{d\omega}{2\pi} f(\omega)e^{-i\omega t}$.

imaginary constant to render the integral convergent,

$$G^{\text{zero}}(\omega) = G^>(\omega + i0^+) + G^<(\omega - i0^+), \tag{A.6a}$$

$$G^{\text{ret}}(\omega) = G^>(\omega + i0^+) + G^<(\omega + i0^+). \tag{A.6b}$$

Again the greater and lesser Green's functions $G^{\gtrless}(\omega \pm i0^+)$ are of type (A.1a). On the real axis, one therefore defines their Fourier transforms as $G^>(t) = -i\theta(t)\widetilde{G}^>(it)$ and $G^<(t) = i\theta(-t)\widetilde{G}^<(it)$, respectively.[2] The retarded Green's function directly yields the spectral function $A(\omega) = -\frac{1}{\pi}\text{Im}\,G^{\text{ret}}(\omega)$[3] and equivalently

$$A^>(\omega) = \frac{1}{2\pi i}(G(\omega + i0^+) - G(\omega - i0^+)). \tag{A.10}$$

Conversely,

$$G^>(z) = \int d\omega \frac{A^>(\omega)}{z - \omega}. \tag{A.11}$$

All of this follows from the fact that $G^>(z)$ only has poles on a finite range on the real axis and is analytic everywhere else in the complex plane. The previous identities therefore hold for all functions with these properties.

Evidently, from inspection of (A.4) one has $G^{\text{ret}}(\omega) = G^{\text{mat}}(\omega + i0^+)$.

---

[2] Let us compute the Fourier transform relations explicitly

$$\begin{aligned}
G^>(\omega + i0^+) &= \int_{-\infty}^{\infty} dt\, G^>(t)e^{i(\omega+i0^+)t} \\
&= \lim_{\epsilon \to 0^+} -i\int_0^{\infty} dt\, \langle de^{-i(H-E_0)t}d^\dagger\rangle_0 e^{i\omega t - \epsilon t} \\
&= \lim_{\epsilon \to 0^+} i\langle d\frac{1}{i\omega - i(H - E_0) - \epsilon}d^\dagger\rangle_0 \\
&= i\langle d\frac{1}{i\omega - i(H - E_0) - 0^+}d^\dagger\rangle_0 \\
&= i\langle d\frac{-i}{\omega - (H - E_0) + i0^+}d^\dagger\rangle_0 \\
&= \langle d\frac{1}{\omega - (H - E_0) + i0^+}d^\dagger\rangle_0.
\end{aligned} \tag{A.7}$$

Analogously

$$\begin{aligned}
G^<(\omega - i0^+) &= \int_{-\infty}^{\infty} dt\, G^<(t)e^{i(\omega-i0^+)t} \\
&= \langle \psi_0^<|\frac{1}{\omega - (E_0 - H) - i0^+}|\psi_0^<\rangle,
\end{aligned} \tag{A.8}$$

to give

$$\begin{aligned}
G^{\text{zero}}(\omega) &= -i\int_0^{\infty} dt\, \widetilde{G}^>(it)e^{i\omega t - 0^+t} + i\int_{-\infty}^0 dt\widetilde{G}^<(it)e^{i\omega t + 0^+t} \\
&= G^>(\omega + i0^+) + G^<(\omega - i0^+)
\end{aligned} \tag{A.9a}$$

$$\begin{aligned}
G^{\text{ret}}(\omega) &= -i\int_0^{\infty} dt\, \big(\widetilde{G}^>(it) + \widetilde{G}^<(it)\big)e^{i\omega t - 0^+t}
\end{aligned} \tag{A.9b}$$

$$= G^>(\omega + i0^+) + G^<(\omega + i0^+). \tag{A.9c}$$

[3] For any integral over x it holds $\int_{-\infty}^{\infty} dx \frac{f(x)}{x - x_0 + i0^+} = \mathcal{P}\int_{-\infty}^{\infty} dx \frac{f(x)}{x - x_0} - i\pi f(x_0)$. Often we write simply $\frac{1}{x - x_0 + i0^+} = \mathcal{P}\frac{1}{x - x_0} - i\pi\delta(x - x_0)$. This should not be confusing when understood in the previous sense even though the Cauchy principal value of $\frac{1}{x - x_0}$ is zero.

B. Curriculum Vitae

Coordinates

Affiliation	Theoretical Nanophysics
	Arnold Sommerfeld Center for Theoretical Physics
	Ludwig-Maximilians-Universität München
	80333 München, Theresienstr. 37, Germany
Year of Birth	1986
Webpage	falexwolf.de

Education

04.13 - 07.15 **PhD in theo. physics**, LMU Munich (submitted 07.15, defended 10.15)
    ▷ **visiting scientist**, (03.15 - 05.15), Columbia U, New York City
    Solving dynamical mean-field theory using matrix product states

02.12 - 03.13 **PhD in electrical eng.**, U Erlangen-Nuremberg (subm. 11.13, defended 06.14)
    Modeling annealing processes for ion-implanted cSi solar cells

10.06 - 07.11 **Studies of physics** Minors mathematics, philosophy and computer science.
    ▷ **MSc in physics** (07.11), U Augsburg
    Supercurrent through grain boundaries in the presence of strong correlations
    ▷ **visiting student** (09.10 - 01.11), École Normale Supérieure, Paris
    ▷ **visiting student researcher** (02.10 - 06.10), Georgetown U, Washington D.C.
    ▷ **BSc in physics** (07.09), U Augsburg
    Orbital order in a spin-polarized two-band Hubbard model

09.96 - 07.05 **High School**
    ▷ **Abitur** (07.05), Finsterwalder Gymnasium, Rosenheim
    Sartre à Stammheim: Son éxistentialisme et l'idéologie de la fraction armée rouge

Practical Experience

04.13 - 07.15 **PhD position** with U. Schollwöck (DFG FOR 1807), LMU Munich [P12-P18]

03.15 - 05.15 **Visiting scientist** with A. J. Millis, Columbia U, New York City [P18]

02.12 - 03.13 **PhD position** with P. Pichler, Bosch Research, Stuttgart [P8-P11]

10.11 - 01.12 **Research assistant** with D. Braak (DFG TRR 80), U Augsburg [P6,P7]

02.11 - 06.11 **Master's thesis** with T. Kopp (chair J. Mannhardt), U Augsburg [P5]

02.10 - 06.10 **Student researcher** with M. Rigol, Georgetown U, Washington D.C. [P2,P4]

10.09 - 01.10 **Tutor** for *statistical physics*, U Augsburg

07.09 - 10.09 **Student researcher** with M. Kollar (DFG SFB 484), U Augsburg [P1,P3]

03.09 - 06.09 **Bachelor's thesis** with M. Kollar (chair D. Vollhardt), U Augsburg

02.08 - 07.08 **Student researcher** with M. Schneider, experimental bio physics, U Augsburg

08.06 - 09.06 **Internship** in an *aid project* of the *Agnes Kunze Society*, Dehra Dun, India

09.05 - 06.06 **Civilian Service** in the *Caritas* center *Wendelstein Werkstätten*, Rosenheim

Refereed journal articles

18 *Imaginary-time matrix product state impurity solver for dynamical mean-field theory*
    FA Wolf, A Go, IP McCulloch, AJ Millis, and U Schollwöck   Phys. Rev. X **5**, 041032 (2015)

17 *How to discretize a quantum bath for real-time evolution*
    I de Vega, U Schollwöck and **FA Wolf**   Phys. Rev. B **92**, 155126 (2015)

16 *Non-thermal melting of Neel order in the Hubbard model*
    K Balzer, **FA Wolf**, IP McCulloch, P Werner and M Eckstein Phys. Rev. X **5**, 031039 (2015)

15 *Strictly single-site DMRG algorithm with subspace expansion*
    C Hubig, IP McCulloch, U Schollwöck, and **FA Wolf**   Phys. Rev. B **91** 155115 (2015)

14 *Spectral functions and time evolution from the Chebyshev recursion*
    FA Wolf, JA Justiniano, IP McCulloch, and U Schollwöck   Phys. Rev. B **91** 115144 (2015)

13 *Solving nonequilibrium dynamical mean-field theory using matrix product states*
    FA Wolf, IP McCulloch, and U Schollwöck   Phys. Rev. B **90** 235131 (2014)

12 *Chebyshev matrix product state impurity solver for dynamical mean-field theory*
    FA Wolf, IP McCulloch, O Parcollet and U Schollwöck   Phys. Rev. B **90** 115124 (2014)

11 *Electrical and structural analysis of crystal defects after high-temperature rapid thermal annealing of highly boron ion-implanted emitters*
    J Krügener, R Peibst, **FA Wolf**, F Kiefer, C Schöllhorn, A Grohe, R Brendel, and H J Osten
                                                                   IEEE J. Photovoltaics **5** 166 (2014)

10 *Diffusion and segregation model for the annealing of silicon solar cells implanted with phosphorus*
    FA Wolf, A Martinez-Limia, D Grote, D Stichtenoth and P Pichler
                                                                   IEEE J. Photovoltaics **5** 129 (2014)

 9 *Modeling the annealing of dislocation loops in implanted c-Si solar cells*
    FA Wolf, A Martinez-Limia, D Stichtenoth and P Pichler
                                                                   IEEE J. Photovoltaics **4** 851 (2014)

 8 *Comprehensive model for the diffusion of boron in silicon in presence of fluorine*
    FA Wolf, A Martinez-Limia and P Pichler   Solid-State Electronics **87** 4 (2013)

 7 *Dynamical correlation functions and the quantum Rabi model*
    FA Wolf, F Vallone, G Romero, M. Kollar, E Solano and D Braak
                                                                   Phys. Rev. A **87** 023835 (2013)

 6 *Exact real-time dynamics of the quantum Rabi model*
    FA Wolf, M Kollar and D Braak   Phys. Rev. A **85** 053817 (2012)

 5 *Supercurrent through grain boundaries in the presence of strong correlations*
    FA Wolf, S Graser, F Loder and T Kopp   Phys. Rev. Lett. **108** 117002 (2012)

 4 *Expansion of Bose-Hubbard Mott insulators in optical lattices*
    M Jreissaty, J Carrasquilla, **FA Wolf** and M Rigol   Phys. Rev. A **84** 043610 (2011)

 3 *Generalized Gibbs ensemble prediction of prethermalization plateaus and their relation to non-thermal steady states in integrable systems*
    M Kollar, **FA Wolf** and M Eckstein   Phys. Rev. B (editor's sugg.) **84** 054304 (2011)

 2 *Collapse and revival oscillations as a probe for the tunneling amplitude in an ultra-cold Bose gas*
    FA Wolf, I Hen and M Rigol   Phys. Rev. A **82**, 043601 (2010)

 1 *New theoretical approaches for correlated systems in nonequilibrium*
    M Eckstein, A Hackl, S Kehrein, M Kollar, M Moeckel, P Werner and **FA Wolf**
                                                                   Eur. Phys. J. ST **180**, 217 (2009)

Bibliography

Altland, A., and B. Simons (2010), *Condensed Matter Field Theory* (Cambridge University Press).

Amico, L., R. Fazio, A. Osterloh, and V. Vedral (2008), *Entanglement in Many-Body Systems*, Rev. Mod. Phys. **80**, 517, arXiv:quant-ph/0703044.

Aoki, H., N. Tsuji, M. Eckstein, M. Kollar, T. Oka, and P. Werner (2014), *Nonequilibrium dynamical mean-field theory and its applications*, Rev. Mod. Phys. **86**, 779.

Arbenz, P. (2012), *Numerical Methods for Solving Large Scale Eigenvalue Problems* (Lecture Notes, ETH Zürich).

Arsenault, L.-F., O. A. von Lilienfeld, and A. J. Millis (2015), *Machine learning for many-body physics: efficient solution of dynamical mean-field theory*, arXiv:1506.08858.

Assmann, E., P. Blaha, R. Laskowski, K. Held, S. Okamoto, and G. Sangiovanni (2013), *Oxide Heterostructures for Efficient Solar Cells*, Phys. Rev. Lett. **110**, 078701, arXiv:1301.1314.

Balzer, K., F. A. Wolf, I. P. McCulloch, P. Werner, and M. Eckstein (2015), *Non-thermal melting of Neel order in the Hubbard model*, Phys. Rev. X **5**, 031039, arXiv:1504.02461.

Baym, G., and L. P. Kadanoff (1961), *Conservation Laws and Correlation Functions*, Phys. Rev. **124**, 287.

Bilitewski, T. (2013), *Superconductivity in two dimensional Bose-Fermi-Mixtures: A Dynamical-Cluster-Approximation Study*, Master's thesis (LMU Munich).

Bulla, R., T. Costi, and T. Pruschke (2008), *Numerical renormalization group method for quantum impurity systems*, Rev. Mod. Phys. **80**, 395.

Burkey, R. S., and C. D. Cantrell (1984), *Discretization in the quasi-continuum*, Journal of the Optical Society of America B **1**, 169.

Caffarel, M., and W. Krauth (1994), *Exact diagonalization approach to correlated fermions in infinite dimensions: Mott transition and superconductivity*, Phys. Rev. Lett. **72**, 1545.

Capone, M., L. de Medici, and A. Georges (2007), *Solving the dynamical mean-field theory at very low temperatures using the Lanczos exact diagonalization*, Phys. Rev. B **76**, 245116.

Cohen, G., E. Gull, D. R. Reichman, and A. J. Millis (2014a), *Green's functions from real-time bold-line Monte Carlo: spectral properties of the nonequilibrium Anderson impurity model*, Phys. Rev. Lett. **112**, 146802, arXiv:1310.4151.

Cohen, G., D. R. Reichman, A. J. Millis, and E. Gull (2014b), *Green's functions from real-time bold-line Monte Carlo*, Phys. Rev. B **89**, 115139, arXiv:1401.0526.

Cohen, G., E. Y. Wilner, and E. Rabani (2013), *Generalized projected dynamics for non-system observables of non-equilibrium quantum impurity models*, New J. Phys. **15**, 073018, arXiv:1304.2216.

Conte, S. D., L. Vidmar, D. Golez, M. Mierzejewski, G. Soavi, S. Peli, F. Banfi, G. Ferrini, R. Comin, B. M. Ludbrook, L. Chauviere, N. D. Zhigadlo, H. Eisaki, M. Greven, S. Lupi, A. Damascelli, D. Brida, M. Capone, J. Bonca, G. Cerullo, and C. Giannetti (2015), *Snapshots of the retarded interaction of charge carriers with ultrafast fluctuations in cuprates*, Nature Physics **11**, 421, arXiv:1501.03833.

Daley, A. J., C. Kollath, U. Schollwöck, and G. Vidal (2004), *Time-dependent density-matrix renormalization-group using adaptive effective Hilbert spaces*, J. Stat. Mech. **2004**, P04005, arXiv:cond-mat/0403313.

Dargel, P. E., A. Wöllert, A. Honecker, I. P. McCulloch, U. Schollwöck, and T. Pruschke (2012), *Lanczos algorithm with matrix product states for dynamical correlation functions*, Phys. Rev. B **85**, 205119.

Dirks, A., M. Eckstein, T. Pruschke, and P. Werner (2013), *Extracting spectral properties from Keldysh Green functions*, Phys. Rev. E **87**, 023305.

Dolgov, S. V., and D. V. Savostyanov (2014), *Alternating minimal energy methods for linear systems in higher dimensions.*, SIAM J. Sci. Comput. **36**, A2248, arXiv:1301.6068.

Dorda, A., M. Nuss, W. von der Linden, and E. Arrigoni (2014), *Auxiliary master equation approach to non-equilibrium correlated impurities*, Phys. Rev. B **89**, 165105, arXiv:1312.4586.

Eckstein, M. (2009), *Nonequilibrium DMFT*, Ph.D. thesis (University of Augsburg).

Eisert, J. (2013), *Entanglement and Tensor Network States*, Modeling and Simulation **3**, 520, arXiv:1308.3318.

Eisert, J., M. Cramer, and M. B. Plenio (2010), *Area laws for the entanglement entropy*, Rev. Mod. Phys. **82**, 277, arXiv:0808.3773.

Evenbly, G., and G. Vidal (2014), *Tensor Network Renormalization*, arXiv:1412.0732.

Fannes, M., B. Nachtergaele, and R. F. Werner (1992), *Finitely correlated states on quantum spin chains*, Comm. Math. Phys. **144**, 443.

Ferrero, M., P. S. Cornaglia, L. De Leo, O. Parcollet, G. Kotliar, and A. Georges (2009), *Pseudogap opening and formation of Fermi arcs as an orbital-selective Mott transition in momentum space*, Physical Review B **80**, 064501.

Freericks, J. K., V. M. Turkowski, and V. Zlatić (2006), *Nonequilibrium Dynamical Mean-Field Theory*, Physical Review Letters **97**, 266408.

Gagliano, E., and C. Balseiro (1987), *Dynamical Properties of Quantum Many-Body Systems at Zero Temperature*, Phys. Rev. Lett. **59**, 2999.

Ganahl, M., M. Aichhorn, P. Thunström, K. Held, H. G. Evertz, and F. Verstraete (2014a), *Efficient DMFT impurity solver using real-time dynamics with Matrix Product States*, arXiv:1405.6728.

Ganahl, M., P. Thunström, F. Verstraete, K. Held, and H. G. Evertz (2014b), *Chebyshev expansion for impurity models using matrix product states*, Phys. Rev. B **90**, 045144.

García, D. J., K. Hallberg, and M. J. Rozenberg (2004), *Dynamical Mean Field Theory with the Density Matrix Renormalization Group*, Phys. Rev. Lett. **93**, 246403.

García, D. J., E. Miranda, K. Hallberg, and M. J. Rozenberg (2007), *Mott transition in the Hubbard model away from particle-hole symmetry*, Phys. Rev. B **75**, 121102.

Georges, A., and G. Kotliar (1992), *Hubbard model in infinite dimensions*, Phys. Rev. B **45**, 6479.

Georges, A., G. Kotliar, W. Krauth, and M. J. Rozenberg (1996), *Dynamical mean-field theory of strongly correlated fermion systems and the limit of infinite dimensions*, Rev. Mod. Phys. **68**, 13.

Go, A., and A. J. Millis (2015), *Spatial Correlations and the Insulating Phase of the High-T_c Cuprates: Insights from a Configuration-Interaction-Based Solver for Dynamical Mean Field Theory*, Phys. Rev. Lett. **114**, 016402, arXiv:1311.6819.

Gramsch, C., K. Balzer, M. Eckstein, and M. Kollar (2013), *Hamiltonian-based impurity solver for nonequilibrium dynamical mean-field theory*, Phys. Rev. B **88**, 235106, arXiv:1306.6315.

Granath, M., and H. U. R. Strand (2012), *Distributional exact diagonalization formalism for quantum impurity models*, Phys. Rev. B **86**, 115111, arXiv:1201.6160.

Graser, S., P. J. Hirschfeld, T. Kopp, R. Gutser, B. M. Andersen, and J. Mannhart (2010), *How grain boundaries limit supercurrents in high-temperature superconductors*, Nature Physics **6**, 609, arXiv:0912.4191.

Gull, E., A. J. Millis, A. I. Lichtenstein, A. N. Rubtsov, M. Troyer, and P. Werner (2011a), *Continuous-time Monte Carlo methods for quantum impurity models*, Rev. Mod. Phys. **83**, 349.

Gull, E., D. R. Reichman, and A. J. Millis (2011b), *Numerically Exact Long Time Behavior of Nonequilibrium Quantum Impurity Models*, Phys. Rev. B **84**, 085134, arXiv:1105.1175.

Hallberg, K. A. (1995), *Density matrix algorithm for the calculation of dynamical properties of low dimensional systems*, Phys. Rev. B **52**, 9827, arXiv:cond-mat/9503094.

Hastings, M. B. (2007a), *An Area Law for One Dimensional Quantum Systems*, J. Stat. Mech. **2007**, 08024, arXiv:0705.2024.

Hastings, M. B. (2007b), *Entropy and entanglement in quantum ground states*, Physical Review B **76**, 035114.

Hewson, A. C. (2003), *The Kondo Problem to Heavy Fermions* (Cambridge University Press).

Holzner, A., A. Weichselbaum, I. P. McCulloch, U. Schollwöck, and J. von Delft (2011), *Chebyshev matrix product state approach for spectral functions*, Phys. Rev. B **83**, 195115.

Hubig, C., I. P. McCulloch, U. Schollwöck, and F. A. Wolf (2015), *Strictly Single-Site DMRG Algorithm with Subspace Expansion*, Phys. Rev. B **91**, 155115, arXiv:1501.05504.

Jeckelmann, E. (2002), *Dynamical density-matrix renormalization-group method*, Phys. Rev. B **66**, 045114, arXiv:cond-mat/0203500.

Johnson, T. H., S. R. Clark, and D. Jaksch (2010), *Dynamical simulations of classical stochastic systems using matrix product states*, Phys. Rev. E **82,**, 036702, arXiv:1006.2639.

Johnson, T. H., T. J. Elliott, S. R. Clark, and D. Jaksch (2014), *Capturing exponential variance using polynomial resources: applying tensor networks to non-equilibrium stochastic processes*, Phys. Rev. Lett. **114**, 090602, arXiv:1410.3319.

Karski, M., C. Raas, and G. S. Uhrig (2005), *Electron spectra close to a metal-to-insulator transition*, Phys. Rev. B **72**, 113110.

Karski, M., C. Raas, and G. S. Uhrig (2008), *Single-particle dynamics in the vicinity of the Mott-Hubbard metal-to-insulator transition*, Phys. Rev. B **77**, 075116, arXiv:0710.2272.

Ketterle, W. (2015), *Inside the quantum Hall effect*, Nature Physics **11**, 90.

Knizia, G., and G. K.-L. Chan (2012), *Density matrix embedding: A simple alternative to dynamical mean-field theory*, Phys. Rev. Lett. **109**, 186404, arXiv:1204.5783.

Kollar, M., F. A. Wolf, and M. Eckstein (2011), *Generalized Gibbs ensemble prediction of prethermalization plateaus and their relation to nonthermal steady states in integrable systems*, Phys. Rev. B **84**, 054304, arXiv:1102.2117.

Kotliar, G., S. Savrasov, K. Haule, V. Oudovenko, O. Parcollet, and C. Marianetti (2006), *Electronic structure calculations with dynamical mean-field theory*, Rev. of Mod. Phys. **78**, 865.

Kühner, T. D., and S. R. White (1999), *Dynamical correlation functions using the density matrix renormalization group*, Phys. Rev. B **60**, 335.

Lanczos, C. (1950), *An Iteration Method for the Solution of the Eigenvalue Problem of Linear Differential and Integral Operators*, Journal of Research of the National Bureau of Standards **45**, 2133.

LeBlanc, J. P. F., A. E. Antipov, F. Becca, I. W. Bulik, G. K.-L. Chan, C.-M. Chung, Y. Deng, M. Ferrero, T. M. Henderson, C. A. Jiménez-Hoyos, E. Kozik, X.-W. Liu, A. J. Millis, N. V. Prokof'ev, M. Qin, G. E. Scuseria, H. Shi, B. V. Svistunov, L. F. Tocchio, I. S. Tupitsyn, S. R. White, S. Zhang, B.-X. Zheng, Z. Zhu, and E. Gull (2015), *Solutions of the Two Dimensional Hubbard Model: Benchmarks and Results from a Wide Range of Numerical Algorithms*, arXiv:1505.02290.

Lee, S. S. B., J. Park, and H. S. Sim (2015), *Macroscopic Quantum Entanglement of a Kondo Cloud at Finite Temperature*, Phys. Rev. Lett. **114**, 057203, arXiv:1408.1757.

Li, H., and N.-H. Tong (2015), *A Standard Basis Operator Equation of Motion Impurity Solver for Dynamical Mean Field Theory*, arXiv:1501.07689.

Liebsch, A., and H. Ishida (2012), *Temperature and bath size in exact diagonalization dynamical mean field theory*, J. Phys.: Condens. Matter **24**, 053201.

Lin, C., and A. A. Demkov (2013a), *Efficient variational approach to the impurity problem and its application to the dynamical mean-field theory*, Phys. Rev. B **88**, 035123, arXiv:1307.4982.

Lin, C., and A. A. Demkov (2013b), *Electron Correlation in Oxygen Vacancy in $SrTiO_3$*, Phys. Rev. Lett. **111**, 217601, arXiv:1311.5160.

Lin, N., C. A. Marianetti, A. J. Millis, and D. R. Reichman (2011), *Dynamical Mean-Field Theory for Quantum Chemistry*, Physical Review Letters **106**, 096402.

Lu, Y., M. Höppner, O. Gunnarsson, and M. W. Haverkort (2014), *Efficient real-frequency solver for dynamical mean-field theory*, Phys. Rev. B **90**, 085102.

Ma, Y., and H. Ma (2013), *Assessment of various natural orbitals as the basis of large active space density matrix renormalization group calculations*, J. Chem. Phys. **138**, 224105, arXiv:1303.0616.

Maier, T., M. Jarrell, T. Pruschke, and M. Hettler (2005), *Quantum cluster theories*, Rev. Mod. Phys. **77**, 1027.

Mannhart, J., and D. G. Schlom (2010), *Oxide Interfaces–An Opportunity for Electronics*, Science **327**, 1607.

McCulloch, I. P. (2007), *From density-matrix renormalization group to matrix product states*, Journal of Statistical Mechanics **2007**, P10014.

Metzner, W., and D. Vollhardt (1989), *Correlated Lattice Fermions in $d = \infty$ Dimensions*, Phys. Rev. Lett. **62**, 324.

Millis, A. J., and D. G. Schlom (2010), *Electron-hole liquids in transition-metal oxide heterostructures*, Physical Review B **82**, 073101.

Murg, V., F. Verstraete, and J. I. Cirac (2005), *Efficient evaluation of partition functions of frustrated and inhomogeneous spin systems*, Phys. Rev. Lett. **95**, 057206, arXiv:cond-mat/0501493.

Nishimoto, S., F. Gebhard, and E. Jeckelmann (2004), *Dynamical density-matrix renormalization group for the Mott-Hubbard insulator in high dimensions*, J. Phys.: Condens. Matter **16**, 7063.

Nishimoto, S., F. Gebhard, and E. Jeckelmann (2006), *Dynamical mean-field theory calculation with the dynamical density-matrix renormalization group*, Physica B: Condensed Matter **378-380**, 283.

Okamoto, S., and A. J. Millis (2004), *Electronic reconstruction at an interface between a Mott insulator and a band insulator*, Nature **428**, 630.

Östlund, S., and S. Rommer (1995), *Thermodynamic limit of the density matrix renormalization for the spin-1 Heisenberg chain*, Phys.Rev.Lett. **75**, 3537, arXiv:cond-mat/9503107.

Ozawa, T. (2015), *Ultracold atoms: Feel the gauge*, Nature Physics **11**, 801.

Peters, R. (2011), *Spectral functions for single- and multi-impurity models using density matrix renormalization group*, Phys. Rev. B **84**, 075139.

Rommer, S., and S. Ostlund (1997), *A class of ansatz wave functions for 1D spin systems and their relation to DMRG*, Phys. Rev. B **55**, 2164, arXiv:cond-mat/9606213.

Rubtsov, A. N., V. V. Savkin, and A. I. Lichtenstein (2005), *Continuous-time quantum Monte Carlo method for fermions*, Phys. Rev. B **72**, 035122, arXiv:cond-mat/0411344.

Savostyanov, D. V., S. V. Dolgov, J. M. Werner, and I. Kuprov (2014), *Exact NMR simulation of protein-size spin systems using tensor train formalism*, Phys. Rev. B **90**, 085139, arXiv:1402.4516.

Schollwöck, U. (2005), *The density-matrix renormalization group*, Rev. Mod. Phys. **77**, 259.

Schollwöck, U. (2011), *The density-matrix renormalization group in the age of matrix product states*, Annals of Physics **326**, 96, arXiv:1008.3477.

Schollwöck, U. (2013), "DMRG: Ground states, time evolution, and spectral functions," Chap. 16 (Verlag des Forschungszentrum Jülich) p. 16.1.

Schuch, N., M. M. Wolf, F. Verstraete, and J. I. Cirac (2007), *Entropy scaling and simulability by Matrix Product States*, Phys. Rev. Lett. **100**, 030504, arXiv:0705.0292.

Schüler, M., C. Renk, and T. O. Wehling (2015), *Variational exact diagonalization method for Anderson impurity models*, Phys. Rev. B **91**, 235142, arXiv:1503.09047.

Shinaoka, H., M. Dolfi, M. Troyer, and P. Werner (2014), *Hybridization expansion Monte Carlo simulation of multi-orbital quantum impurity problems: matrix product formalism and improved Monte Carlo sampling*, J. Stat. Mech., P **2014**, P0601, arXiv:1404.1259.

Simons, B. (2012), *Quantum Condensed Matter Field Theory* (Lecture Notes, University of Cambridge).

Stadler, K. M., A. Weichselbaum, Z. P. Yin, J. von Delft, and G. Kotliar (2015), *DMFT+NRG study of spin-orbital separation in a three-band Hund's metal*, arXiv:1503.06467.

Temme, K., and F. Verstraete (2010), *Stochastic Matrix Product States*, Phys. Rev. Lett. **104**, 210502, arXiv:1003.2545.

Udagawa, M., and Y. Motome (2015), *Entanglement Spectrum in Cluster Dynamical Mean-Field Theory*, J. Stat. Mech. **2015**, P01016, arXiv:1406.5960.

de Vega, I., U. Schollwöck, and F. A. Wolf (2015), *How to discretize a quantum bath for real-time evolution?*, Phys. Rev. B **92**, 155126, arXiv:1507.07468.

Verstraete, F., D. Porras, and J. Cirac (2004), *Density Matrix Renormalization Group and Periodic Boundary Conditions: A Quantum Information Perspective*, Phys. Rev. Lett. **93**, 227205.

Wang, P., G. Cohen, and S. Xu (2015), *Numerical operator method for the real time dynamics of strongly-correlated quantum impurity systems far from equilibrium*, Phys. Rev. B **84**, 085134, arXiv:1410.1480.

Weiße, A., G. Wellein, A. Alvermann, and H. Fehske (2006), *The kernel polynomial method*, Rev. Mod. Phys. **78**, 275.

Werner, P., M. Casula, T. Miyake, F. Aryasetiawan, A. J. Millis, and S. Biermann (2012), *Satellites and large doping and temperature dependence of electronic properties in hole-doped BaFe2As2*, Nature Physics **8**, 331.

Werner, P., A. Comanac, L. D. Medici, M. Troyer, and A. J. Millis (2006), *A continuous-time solver for quantum impurity models*, Phys. Rev. Lett. **97**, 076405, arXiv:cond-mat/0512727.

White, S. R. (1992), *Density matrix formulation for quantum renormalization groups*, Phys. Rev. Lett. **69**, 2863.

White, S. R. (2005), *Density matrix renormalization group algorithms with a single center site*, Phys. Rev. B **72**, 180403.

White, S. R., and I. Affleck (2008), *Spectral function for the S=1 Heisenberg antiferromagetic chain*, Phys. Rev. B **77**, 134437.

White, S. R., and A. E. Feiguin (2004), *Real time evolution using the density matrix renormalization group*, Phys. Rev. Lett. **93**, 076401, arXiv:cond-mat/0403310.

Wolf, F. A., A. Go, I. P. McCulloch, A. J. Millis, and U. Schollwöck (2015a), *Imaginary-time matrix product state impurity solver for dynamical mean-field theory*, Phys. Rev. X **5**, 041032, arXiv:1507.08650.

Wolf, F. A., S. Graser, F. Loder, and T. Kopp (2012), *Supercurrent through grain boundaries in the presence of strong correlations*, Phys. Rev. Lett. **108**, 117002, arXiv:1106.5759.

Wolf, F. A., J. A. Justiniano, I. P. McCulloch, and U. Schollwöck (2015b), *Spectral functions and time evolution from the Chebyshev recursion*, Phys. Rev. B **91**, 115144, arXiv:1501.07216.

Wolf, F. A., I. P. McCulloch, O. Parcollet, and U. Schollwöck (2014a), *Chebyshev matrix product state impurity solver for dynamical mean-field theory*, Phys. Rev. B **90**, 115124, arXiv:1407.1622.

Wolf, F. A., I. P. McCulloch, and U. Schollwöck (2014b), *Solving nonequilibrium dynamical mean-field theory using matrix product states*, Phys. Rev. B **90**, 235131, arXiv:1410.3342.

Wouters, S., W. Poelmans, P. W. Ayers, and D. V. Neck (2014), *CheMPS2: a free open-source spin-adapted implementation of the density matrix renormalization group for ab initio quantum chemistry*, Computer Physics Communications **185**, 1501, arXiv:1312.2415.

Zgid, D., and G. K.-L. Chan (2010), *Dynamical mean-field theory from a quantum chemical perspective*, The Journal of Chemical Physics **134**, 094115, arXiv:1012.3609.

Zgid, D., E. Gull, and G. Chan (2012), *Truncated Configuration Interaction expansions as solvers for correlated quantum impurity models and dynamical mean field theory*, Phys. Rev. B **86**, 165128, arXiv:1203.1914.

Zheng, B.-X., and G. K.-L. Chan (2015), *Ground-state phase diagram of the square lattice Hubbard model from density matrix embedding theory*, arXiv:1504.01784.